Inaugural - Dissertation

zur Erlangung der Doktorwürde der
Gesamtfakultät für Mathematik, Ingenieur-
und Naturwissenschaften der
Ruprecht-Karls-Universität
Heidelberg

Vorgelegt von
Anna Marleen Weidlich

Tag der müdlichen Prüfung:
26.02.2026

Quantum Chemical Investigation of Open-Shell Functional Organic Molecules

Anna Marleen Weidlich

Dezember 2026

Gutachter:

Prof. Dr. Andreas Dreuw
Prof. Dr. Oriol Vendrell

Für meine Eltern Martina und Gerd

Abstract

Functional molecules are species that hold properties which enable them to perform a specific function. In their targeted design, quantum mechanical investigations play a central role, as they complement experimental data and enable the prediction of molecular properties. Functional organic molecules are the focus of research efforts in various fields, where organic electronics is one of the most prominent.

Especially acenes and their derivatives are promising candidates for various applications in organic electronics. In this regard, their absorption spectra present a feature of particular interest and are well-characterized experimentally and theoretically. In **Chapter 3**, the excited states of acene cations are examined using algebraic diagrammatic construction (ADC) methods and time-dependent density functional theory (TD-DFT). Benchmark studies are performed to assess the accuracy of excitation energies obtained at different levels of ADC and different exchange-correlation kernels for TD-DFT against experimental values. It is shown that excited states observed in neutral acenes are retained in their cationic counterparts by analyzing the main orbital contributions of the excitations. Furthermore, new excited states that appear in the spectra of the cations are characterized. The behavior of the excitation energies of both neutral and cationic acenes with increasing length is examined using TD-DFT, which shows that excitation energies decrease with increasing acene length and converge towards a certain value. The increasingly poor description of longer acenes using DFT, due to the single-reference ground state description, is discussed.

Furthermore, the exciton properties, i.e. exciton size, hole and electron size and correlation coefficient are computed for the excited states of neutral and cationic acenes using TD-DFT. Their behavior with increasing acene length is explored, where different trends can be observed for the excited states of neutral and cationic acenes. For excited states of the same character, the excited state of the neutral acene shows a larger exciton size, than that of the corresponding cationic acene. It is also observed that with increasing acene length, the hole size grows faster than the electron size for cationic excited states, while for neutral excited states they increase equally fast. Furthermore, the correlation coefficient is larger and grows faster for excited states that are described by at least two orbital transitions, while it is smaller and grows slower for excited states that are mainly described by one orbital transition. Finally, previously established criteria are employed to show that the excited states ^1B_b and ^2B_b have plasmonic character.

Organic molecules with high degrees of diradical character are another class of molecules which show favorable properties for the application in organic electronics. As open-shell systems they are generally unstable so that the design of stable organic diradicals is an active field of research. The theoretical description of most species of interest is challenging, since the use of multi-reference methods would be required, but is not computationally feasible. The open-shell nature of several organic diradicals is investigated in **Chapter 4** by computing and analyzing the diradical

character, multiplicity of the ground state, singlet-triplet gap and other properties using DFT, TD-DFT and spin-flip TD-DFT (SF-TD-DFT). The first project investigates two regioisomeric benzodithiophenes, where the *ortho*-isomer shows dimerization to form a dimer cage. The results show a closed-shell ground state for the *para*-isomer and a diradical ground state for the *ortho*-isomer. Furthermore, the reaction mechanism of the dimerization is proposed to proceed via the consecutive formation of two sets of two σ-bonds. In the second project, the open-shell nature of an indeno-diazatetracene-σ-dimer, built from two radical monomer units, is investigated and indicates a high diradical character of the ground state. Derived from this system, two diradical model dimers are designed and examined in the third project to explore the relation between their molecular geometry, ground state description and open-shell character. Both dimers show the expected interdependence of the angle between the monomers, the ground state employed for optimization and the diradical character. Furthermore, the development of the excitation energies of the first excited singlet and triplet states with varying diradical character is analyzed and the expected mirrored behavior of the singlet-triplet gap and the diradical character is observed.

The possibility of inverted energy gaps between the first excited singlet and triplet states present an interesting opportunity with regard to fluorescence emitters in organic light-emitting diode (OLED) applications. While this singlet-triplet gap is positive for most systems, the inversion could increase the population of the emissive singlet state and thereby increase OLED efficiency. It was observed in a previous study that negative singlet-triplet gaps become smaller and eventually positive as the accuracy of the theoretical treatment is increased. In **Chapter 5**, the influence of the employed level of theory on the singlet-triplet gaps is investigated by computing them at increasing ADC orders and increasing basis set size. Initial computations show that inverted singlet-triplet gaps are obtained for the investigated molecules only at highly symmetric geometries. The singlet-triplet gaps obtained at ADC(1) are positive and then decrease going to ADC(2), where only negative values are observed. The trend shows another increase for ADC(3), however only resulting in a positive value for one of the investigated systems. The singlet-triplet gap then decreases again for ADC(4) and is negative for all investigated molecules. Furthermore, the effect of the basis set size on the singlet-triplet gap is examined and shows an increase with increasing basis set size, which is however small in comparison to the effect of the employed level of ADC.

Label molecules enable the performance of fluorescence and electron paramagnetic resonance (EPR) spectroscopy on biomolecules, which support the elucidation of their structure. In previous work, a mechanism for quenching of fluorescence in an established spin label via internal conversion (IC) to a dark low-lying excited state was presented. Based on this, the design of a combined fluorescence and spin label is explored in **Chapter 6** using TD-DFT. Excitation energies, oscillator strengths and transition densities are computed for the excited states of the existing spin label and derivatives. A dark first excited doublet state and bright second excited doublet state are observed for all investigated molecules. Furthermore, the equilibrium geometries of both excited states and the minimum energy crossing point of the conical intersection (CI) seam space between them is computed. The efficiency of the proposed fluorescence quenching pathway is analyzed using the computed points on the potential energy surfaces. Based on this investigation, a decreased rate of IC is expected for one of the derivatives.

Zusammenfassung

Funktionelle Moleküle sind chemische Spezies, die Eigenschaften aufweisen, die es ihnen ermöglichen, eine bestimmte Funktion zu erfüllen. Bei ihrer gezielten Entwicklung spielen quantenmechanische Untersuchungen eine zentrale Rolle, da sie experimentelle Daten ergänzen und die Vorhersage molekularer Eigenschaften ermöglichen. Funktionelle organische Moleküle stehen im Mittelpunkt der Forschung in verschiedenen Bereichen, wobei die organische Elektronik einer der bekanntesten ist.

Insbesondere Acene und ihre Derivate sind vielversprechende Kandidaten für verschiedene Anwendungen in der organischen Elektronik. In dieser Hinsicht sind insbesondere ihre Absorptionsspektren von Interesse und sind experimentell und theoretisch gut charakterisiert. In **Kapitel 3** werden die angeregten Zustände von Acen-Kationen mit Hilfe algebraische diagrammatische Konstruktions (ADC) Methoden und zeitabhängige Dichtefunktionaltheorie (TD-DFT) untersucht. Es werden Benchmark-Studien durchgeführt, um die Genauigkeit der mit verschiedenen ADC-Methoden und verschiedenen Austausch-Korrelations-Funktionalen für TD-DFT berechneten Anregungsenergien zu bestimmen. Durch die Analyse der wichtigsten Orbitalbeiträge der Anregungen wird gezeigt, dass die in neutralen Acenen beobachteten angeregten Zustände in ihren kationischen Gegenstücken erhalten bleiben. Darüber hinaus werden neue angeregte Zustände, die in den Spektren der Kationen auftreten charakterisiert. Das Verhalten der Anregungsenergien sowohl neutraler als auch kationischer Acene mit zunehmender Länge wird mittels TD-DFT untersucht, was zeigt, dass die Anregungsenergien mit zunehmender Acenlänge abnehmen und gegen einen bestimmten Wert konvergieren. Die zunehmend schlechtere Beschreibung längerer Acene mittels DFT aufgrund der Beschreibung des Grundzustands mit nur einer Determinante wird diskutiert.

Darüber hinaus werden die Exzitoneigenschaften, d. h. die Exzitongröße, die Loch- und Elektronengröße sowie der Korrelationskoeffizient, für die angeregten Zustände von neutralen und kationischen Acenen unter Verwendung von TD-DFT berechnet. Ihr Verhalten bei zunehmender Acenlänge wird untersucht, wobei unterschiedliche Trends für die angeregten Zustände von neutralen und kationischen Acenen beobachtet werden können. Bei angeregten Zuständen gleichen Charakters weist der angeregte Zustand des neutralen Acens eine größere Exzitongröße auf als der des entsprechenden kationischen Acens. Es wird auch beobachtet, dass mit zunehmender Acenlänge die Lochgröße bei kationischen angeregten Zuständen schneller wächst als die Elektronengröße, während sie bei neutralen angeregten Zuständen gleich schnell zunehmen. Darüber hinaus ist der Korrelationskoeffizient größer und wächst schneller für angeregte Zustände, die durch mindestens zwei Orbitalübergänge beschrieben werden, während er kleiner ist und langsamer wächst für angeregte Zustände, die hauptsächlich durch einen Orbitalübergang beschrieben werden. Schließlich werden in vorherigen Arbeiten festgelegte Kriterien verwendet, um zu zeigen, dass die angeregten Zustände ^1B_b und ^2B_b plasmonischen Charakter haben.

Organische Moleküle mit einem hohen Grad an Diradikalcharakter sind eine weitere Klasse von Molekülen, die vorteilhafte Eigenschaften für die Anwendung in der organischen Elektronik aufweisen. Als Systeme mit ungepaarten Elektronen, sind sie im Allgemeinen instabil, sodass die Entwicklung stabiler organischer Diradikale ein aktives Forschungsgebiet ist. Die theoretische Beschreibung der meisten chemischen Spezies von Interesse ist eine Herausforderung, da hierfür Multi-Referenz-Methoden erforderlich wären, die jedoch aufgrund des rechnerischen Anspruchs nicht verwendbar sind. Das Ausmaß der offenschaligen Natur mehrerer organischer Diradikale wird in **Kapitel 4** untersucht, indem der Diradikalcharakter, die Multiplizität des Grundzustands, der Singulett-Triplett-Abstand und andere Eigenschaften mit Hilfe von DFT, TD-DFT und Spin-Flip-TD-DFT (SF-TD-DFT) berechnet und analysiert werden. Das erste Projekt untersucht zwei regioisomere Benzodithiophene, wobei das *ortho*-Isomer eine Dimerisierung zu einem Dimerkäfig zeigt. Die Ergebnisse zeigen einen geschlossenenschaligen Grundzustand für das *para*-Isomer und einen diradikalen Grundzustand für das *ortho*-Isomer. Darüber hinaus wird vorgeschlagen, dass der Reaktionsmechanismus der Dimerisierung über die aufeinanderfolgende Bildung von jeweils zwei σ-Bindungen abläuft. Im zweiten Projekt wird die offenschalige Natur eines Indeno-Diazatetracen-σ-Dimers untersucht, das aus zwei radikalischen Monomereinheiten aufgebaut ist, und weist auf einen hohen Diradikalcharakter des Grundzustands hin. Aus diesem System abgeleitet, werden im dritten Projekt zwei diradikale Modell-Dimere entworfen und untersucht, um den Zusammenhang zwischen ihrer Molekülgeometrie, der Beschreibung des Grundzustands und dem offenschaligen Charakter zu erforschen. Beide Dimere zeigen den erwarteten Zusammenhang zwischen dem Winkel zwischen den Monomeren, dem für die Optimierung verwendeten Grundzustand und dem Diradikalcharakter. Darüber hinaus wird die Entwicklung der Anregungsenergien des ersten angeregten Singulett- und Triplettzustands bei unterschiedlichem diradikalem Charakter analysiert und das erwartete gespiegelte Verhalten des Singulett-Triplett-Abstands und des Diradikalcharakters beobachtet.
Die Möglichkeit invertierter Energieabstände zwischen dem ersten angeregten Singulett- und Triplettzustand bietet interessante Möglichkeiten für Fluoreszenzemitter in organischen Leuchtdioden (OLED). Während dieser Singulett-Triplett-Abstand bei den meisten Systemen positiv ist, könnte die Inversion die Population des emittierenden Singulettzustands erhöhen und damit die Effizienz der OLED steigern. In einer früheren Studie wurde beobachtet, dass negative Singulett-Triplett-Abstände kleiner werden und schließlich positiv werden, wenn die Genauigkeit der theoretischen Beschreibung erhöht wird. In **Kapitel 5** wird der Einfluss des verwendeten Theorie-Niveaus auf die Singulett-Triplett-Abstände untersucht, indem diese bei steigenden Ordnungen der ADC Methode und steigender Basis Satz Größe berechnet werden. Erste Berechnungen zeigen, dass invertierte Singulett-Triplett-Abstände für die untersuchten Moleküle nur bei hochsymmetrischen Geometrien erhalten werden. Die bei ADC(1) erhaltenen Singulett-Triplett-Abstände sind positiv und nehmen dann bis ADC(2) ab, wo nur negative Werte beobachtet werden. Der Trend zeigt einen weiteren Anstieg für ADC(3), führt jedoch nur bei einem der untersuchten Systeme zu einem positiven Wert. Der Singulett-Triplett-Abständ nimmt dann für ADC(4) wieder ab und ist für alle untersuchten Moleküle negativ. Darüber hinaus wird der Einfluss der Basis Satz Größe auf die Singulett-Triplett-Abstände untersucht und zeigt einen Anstieg mit zunehmender Basis Satz Größe, der jedoch im Vergleich zum Einfluss der verwendeten ADC-Ordnung gering ist.
Markermoleküle ermöglichen die Durchführung von Fluoreszenz- und Elektronenspinresonanzspektroskopie (EPR) an Biomolekülen, was zur Aufklärung ihrer Struktur beiträgt. In früheren Arbeiten wurde ein Mechanismus zur Löschung der Fluoreszenz in einem etablierten Spinmarker

durch interne Konversion (IC) in einen dunklen, niedrig liegenden angeregten Zustand vorgestellt. Auf dieser Grundlage wird in **Kapitel 6** die Konstruktion eines kombinierten Fluoreszenz- und Spinmarkers unter Verwendung von TD-DFT untersucht. Für die angeregten Zustände des bestehenden Spinmarkers und seiner Derivate werden Anregungsenergien, Oszillatorstärken und Übergangsdichten berechnet. Für alle untersuchten Moleküle werden ein dunkler erster angeregter Dublettzustand und ein heller zweiter angeregter Dublettzustand beobachtet. Darüber hinaus werden die Gleichgewichtsgeometrien beider angeregter Zustände und der Punkt minimaler Energie des konischen Schnitts (CI) zwischen ihnen berechnet. Die Effizienz des vorgeschlagenen Fluoreszenzlöschungsweges wird anhand der berechneten Punkte auf den Potenzialenergieoberflächen analysiert. Basierend auf dieser Untersuchung wird für eines der Derivate eine verringerte IC-Rate erwartet.

Contents

Chapter 1

Introduction

The understanding and design of functional molecules is an essential part in the development of new technologies. Functional molecules in general are species, which possess a property that enables them to fulfill a certain purpose. This purpose naturally depends on the desired application. The targeted design of such species is a central part of research in areas such as electronics, energy management, sensor technology, catalysis, biomedicine and many others.[1–15] In any case however, quantum chemical simulations play a crucial role in the investigation and design of novel and existing functional molecules.[16–27] On the one hand, simulations enable the computation of molecular properties, which are not easily accessible experimentally. Furthermore, computational results can complement experimental measurements and aid in their interpretation. On the other hand, molecular properties can be predicted for a large number of species in a relatively short amount of time, which can greatly reduce experimental efforts. The great amount of data, which can be gathered using quantum chemical simulations, can be very useful for the understanding of structure-property relationships and can furthermore provide data sets for the development of machine learning models.

The application of quantum chemical methods to chemical systems is, however, fundamentally limited by the complexity of the problem.[28] Any system that consists of more than two particles cannot be described exactly so that approximations have to be introduced, which lower the computational cost, but also the accuracy of the simulation at the same time. The choice of methodology is therefore always influenced by an assessment of cost versus accuracy and the obtained results have to be evaluated with the quality of the results in mind. In this thesis, various potential functional organic molecules are investigated employing different quantum chemical methods to gain understanding about their molecular properties.

Due to their existing and potential application as organic semiconductors, acenes are a prominent class of functional organic molecules.[1,2,4,5,29–33] With an increase in the number of rings, the excitation energy of the first excited state decreases rapidly, which is an interesting property with respect to their application. However, it also entails a decrease in stability and an increasing diradical character, which is why larger acenes are on the one hand difficult to synthesize and on the other hand difficult to describe theoretically.[4,34,35] In the description of the excited states of potential organic materials, both the quantum chemical and the solid state picture are relevant. While the former describes the excited states of single molecules, the latter is a framework for excited states in extended solids, called excitons or plasmons.[36–41] The absorption spectra and excited state properties of acenes are important for various applications. They show three characteristic

peaks called the p-, α- and β-bands, which correspond to the excited states ^1L_w, ^1L_s and ^1B_b according to Platt's nomenclature and re-labeling in work previously published.[29,30,42] They are described by the orbital transitions H→L for ^1L_w and linear combination of H−1→L and H→L+1 for ^1L_s and ^1B_b. In **Chapter 3**, the excited states of acene radical cations are set into relation to the well-known excited states of neutral acenes, by analyzing their prominent orbital transitions. The trend of the excitation energies as well as exciton properties with increasing acene length of both the excited states of neutrals and cations are examined. Furthermore, the excited states ^1B_b and ^2B_b of anthracene and the anthracene cation, respectively, are investigated regarding plasmon characteristics.

Diradicals are another class of molecules, which have gained attention for possible applications in organic electronics as well as non-linear optics and spintronics.[43–50] Due to their open-shell nature, they are generally unstable, which is why research efforts are directed at the development of stable diradical organic molecules.[51–63] The quantum chemical description of diradicals presents a challenge, since it requires a multi-reference method, which can however not be applied to a majority of organic molecules of interest, due to the high computational cost.[43] Options to approximately describe diradicals within a single-reference formalism include spin-flip methods and the employment of a broken-symmetry wavefunction.[64–66] In **Chapter 4**, different organic molecules are examined regarding their open-shell nature by computing the diradical character, multiplicity of their ground state, singlet-triplet gap, spin densities and NICS-values. Furthermore, the relation between molecular geometry, chosen ground state description and diradical character is explored.

The development of fluorescence organic light-emitting diode (OLED) materials is an active area of research, where organic molecules with inverted singlet-triplet gaps have gained special interest.[67–71] Here, the singlet-triplet gap refers to the energy difference between the first excited singlet and triplet states, which is positive for most systems.[72–74] A negative singlet-triplet gap however could increase the population of the emissive singlet state are thereby increase OLED efficiency.[75,76] It was suggested in previous work that quantum chemical studies incorrectly predict inverted singlet-triplet gaps, due to insufficient accuracy of the employed methodology.[77] In **Chapter 5**, several small organic molecules, which are expected to show inverted singlet-triplet gaps, are chosen. Their singlet-triplet gaps are computed at increasing levels of theory to examine whether negative singlet-triplet gaps vanish with increasing accuracy of the employed description.

The function and mechanism of biomolecules is closely related to their structure, which can be investigated using spectroscopic experiments. Here, label molecules play an important role to enable the application of fluorescence and electron paramagnetic resonance (EPR) spectroscopy to otherwise unresponsive species.[78–89] An existing ribonucleic acid (RNA) spin label and a structurally related fluorescence label were studied in previous work, to investigate the fluorescence quenching in the spin label.[15,90–95] The quenching mechanism was proposed to proceed via IC to a dark low-lying excited state. In **Chapter 6** this spin label and derivatives are examined with the goal of exploring the design of a combined fluorescence and spin label as such a label would facilitate the performance of fluorescence and EPR spectroscopy on the same RNA sample. The excited state landscape of the spin label and derivatives is therefore investigated with respect to the previously proposed de-excitation pathway.

Chapter 2

Theoretical Background

This section presents an overview of the established theoretical framework employed throughout this work. The reader is assumed to be familiar with basic concepts of quantum chemistry including the Born-Oppenheimer approximation, Hartree-Fock theory and Møller-Plesset perturbation theory.

2.1 Density Functional Theory

One of the most widely employed quantum chemical approaches to describe molecular systems is density-functional theory (DFT), due to its favorable balance between computational cost and accuracy. In DFT, the electron density $\rho(r)$ of a system is chosen as a physical observable that allows for the construction of the molecular Hamiltonian, where $\rho(r)$ describes the electron density at a point r in space.[96] The ground state energy of a system is therefore a functional of the electron density. A fundamental advantage of DFT over wavefunction-based methods is the dependence of the electron density on only three variables as opposed to the dependence of a wavefunction on $4N$ variables, where N is the number of electrons.
The electronic Hamiltonian $\hat{H}$ for any atom or molecule with N electrons within the Born-Oppenheimer (BO) approximation is given by

$$\hat{H} = \hat{T} + \hat{V}_{ne} + \hat{V}_{ee} + \hat{V}_{nn}, \tag{2.1}$$

where the first term is the kinetic energy operator of the electrons

$$\hat{T} = \sum_{i=1}^{N} (-\frac{1}{2}\nabla_i^2), \tag{2.2}$$

with the electron index i. The second term is the external potential or electron-nucleus attraction

$$\hat{V}_{ne} = \sum_{i=1}^{N} v(r_i), \tag{2.3}$$

$$\text{with} \quad v(r_i) = -\sum_{K}^{N_n} \frac{Z_K}{r_{iK}}, \tag{2.4}$$

which is a sum of one-particle potentials $v(r_i)$, with the number of nuclei N_n, the nuclei index K, and nuclear charge Z_K of nucleus K. The third term is the electron-electron repulsion energy

operator

$$\hat{V}_{ee} = \sum_{i>j}^{N} \frac{1}{r_{ij}} \tag{2.5}$$

and the fourth term is the nucleus-nucleus repulsion operator

$$\hat{V}_{nn} = \sum_{K<L} \frac{Z_K Z_L}{R_{KL}}, \tag{2.6}$$

which is a constant within the BO approximation and will be omitted in the following. As the electron density inherently delivers both the total number of electrons, when integrated over all space, as well as the position of the nuclei as maxima of the electron density, it carries all the required information for the construction of the Hamiltonian. The Thomas-Fermi method presents an early attempt at formulating an energy functional, where the potential energy terms are described classically and the kinetic and exchange terms are derived from the uniform electron gas.[97,98] However, this approach does not yield sufficiently exact results for chemical systems, as it does not predict the formation of chemical bonds.

The theoretical basis for DFT is set by the Hohenberg-Kohn theorems.[99] The Hamiltonian of an electronic system is completely determined by the number of electrons N and the external potential $v(r)$. As mentioned above, the electron density inherently delivers the number of electrons by integration of the density over all space. The first Hohenberg-Kohn theorem (HKI) states that the external potential $v(r)$ is determined by the electron density $\rho(r)$ to within a constant. The electron density of a system therefore determines the ground state Hamiltonian, the ground state wavefunction and all other ground state electronic properties. In other words, HKI states that there is a one-to-one mapping between the electron density and the ground state energy E_0 of the system so that the ground state energy is a functional of the electron density

$$E_0 = E_0[\rho_0]. \tag{2.7}$$

The second Hohenberg-Kohn theorem (KHII) shows that the density obeys a variational principle. Given a trial electron density $\rho_{trial}(r)$, the expectation value of the asscociated wavefunction Ψ_{trial} can be evaluated as follows and will be greater or equal to the true ground state energy.

$$\langle \Psi_{trial} | \, H_{trial} \, | \Psi_{trial} \rangle = E_{trial} \geq E_0. \tag{2.8}$$

The foundation for the applicability of DFT to molecular systems is the Kohn-Sham method.[100] In Kohn-Sham DFT, orbitals (one-electron functions) ϕ_i are reintroduced to construct an electron density of non-interacting electrons. The external potential is then chosen in such a way that the density of this fictitious system of non-interacting electrons is identical to that of the interacting system. Due to the introduction of orbitals, the Hamiltonian can be constructed as a sum of one-electron operators. Furthermore, the eigenfunctions are Slater determinants of the one-electron functions and the eigenvalues are the sum of the one-electron eigenvalues. The energy functional

$E[\rho(r)]$ can then be expressed as

$$E[\rho(r)] = T_{ni}[\rho(r)] + V_{ne}[\rho(r)] + V_{ee}[\rho(r)] + \underbrace{\Delta T[\rho(r)] + \Delta V_{ee}[\rho(r)]}_{E_{xc}[\rho(r)]}, \tag{2.9}$$

where $T_{ni}[\rho(r)]$ is the kinetic energy of the non-interacting electrons, $V_{ne}[\rho(r)]$ is the nuclear-electron repulsion and $V_{ee}[\rho(r)]$ is the classical electron-electron repulsion or Coulomb interaction. The last two terms represent correction terms, where the first one $\Delta T[\rho(r)]$ corrects the kinetic energy due to the interacting nature of the electrons and the second one $\Delta V_{ee}[\rho(r)]$ includes all non-classical corrections to the electron-electron repulsion energy. These can be summarized as the exchange-correlation term $E_{xc}[\rho(r)]$, which is the only unknown term in this expression.
Since the wavefunction is a Slater-determinant, the density can be obtained from the orbitals ϕ_i as

$$\rho(r) = \sum_{i=1}^{N} \langle \phi_i | \phi_i \rangle . \tag{2.10}$$

The orbitals that satisfy the pseudo eigenvalue equation

$$\hat{h}_i^{KS} \phi_i = \epsilon_i \phi_i \tag{2.11}$$

with the orbital energy ϵ_i of orbital i, minimize the energy, where the Kohn-Sham one-electron operator $\hat{h}_i^{KS}$ is defined as

$$\hat{h}_i^{KS} = -\frac{1}{2}\nabla_i^2 + v(r) + \int \frac{\rho(r')}{|r - r'|} dr' + \frac{\delta E_{xc}}{\delta \rho(r)} \tag{2.12}$$

$$\hat{h}_i^{KS} = -\frac{1}{2}\nabla_i^2 + v_{KS}(r). \tag{2.13}$$

Analogous to Hartee-Fock (HF) theory, the orbitals ϕ_i are found via an iterative self-consistent field (SFC) procedure, as the Hamiltonian depends on the density, which in turn depends on the orbitals. An important difference to HF theory is that for $i = j$, the Coulomb functional and the exchange correlation functional are not equal so that they do not cancel each other out.

$$V_{ee}[\rho(r)] + E_{xc}[\rho(r)] \neq 0. \tag{2.14}$$

This leads to the self-interaction error, which allows unphysical interactions of electrons with themselves and causes DFT to give inaccurate descriptions of various properties such as for example binding energies and reaction barriers.
In the unrestricted case, the densities of α- and β- electrons are allowed to be different or, from the perspective of the orbitals, the spatial component of α- and β-orbitals is not restricted to be identical.[101] The electron densities of α- and β-electrons are

$$\rho_\alpha(r) = \sum_{i=1}^{n_\alpha} |\phi_i^\alpha|^2 \tag{2.15}$$

$$\rho_\beta(r) = \sum_{i=1}^{n_\beta} |\phi_i^\beta|^2 \tag{2.16}$$

and the total electron density is given by

$$\rho(r) = \rho_\alpha(r) + \rho_\beta(r). \tag{2.17}$$

The energy functional for unrestricted Kohn-Sham DFT is similar to the restricted case

$$E^{UKS}[\rho_\alpha, \rho_\beta] = T^{UKS}[\rho_\alpha, \rho_\beta] + V_{ne}[\rho] + V_{ee}[\rho] + E_{xc}^{UKS}[\rho_\alpha, \rho_\beta], \tag{2.18}$$

with the unrestricted kinetic energy functional $T^{UKS}[\rho_\alpha, \rho_\beta]$, the electron-nuclei attraction or external potential $V_{ne}[\rho]$, the electron-electron repulsion $V_{ee}[\rho]$ and the unrestricted exchange-correlation term $E_{xc}^{UKS}[\rho_\alpha, \rho_\beta]$. The unrestricted Kohn-Sham orbitals can be obtained from solving the equations

$$\hat{h}_i^{UKS,\alpha}\phi_i^\alpha = \epsilon_i^\alpha \phi_i^\alpha \tag{2.19}$$

$$\hat{h}_i^{UKS,\beta}\phi_i^\beta = \epsilon_i^\beta \phi_i^\beta \tag{2.20}$$

$$\tag{2.21}$$

with the unrestricted Kohn-Sham one-electron operators

$$\hat{h}_i^{UKS,\alpha} = -\frac{1}{2}\nabla_i^2 + v(r) + \int \frac{\rho(r')}{|r_i - r'|}dr' + \frac{\delta E_{xc}^{UKS}[\rho_\alpha, \rho_\beta]}{\delta \rho_\alpha(r)} \tag{2.22}$$

$$\hat{h}_i^{UKS,\beta} = -\frac{1}{2}\nabla_i^2 + v(r) + \int \frac{\rho(r')}{|r_i - r'|}dr' + \frac{\delta E_{xc}^{UKS}[\rho_\alpha, \rho_\beta]}{\delta \rho_\beta(r)} \tag{2.23}$$

in analogy to the restricted case by employing an iterative SCF procedure.
The expression for the energy functional in **Equation 2.9** is exact and the only unknown term is the exchange-correlation correction. The development of approximations for E_{xc} is therefore the subject of substantial research efforts. It is worth noting that with the introduction of approximations for E_{xc}, DFT is no longer a variational method.
DFT functionals are divided into different groups dependent on their construction, which are also referred to as rungs of Jacob's ladder, where the rung increases with increasing complexity of the functional.[102] The first generation or rung of E_{xc} functionals are based on the local-density approximation (LDA), where the exchange-correlation functional depends only on the electron density at each point in space.[103,104] The next two groups are generalized gradient approximation (GGA) functionals, where in addition to the local density, the gradient of the electron density is employed and meta-GGA functionals, which furthermore incorporate the second derivative of the density and/or the kinetic energy density.[102,105] The fourth generation of E_{xc} functionals are called hybrid functionals, which include a certain fraction of "exact" HF exchange to replace a corresponding fraction of exchange obtained from LDA, GGA or meta-GGA functionals.[106] The fifth and last rung is that of double hybrid functionals, which additionally to HF exchange include a certain contribution of a second order Møller-Plesset perturbation theory (MP2) energy, obtained based on the DFT orbitals.[107,108] Another feature of DFT functionals, which can be combined with either hybrid or double hybrid functionals, is range-separation of the amount of incorporated HF exchange so that short-range interactions are mostly described by DFT exchange, while long-range interactions are mainly described by HF exchange.[109,110]
It is important to note that while the complexity of DFT functionals increases with the rungs

of Jacob's ladder, their overall performance does not necessarily improve. Due to the unknown nature of the exchange-correlation functional, DFT is not systematically improvable, which is why benchmarks have to be performed to determine the performance of a DFT functional for different molecule classes and properties of interest.
Another important weakness of DFT is the missing incorporation of long-range interactions or dispersion.[111,112] For this reason, dispersion corrections have been developed, which are essential for the description of any molecular system using DFT.[113–115] Furthermore, the self-interaction error leads to the preference of delocalized electron distributions, which causes DFT to incorrectly describe, for example, the stretching of $H_2{}^+$, giving fractional charges upon dissociation and an incorrect energy barrier.[116] As a single-determinant method, DFT is also limited to systems with a single-determinant ground state and fails to describe, for example, the stretching of H_2, as well as systems with a high diradical character.[116]

2.2 Time-dependent Density Functional Theory

Time-dependent density functional theory (TD-DFT) presents an extension of DFT to describe excited states.[117–120] Here, the Runge-Gross theorem presents the theoretical basis, as HKI for ground state DFT, as it states that the time-dependent electron density $\rho(r,t)$ determines the time-dependent external potential $v(r,t)$ up to a time-dependent function and therefore determines the time-dependent electronic Hamiltonian

$$\hat{H}(t) = \hat{T} + \hat{V}_{ee} + \hat{V}_{ne}(t), \tag{2.24}$$

where the first two terms refer to the kinetic energy operator of the electrons and the electron-electron repulsion operator described above, respectively.[117] The last term is a time-dependent external potential, which is a sum of time-dependent one-particle potentials

$$\hat{V}_{ne}(t) = \sum_{i}^{N} v(r_i, t). \tag{2.25}$$

The time-dependent density therefore furthermore determines the time-dependent wavefunction up to a time-dependent phase factor. An equivalent for HKII is required as well, which shows that the variational principle applies for the time-dependent density. The exact time-dependent electron density can be obtained using the quantum-mechanical action integral

$$A[\rho] = \int_{t_0}^{t_1} \langle \Psi[\rho](r,t)| \, i\frac{\partial}{\partial t} - \hat{H}(r,t) \, |\Psi[\rho](r,t)\rangle \, dt \tag{2.26}$$

and the stationary action principle, which states that the action integral is stationary for the exact electron density

$$\frac{\delta A[\rho]}{\delta \rho(r,t)} = 0. \tag{2.27}$$

This has been shown to be trivial recently, however, an extended discussion is out of the scope of this thesis.[121] As for the time-independent case, a time-dependent reference system of non-interacting electrons is constructed from orbitals $\phi_i(r,t)$ and is equal to the exact time-dependent

electron density of interacting electrons due to the time-dependent external one-particle potential $v(r,t)$. The time-dependent density is then given by

$$\rho(r,t) = \sum_{i}^{N} |\phi_i(r,t)|^2. \tag{2.28}$$

In analogy to the time-independent case, the time-dependent Kohn-Sham one-electron operator is given by

$$\hat{h}_i^{TDKS} = -\frac{1}{2}\nabla_i^2 + v(r,t) + \int \frac{\rho(r',t)}{|r-r'|} d^3r' + \frac{\delta A_{xc}[\rho]}{\delta\rho(r,t)}. \tag{2.29}$$

As for ground state DFT, the time-dependent exchange-correlation action functional or exchange-correlation kernel functional is not known and has to be approximated. For the construction of the exchange-correlation kernel, the adiabatic local density approximation (ALDA) is applied, which assumes that the density varies slowly in time. This allows for the replacement of time-independent exchange-correlation kernels with time-independent functionals. Based on this approximation, ground state exchange-correlation functionals can be employed in TD-DFT.
In the unrestricted formalism the time-dependent Kohn-Sham one-electron operators are given as follows.[122]

$$\hat{h}_i^{UTDKS,\alpha} = -\frac{1}{2}\nabla_i^2 + v(r,t) + \int \frac{\rho(r',t)}{|r-r'|} d^3r' + \frac{\delta A_{xc}[\rho]}{\delta\rho_\alpha(r,t)} \tag{2.30}$$

$$\hat{h}_i^{UTDKS,\beta} = -\frac{1}{2}\nabla_i^2 + v(r,t) + \int \frac{\rho(r',t)}{|r-r'|} d^3r' + \frac{\delta A_{xc}[\rho]}{\delta\rho_\beta(r,t)}. \tag{2.31}$$

The most popular approach for the calculation of excitation energies and oscillator strengths using TD-DFT is linear-response TD-DFT (LR-TD-DFT).[123] Here, a time-dependent external field is applied to the DFT ground state and the linear response of the electron density is computed. The excitation energies ω can be obtained by solving the TD-DFT secular equations

$$\begin{bmatrix} \mathbf{A} & \mathbf{B} \\ \mathbf{B}^* & \mathbf{A}^* \end{bmatrix} \begin{bmatrix} \mathbf{X} \\ \mathbf{Y} \end{bmatrix} = \omega \begin{bmatrix} 1 & 0 \\ 0 & -1 \end{bmatrix} \begin{bmatrix} \mathbf{X} \\ \mathbf{Y} \end{bmatrix}, \tag{2.32}$$

where

$$A_{ia,jb} = \delta_{ij}\delta_{ab}(\epsilon_a - \epsilon_i) + (ia|jb) + (ia|f_{xc}|jb) \tag{2.33}$$

$$B_{ia,jb} = (ia|bj) + (ia|f_{xc}|bj). \tag{2.34}$$

The first term of matrix $\mathbf{A}$ is the difference in orbital energies of orbitals i and a. The following terms describe the linear response of the exchange-correlation potential, where

$$(ia|f_{xc}|jb) = \int \phi_i^*(r)\phi_a(r) \frac{\delta^2 E_{xc}}{\delta\rho(r)\delta\rho(r')} \phi_b^*(r')\phi_j(r'). \tag{2.35}$$

In the unrestricted case, the matrices are expressed as

$$A_{ia\alpha,jb\alpha} = \delta_{ij}\delta_{ab}(\epsilon_{a\alpha} - \epsilon_{i\alpha}) + (i_\alpha a_\alpha|j_\alpha b_\alpha) + (i_\alpha a_\alpha|f_{xc}|j_\alpha b_\alpha) \tag{2.36}$$

$$A_{ia\alpha,jb\beta} = (i_\alpha a_\alpha|j_\beta b_\beta) + (i_\alpha a_\alpha|f_{xc}|j_\beta b_\beta) \tag{2.37}$$

$$B_{ia\alpha,jb\alpha} = (i_\alpha a_\alpha|b_\alpha j_\alpha) + (i_\alpha a_\alpha|f_{xc}|b_\alpha j_\alpha) \tag{2.38}$$

$$B_{ia\alpha,jb\beta} = (i_\alpha a_\alpha|b_\beta j_\beta) + (i_\alpha a_\alpha|f_{xc}|b_\beta j_\beta), \tag{2.39}$$

with the exchange-correlation potential

$$(i_\sigma a_\sigma|f_{xc}|j_\tau b_\tau) = \int \phi_i^{\sigma *}(r)\phi_a^\sigma(r)\frac{\delta^2 E_{xc}}{\delta\rho_\sigma(r)\delta\rho_\tau(r')}\phi_b^{\tau *}(r')\phi_j^\tau(r'), \tag{2.40}$$

where σ and τ denote spin variables ($\sigma = \alpha, \beta$, $\tau = \alpha, \beta$).[122,124,125] The corresponding $\beta\beta$ and $\beta\alpha$ matrix elements can be obtained by interchanging the indices α and β.
As in time-dependent HF (TD-HF), the Tamm-Danncoff approximation (TDA) can be applied to LR-TD-DFT by neglecting the **B** matrix in **Equation 2.32**, where the eigenvalue equation is

$$\mathbf{AX} = \omega\mathbf{X}, \tag{2.41}$$

which presents a good approximation to TD-DFT in many cases and can solve problems encountered due to ground state instabilities.[126] As for ground state DFT, the accuracy of a certain functional/kernel is not systematically improvable, which is why benchmark studies are necessary to investigate the suitability of their application to different molecule groups and properties. Since TD-DFT builds on the single-determinant DFT ground state, the application is restricted to systems with a single-determinant ground state. Since only the singly excited manifold is taken into account, doubly and higher excited states cannot be described within TD-DFT. Furthermore, it has been shown that TD-DFT has weaknesses in the description of extended π-systems, Rydberg states and charge-transfer states.[123]

2.3 Algebraic Diagrammatic Construction

Another method for the computation of excited states is the algebraic diagrammatic construction (ADC) scheme for the polarization propagator, which is based on perturbation theory and presents a series of *ab initio* methods.[127] The ADC method was originally derived within Green's function theory, however the formulation using the intermediate state representation (ISR) is necessary to access properties and will be outlined in the following.[128–133] In ADC, excited states are obtained by solving a hermitian eigenvalue problem

$$\mathbf{MY} = \mathbf{Y}^\dagger\mathbf{\Omega}; \quad \mathbf{Y}^\dagger\mathbf{Y}, \tag{2.42}$$

where **M** is the shifted Hamiltonian matrix, **Y** is the eigenvector matrix and $\mathbf{\Omega}$ is the diagonal matrix of excitation energies ω_n. In the ISR, the ADC matrix **M** is given by

$$\{\mathbf{M}\}_{IJ} = \langle\tilde{\Psi}_I|\,\mathbf{H} - E_0^{\mathrm{MP}}\,|\tilde{\Psi}_J\rangle\,, \tag{2.43}$$

with intermediate state $|\tilde{\Psi}_J\rangle$. These intermediate states are constructed from a correlated ground state wavefunction Ψ_0^{MP}, where MP indicates the ground state obtained from Møller-Plesset perturbation theory, by acting on it with excitation operators $\hat{C}_J$

$$\Psi_J^0 = \hat{C}_J \Psi_0^{\mathrm{MP}}, \tag{2.44}$$

where

$$\hat{C}_J = \{\hat{c}_a^\dagger \hat{c}_i, \hat{c}_a^\dagger \hat{c}_b^\dagger \hat{c}_i \hat{c}_j, ...\} \tag{2.45}$$

represents single, double, ... excitations.[107] Here, $\hat{c}_a^\dagger$ and $\hat{c}_a$ are the one-particle creation annihilation operators, respectively, the indices $i, j, ...$ denote occupied molecular orbitals and $a, b, ...$ denote virtual orbitals. The unrestricted variant of ADC can be obtained by constructing the intermediate states from an unrestricted MP ground state and by employing the excitation operators

$$\hat{C}_J = \{\hat{c}_{a\sigma}^\dagger \hat{c}_{i\sigma},\, \hat{c}_{a\sigma}^\dagger \hat{c}_{b\sigma}^\dagger \hat{c}_{i\tau} \hat{c}_{j\tau},\, ...,\, a\alpha < b\tau,\, i\sigma < j\tau,\, ...\}, \tag{2.46}$$

where σ and τ are spin variables ($\sigma = \alpha, \beta,\ \tau = \alpha, \beta$).[134] Furthermore, ionization potentials (IP) and electron affinities (EA) can be computed using the excitation operators $\hat{C}_J^{IP}$ and $\hat{C}_J^{EA}$, respectively, as follows.[135,136]

$$\hat{C}_J^{IP} = \{\hat{c}_i, \hat{c}_a^\dagger \hat{c}_i \hat{c}_j, ...\} \tag{2.47}$$

$$\hat{C}_J^{EA} = \{\hat{c}_a^\dagger, \hat{c}_a^\dagger \hat{c}_b^\dagger \hat{c}_i, ...\}. \tag{2.48}$$

Since these excited states are generally not orthogonal, they are successively orthogonalized employing the Gram-Schmidt and Löwdin symmetric orthogonalization procedures to give the final intermediate state basis. The ADC matrix can then be constructed from the intermediate basis state functions and yields the excitation energies of the excited states upon diagonalization. The wavefunction of the excited states can then be built from the ADC vectors as

$$|\Psi_n\rangle = \sum_J Y_{Jn} |\tilde{\Psi}_J\rangle \tag{2.49}$$

The perturbation-theoretical order n of ADC(n) as well as the structure of the ADC matrix depend on the level of perturbation-theoretical order to which the corresponding ground state $\Psi_0^{\mathrm{MP}n}$ is expanded. The ADC matrix exhibits a block structure with respect to the excitation classes of the intermediate basis states. The singly excited configurations form the singles or p-h,p-h block, which is present at all levels of ADC and the only block for ADC(0) and ADC(1). At the ADC(2) level, also the block of doubly excited configurations is added, which is called the doubles or 2p-2h,2p-2h block, while at ADC(4) also triply excited configurations are introduced (triples or 3p-3h,3p-3h block). The singles block is always expanded to the maximum perturbation-theoretical order n of the ADC(n) scheme. The order of perturbation applied to each block for ADC(0) to ADC(4) can be seen in **Table 2.1**.

Table 2.1: Perturbation-theoretical order of different blocks in the ADC matrix at ADC levels from ADC(0) to ADC(4).

	p-h,p-h	p-h,2p-2h	2p-2h,2p-2h	1p-1h,3p-3h	2p-2h,3p-3h	3p-3h,3p-3h
ADC(0)	0	-	-	-	-	-
ADC(1)	1	-	-	-	-	-
ADC(2)	2	1	0	-	-	-
ADC(3)	3	2	1	-	-	-
ADC(4)	4	3	2	2	1	0

A closer look at the diagonal terms of the ADC matrix prior to diagonalization allows for insight into the physical properties of the intermediate states included at different ADC levels. Here, only the diagonal elements of the singles block up to the second order of ADC will be discussed. At the ADC(0) level, the energy of the singly excited intermediate basis states is given by the orbital energy difference of the orbitals involved in the transition

$$D_{ia}^{ADC(0)} = \epsilon_a - \epsilon_i, \tag{2.50}$$

where ϵ_i and ϵ_a are the orbital energies of molecular orbitals i and a. respectively. For ADC(1), the Coulomb and exchange interaction between elecron and hole are included to give

$$D_{ia}^{ADC(1)} = \epsilon_a - \epsilon_i - \langle ia| \, |ia\rangle \, . \tag{2.51}$$

At the ADC(2) level, correlation effects are included and the diagonal element is given as

$$\begin{aligned} D_{ia}^{ADC(2)} =& \epsilon_a - \epsilon_i - \langle ia| \, |ia\rangle && (2.52)\\ &+ \frac{1}{2} \sum_{ckl} \frac{\langle ac| \, |kl\rangle \, \langle kl| \, |ac\rangle}{\epsilon_a + \epsilon_c - \epsilon_k - \epsilon_l} && (2.53)\\ &+ \frac{1}{2} \sum_{cdk} \frac{\langle cd| \, |ik\rangle \, \langle ik| \, |cd\rangle}{\epsilon_c + \epsilon_d - \epsilon_i - \epsilon_k} && (2.54)\\ &- \sum_{ck} \frac{\langle ac| \, |ik\rangle \, \langle ik| \, |ac\rangle}{\epsilon_a + \epsilon_c - \epsilon_i - \epsilon_k}. && (2.55)\\ & && (2.56) \end{aligned}$$

Overall, the ADC methods can be considered as a combination of a CI diagonalization problem and many-body perturbation theory. The advantages of these methods include being compact, size-consistent, size-intensive, Hermitian, systematically improvable and correct through the provided perturbation theoretical order. However, the single-reference MP ground state presents a limitation to the applicability of ADC to single-reference problems.[133,137]

2.4 Diradicals

2.4.1 Definition of Diradicals

Diradicals are chemical species with two unpaired electrons or, more specifically, with two (nearly) independent electrons in two (nearly) degenerate molecular orbitals.[43] Due to their open-shell character, they are generally unstable and occur mainly as reaction intermediates, but also as stable molecules with various promising applications. In the literature, both the terms diradical and biradical are used, often interchangeably. However, the *IUPAC* Gold Book defines a biradical as a molecule with two unpaired electrons which act nearly independent of each other and a diradical as a molecule with two unpaired electron that have two spin states, a singlet (S, 2S+1=1) and a triplet (T, 2S+1=3), which is threefold degenerate with the $\alpha\alpha$ ($m_s = +1$), the $\beta\beta$ ($m_s = -1$) and the $\alpha\beta$ ($m_s = 0$) triplet states.[138,139] The difference can be illustrated by considering an electron paramagnetic resonance (EPR) spectrum of different molecules with two unpaired electrons.[45] In the case of a biradical, the two radical centers can be considered as two independent doublet states and the EPR spectrum therefore shows one or two doublet signals, depending on the symmetry of the molecule. The spectrum of a diradical however would show the signal of a triplet state, while the singlet state naturally does not produce an EPR signal. Whether or not the unpaired electrons interact, depends strongly on the distance between the radical centers. Diradicals can be classified as localized and delocalized diradicals, which are further distinguished as either Kekulé or non-Kekulé diradicals. In a Kekulé diradical, the two unpaired electrons can recombine through the formation of a bond, while in a non-Kekulé diradical this is not the case.
It is important to note that the transition from a closed-shell to an open-shell system is gradual and depends on the extend to which the criteria of independent electrons in degenerate orbitals are fulfilled. The term diradicaloid is used to describe a system, which does not entirely fulfill these criteria, but still shows some open-shell or diradical character.

2.4.2 The Ground State of Diradicals

In this section the character of the ground state of diradicals as presented by Salem *et al* is discussed.[43] In a localized picture, the two unpaired electrons can be assigned to one localized orbital each, which will be labeled ϕ_A and ϕ_B. The interactions between these orbitals are the one-electron overlap integral S_{AB}

$$S_{AB} = \int \phi_A \phi_B d\tau \tag{2.57}$$

and the two-electron exchange integral

$$K_{AB} = \int \phi_A(1)\phi_B(1)\frac{1}{r_{12}}\phi_A(2)\phi_B(2)d\tau_1 d\tau_2. \tag{2.58}$$

The type of interaction, via S_{AB} or K_{AB}, between the unpaired electron depends on the shape and relative orientation of the localized orbitals, but does not have an influence on the diradical nature. However, if the overlap integral increases, the two electrons can no longer be considered nearly independent and the diradical character is gradually lost. The same is the case for an increased energy gap between the two localized orbitals, so that they are no longer degenerate. An increased orbital overlap can be considered as the formation of a bond, while the increased orbital energy

difference would result in a localized electron pair in the lower orbital.
Diradicals can also be described in the picture of molecular orbitals (MOs), where the difference in energy between the MOs or the energy gap between the singlet and triplet state can be considered as a measure for the diradical character of the system. We now consider a pair of molecular orbitals build from the localized orbitals ϕ_A and ϕ_B, which are nearly degenerate, if the overlap between ϕ_A and ϕ_B is small and if the local orbital energies are nearly degenerate. The molecular orbitals are denoted as ϕ_H and ϕ_L for the highest occupied molecular orbital (HOMO) and lowest unoccupied molecular orbital (LUMO)

$$\phi_H = \frac{1}{\sqrt{2+2S_{AB}}}(\phi_A + \phi_B) \tag{2.59}$$

$$\phi_L = \frac{1}{\sqrt{2-2S_{AB}}}(\phi_A - \phi_B). \tag{2.60}$$

For degenerate MOs, the triplet has to be lower in energy according to Hund's rule. However, if the overlap between the localized orbitals increases, the MOs become a pair of bonding and anti-bonding orbitals so that the bonding orbital decreases in energy and the anti-bonding orbital increases in energy. In this situation, the energy of the triplet state increases, while that of the singlet is decreased as the pairing of the two electrons in the lower MO becomes energetically favorable. As a consequence, the diradical character decreases and the ground state eventually becomes a closed-shell singlet with covalent character. If otherwise the energy difference between the localized orbitals increases, one of the MOs is lowered in energy and will be increasingly described by the corresponding localized orbital of lower energy. In this case as well, the energy of the triplet state increases, as it becomes energetically favorable for the unpaired electrons to occupy the same lower energy orbital. Similar to the other case, the diradical character decreases with the energy difference between ϕ_A and ϕ_B and for the case of a sufficiently large gap the ground state becomes a singlet with ionic character. Therefore, the character of the singlet state changes from open-shell to closed-shell with decreasing diradical character.

2.4.3 Wavefunction of Diradicals

In this section the wavefunctions of diradical as presented by Salem *et al* are discussed.[43] The wavefunctions of diradicals within the molecular orbital picture depend on the nature of the orbitals, where heterosymmetric and homosymmetric diradicals are distinguished. In heterosymmetric diradicals, the two nearly degenerate MOs ϕ_H and ϕ_L are non-bonding, while in homosymmetric diradicals they form a pair of one bonding and one antibonding MO. In heterosymmetric diradicals,

the resulting wavefunctions for two electrons distributed in two orbitals are

$$\Psi_1^s = \frac{1}{2}[\mu(\phi_A)^2 - \sqrt{1-\mu^2}(\phi_B)^2](\alpha\beta - \beta\alpha) \tag{2.61}$$

$$\Psi_2^s = \frac{1}{2}[\mu(\phi_A)^2 + \sqrt{1-\mu^2}(\phi_B)^2](\alpha\beta - \beta\alpha) \tag{2.62}$$

$$\Psi_3^s = \frac{1}{2}(\phi_A\phi_B + \phi_B\phi_A)(\alpha\beta - \beta\alpha) \tag{2.63}$$

$$\Psi_1^t = \frac{1}{2}(\phi_A\phi_B - \phi_B\phi_A)(\alpha\beta + \beta\alpha) \tag{2.64}$$

$$\Psi_2^t = \frac{1}{2}(\phi_A\phi_B - \phi_B\phi_A)(\alpha\alpha) \tag{2.65}$$

$$\Psi_3^t = \frac{1}{2}(\phi_A\phi_B - \phi_B\phi_A)(\beta\beta), \tag{2.66}$$

where the singlet states Ψ_1^s and Ψ_2^s are purely ionic states and present the zwitterionic states. The state Ψ_3^s and the triplet states Ψ_1^t, Ψ_2^t and Ψ_3^t however, are purely covalent states and present the diradical states, which are lower in energy than the zwitterionic states. The coefficient μ depends on the energy difference between ϕ_A and ϕ_B.
The wavefunctions that describe homosymmetric diradicals are

$$\Psi_1^s = \frac{1}{2}[\lambda(\phi_H)^2 - \sqrt{1-\lambda^2}(\phi_L)^2](\alpha\beta - \beta\alpha) \tag{2.67}$$

$$\Psi_2^s = \frac{1}{2}[\lambda(\phi_H)^2 + \sqrt{1-\lambda^2}(\phi_L)^2](\alpha\beta - \beta\alpha) \tag{2.68}$$

$$\Psi_3^s = \frac{1}{2}(\phi_H\phi_L + \phi_L\phi_H)(\alpha\beta - \beta\alpha) \tag{2.69}$$

$$\Psi_1^t = \frac{1}{2}(\phi_H\phi_L - \phi_L\phi_H)(\alpha\beta + \beta\alpha) \tag{2.70}$$

$$\Psi_2^t = \frac{1}{2}(\phi_H\phi_L - \phi_L\phi_H)(\alpha\alpha) \tag{2.71}$$

$$\Psi_3^t = \frac{1}{2}(\phi_H\phi_L - \phi_L\phi_H)(\beta\beta), \tag{2.72}$$

where the wavefunctions Ψ_1^s and Ψ_2^s describe singlet states, which are of mainly covalent and ionic character, respectively. In the closed shell limit, the former describes the singlet ground state, while the latter describes the doubly excited singlet state. Furthermore, in the case of no orbital overlap S_{AB}, Ψ_1^s and Ψ_2^s become completely covalent and ionic singlet states. The wavefunction Ψ_3^s is an ionic singlet state, while all triplet wavefunctions are covalent states. Here, the state Ψ_1^s and the three-fold degenerate triplet Ψ_1^t, Ψ_2^t and Ψ_3^t are the diradical states, which are lower in energy, while the ionic states Ψ_2^s and Ψ_3^s are the zwitterionic states and higher in energy. The coefficient λ depends on the orbital overlap S_{AB}.

2.4.4 Computational Methods for Larger Diradicals

It is apparent that all the singlet wavefunctions of a diradical system are of two-determinant form. Their proper quantum-chemical description therefore requires a multi-reference method such as complete active space self-consistent field (CAS-SCF), complete active space perturbation theory (CASPT2), multireference configuration interaction (MRCI), etc. However, the systems investigated in this work are medium to large sized organic molecules, which prohibits the employment of multi-reference methods due to their computational cost. One of the most prominent approaches to circumvent this issue are spin-flip methods.[64–66] Here, the triplet state Ψ_2^t, which is well-described

by a single determinant, is used as a reference state. Similar to a regular electronic excitation, spin-flip excitations excite one electron while also flipping its spin $\alpha \rightarrow \beta$. Considering the reference wavefunction, all other configurations, which are necessary to build the proper wavefunctions of a diradical mentioned above, can be obtained. The spin-flip approach therefore enables the description of closed and open-shell singlet states, as well as the triplet state Ψ_1^t within a single-reference formalism. Furthermore this method can be combined with different excited state formalisms and has been shown to deliver accurate values for molecular properties, such as singlet-triplet gaps of diradicals. A disadvantage of this method is the possibility of obtaining spin-flip excited states with high spin-contamination. Another possibility for the description of larger diradicals is the use of a broken-symmetry wavefunction, which constitutes one of the two configuration needed to build the Ψ_3^s and Ψ_1^t states. It is therefore also a single-reference wavefunction and can be obtained from a closed-shell singlet wavefunction by mixing the HOMO and LUMO in the initial guess of the SCF, thereby breaking the spin-symmetry and obtaining an unrestricted broken-symmetry wavefunction. As mentioned above, molecular species can possess varying degrees of diradical character. The extend of open-shell nature can be described using different measures, where the most prominent one is the diradical character y_0. It was first introduced by Yamaguchi and can be computed from the occupation numbers of the highest occupied natural orbital (HONO) and lowest unoccupied natural orbital (LUNO) of a broken-symmetry singlet state according as follows.[140]

$$y_0 = 1 - \frac{2T}{1+T^2}, \tag{2.73}$$

$$\text{with} \quad T = \frac{n_{HONO} - n_{LUNO}}{2}. \tag{2.74}$$

The diradical character therefore takes values between 0 and 1, where 0 indicates a completely closed-shell system and 1 a fully open-shell system. Furthermore, the energy gap between the lowest singlet and triplet state of a diradical(oid) is directly linked with its open-shell nature. It can be obtained from the excitation energies of the lowest spin-flip excited singlet and triplet states.[66]

$$\Delta \mathrm{E_{ST}} = \mathrm{E_{S_1,sf}} - \mathrm{E_{T_1,sf}}. \tag{2.75}$$

It is important to note that this energy difference has to be calculated between the two spin-flip excited states and not between the spin-flip excited singlet and the reference triplet, as the reference is not described equally well as the spin-flip excited states. Another measure, which can be considered in the context of spin-flip excited states, is the index for number of unpaired electrons according to

$$n_{u,nl} = \sum_i n_i^2 (2 - n_i)^2, \tag{2.76}$$

where n_i is the occupation number of natural orbital i and the sum runs over all natural orbitals.[141] Other properties, which can give insight into the electronic structure of a diradical are spin-densities and nucleus independent shift (NICS) values, which will be discussed in **Chapter 4**.

2.5 Exciton Properties

For the understanding of photochemical processes, excited state properties play a crucial role. The description of transitions within the molecular orbital picture can deliver valuable insight by inspection of the orbitals involved in a transition. However, this approach reaches its limits for excited states described by more than one orbital transition.[39] Another quantity that carries information about excited states is the one-particle electron density $\rho(r)$, which can be easily visualized and furthermore presents a physical observable. The one-particle transition density $\rho_T^{0I}(r_1)$ describes the transition from one state to another state and can be employed for the analysis of excited states. It is given by

$$\rho_T^{0I}(r_1) = \int ... \int \Psi_0(r_1, r_2, ..., r_N)\Psi_I(r_1, r_2, ..., r_N)dr_2...dr_N, \tag{2.77}$$

where N is the number of electrons and r_i are spin-spatial coordinates. The molecular orbital (MO) representation of the transition density is the one-particle transition density matrix (1TDM), which can serve in the definition of an exciton wavefunction within a single-molecule picture.[37–39] This is especially interesting, since it allows for a connection between two fundamentally different frameworks for the description of excited states. The exciton picture originates from solid state physics and utilizes the concept of quasi-particles to simplify the description of electrons or electron-holes in extended solids. An example would be to describe the movement of an electron through a solid by that of the electron quasi particle, which is constructed to only weakly interact with all other particles in the system. This reduces the many-body problem of the electron interacting with all other particles in the solid to that of a single particle, which only weakly interacts with the other particles in the solid. Excitons are then defined as bound electron-hole pairs and are the equivalent to excited states in single molecules. By defining excitons in terms of quantum-chemical methods, the description of exciton properties, such as exciton size, is possible, allowing for valuable insight into the character of excited states.
This is done by defining the 1TDM as the exciton wavefunction, where the ground state part (Ψ_0) describes the electron-hole and the excited state part (Ψ_I) describes the electron

$$\chi_{exc}(r_h, r_e) = \int ... \int \Psi_0(r_h, r_2, ..., r_N)\Psi_I(r_e, r_2, ..., r_N)dr_2...dr_N. \tag{2.78}$$

Based on this, exciton properties can be formulated as expectation values of the exciton wavefunction $\chi_{exc}(r_h, r_e)$.
The distance between hole and electron $d_{h\to e}$, can be obtained as the distance between the centroids of the hole and electron, which are the expectation values of the position operator $\hat{x}$ as

$$d_{h\to e} = |\langle \overrightarrow{x}_e - \overrightarrow{x}_h \rangle| = |\langle \overrightarrow{x}_e \rangle_{exc} - \langle \overrightarrow{x}_h \rangle_{exc}| \tag{2.79}$$

and can serve as a measure for the charge-transfer (CT) character of a transition. A similar descriptor is the exciton size d_{exc}, which also takes the spatial extend of the electron and hole into account and is the root-mean-square separation of the electron and hole position

$$d_{exc} = \sqrt{\langle |\overrightarrow{x_h} - \overrightarrow{x_e}|^2 \rangle_{exc}}. \tag{2.80}$$

Here, the dynamic distance between hole and electron due to their correlated movement is considered. The exciton size can be a measure for hidden charge transfer character. The size of the hole σ_h and electron σ_e can be calculated as the variance of the position operator as

$$\sigma_h = \sqrt{\langle \overrightarrow{x_h}^2 \rangle_{exc} - \langle \overrightarrow{x_h} \rangle_{exc}^2} \tag{2.81}$$

and

$$\sigma_e = \sqrt{\langle \overrightarrow{x_e}^2 \rangle_{exc} - \langle \overrightarrow{x_e} \rangle_{exc}^2}. \tag{2.82}$$

The correlation of the movement of the hole and electron can be described by the correlation coefficient R_{eh}

$$R_{eh} = \frac{\langle \overrightarrow{x_h} \cdot \overrightarrow{x_e} \rangle_{exc} - \langle \overrightarrow{x_h} \rangle_{exc} \cdot \langle \overrightarrow{x_e} \rangle_{exc}}{\sigma_h \sigma_e}, \tag{2.83}$$

which is the covariance of the correlated spatial distribution of hole and electron normed with respect to the hole and electron size. Here, a positive value of R_{eh} indicates that hole and electron move together, while a negative value indicates that they move away from each other. Furthermore, the relationship between the exciton size, the electron and hole size and the correlation coefficient is

$$d_{exc} = \sqrt{\sigma_h^2 + \sigma_e^2 - 2R_{eh}\sigma_h\sigma_e}. \tag{2.84}$$

Using these descriptors, exciton properties of excited states can be computed based on the 1TDM and are therefore applicable for every excited state method that provides a 1TDM.

2.6 Plasmons in Molecules

In this section an overview of the theory of plasmons in molecules as discussed by Krauter *et al* is given.[40] Plasmons are a special kind of exciton, which arise in extended systems as the collective oscillation of the electron density and are defined within classical electrodynamics.[36] The definition and description of plasmons within the quantum-chemical picture however, is elusive and many different approaches have been explored and have allowed for the identification of plasmonic character of electronic excitations in metal nanoparticles as well as molecules.[40,41,142–152] One possible definition employs the Random-phase approximation (RPA) for the homogenous electron gas to identify the properties of a plasmon.[40] Following the derivation by Krauter *et al*, the single-particle states of a homogenous electron gas in a box ($V = L^3$) with periodic boundary conditions are given as

$$\psi_{\mathbf{k},\gamma}(x,s) = \phi_{\mathbf{k}}(x)\gamma(s) = \frac{1}{\sqrt{V}} e^{i\mathbf{k}x}\gamma(s),\ \gamma \in \{\alpha,\beta\}, \tag{2.85}$$

where ϕ_k denotes a spatial orbital, $\gamma(s)$ denotes a spin-function and x and s are Cartesian and spin-coordinates, respectively. The wave vector $\mathbf{k}$ is given as

$$k_i = \frac{2\pi n_i}{L}\ (i = x,y,z, n_i = 0, \pm1, \pm2, ...). \tag{2.86}$$

and determines the single-particle energies $\epsilon_{\mathbf{k}}$

$$\epsilon_{\mathbf{k}} = \frac{\hbar^2 |\mathbf{k}|^2}{2m_e}. \tag{2.87}$$

The single-particle states correspond to spin-orbitals and in the ground state of an N-electron system, the N energetically lowest spin-orbitals are occupied. The occupation number $n_{\mathbf{k}}$, is 0 for unoccupied and 1 for occupied spin-orbitals.
Employing the RPA, the polarization propagator is given as

$$\Pi^{RPA}_{pr,p'r'}(\omega) = \Pi^{0}_{pr,p'r'}(\omega) + \Pi^{0}_{pr,pr}(\omega) \sum_{p'',r''} U_{pr,p''r''} \Pi^{RPA}_{p''r'',p'r'}(\omega), \tag{2.88}$$

where p and r are spin-orbitals. The first term is the zeroth order polarization propagator

$$\Pi^{0}_{pr,p'r'}(\omega) = \left[\frac{(1-n_p)n_r}{\omega + \epsilon_r - \epsilon_p + i\eta} - \frac{n_p(1-n_p)}{\omega + \epsilon_r - \epsilon_p - i\eta} \right] \delta_{rr'}\delta_{pp'} \tag{2.89}$$

and $U_{rp,r'p'}$ are elements of the interaction matrix

$$U_{pr,p'r'} = -V_{pr'[p'r]} = -\langle pr' | \, | p'r \rangle = -\langle pr' | \, | p'r \rangle + \langle pr' | \, | rp' \rangle \, . \tag{2.90}$$

In the further derivation, the Coulomb type term is neglected, which is an approximation often applied in solid state physics and only the singlet excited states are considered. The spin-adapted polarization propagator can then be expressed as

$$\Pi^{RPA}_{\mathbf{jk},\mathbf{j'k'}}(\omega) = \Pi^{0}_{\mathbf{jk},\mathbf{j'k'}}(\omega) + \Pi^{0}_{\mathbf{jk},\mathbf{jk}}(\omega) \sum_{\mathbf{j''},\mathbf{k''}} U_{\mathbf{jk},\mathbf{j''k''}} \Pi^{RPA}_{\mathbf{j''k''},\mathbf{j'k'}}(\omega), \tag{2.91}$$

with the zeroth order polarization propagator

$$\Pi^{0}_{\mathbf{j}k,\mathbf{j'k'}}(\omega) = \left[\frac{(1-n_{\mathbf{j}})n_{\mathbf{k}}}{\omega + \epsilon_{\mathbf{k}} - \epsilon_{\mathbf{j}} + i\eta} - \frac{n_{\mathbf{j}}(1-n_{\mathbf{k}})}{\omega + \epsilon_{\mathbf{k}} - \epsilon_{\mathbf{j}} - i\eta} \right] \delta_{\mathbf{kk'}}\delta_{\mathbf{jj'}}. \tag{2.92}$$

The two electron integrals can be computed as

$$V_{\mathbf{jk'},\mathbf{kj'}} = \frac{4\pi e^2}{V} \frac{1}{(\mathbf{j}-\mathbf{k})^2} \delta_{\mathbf{j}+\mathbf{k'},\mathbf{j'}+\mathbf{k}}. \tag{2.93}$$

and by defining the momentum transfer $\mathbf{q} \equiv \mathbf{j} - \mathbf{k}, = \mathbf{j'} - \mathbf{k'}$, can be written as

$$V_{\mathbf{k},\mathbf{k'}}(\mathbf{q}) = \frac{4\pi e^2}{V} \frac{1}{\mathbf{q}^2} = V(\mathbf{q}) \tag{2.94}$$

so that $V_{\mathbf{jk'},\mathbf{kj'}}$ only depends on the momentum transfer $\mathbf{q}$. The polarization propagator can then be expressed as

$$\Pi^{RPA}_{\mathbf{k},\mathbf{k'}}(\mathbf{q},\omega) = \Pi^{0}_{\mathbf{k},\mathbf{k'}}(\mathbf{q},\omega) + \Pi^{0}_{\mathbf{k},\mathbf{k}}(\mathbf{q},\omega) 2V(\mathbf{q}) \sum_{\mathbf{k''}} \Pi^{RPA}_{\mathbf{k''},\mathbf{k'}}(\mathbf{q},\omega), \tag{2.95}$$

so that a separate set of equations for each value of $\mathbf{q}$ is obtained. The polarization propagator can also be expressed in matrix notation as

$$\Pi^{RPA}(\mathbf{q},\omega) = \Pi^0(\mathbf{q},\omega) + \Pi^0(\mathbf{q},\omega)U(\mathbf{q})\Pi^{RPA}(\mathbf{q},\omega), \tag{2.96}$$

where the interaction matrix $U(\mathbf{q})$ has elements $U_{\mathbf{k},\mathbf{k}'}(\mathbf{q}) = 2V(\mathbf{q})$. The formal solution is

$$\Pi^{RPA}(\mathbf{q},\omega) = (\Pi^0(\mathbf{q},\omega)^{-1} - U(\mathbf{q}))^{-1}, \tag{2.97}$$

which can also be expressed as a pseudo-eigenvalue equation

$$\begin{pmatrix} A(\mathbf{q}) & B(\mathbf{q}) \\ B^*(\mathbf{q}) & A^*(\mathbf{q}) \end{pmatrix} \begin{pmatrix} \mathbf{x} \\ \mathbf{y} \end{pmatrix} = \omega_n \begin{pmatrix} \mathbf{x} \\ -\mathbf{y} \end{pmatrix} \tag{2.98}$$

with

$$A_{\mathbf{k},\mathbf{k}'}(\mathbf{q}) = (\epsilon_{\mathbf{k}+\mathbf{q}} - \epsilon_{\mathbf{k}})\delta_{\mathbf{k},\mathbf{k}'} + 2V(\mathbf{q}), \tag{2.99}$$

$$B_{\mathbf{k},\mathbf{k}'}(\mathbf{q}) = 2V(\mathbf{q}). \tag{2.100}$$

Since particle-hole excitation of different $\mathbf{q}$ are decoupled, we obtain a separate pseudo-eigenvalue equation for each value of $\mathbf{q}$. Furthermore, the m single-particle excitations with the same momentum transfer $\mathbf{q}$ interact in a uniform way. Based on this framework, it can be shown that a plasmonic excitation is a positive linear combination of all m possible particle-hole excitations with a given momentum transfer $\mathbf{q}$, which reflects the collective character of the state. Furthermore, of all excitations described by the same m transitions, the plasmonic excitation has the highest excitation energy and the only non-zero transition strength.

This approach has been employed to show that excited states of linear polyenes show plasmonic character. In order to identify these excitations, the π-electrons are viewed as a quasi one-dimensional electron gas. This way one can assign wavevectors to the HF π-orbitals of the polyenes in the same fashion as is done for the homogenous one-dimensional electron gas in a box model. This assignment provides a useful qualitative measure to classify the momentum transfer of the particle-hole excitations. Since in the one-dimensional model, the wave vectors have only one component, the momentum-transfer can be directly related to the corresponding change in the quantum number of the orbitals involved Δn, which is also equal to the change in number of nodes in the involved orbitals. It was furthermore mentioned that this analysis could be extended to non-linear systems using a electron gas model of appropriate symmetry.

Chapter 3

Excited States of Acenes and their Radical Cations

Parts of the results presented in this chapter have already been published in:

- A. M. Weidlich and A. Dreuw, "The Relation Between the Excited Electronic States of Acene Radical Cations and Neutrals - A Computational Analysis", *J. Comput. Chem.*, **2025**, *46*, e70095.
- A. M. Weidlich and A. Dreuw, "Molecular Excitons and Plasmons in Acenes and Their Radical Cations", *J. Comput. Chem.*, **2025**, *46*,e70211.

3.1 Introduction

Acenes are widely investigated systems both with focus on their fundamental electronic structure and properties as well as on their various existing and potential applications.[4,29–32] While these are numerous, the currently most prominent application is as organic semiconductors in organic electronics, due to their promising charge carrier mobilities, processability and chemical versatility.[1,2,5,33] Increasing the extended π-system leads to a rapid development of the electronic properties of acenes. Their excited states decrease in energy, which presents a favorable property in regard to their use as organic materials. However, the decrease of the first excited state leads to an increasing diradical character and a decreased stability towards oxidation and dimerization. For this reason, the synthesis of acenes larger than hexacene is generally difficult.[4,34,35] The increasing diradical character presents a challenge for quantum-chemical investigations as well, since a multi-configurational wavefunction is required for the proper description of diradical(iod)s.[43]
The character of the ground state of acenes has been the subject of several quantum-chemical studies, where initial investigations using DFT suggested that the ground state of acenes larger than nonacene, would be a triplet.[153] Another study, which also employed DFT, subsequently showed that an open-shell singlet instead becomes the ground state of longer acenes.[34] The same conclusion was drawn in an investigation using density matrix renormalization group (DMRG), which, among others, further discovered that acenes possess an increasing polyradical character with increasing length.[35,154,155] While this has been challenged by a study employing coupled cluster singles-doubles (CCSD), a more recent investigation using the multireference averaged quadratic coupled cluster method (MR-AQCC) again points to a multiradical singlet ground state for longer

acenes.[156,157]

In the area of organic electronics, both the treatment of single molecules using quantum-chemistry as well as the treatment of extended materials from solid-state physics are relevant. The latter employs the concept of quasi-particles to approximate the description of the collective behavior of particles in a solid by that of a single particle, which interacts weakly with the other particles. An electron moving through a solid can then be described by the corresponding electron quasi-particle. In this picture, an electronically excited state is described as an electron and an electron-hole bound together, which is called an exciton. A plasmon is a special case of an exciton, where all the electrons oscillate simultaneously.[36]

The excited state description of quantum-chemistry offers important properties such as excitation energies and a framework for the description of the character of a transition using molecular orbitals. Exciton properties, however are difficult to grasp in this picture. The quasi-particle picture can offer insights into these properties, such as exciton size, correlation between electron and hole and the characterization as either a single-particle or plasmonic excitation. Furthermore, the molecular orbital framework faces its limit in excitations described by more than one transition. In order to benefit from the quasi-particle framework, a definition of excitons and plasmons within wavefunction- and density-based methods for single molecules is needed, which was discussed in **Section 2.6**.[37–41]

The absorption spectra of smaller acenes are well-characterized both experimentally and theoretically. They show three characteristic peaks, the p-, α- and β-band, which can be shown using quantum-chemical methods to originate from the excited states ^1L_w, ^1L_s and ^1B_b, respectively.[29,30] The state ^1L_w is the first excited state for acenes larger than naphthalene and shows a moderate oscillator strength. It is primarily described by the orbital transition H→L and belongs to the irreducible representation B_{2u}. The state ^1L_s is almost dark in unsubstituted acenes, while the state ^1B_b has the highest oscillator strength and excitation energy. Both excited states ^1L_s and ^1B_b are described by a symmetric linear combination of H−1→L and H→L+1 (up to tetracene) and belong to the irreducible representation B_{3u}. A schematic representation of a typical absorption spectrum and the described excited states can be seen in **Figure 3.1**.

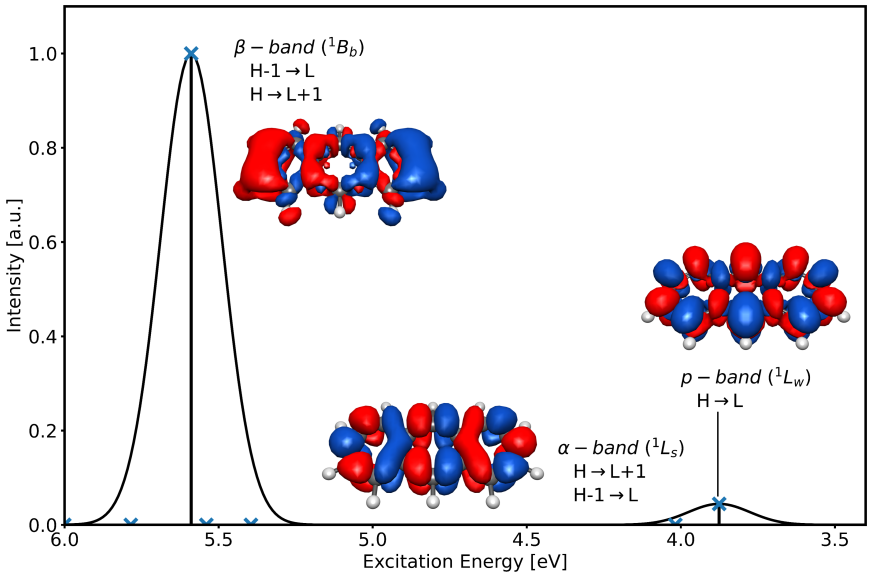

Figure 3.1: Schematic representation of the absorption spectrum of anthracene with the characteristic absorption bands (p-, α- and β-band) and their respective excited states (^{1}L$_w$, ^{1}L$_s$ and ^{1}B$_b$), prominent orbital transitions and transition densities.

The labels for these excited states originate from Platt's nomenclature for $\pi\pi^*$ states of catacondensed hydrocarbons, which is based on excitation energy, oscillator strength and so called polarization diagrams.[29] These can be directly related to the transition density of an excited state.[42] According to the number of nodal planes on the perimeter of the molecule of the transition density, the state is either labeled with respect to the total number of nodal planes 1, 2, 3, etc. as *B*, *C*, *D*, etc. or with respect to the number of nodal planes relative to the number of rings *n* with 2*n*+1, 2*n*+2, 2*n*+3, etc. for *L*, *M*, *N*, etc.. The direction of polarization, which is the orientation of the transition dipole moment, determines the subscript, where *a* stands for the direction of polarization along the short molecular axis and *b* stands for the direction of polarization along the long molecular axis.

In previously published work, it was observed that the states ^{1}L$_a$ and ^{1}L$_b$ of substituted derivatives, such as *N*-heteropolycycles, can not be unambiguously assigned based on these criteria.[42] The electron-hole correlation coefficient was identified as a physical criterion to further characterize and distinguish the excited states leading to the labels ^{1}L$_w$ and ^{1}L$_s$ for weakly and strongly correlated, respectively.

Furthermore, previous studies have shown that the oscillator strength of the states ^{1}L$_s$ and ^{1}B$_b$ of anthracene depends on the orbital energy differences between the orbitals participating in the transitions H−1→L and H→L+1.[158] In the unsubstituted case, these transition are energetically degenerate and therefore mix symmetrically, so that the ^{1}B$_b$ state has a high oscillator strength, while ^{1}L$_s$ state is almost dark. By chemical substitution, the orbital energies can be influenced, lifting the energetic degeneracy of the transitions and leading to a brighter ^{1}L$_s$ state. This was shown to be the case for substitution with nitrogen, phosphorous and halogens.[159,160]

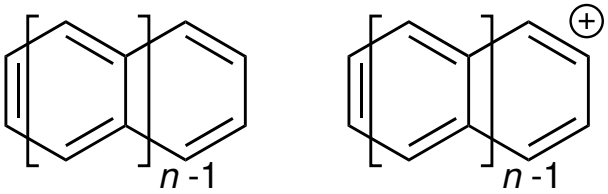

Figure 3.2: Systems investigated in this chapter: acenes from naphthalene (n=2) to dodecacene (n=12) and their respective radical cations.

Subject of this chapter are the excited states of acenes from naphthalene to dodecacene and their respective radical cations, shown in **Figure 3.2**. The molecules are labeled according to their respective number of rings n, e.g. naphthalene is **2** and the naphthalene cation is $\mathbf{2}^+$. The excited states of the acene radical cations are thoroughly investigated with focus on their relation to the typical excited states of their neutral counterparts. Furthermore, the development of the excitation energies of both neutral and cationic acenes with increasing length is explored as well as the development of their exciton properties. Finally, the excited states ^1B_b and ^2B_b of anthracene and its respective cation are investigated regarding their plasmonic character. Generally, the fact that acene cations are open-shell systems allows for an investigation of the performance of the employed methodology in the open-shell picture.

3.2 Methodology

The calculations were performed using the Q-Chem 5.2 program package.[161] The investigated systems are acenes from naphthalene to dodecacene (**2**-**12**) and their respective cations ($\mathbf{2}^+$-$\mathbf{12}^+$). All molecular geometries were obtained at the CAM-B3LYP(D3-BJ)/6-311G* level of theory and were ensured to have D_{2h} symmetry.[162–164] The stationary points were confirmed to be minima by harmonic frequency analysis. The $\langle \hat{S}^2 \rangle$-values of $\mathbf{2}^+$ to $\mathbf{12}^+$ are 0.78, 0.78, 0.79, 0.79, 0.80, 0.80, 0.80, 0.81, 0.82, 0.83 and 0.84, respectively. The long molecular axis is aligned with the x-axis, the short molecular axis with the y-axis and the z-axis lies out of plane. This orientation is adopted by Q-Chem and frequently adopted in the literature, however is not compliant with the Mulliken convention. In the chosen orientation, the symmetry of the ground state is A_u for acene cations with an even number of rings and B_{3g} for acene cations with an odd number of rings. In all excited state calculations, the basis set 6-311G* was used.[164] The absorption spectra were created by convolution of the excitation energies with a Gaussian broadening function with a standard deviation of 0.1 eV. The corresponding plots were created using Python 3 and the matplotlib library.[165] Experimental excitation energies were taken from literature for **2**-**5** and $\mathbf{2}^+$-$\mathbf{5}^+$, where the acene cations were created using vacuum ultraviolet irradiation or vapor phase electron impact and the absorption spectra were subsequently measured in argon and/or neon matrices.[31,166–168] Excitation energies for the low-energy singlet/doublet excited states of **2**-**4** and $\mathbf{2}^+$-$\mathbf{4}^+$ were calculated using ADC(2), ADC(2)-x, ADC(3) and, only for the cations, IP-ADC(3) and were compared to experimental values.[127,136,169,170] In the case of IP-ADC(3), the excitation energies were calculated as the difference in energy of the higher-lying ionized state to the first ionized state, which is the cation ground state. The ADC(2) method was used for the detailed investigation of the excited states of the acene cations. The HF orbitals and transition densities were visualized with an isovalues of 0.02 and 0.001, respectively, using IQmol 2.8.0.

The excitation energies of **2**-**5** and $\mathbf{2}^+$-$\mathbf{5}^+$ were calculated using the DFT functionals BLYP, B3LYP, BHHLYP and CAM-B3LYP at the full TD-DFT level and compared to experimental values.[162,171–174] The excited states of **2**-**12** and $\mathbf{2}^+$-$\mathbf{12}^+$ were computed at the TDA/CAM-B3LYP level of theory. For acenes larger than **9**, triplet instabilities were encountered, which is likely the reason it was not possible to perform full TD-DFT calculations for these systems. For acene cations larger than $\mathbf{9}^+$, the SCF converges to an unstable solution due to orbital degeneracies. The first excited state has a negative excitation energy and is described by the transition αH→αL. These two orbitals were therefore switched in the initial guess for acene cations larger than $\mathbf{9}^+$, which lead to a lower final SCF energy. Exciton properties (exciton, hole and electron size and electron-hole correlation) were computed as implemented in Q-Chem.[37,38] The Kohn-Sham orbitals and transition densities were visualized with an isovalues of 0.02 and 0.001, respectively, using IQmol 2.8.0. Chemical structures were created using ChemDraw 21.0.0. All plots of excitation energies and exciton properties were created using Python 3 and the matplotlib library.[165]

3.3 Results and Discussion

3.3.1 ADC Benchmark of Excited States of Naphthalene, Anthracene, Tetracene and Their Radical Cations

The excitation energies of ^1L_w, ^1L_s and ^1B_b of **2**, **3** and **4** calculated using ADC(2), ADC(2)-x and ADC(3) were benchmarked against experimental values from literature.[31] The excited states were assigned based on their symmetry and participating orbital transitions. **Table 3.1** shows that for **2** and **3** the best agreement is achieved using ADC(2)-x with mean average percentage errors (MAPEs) of 6.0 % and 6.7 %, respectively. Overall, all ADC methods overestimate the excitation energies. It has been observed that ADC(2)-x consistently underestimates excitation energies, which in this case causes them to agree better with experimental values.[175] For **4**, ADC(3) shows the best agreement with experiment with a MAPE of 5.6 %.

Table 3.1: Excitation energies [eV] of ^1L_w, ^1L_s and ^1B_b of **2**, **3** and **4** calculated using ADC(2), ADC(2)-x and ADC(3), as well as experimental values.

naphthalene **2**				
state	exp[31]	ADC(2)	ADC(2)-x	ADC(3)
^1L_w (1^1B_{2u}, p-band)	4.38	5.06	4.58	5.04
^1L_s (1^1B_{3u}, α-band)	4.03	4.6	3.62	4.29
^1B_b (2^1B_{3u}, β-band)	5.62	6.39	5.75	6.44
MAE [eV]		0.67	0.25	0.58
MAPE [%]		12.6	6.0	10.6
anthracene **3**				
state	exp[31]	ADC(2)	ADC(2)-x	ADC(3)
^1L_w (1^1B_{2u}, p-band)	3.38	3.88	3.40	3.89
^1L_s (1^1B_{3u}, α-band)	3.57	4.02	3.11	3.72
^1B_b (2^1B_{3u}, β-band)	4.86	5.59	5.10	5.66
MAE [eV]		0.56	0.24	0.49
MAPE [%]		12.4	6.7	10.4
tetracene **4**				
state	exp[31]	ADC(2)	ADC(2)-x	ADC(3)
^1L_w (1^1B_{2u}, p-band)	2.71	3.08	2.52	3.10
^1L_s (1^1B_{3u}, α-band)	3.32	3.65	2.75	3.34
^1B_b (2^1B_{3u}, β-band)	4.52	5.03	4.45	4.34
MAE [eV]		0.40	0.28	0.20
MAPE [%]		10.4	10.0	5.8

Another benchmark was performed for the low-energy excitation energies of $\mathbf{2}^+$, $\mathbf{3}^+$ and $\mathbf{4}^+$ obtained using ADC(2), ADC(2)-x, ADC(3) and IP-ADC(3) against experimental absorption spectra.[166–168] The excited states were assigned according to their excitation energies and irreducible representations. From **Table 3.2** it can be seen that ADC(3) and IP-ADC(3) show the highest accuracy with respect to experimental values, since the MAPEs are 5.3 % (7.0 %), 7.3 % (8.4 %) and 4.9 % (2.5 %) using ADC(3) (IP-ADC(3)) for $\mathbf{2}^+$, $\mathbf{3}^+$ and $\mathbf{4}^+$, respectively.

Table 3.2: Excitation energies [eV] of $\mathbf{2}^+$, $\mathbf{3}^+$ and $\mathbf{4}^+$ calculated using ADC(2), ADC(2)-x, ADC(3), IP-ADC(3), as well as experimental values.

naphthalene cation $\mathbf{2}^+$					
state[166,176]	exp[166]	ADC(2)	ADC(2)-x	ADC(3)	IP-ADC(3)
1^2B_{1u}	forb.	1.36	0.49	1.03	0.66
1^2B_{3g}	1.83	2.08	1.31	1.82	2.08
1^2B_{2g}	2.72	3.26	2.29	2.94	3.03
2^2B_{2g}	3.29	3.84	2.87	3.47	3.28
2^2B_{3g}	4.02	4.24	3.23	3.73	4.28
3^2B_{3g}	4.49	4.92	3.66	-	4.8
3^2B_{2g}	5.08	5.27	4.31	4.86	5.57
4^2B_{2g}	5.58	6.91	5.41	5.66	6.24
MAE [eV]		0.40	0.60	0.18	0.23
MAPE [%]		11.4	24.0	5.3	7.0
anthracene cation $\mathbf{3}^+$*					
state[167]	exp[167]	ADC(2)	ADC(2)-x	ADC(3)	IP-ADC(3)
1^2B_{2g}	forb.	1.81	0.93	1.44	1.14
1^2A_u	1.73	2.00	1.20	1.76	1.94
1^2B_{1u}	2.02	2.56	1.76	2.29	2.11
1^2B_{3g}	forb.	-	2.30	2.92	-
2^2B_{1u}	2.90	3.50	2.51	3.17	3.23
3^2B_{1u}	3.52	-	-	-	-
2^2A_u	3.95	3.67	2.82	3.28	3.84
MAE [eV]		0.47	0.39	0.19	0.21
MAPE [%]		17.2	24.8	7.3	8.4

tetracene cation $\mathbf{4}^{+}$*

state[168]	exp[168]	ADC(2)	ADC(2)-x	ADC(3)	IP-ADC(3)
1^2B_{3g}	1.43	1.77	1.00	1.52	1.44
1^2B_{1u}	forb.	2.15	1.27	1.76	1.49
1^2B_{2g}	1.66	1.95	1.21	1.68	1.73
1^2A_u	forb.	3.09	2.23	2.88	3.03
2^2B_{2g}	-	3.44	2.49	3.10	3.48
2^2B_{3g}	3.16	3.27	2.53	2.94	3.18
MAE [eV]		0.25	0.50	0.11	0.05
MAPE [%]		12.5	35.0	4.9	2.5

* A different molecular orientation was used in Ref.

resulting in a different labeling of some states: B_{3g} in Ref.

corresponds to B_{2g} in this work, and vice versa.

3.3.2 Characterization of Excited States of Naphthalene, Anthracene, Tetracene and Their Radical Cations

The low-lying excited states of the acene cations were then set into relation to the typical excited states of neutral acenes ^1L_w, ^1L_s and ^1B_b based on the orbital transitions that describe the excitations. It was therefore necessary to assign the relevant HF orbitals of each radical cation ($\mathbf{2}^{+}$-$\mathbf{4}^{+}$) to those of their neutral counterpart (**2**-**4**). This is done exemplarily in **Figure 3.3** for $\mathbf{2}^{+}$ and **2**. The assignment of all relevant orbitals can be found in **Appendix A** (**Table A.1-A.3**). Since acene cations are open-shell systems, the α- and β-orbitals are not equivalent and each neutral orbital can be assigned to one α- and one β-orbital. This also means that each orbital transition of the neutral system will have two counterparts, one α- and one β-transition, in the cationic system. Based on the assignment, it is possible to identify excited states of the cations that are described by transitions equivalent to H→L, H−1→L and H→L+1 and therefore relate to the excited states ^1L_w, ^1L_s and ^1B_b of their neutral counterpart.

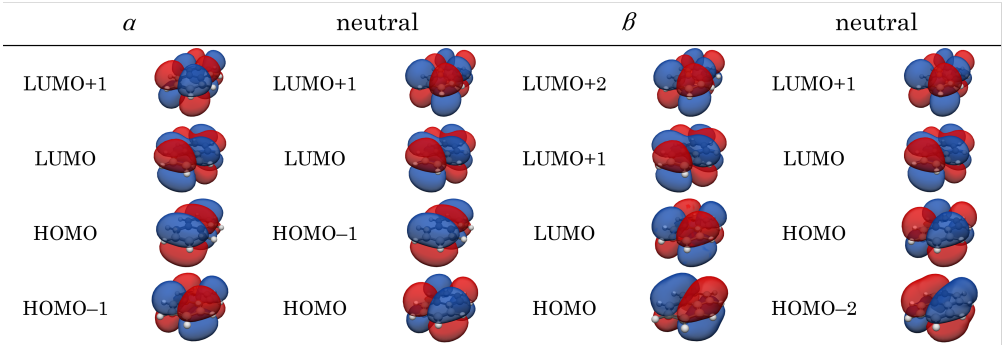

Figure 3.3: Assignment of the relevant orbitals obtained at HF/6-311G* of $\mathbf{2}^+$ to those of **2** according to their shape and irreducible representation.

Here, the excited states obtained using ADC(2) will be analyzed. Since double excitations are included in zeroth-order, the relation to the excited states of the neutral acenes is unambiguous and the comparison to excited states obtained using TD-DFT (**Section 3.3.4**) is facilitated. This is further discussed in **Section 3.3.3**.

Table 3.3 shows the assigned and labeled excited states of $\mathbf{2}^+$. The first excited state is mainly described by the orbital transition βH−1→βL. It belongs to the irreducible representation B_{1u} and is therefore optically forbidden. Based on the number of nodal planes in the transition density (**Figure A.2a**), this state was labeled ^{2}K. The transition density is neither polarized along the short, nor the long molecular axis, which is why there is no subscript. Since this state is not visible in the absorption spectrum, no label for the absorption band was given. The β-L orbital is occupied in the neutral compound, so that there is no counterpart to this state in **2**. This is also the case for the next state, which is primarily described by the transition βH→βL. The symmetry of this state is B_{3g} and it was labeled ^2I_b, due to the number of nodal planes in the transition density (**Figure A.2b**) relating to the number of rings n as $2n$-2 and the direction of polarization lying along the long molecular axis. In continuation of the existing nomenclature of the p-band, the corresponding absorption band was labeled cation q-band, based on the main transition being βH→βL. Subsequently, **Table 3.3** shows two excited states that are described by the transitions αH−1→αL and βH−2→βL. The transition αH−1→αL corresponds to H→L in the neutral compound so that the excited state described by this transition would be the counterpart to the ^1L_w state. Since in the case of $\mathbf{2}^+$, there are two such states, the assignment can be made based on the transition density (**Figure A.2c**) to 2^2B_{2g}. This state was therefore labeled ^2L_w and the absorption band was labeled cation p-band. The other state was not labeled, since is nearly dark and does not appear for the other investigated acenes. From **Table 3.3** and **Figure 3.4** it can be seen that there is a bright state, which is described by the transitions αH→αL and βH−1→βL+1, which are both equivalent to the transition H−1→L. This state has B_{3g} symmetry and was labeled ^2L_b, after Platt's nomenclature (**Figure A.2d**). Noticeably, this state has an $\langle\hat{S}^2\rangle$-value of around 2.5, which deviates strongly from the value for a spin-pure doublet state of 0.75. In ADC(2), transitions that would be necessary for a spin-complete description of this state are not included, leading to spin-contamination. The IP-ADC(3) approach however does not suffer from this issue and gives a similar excitation energy for this state with 4.24 eV for ADC(2) and 4.28 eV for IP-ADC(3). The absorption band of this state was labeled cation γ-band, relating to the existing nomenclature of the α- and β-band. Finally, the counterparts for the neutral excited states ^2L_s and ^2B_b can be found in the excited states 3^2B_{3g} and 4^2B_{3g}, respectively, which are described by

transitions corresponding to H−1→L+1 and H→L+1. These excited state were therefore labeled ^2L_s and ^2B_b and the absorption bands cation α- and cation β-band. The transition densities of ^2L_s and ^2B_b can be found in **Figure A.2e** and **Figure A.2f**, respectively. In the following, the excited states of acene cations and their absorption bands will be labeled according to the assignment in **Table 3.3**.

Table 3.3: Excitation energies [eV], oscillator strengths, orbital contributions and assignment of ADC(2) states of $\mathbf{2}^+$.

ADC(2)	f_{osc} [10^{-2}]	main contrib.	assignment neutral	state (name)
1.36	0.00	βH−1→βL	-	1^2B_{1u} (^{2}K)
2.08	0.73	βH→βL	-	1^2B_{3g} (^2I_b, cation q-band)
3.26	0.04	βH−2→βL	-	1^2B_{2g}
		αH−1→αL	H→L	
3.84	1.05	αH−1→αL	H→L	2^2B_{2g} (^2L_w, cation p-band)
		βH−2→βL	-	
4.24	1.21	αH→αL	H−1→L	2^2B_{3g} (^2L_b, cation γ-band)
		βH−1→βL+1	H−1→L	
4.92	0.35	βH−1→βL+1	H−1→L	3^2B_{3g} (^2L_s, cation α-band)
		αH−1→αL+1	H→L+1	
6.14	11.07	αH−1→αL+1	H→L+1	4^2B_{3g} (^2B_b, cation β-band)
		βH−1→βL+1	H−1→L	

The simulated absorption spectra of **2** and $\mathbf{2}^+$ created based on excitation energies obtained using ADC(2) are shown in **Figure 3.4**. Compared to the spectrum of **2**, the spectrum of $\mathbf{2}^+$ is naturally red-shifted due to new excitations involving the β-L orbital. Also the cation p-band is red-shifted compared to its neutral counterpart with 5.06 eV for the p-band and 3.84 eV for the cation p-band. The reason for this could be that the state is split up due to mixing with another transition (βH−2→βL). The cation α- and cation β-band are similar to their neutral counterparts, however they are energetically closer together, with excitation energies 4.60 eV and 6.39 eV for the neutral and 4.92 eV and 6.14 eV for the cation α- and cation β-band, respectively. Furthermore, the cation α-band has a higher oscillator strength than the neutral α-band.

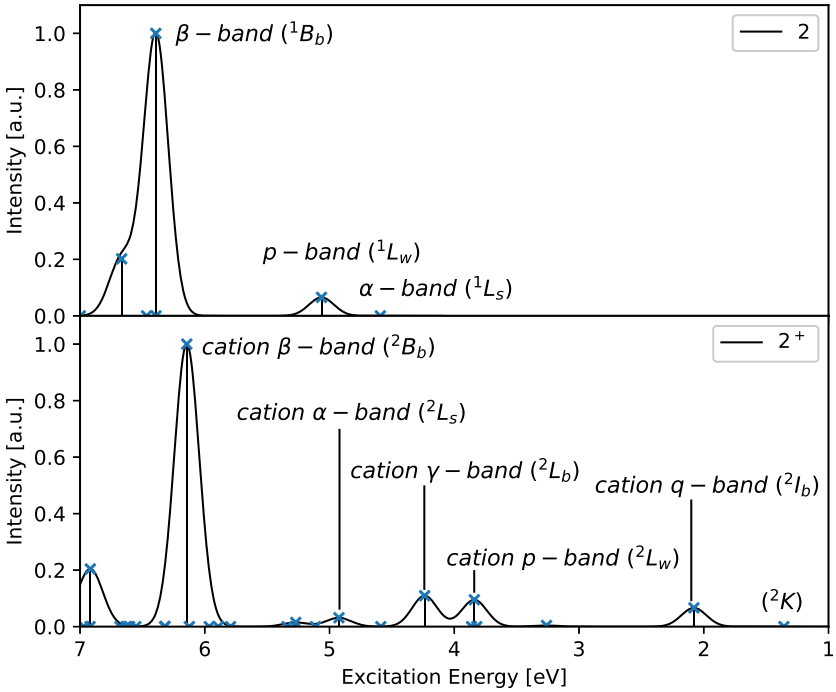

Figure 3.4: Simulated absorption spectra of **2** (top) and $\mathbf{2}^+$ (bottom) obtained by convolution of excitation energies (ADC(2)/6-311G*) using a Gaussian broadening function with a standard deviation of 0.1 eV.

The low-energy excited states of $\mathbf{3}^+$ were analyzed with regard to their main orbital transitions and then assigned to the states identified for $\mathbf{2}^+$. **Table 3.4** shows that all the states are present in $\mathbf{3}^+$ as well. The order of the excited states is not changed compared to $\mathbf{2}^+$, however there is now only one excited state described by the transition αH→αL, which corresponds to H→L in **3**. This state was therefore identified as ^2L_w without considering the transition density. It is important to note that the symmetry of the ground state of acene radical cations depends on the number of rings being even or odd. For an even number of rings the symmetry is A_u and for an odd number of rings it is B_{3g}. Excited states of the same character therefore also belong to different irreducible representations depending on the whether the number of rings is even or odd.

Table 3.4: Excitation energies [eV], oscillator strengths, orbital contributions and assignment of ADC(2) states of $\mathbf{3}^+$.

ADC(2)	f_{osc} [10^{-2}]	main contrib.	assignment neutral	state (name)
1.81	0.00	βH$-1\rightarrow\beta$L	-	1^2B_{2g} (^{2}K)
2.00	1.43	βH$\rightarrow\beta$L	-	1^2A_u (^2I_b, cation q-band)
2.56	0.15	αH$\rightarrow\alpha$L	H$\rightarrow$L	1^2B_{1u} (^2L_w, cation p-band)
3.67	2.34	αH$-1\rightarrow\alpha$L	H$-1\rightarrow$L	2^2A_u (^2L_b, cation γ-band)
		βH$-1\rightarrow\beta$L$+1$	H$-1\rightarrow$L	
4.37	0.42	βH$-1\rightarrow\beta$L$+1$	H$-1\rightarrow$L	3^2A_u (^2L_s, cation α-band)
		αH$\rightarrow\alpha$L$+1$	H$\rightarrow$L$+1$	
5.37	16.34	αH$\rightarrow\alpha$L$+1$	H$\rightarrow$L$+1$	4^2A_u (^2B_b, cation β-band)
		βH$-1\rightarrow\beta$L$+1$	H$-1\rightarrow$L	

Figure 3.5 shows the simulated absorption spectra of **3** and $\mathbf{3}^+$ created based on excitation energies obtained using ADC(2). Similar to $\mathbf{2}^+$, the cation p-band is red-shifted compared to the neutral p-band, even though it is not split up. The excitation energies are 3.88 eV and 2.56 eV for the neutral and cation p-band, respectively. It can again be observed that the cation α-band is blue-shifted and the cation β-band red-shifted compared to their neutral counterparts and that the cation α-band has a higher oscillator strength than the neutral α-band. The excitation energies are 4.02 eV and 5.59 eV for the neutral and 4.37 eV and 5.37 eV for the cation α- and cation β-band, respectively.

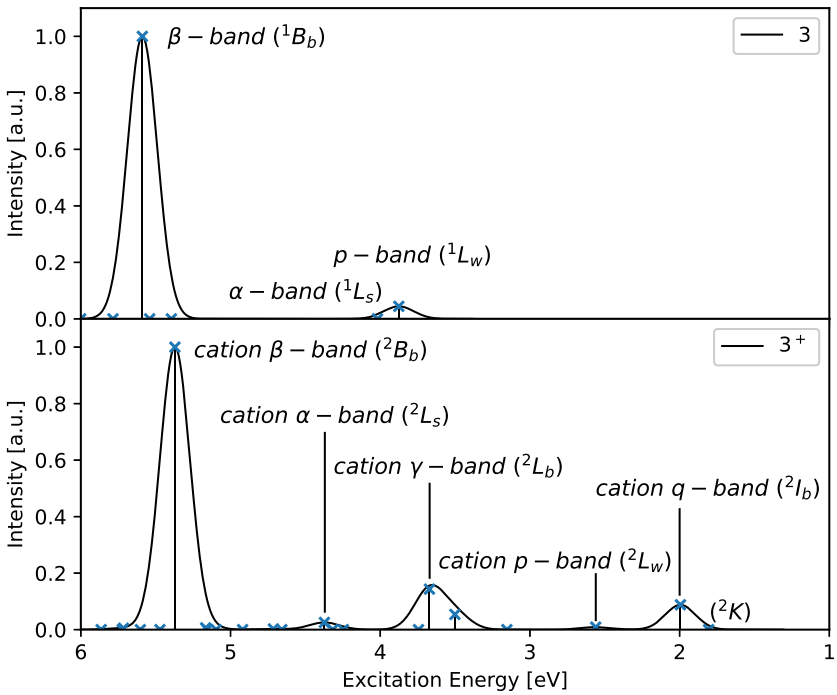

Figure 3.5: Simulated absorption spectra of **3** (top) and $\mathbf{3}^+$ (bottom) obtained by convolution of excitation energies (ADC(2)/6-311G*) using a Gaussian broadening function with a standard deviation of 0.1 eV.

Finally, the established excited states were identified in $\mathbf{4}^+$ and are shown in **Table 3.5**. A different order in the low-lying states can be observed, where ^{2}K, which was the first excited state for $\mathbf{2}^+$ and $\mathbf{3}^+$, is now the third excited state. As for $\mathbf{3}^+$, the excited state ^2L_w is not split up due to mixing with another transition, which suggests that $\mathbf{2}^+$ presents a special case in this regard.

Table 3.5: Excitation energies [eV], oscillator strengths, orbital contributions and assignment of ADC(2) states of $\mathbf{4}^+$.

ADC(2)	f_{osc} [10^{-2}]	main contrib.	assignment neutral	state (name)
1.77	2.15	βH→βL	-	1^2B_{3g} (^2I_b, cation q-band)
1.95	0.22	αH→αL	H→L	1^2B_{2g} (^2L_w, cation p-band)
2.15	0.00	βH−1→βL	-	1^2B_{1u} (^{2}K)
3.27	4.03	αH−1→αL	H−1→L	2^2B_{3g} (^2L_b, cation γ-band)
		βH−1→βL+1	H−1→L	
4.04	0.58	βH−1→βL+1	H−1→L	4^2B_{3g} (^2L_s, cation α-band)
		αH→αL+2	H→L+1	
4.88	21.09	αH→αL+2	H→L+1	5^2B_{3g} (^2B_b, cation β-band)
		βH−1→βL+1	H−1→L	

The simulated absorption spectra of **4** and $\mathbf{4}^+$ created based on excitation energies obtained using ADC(2) can be seen in **Figure 3.6** and show a similar structure to those of $\mathbf{2}^+$ and $\mathbf{3}^+$, except for the different excited state order mentioned above. As before, the cation p-band is red-shifted with an excitation energy of 3.08 eV compared to an excitation energy of 1.95 eV for the neutral p-band. The cation α- and cation β-band show a similar shift as for $\mathbf{2}^+$ and $\mathbf{3}^+$ compared to their neutral counterparts with 3.65 eV and 5.03 eV for the neutral and 4.04 eV and 4.88 eV for the cation α- and β-band, respectively. The cation α-band has a higher oscillator strength than the neutral α-band.

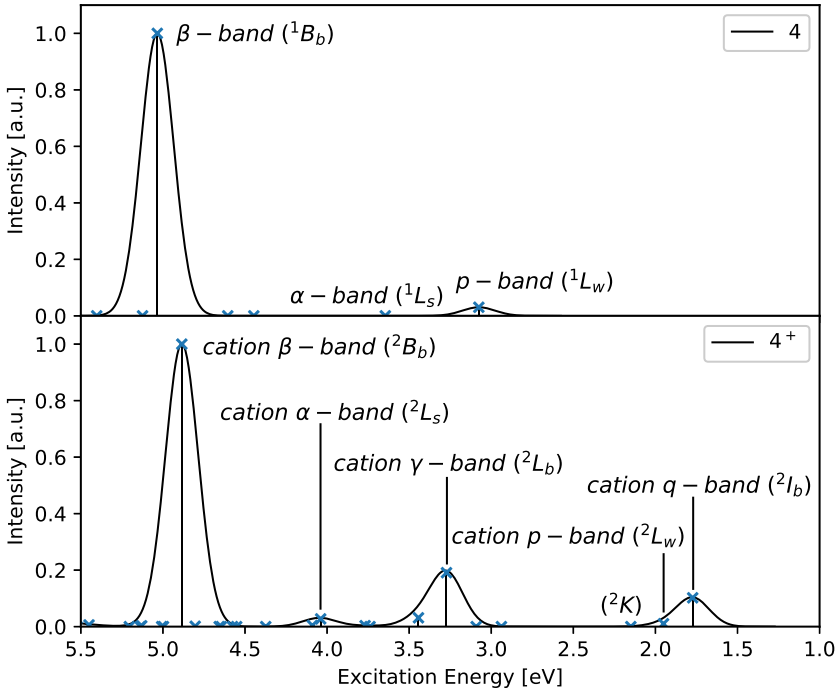

Figure 3.6: Simulated absorption spectra of **4** (top) and $\mathbf{4}^+$ (bottom) obtained by convolution of excitation energies (ADC(2)/6-311G*) using a Gaussian broadening function with a standard deviation of 0.1 eV.

3.3.3 Comparison of Excited States of Naphthalene, Anthracene, Tetracene and Their Radical Cations calculated using ADC(2) and ADC(3)

As mentioned in the previous section, the excited states obtained using ADC(2) were chosen for the analysis of the low-lying excited states of $\mathbf{2}^+$-$\mathbf{4}^+$, since the assignment of the characteristic states and the relation to the neutral excited states is apparent. This is illustrated by comparing the excited states and simulated absorption spectra calculated using ADC(2) to those calculated using ADC(3). In **Figure 3.7** both simulated spectra for $\mathbf{2}^+$ are shown and the assigned excited states using ADC(3) are shown in **Table 3.6**.

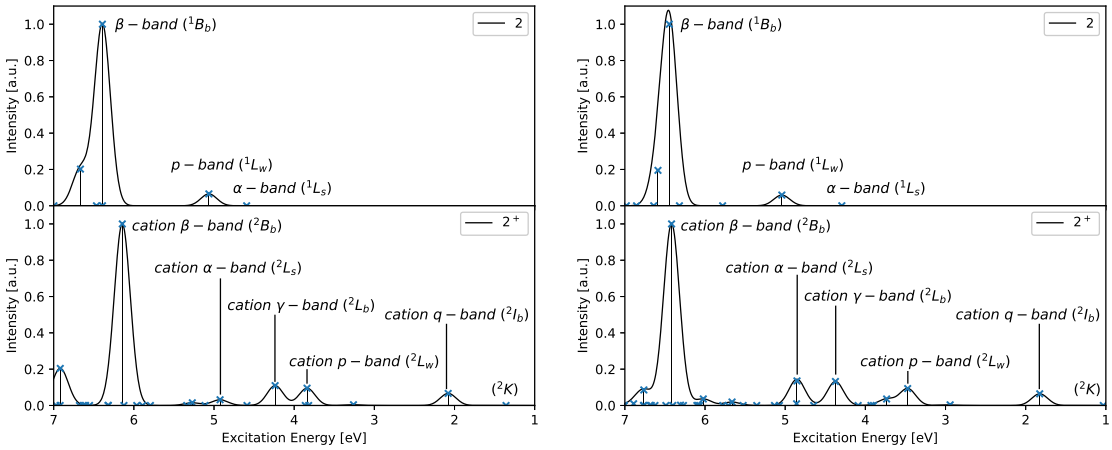

(a) ADC(2)/6-311G*. **(b)** ADC(3)/6-311G*.

Figure 3.7: Simulated absorption spectra of **2** (top) and $\mathbf{2}^+$ (bottom) obtained by convolution of excitation energies using a Gaussian broadening function with a standard deviation of 0.1 eV.

Table 3.6: Excitation energies [eV], oscillator strengths, orbital contributions and assignment of ADC(3) states of $\mathbf{2}^+$.

ADC(3)	f_{osc} [10^{-2}]	main contrib.	assignment neutral	state (name)
1.03	0.00	βH−1→βL	-	1^2B_{1u} (^{2}K)
1.83	0.57	βH→βL	-	1^2B_{3g} (^2I_b, cation q-band)
2.94	0.03	βH−2→βL	-	1^2B_{2g}
		αH−1→αL	H→L	
3.47	0.83	αH−1→αL	H→L	2^2B_{2g} (^2L_w, cation p-band)
		βH−2→βL	-	
3.74	0.32	αH→αL	H−1→L	2^2B_{3g}
		βH−1→βL+1	H−1→L	
4.37	1.18	βH−1→βL+1	H−1→L	3^2B_{3g} (^2L_b, cation γ-band)
		αH→αL	H−1→L	
4.85	1.21	αH−1→αL+1	H→L+1	4^2B_{3g} (^2L_s, cation α-band)
		βH−1→βL+1	H−1→L	
6.42	8.96	βH−1→βL+1	H−1→L	5^2B_{3g} (^2B_b, cation β-band)
		αH−1→αL+1	H→L+1	

In the case of $\mathbf{2}^+$, the excited states obtained using ADC(3) are similar to those obtained using ADC(2). All the states that were labeled using ADC(2), could be clearly identified in the excites states using ADC(3). As for ADC(2), there are two excited states, 1^2B_{2g} and 2^2B_{2g}, which are described by αH−1→αL (H→L) and βH−2→βL, where 2^2B_{2g} was identified as ^2L_w. There are however also two excited states, 2^2B_{3g} and 3^2B_{3g}, described by αH→αL (H−1→L) and βH−1→βL+1 (H−1→L) suggesting that the state ^2L_b is split up, which is not observed in the excited states obtained using ADC(2). The second state was identified as ^2L_b based the oscillator strength.

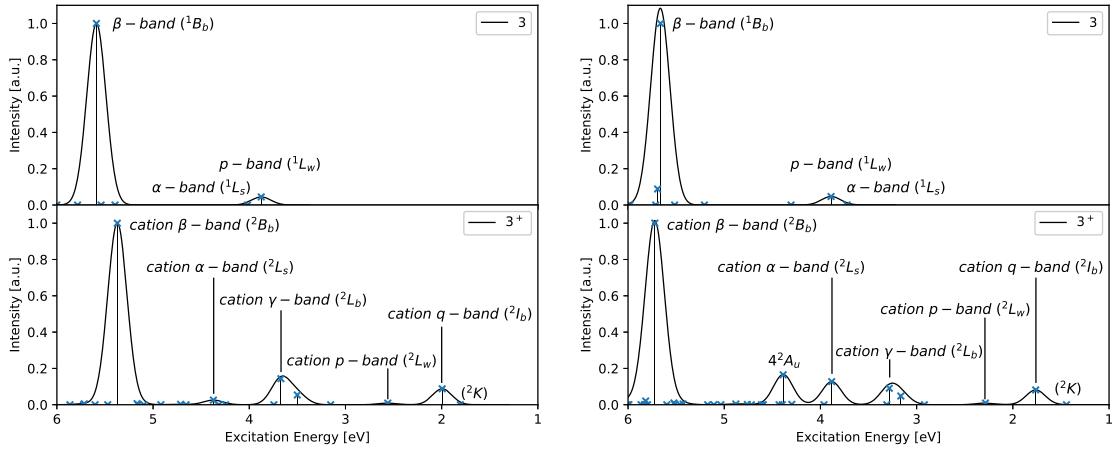

(a) ADC(2)/6-311G*. **(b)** ADC(3)/6-311G*.

Figure 3.8: Simulated absorption spectra of **3** (top) and $\mathbf{3}^+$ (bottom) obtained by convolution of excitation energies using a Gaussian broadening function with a standard deviation of 0.1 eV.

Table 3.7: Excitation energies [eV], oscillator strengths, orbital contributions and assignment of ADC(3) states of $\mathbf{3}^+$.

ADC(3)	f_{osc} [10^{-2}]	main contrib.	assignment neutral	state (name)
1.44	0.00	βH−1→βL	-	1^2B_{2g} (^{2}K)
1.76	1.10	βH→βL	-	1^2A_u (^2I_b, cation q-band)
2.29	0.12	αH→αL	H→L	1^2B_{1u} (^2L_w, cation p-band)
3.28	1.22	αH−1→αL	H−1→L	2^2A_u (^2L_b, cation γ-band)
		βH−1→βL+1	H−1→L	
3.88	1.71	βH−1→βL+1	H−1→L	3^2A_u (^2L_s, cation α-band)
		αH→αL+1	H→L+1	
4.39	2.22	αH→αL+1	H→L+1	4^2A_u
		αH, βH−1→αL, βL	-	
5.72	13.46	αH→αL+1	H→L+1	6^2A_u (^2B_b, cation β-band)
		βH−1→βL+1	H−1→L	

When comparing the excited states and simulated absorption spectra of **3** and $\mathbf{3}^+$ calculated using ADC(2) and ADC(3), in **Figure 3.8**, a stronger deviation can be seen. The assignment of the excited states obtained using ADC(3) is shown in **Table 3.7**. It was possible to identify all the states, which were labeled using ADC(2), however there is an additional bright state, 4^2A_u, which is not present in the spectrum simulated using ADC(2). This state is described by the orbital transitions αH→αL+1 (H→L+1) and αH, βH−1→αL, βL. Since in the description of the excited states ^1L_w, ^1L_s and ^1B_b double excitations do not participate with meaningful amplitudes, these transitions can not be related to any relevant transition in the neutral system.
For **4** and $\mathbf{4}^+$ the absorption spectra simulated based on excitation energies obtained using ADC(2) and ADC(3) are shown in **Figure 3.9**. The assignment of excited states using ADC(3) can be seen in **Table 3.8**. It was possible to assign the labeled excited states to those calculated using ADC(3) except for ^2L_s. **Table 3.8** shows several excited states, 3^2B_{3g}-7^2B_{3g} that are described by orbital transitions relating to H→L, H−1→L or H→L+1 in the neutral compound, but which could not be clearly assigned. Further, a stronger involvement of double excitations in the description of the excited states is noticeable, which complicates the assignment to the neutral characteristic excited states.

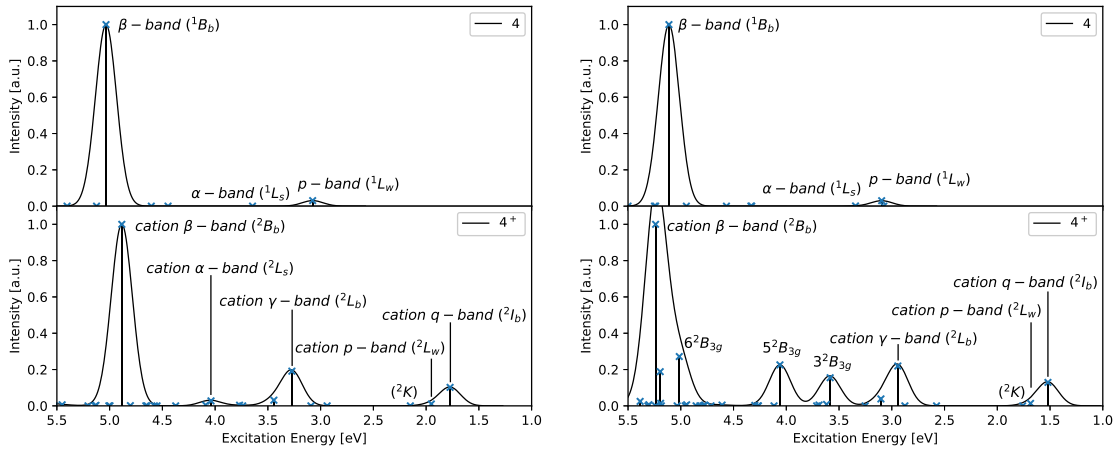

(a) ADC(2)/6-311G*. **(b)** ADC(3)/6-311G*.

Figure 3.9: Simulated absorption spectra of **4** (top) and $\mathbf{4}^+$ (bottom) obtained by convolution of excitation energies using a Gaussian broadening function with a standard deviation of 0.1 eV.

Table 3.8: Excitation energies [eV], oscillator strengths, orbital contributions and assignment of ADC(3) states of $\mathbf{4}^+$.

ADC(3)	f_{osc} [10^{-2}]	main contrib.	assignment neutral	state (name)
1.52	1.60	βH→βL	-	1^2B_{3g} (^2I_b, cation q-band)
1.68	0.17	αH→αL	H→L	1^2B_{2g} (^2L_w, cation p-band)
1.76	0.00	βH−1→βL	-	1^2B_{1u} (^2K)
2.94	2.71	αH−1→αL	H−1→L	2^2B_{3g} (^2L_b, cation γ-band)
		βH−1→βL+1	H−1→L	
3.58	1.91	βH−1→βL+1	H−1→L	3^2B_{3g}
		βH−4→βL	-	
3.62	0.10	βH−4→βL	-	4^2B_{3g}
		βH−1→βL+1	H−1→L	
4.06	2.79	αH→αL	H→L	5^2B_{3g}
		αH, βH−1→αL, βL	-	
5.01	3.35	αH, βH→αL, βL+1	-	6^2B_{3g}
		αH→αL+2	H→L+1	
5.20	2.33	βH−1→βL+1	H−1→L	7^2B_{3g}
		αH−1→αL	H−1→L	
5.24	12.35	βH−1→βL+1	H−1→L	8^2B_{3g} (^2B_b, cation β-band)
		αH→αL+2	H→L+1	

By comparing the excited states of $\mathbf{2}^+$-$\mathbf{4}^+$ using ADC(2) and ADC(3), it is apparent that the identification and relation to the neutral excited states is more apparent in the excited states of ADC(2). With increasing acene length, the participation of double excitations increases, which

makes the comparison to the neutral excited states more difficult. Furthermore, the extension of the analysis to excited states using TD-DFT is facilitated by using ADC(2), since in TD-DFT double excitations are not included.
The simulated absorption spectra of **2**-**4** using ADC(2)-x and those of $\mathbf{2}^+$-$\mathbf{4}^+$ using ADC(2)-x and IP-ADC(3) and the assignment of the characteristic existed states can be found the **Appendix A** (**Figure A.3**-**A.8** and **Table A.4**-**A.9**). In the case of IP-ADC(3) orbital transitions for the excitations are not available, which is why the assignment was done based on irreducible representations and visual inspection of the simulated spectra.

3.3.4 TD-DFT Benchmark of Excited States of Naphthalene, Anthracene, Tetracene, Pentacene and Their Radical Cations

The investigation of the excited states was extended to longer acenes up to **12** and $\mathbf{12}^+$ using TD-DFT. The excitations energies of low-lying excited states of **2**-**5** and $\mathbf{2}^+$-$\mathbf{5}^+$ were calculated using the DFT functionals BLYP, B3LYP, BHHLYP and CAM-B3LYP and compared to experimental values.[31,166–168,177] The results for the excitation energies of the neutral states can be seen in **Table 3.9**. For **2** and **3**, the best agreement with experiment is achieved using the BLYP functional with MAPEs of 5.3 % and 6.5 % for **2** and **3** respectively, followed by the B3LYP functional with MAPEs of 7.2 % and 6.8 % for **2** and **3**, respectively. The B3LYP functional then shows the best accuracy for **4** and **5** with MAPEs of 6.3 % and 8.1 % for **4** and **5** respectively and has therefore the best agreement overall. The performance of the functionals BHHLYP and CAM-B3LYP improves as the size of the acenes increases from 12.5 % (11.2 %) to 9.6 % (9.9 %) for **2** and **5** respectively using BHHLYP (CAM-B3LYP).

Table 3.9: Excitation energies [eV] of low-lying excited states of **2**-**5** calculated using the BLYP, B3LYP, BHHLYP and CAM-B3LYP functionals and comparison to experimental values.

naphthalene					
state	exp[31]	BLYP	B3LYP	BHHLYP	CAM-B3LYP
1^1B_{2u}	4.48	4.17	4.48	4.80	4.79
1^1B_{3u}	4.03	4.31	4.56	4.84	4.72
2^1B_{3u}	5.62	5.88	6.10	6.39	6.28
MAE [eV]		0.25	0.37	0.67	0.59
MAPE [%]		5.3	7.2	12.5	11.2
anthracene					
state	exp[31]	BLYP	B3LYP	BHHLYP	CAM-B3LYP
1^1B_{2u}	3.38	3.01	3.13	3.67	3.67
1^1B_{3u}	3.57	3.69	3.95	4.23	4.13
2^1B_{3u}	4.86	5.06	5.33	5.64	5.55
MAE [eV]		0.23	0.31	0.58	0.51
MAPE [%]		6.5	6.8	12.4	11.2
tetracene					
state	exp[31]	BLYP	B3LYP	BHHLYP	CAM-B3LYP
1^1B_{2u}	2.71	2.24	2.54	2.88	2.90
1^1B_{3u}	3.32	3.29	3.56	3.83	3.75
2^1B_{3u}	4.52	4.48	4.77	5.11	5.03
MAE [eV]		0.18	0.22	0.42	0.38
MAPE [%]		7.6	6.3	10.2	9.4
pentacene					
state	exp[31]	BLYP	B3LYP	BHHLYP	CAM-B3LYP
1^1B_{2u}	2.23	1.70	1.99	2.35	2.31
1^1B_{3u}	3.05	3.01	3.28	3.49	3.55
2^1B_{3u}	4.14	4.05	4.37	4.65	4.71
MAE [eV]		0.22	0.23	0.36	0.38
MAPE [%]		11.6	8.1	9.6	9.9

For the benchmark of the excitation energies of the cations $\mathbf{2}^+$-$\mathbf{5}^+$, the states were assigned based on their excitation energies and oscillator strength. As for the neutral acenes, the functional BLYP shows the best performance for the smaller acene cations $\mathbf{2}^+$ and $\mathbf{3}^+$ with MAPEs of 7.9 % and 6.9 % for $\mathbf{2}^+$ and $\mathbf{3}^+$, respectively. The functional B3LYP then has the best agreement with experiment for $\mathbf{4}^+$ and $\mathbf{5}^+$ with MAPEs of 6.3 % and 8.1 % for $\mathbf{4}^+$ and $\mathbf{5}^+$, respectively. Overall, these two functionals show the best performance, which is in agreement with other studies employing these

functionals for excited states of small acene cations.[126] It is however noteworthy that again the agreement with experiment improves with increasing acene length from 12.3 % (9.1 %) to 10.8 % (8.0 %) for **2** and **5** respectively using BHHLYP (CAM-B3LYP). Previous studies have shown that the correct description of excited states of molecules with an extended π-system using TD-DFT requires a range-separated functional.[178–180] This is also the case for the investigation of exciton properties in the subsequent chapter.[181,182] Based on these considerations, the functional CAM-B3LYP was chosen for the calculation of the excitation energies of the longer neutral and cationic acenes.

Table 3.10: Excitation energies [eV] of low-lying excited states of $\mathbf{2}^+$-$\mathbf{5}^+$ calculated using the BLYP, B3LYP, BHHLYP and CAM-B3LYP functionals and comparison to experimental values.

naphthalene cation					
state[166,176]	exp[166]	BLYP	B3LYP	BHHLYP	CAM-B3LYP
1^2B_{1u}	forb.	1.08	1.17	1.31	1.22
1^2B_{3g}	1.83	2.19	2.19	2.14	2.14
1^2B_{2g}	2.72	2.84	3.04	3.24	3.28
2^2B_{2g}	3.29	3.56	3.65	3.46	3.65
2^2B_{3g}	4.02	3.80	3.97	4.09	4.06
3^2B_{3g}	4.49	4.35	4.66	5.12	4.94
3^2B_{2g}	5.08	4.60	4.66	5.12	4.94
MAE [eV]		0.19	0.21	0.28	0.31
MAPE [%]		7.9	7.9	12.3	9.1
anthracene cation*					
state[167]	exp[167]	BLYP	B3LYP	BHHLYP	CAM-B3LYP
1^2B_{2g}	forb.	1.45	1.57	1.74	1.66
1^2A_u	1.73	1.90	1.97	2.08	2.03
1^2B_{1u}	2.02	2.24	2.36	2.35	2.48
1^2B_{3g}	forb.	2.84	3.03	3.27	3.26
2^2B_{1u}	2.90	2.96	3.22	3.35	3.42
MAE [eV]		0.15	0.30	0.38	0.43
MAPE [%]		6.9	12.2	14.8	16.3

tetracene cation*					
state[168]	exp[168]	BLYP	B3LYP	BHHLYP	CAM-B3LYP
1^2B_{3g}	1.43	1.64	1.73	1.67	1.83
1^2B_{1u}	forb.	1.68	1.84	1.95	1.94
(1^2B_{2g})	1.66	1.65	1.74	1.85	1.80
1^2A_u	forb.	2.53	2.80	3.20	3.17
2^2B_{2g}	-	2.91	3.43	3.18	3.19
2^2B_{3g}	3.16	2.77	3.08	3.20	3.32
MAE [eV]		0.20	0.15	0.20	0.23
MAPE [%]		9.2	8.2	9.9	11.5
pentacene cation					
state[177]	exp[177]	BLYP	B3LYP	BHHLYP	CAM-B3LYP
1^2B_{1u}	1.27	1.19	1.27	1.15	1.34
1^2A_u	1.31	1.46	1.54	1.66	1.61
2^2A_u	2.95	2.65	2.84	2.92	2.94
MAE [eV]		0.13	0.09	0.13	0.09
MAPE [%]		9.4	6.3	10.8	8.0

*The molecular orientation in reference differs from the one

in this paper so that B_{3g} in the reference corresponds to B_{2g} here.

3.3.5 Excited States of Naphthalene to Dodecacene and Their Radical Cations

The excitation energies of the excited states ^1L_w, ^1L_s and ^1B_b for **2-12** and ^2I_b, ^2L_w, ^2L_b, ^2L_s and ^2B_b for $\mathbf{2}^+$-$\mathbf{12}^+$ were computed at the TDA/CAM-B3LYP/6-311G* level of theory and are shown in **Figure 3.10**. The excitation energies and simulated absorption spectra of $\mathbf{2}^+$-$\mathbf{12}^+$ can be found in **Appendix A** (**Table A.10** and **Figure A.9** and **A.10**).

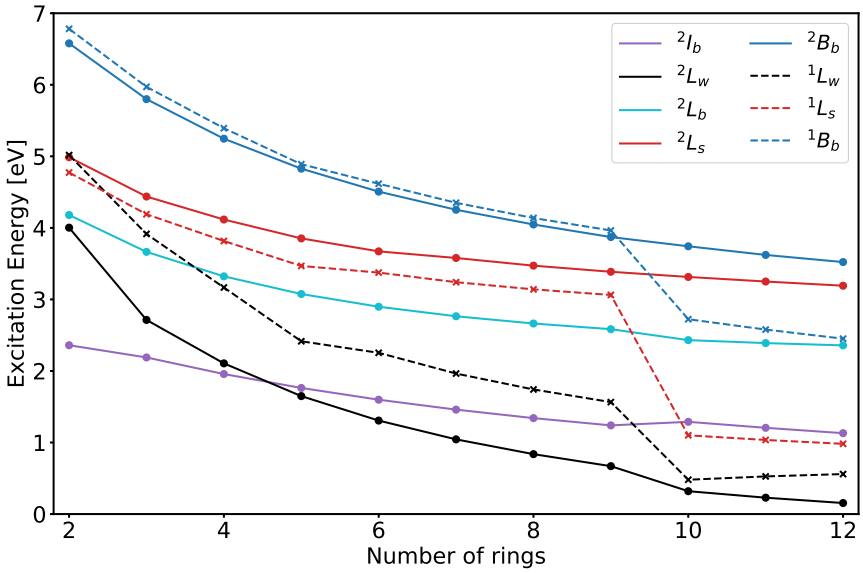

Figure 3.10: Excitation energies [eV] of the excited states ^1L_w, ^1L_s and ^1B_b for **2-12** and ^2I_b, ^2L_w, ^2L_b, ^2L_s and ^2B_b for $\mathbf{2}^+$-$\mathbf{12}^+$ calculated at the TDA/CAM-B3LYP/6-311G* level of theory.

As expected, the excitation energies of all investigated excited states decrease with increasing acene length. Furthermore, they all seem to be converging towards a certain value. The development of the excitation energies of the states ^1L_w, ^1L_s and ^1B_b for **2-12** shows a smooth decrease up to **10**, where a discontinuity can be seen as the excitation energies decrease drastically. As mentioned before, ^1L_w is the lowest-lying excited state for all investigated neutral acenes except for **2**, where ^1L_s has a smaller excitation energy. For all other cases, ^1L_s has a higher excitation energy than ^1L_w, followed by ^1B_b, which has the highest excitation energy of the investigated states.
The excitation energies of ^2I_b, ^2L_w, ^2L_b, ^2L_s and ^2B_b for $\mathbf{2}^+$-$\mathbf{12}^+$ however show only a slight discontinuity, when going from $\mathbf{9}^+$ to $\mathbf{10}^+$. Up to $\mathbf{4}^+$, the lowest-lying excited state of the states displayed in **Figure 3.10** is ^2I_b followed by ^2L_w. For $\mathbf{5}^+$, these two states switch so that ^2L_w becomes the lowest-lying excited state, followed by ^2I_b. The state with the next higher excitation energy is ^2L_b, followed by ^2L_s and ^2B_b for all acene cations investigated.
Comparing the excited states of the same character of the neutral acenes ^1L_w, ^1L_s and ^1B_b and of the acene cations ^2L_w, ^2L_s and ^2B_b up to **9** and $\mathbf{9}^+$, it can be seen that, as observed before, the state ^2L_w is red-shifted compared to its neutral counterpart ^1L_w. The states ^2L_s and ^2B_b are shifted to lower and higher excitation energies respectively compared to ^1L_s and ^1B_b.
The discontinuities in the development of the excited states of the neutral acenes ^1L_w, ^1L_s and ^1B_b can be explained by the increasing diradical character of longer acenes. With increasing size of the π-system, the energies of the first excited singlet state and the lowest triplet state decrease and they start to mix with the closed-shell singlet ground state. The closed-shell singlet therefore becomes an increasingly poor description for the ground state of longer acenes. TD-DFT at the chosen level of theory, predicts a triplet ground state for acenes larger than **9**. This is observed as a so called "triplet instability" and prohibits the performance of a full TD-DFT calculation, which is why the TDA is employed. The prediction of a triplet ground state for longer acenes is however not correct, as it has been shown that the ground state of longer acene is an open-shell singlet.[34,35,154,155,157] For the description of an open-shell singlet, a multi-reference wavefunction is necessary, which is not possible using (TD-)DFT. The quality of the description of longer acenes using (TD-)DFT therefore declines, which is observed in the discontinuities in the development of

the excitation energies. In the case of CAM-B3LYP, there seems to be a "breaking-point" after which the description suffers greatly. The acene length at which this happens likely depends on the chosen functional. This is not only observed in the excitation energies, but also in the orbital transitions describing the excited states ^1L_s and ^1B_b. These are H−1→L and H→L+1 for **2-4**, then H−2→L and H→L+2 for **5-7** and then finally H−3→L and H→L+3 for **8** and **9**. For **10-12** however, they are again H−1→L and H→L+1, while for the cations the trend of an increasing gap between the participating orbitals is continued (**Table A.11**).
In the case of the cations, the decrease of the excitation energy of the first excited state has a smaller effect on the excitation energies. The correct description of the ground state also requires a multi-configurational wavefunction as the two state grow closer in energy. However, since in this case the state mixing with the ground state has the same multiplicity, the effect on the energy of the ground state and therefore the excitation energies is smaller. Nevertheless, it leads to convergence issues as the switching of the α-H and α-L is necessary to obtain the SCF-solution with the lowest energy, as mentioned previously.

3.3.6 Exciton Properties of Excited States of Naphthalene to Dodecacene and Their Radical Cations

The exciton properties, i.e. exciton size, hole and electron size and the electron-hole correlation coefficient of the excited states ^1L_w, ^1L_s and ^1B_b for **2-12** and ^2I_b, ^2L_w, ^2L_b, ^2L_s and ^2B_b for $\mathbf{2}^+$-$\mathbf{12}^+$ were computed at the TDA/CAM-B3LYP/6-311G* level of theory to investigate their behavior with increasing acene size. Since acenes and acene cations larger than **9** and $\mathbf{9}^+$ are not well described using TD-DFT, as previously mentioned, the results for **10-12** and $\mathbf{10}^+$-$\mathbf{12}^+$ will not be discussed here. The figures including these results can be found in **Appendix A** (**Figure A.11-A.15**).
In **Figure 3.11**, the exciton size, hole and electron size of the excited states ^2L_w and ^1L_w of $\mathbf{2}^+$-$\mathbf{9}^+$ and **2-9**, respectively can be seen. The exciton, hole and electron size for both states increase with growing acene length, where the exciton size seem to converge towards a certain value, while the hole and electron size grow more continuously. The exciton size of the state ^1L_w of the neutral molecules is larger than the one of the respective cation state ^2L_w for all molecules. The exciton size increases from 3.4 Å to 7.0 Å for **2-9** and from 3.0 Å to 6.2 Å for $\mathbf{2}^+$-$\mathbf{9}^+$. The hole and electron size of ^2L_w are of similar size in the case of $\mathbf{2}^+$ with 2.4 Å for both. However, the hole size increases faster than the electron size so that it is larger from $\mathbf{3}^+$ on. Finally, for $\mathbf{9}^+$ the hole size is 5.6 Å and the electron size 5.0 Å. For the neutral acenes, the electron size is slightly larger than the hole size for all systems, increasing from 2.3 Å and 2.4 Å for **2** to 5.2 Å and 5.3 Å respectively for **9**.

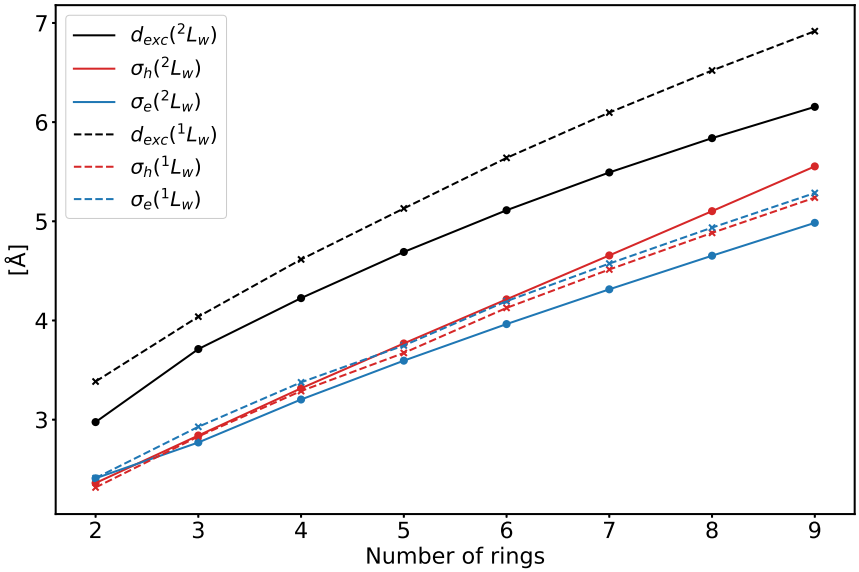

Figure 3.11: Exciton (d_{exc}), hole (σ_h) and electron size (σ_e) of the excited states ^2L_w and ^1L_w of **2**$^+$-**9**$^+$ and **2**-**9** calculated using TDA/CAM-B3LYP/6-311G*.

For the excited states ^2L_s and ^1L_s of **2**$^+$-**9**$^+$ and **2**-**9**, a similar trend can be seen for the exciton size. However, the exciton size of the neutral acenes is only slightly larger ranging from 3.2 Å to 5.7 Å for **2**-**9** and from 3.1 Å to 5.6 Å for the cations **2**$^+$-**9**$^+$. An exception can be seen for **6**/**6**$^+$ and **7**/**7**$^+$, which could be explained by the excited state ^2L_s mixing with another transition βH−4→βL for **4**$^+$-**7**$^+$. The increase of the exciton size seems to converge for both neutral and cationic acenes. Initially, the hole size is again smaller than the electron size with 2.3 Å and 2.4 Å respectively for **2**$^+$. Subsequently. the hole size increases faster than the electron size, reaching the values 6.5 Å and 5.8 Å respectively for **9**$^+$. The irregularities for **4**$^+$-**7**$^+$, likely due to the mixing with another state, can be observed more clearly here. In the case of the hole and electron size of ^1L_s, the electron size is again slightly larger than the hole size for all neutral acenes. The hole size increases from 2.3 Å to 5.2 Å and the electron size increases from 2.4 Å to 5.2 Å for **2**-**9**. Both, the hole and electron size of the neutrals and cations, increase continuously as opposed to the exciton size, so that both are larger than the exciton size for **9**$^+$.

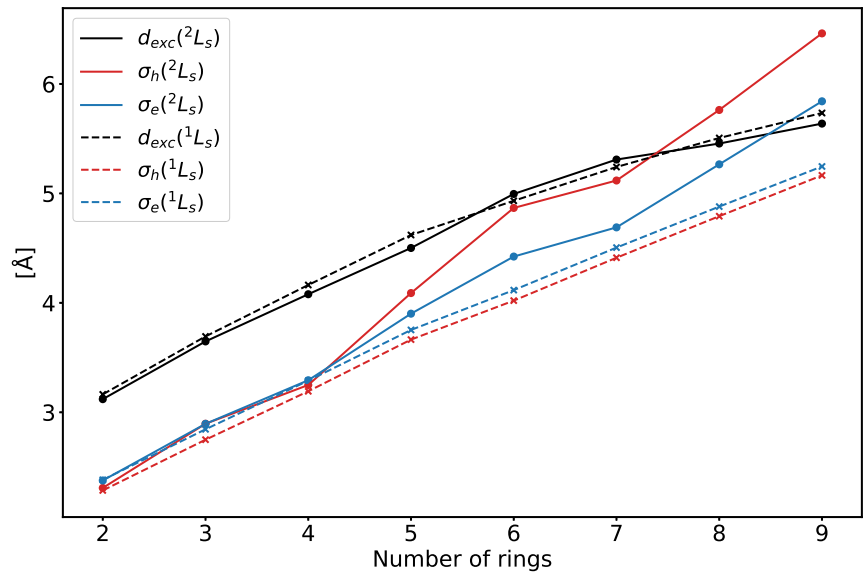

Figure 3.12: Exciton (d_{exc}), hole (σ_h) and electron size (σ_e) of the excited states ^2L_s and ^1L_s of $\mathbf{2}^+$-$\mathbf{9}^+$ and **2**-**9** calculated using TDA/CAM-B3LYP/6-311G*.

Figure 3.13 shows the course of the exciton properties of the excited states ^2B_b and ^1B_b of **2**-**9** with increasing acene size. Again, the exciton size of the neutral excited state ^1B_b is generally larger than that of its cationic counterpart ^2B_b. For the former, the exciton size increased from 3.2 Å to 6.3 Å for **2**-**9**, while for the latter the exciton size increases from 3.1 Å to 5.9 Å for $\mathbf{2}^+$-$\mathbf{9}^+$. As for the other excited states, the increase of the exciton size flattens as the acene length increases. The hole size of ^2B_b increases from 2.3 Å to 7.0 Å for $\mathbf{2}^+$-$\mathbf{9}^+$, while the electron size increases from 2.4 Å to 6.1 Å for $\mathbf{2}^+$-$\mathbf{9}^+$, so that the hole size again shows a stronger increase. Both the hole and electron size of ^2B_b increase faster with growing acene length and surpass the exciton size for $\mathbf{9}^+$. The hole and electron size of ^1B_b show the same trend as before, with the electron size being slightly larger and both showing a continuous increase with growing acene length from 2.3 Å to 5.7 Å for **2**-**9** and 2.4 Å to 5.8 Å **2**-**9** for hole and electron size, respectively.

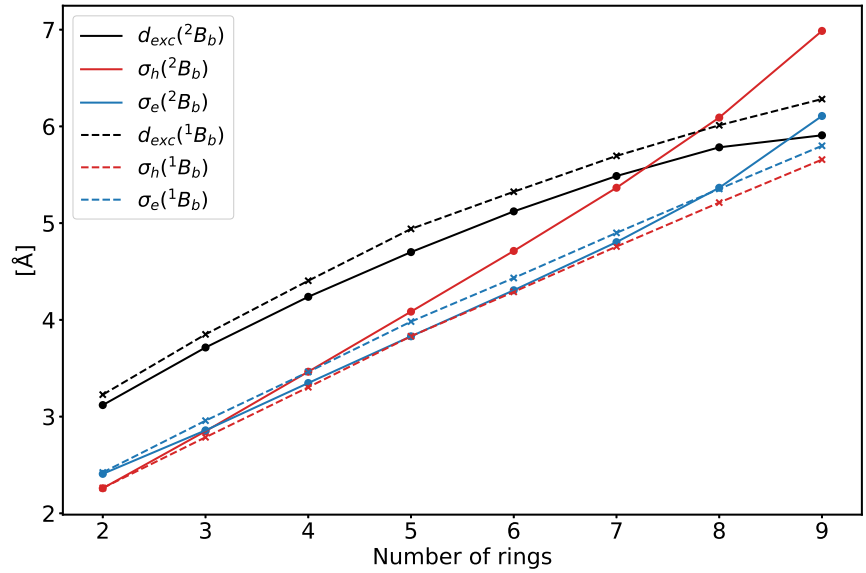

Figure 3.13: Exciton (d_{exc}), hole (σ_h) and electron size (σ_e) of the excited states ^2B_b and ^1B_b of $\mathbf{2}^+$-$\mathbf{9}^+$ and **2**-**9** calculated using TDA/CAM-B3LYP/6-311G*.

The exciton properties of the excited state $^2\mathrm{I_b}$ of $\mathbf{2}^+$-$\mathbf{9}^+$ can be seen in **Figure 3.14**. The exciton size stays larger than both the hole and electron size and increases from 3.5 Å to 7.5 Å for $\mathbf{2}^+$-$\mathbf{9}^+$. The hole size is smaller for $\mathbf{2}^+$ with 2.0 Å, while the electron size is 2.3 Å. Subsequently, the hole size increases faster and reaches 6.1 Å for $\mathbf{9}^+$, while the electron sizes goes up to 5.0 Å. The exciton, hole and electron size all show a similar increase with growing acene length.

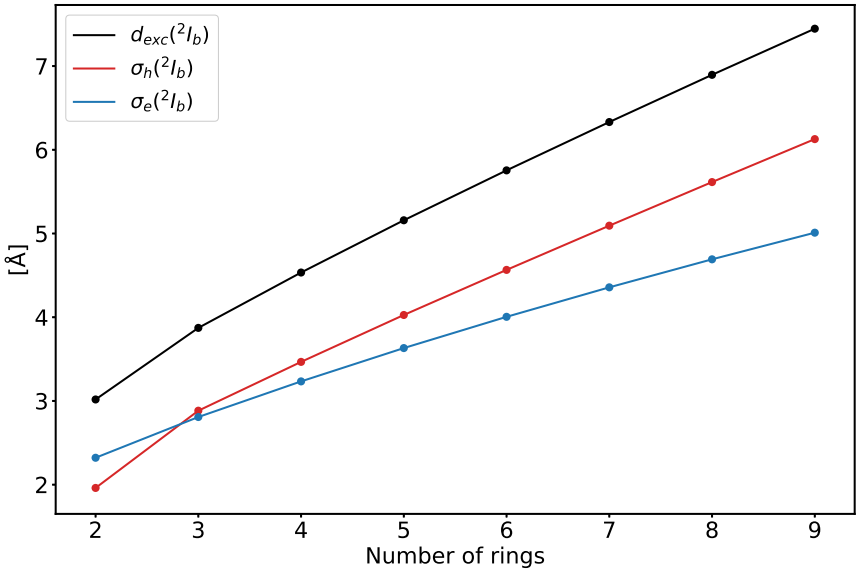

Figure 3.14: Exciton (d_{exc}), hole (σ_h) and electron size (σ_e) of the excited states $^2\mathrm{I_b}$ of $\mathbf{2}^+$-$\mathbf{9}^+$ calculated using TDA/CAM-B3LYP/6-311G*.

In the case of the excited state $^2\mathrm{L_b}$ of $^2\mathrm{I_b}$ for $\mathbf{2}^+$-$\mathbf{9}^+$, the exciton size increases from 3.1 Å to 6.1 Å, which can be seen in **Figure 3.15**. The increase of the exciton size seems to flatten as the acenes get longer. As for all the investigated excited states of the cations, the electron size is larger for $\mathbf{2}^+$, but the hole size increases faster and is larger from $\mathbf{3}^+$ on. The hole size increases from 2.3 Å to 6.0 Å for $\mathbf{2}^+$-$\mathbf{9}^+$ and the hole size increases from 2.4 Å to 5.1 Å for $\mathbf{2}^+$-$\mathbf{9}^+$. Both hole and electron size increase continuously with growing acene size.

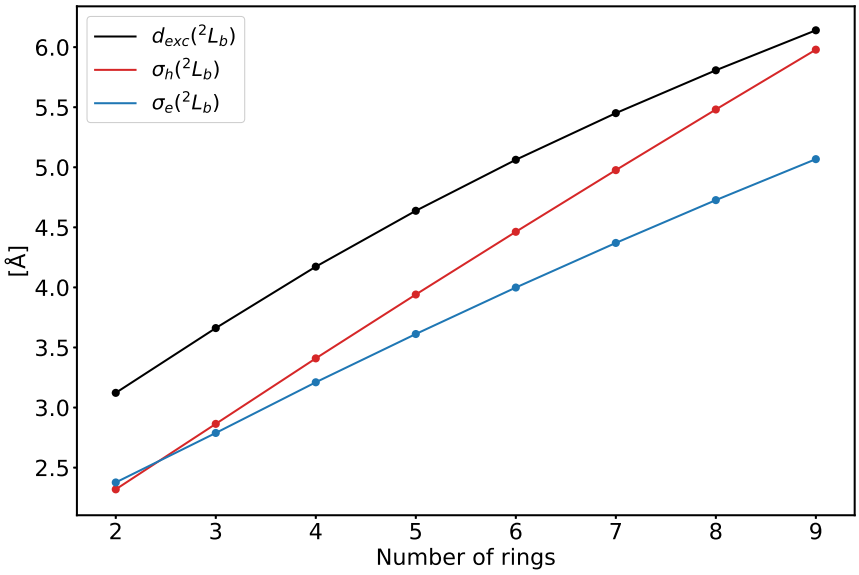

Figure 3.15: Exciton (d_{exc}), hole (σ_h) and electron size (σ_e) of the excited states $^2\mathrm{L_b}$ of $\mathbf{2}^+$-$\mathbf{9}^+$ calculated using TDA/CAM-B3LYP/6-311G*.

The exciton properties of the investigated excited states show general trends, which can be observed for all of them. Overall, the exciton, hole and electron size all increase with increasing acene length. Between excited states with the same character of neutral and cationic acenes, the exciton size of the respective neutral excited state is generally larger, except in the case of ^2L_s for **6**/**6**$^+$ and **7**/**7**$^+$. Here, the excited state mixes with another transition, which could be the reason for the different behavior. The overall smaller exciton size of the excited states of the cations could be explained by the contraction of the electron density upon the removal of an electron due to smaller electron-electron repulsion and weaker shielding of the nuclear attraction. However, it would be expected that in this case the difference between the exciton size of the neutral and cationic excited states would decrease with increasing length, as the effect of removing one electron on the electron density should decrease with an increasing amount of total electrons. However, since this is not observed there has to be another explanation for the smaller exciton size of the excited states of the cations compared to the respective excited states of the neutrals. Also, the hole and electron size of the excited states of the cations are not smaller than those of the corresponding excited states of the neutrals. It is shown below, that the reason for the smaller exciton size of the excited states of the cations might be the larger electron-hole correlation.

In case of the neutral acenes, the electron size is consistently larger than the hole size for all investigated excited states. For the cations, the electron size is only larger than the hole size for **2**$^+$ (and for ^2L_s of **3**$^+$ and **4**$^+$), while it is smaller for all other acene cations, since the hole size increases faster than the electron size. A possible explanation is that the already existing positive charge of the cations is increasingly delocalized with the growing size of the π-system, leading to an overall larger hole size.

Two different trends can be observed for the relative behavior of exciton size and hole and electron size in the investigated excited states. For the excited states ^2L_w, ^1L_w and ^2I_b, the increase of the exciton size and the hole and electron size is similar, while for the excited states ^2L_s, ^1L_s, ^2B_b, ^1B_b and ^2L_b, the hole and electron size increase visibly faster than the exciton size. A characteristic that distinguishes these two groups is that the former excited states are mainly described by one orbital transition, while the latter have significant contributions from at least two orbital transitions.

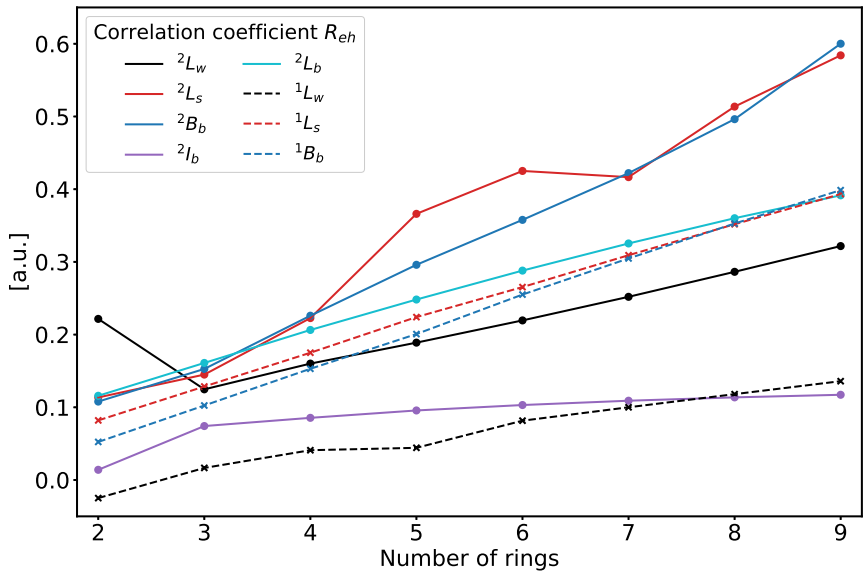

Figure 3.16: Correlation coefficient (R_{eh}) of all investigated excited states of **2**$^+$-**9**$^+$ and **2**-**9** calculated using TDA/CAM-B3LYP/6-311G*.

These different trends can be linked to the development of the correlation coefficient (R_{eh}) of the investigated states, which can be seen in **Figure 3.16**. The excited states ^2L_w, ^1L_w and ^2I_b all show overall lower values for the correlation coefficient, which increases only slowly with growing acene length. Higher values for the correlation coefficient and a faster increase can be seen for the excited states ^2L_s, ^1L_s, ^2B_b, ^1B_b and ^2L_b. Some irregularities in the course of the correlation coefficient can be seen for ^2L_w of $\mathbf{2}^+$ and ^2L_s of $\mathbf{4}^+$-$\mathbf{7}^+$, which are both likely explained by the mixing of these states with other transitions, as explained above. Therefore, the excited states, where the exciton size shows a similar increase to the hole and electron size, show a smaller correlation coefficient that grows slowly with increasing acene length. The other group of excited states, where the hole and electron size grow faster then the exciton size, show higher correlation coefficients, which grow faster with increasing acene size. For localized excited states, the exciton size is related to the hole and electron size according to $d_{exc} = \sqrt{\sigma_h^2 + \sigma_e^2 - 2R_{eh}\sigma_h\sigma_e}$, which explains the observed relation between exciton size and hole and electron size.[38]

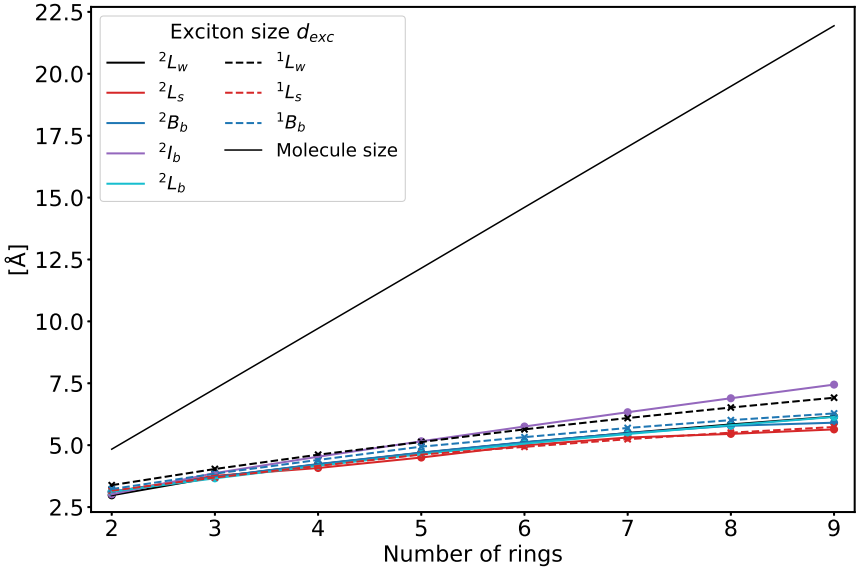

Figure 3.17: Exciton size (d_{exc}) of all investigated excited states of $\mathbf{2}^+$-$\mathbf{9}^+$ and **2**-**9** compared to the molecular size along the long axis calculated using TDA/CAM-B3LYP/6-311G*.

Ultimately, the exciton size of all investigated excited states is set into relation with the size of the molecules along the long molecular axis in **Figure 3.17**. The exciton size clearly grows much slower than the size of the molecule and is quite similar for all investigated excited states in comparison to the molecular size. Here, the difference between the extent of the molecular π- and π^*-orbitals and the exciton size is illustrated. The molecular orbitals essentially have the same spatial extent as the size of the molecule and show the uncorrelated probability of finding an electron at a certain location in the molecule. Since the π- and π^*-orbitals are completely delocalized, this probability is approximately the same over the whole acene. The exciton size however is the expectation value of the actual spatial extent of the exciton, which is smaller than the extent of the molecular orbitals.

3.3.7 Molecular Plasmons in Acenes and Their Radical Cations

As discussed in **Section 2.6**, a molecular plasmon can be defined in the quantum-chemical picture based on the momentum transfer of the participating orbital transitions of an excited state. A plasmonic excitation is a linear combination of the m particle-hole transitions with momentum

transfer **q** and has the highest excitation energy and oscillator strength of all the excited states that are described by the same transitions. Of all excited states described by these m transitions, only one is a plasmonic excitation so that there are m-1 single-particle excitations.[40] In the case of acenes, the ^1B_b state is the obvious candidate for a plasmonic excitation. The orbital transitions H−1→L and H→L+1 describe both the ^1L_s state, which is almost dark, as well as the ^1B_b state, which is higher in energy and has a high oscillator strength (see **Table 3.11**). To fulfill all the requirements of a molecular plasmon, these two transitions need to have the same momentum transfer.

Table 3.11: Excitation energies [eV], oscillator strengths and main orbital contributions of ^1L_s and ^1B_b of **3**, calculated using TDA/CAM-B3LYP/6-311G*.

state	E [eV]	f_{ocs}	main contrib. (amplitude)
^1L_s	4.19	0.00	H−1→L (0.70)
			H→L+1 (0.69)
^1B_b	5.97	3.19	H−1→L (-0.68)
			H→L+1 (0.69)

The momentum transfer can be evaluated based on the change in number of nodes of the orbitals participating in the transitions, since the π-electrons are considered as a one-dimensional electron gas in a box (see **Section 2.6**). The momentum transfer of a certain transition is directly related to the change in number of nodes of the orbitals participating in the transition. For acenes however, a two-dimensional system has to be considered, where the change in number of nodes and therefore the momentum transfer is considered along two directions. These are the x- and y-axis, which are placed along the long and short molecular axis as mentioned above. The molecular orbitals from H−2 to L+2 of **3** can be seen in **Figure 3.18**.

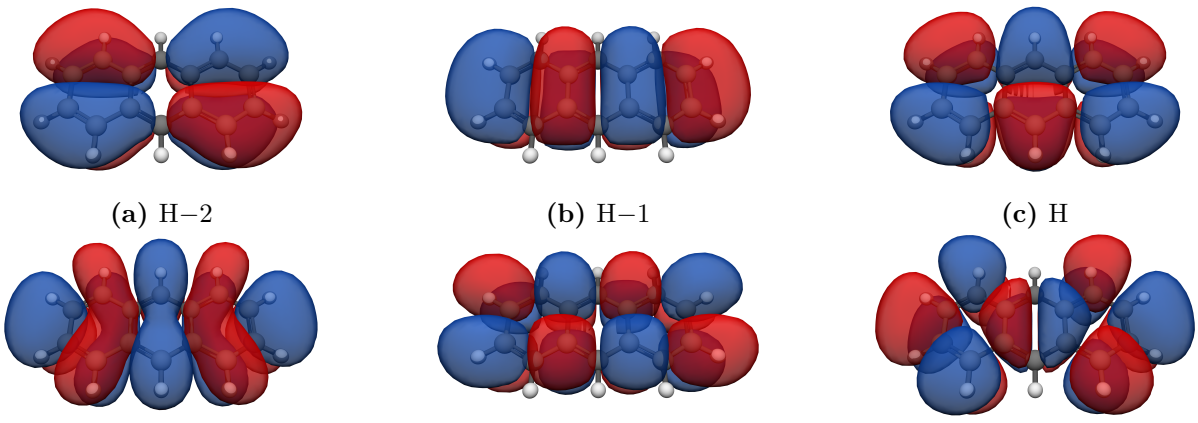

(a) H−2 **(b)** H−1 **(c)** H

(d) L **(e)** L+1 **(f)** L+2

Figure 3.18: Frontier molecular orbitals H−2, H−1, H, L, L+1 and L+2 of **3** obtained at TDA/CAM-B3LYP/6-311G* and visualized with an isovalue of 0.02 using IQmol.

The total number of nodes N of these orbitals and the change in number of nodes ΔN of all possible transitions between them as well as the number of nodes along the x- and y-axis (N_x and N_y) and as their respective change (ΔN_x and ΔN_y) can be seen in **Table 3.12**.

Table 3.12: Number of nodes N in selected molecular orbitals of **3** along the x- and y-axis and change in number of nodes for specific transitions.

MO	N	N_x	N_y
L+2	6	5	0
L+1	5	3	1
L	5	4	0
H	4	2	1
H-1	4	3	0
H -2	3	1	1
transition	ΔN	ΔN_x	ΔN_y
H→L	1	2	-1
H−1→L	1	1	0
H→L+1	1	1	0
H−2→L	2	3	-1
H→L+2	2	3	-1

One can see that there are three transitions with an overall change in number of nodes ΔN of 1, which are H−1→L, H→L and H→L+1. When the change in number of nodes is considered along the x- and y-axis separately, the transition H→L shows ΔN_x=2 and ΔN_y=-1, while H−1→L and H→L+1 show ΔN_x=1 and ΔN_y=0. The ^1B_b state is therefore a linear combination of all the transitions with a certain momentum transfer, when the system is considered two-dimensional and therefore fulfills all the criteria for a molecular plasmon. It is worth noting that the number of nodes does not change along the z-axis, justifying the approximation as a two-dimensional system. The same analysis was performed for the ^1B_b state of **5**, which is described by the transitions H−2→L and H→L+2 (see **Figure 3.13**).

Table 3.13: Excitation energies [eV], oscillator strengths and main orbital contributions of ^1L_s and ^1B_b of **5**, calculated using TDA/CAM-B3LYP/6-311G*.

state	E [eV]	f_{ocs}	main contrib. (amplitude)
^1L_s	3.47	0.00	H−2→L (0.71)
			H→L+2 (-0.67)
^1B_b	4.89	5.44	H−2→L (0.67)
			H→L+2 (0.71)

The change in number of nodes for the all the possible transitions between the orbitals H-2 to L+2 of **5** can be seen in **Table 3.14**. The molecular orbitals H−2 to L+2 of **5** can be found in **Figure A.16** in **Appendix A**. The transitions H−2→L and H→L+2 both show a change in number of nodes of ΔN_x=1 and ΔN_y=0, equal to the transitions H−1→L and H→L+1 of **3**. Furthermore, there are no other transitions with the same change in number of nodes. The ^1B_b state of **5** therefore also fulfills the criteria for a molecular plasmon. This can be shown analogously for the

^1B_b state of **2**-**9**.

Table 3.14: Number of nodes N in the selected molecular orbitals of **5** along the x- and y-axis and change in number of nodes for specific transitions.

MO	N	N_x	N_y
L+2	7	5	1
L+1	8	7	0
L	7	6	0
H	6	4	1
H-1	5	3	1
H-2	6	5	0
transition	ΔN	ΔN_x	ΔN_y
H→L	1	2	-1
H−1→L	2	3	-1
H→L+1	2	3	-1
H−2→L	1	1	0
H→L+2	1	1	0

The transition densities of both the ^1B_b state of **3** and **5** can be seen in **Figure 3.19**, which display the nodal structure characteristic for molecular plasmons. Furthermore, the transition densities reflects the collective oscillation of the electron density from one end of the molecule to the other along the long axis.

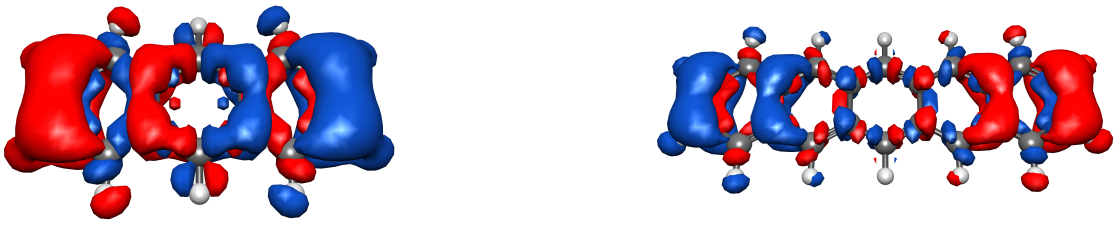

(a) **(b)**

Figure 3.19: Transition densities of the ^1B_b state of (a) **3** and (b) **5** obtained using TDA/CAM-B3LYP/6-311G* and visualized with an isovalue of 0.001 using IQmol.

As discussed above, the radical cation $\mathbf{3}^+$ has an excited state ^2B_b, which is the cation counterpart to ^1B_b of the neutral **3**. It was therefore investigated, whether the excited state ^2B_b also fulfill the criteria for a molecular plasmon.

Table 3.15: Excitation energies [eV], oscillator strengths and main orbital contributions of ^2I_b, ^2L_b, ^2L_s and ^2B_b of $\mathbf{3}^+$, calculated using TDA/CAM-B3LYP/6-311G*. Only contributions with ΔN_x=1 and ΔN_y=0 are included here. Omitted contributions have amplitudes below 0.15.

state	E [eV]	f_{ocs}	relevant contrib. (amplitude)
^2I_b	2.19	0.15	αH→αL+1 (-0.13)
			αH−1 →αL (-0.24)
			βH→βL (0.95)
			βH−1→βL+1 (0.06)
^2L_b	3.67	0.12	αH→αL+1 (-0.2)
			αH−1 →αL (0.8)
			βH→βL (-0.15)
			βH−1→βL+1 (0.44)
^2L_s	4.44	0.00	αH→αL+1 (0.74)
			αH−1 →αL (-0.16)
			βH→βL (0.02)
			βH−1→βL+1 (0.62)
^2B_b	5.80	2.74	αH→αL+1 (-0.59)
			αH−1 →αL (-0.41)
			βH→βL (-0.21)
			βH−1→βL+1 (0.61)

Here, both the change in number of nodes of the α- as well as β-orbitals have to be considered. The relevant orbitals αH-2 to αL+2 and βH-2 to βL+2 can be seen in **Figure A.17** the **Appendix A**. Their respective number of nodes and change in number of nodes of all possible transitions between these orbitals can be seen in **Figure 3.16**.

Table 3.16: Number of nodes N in the selected molecular orbitals of $\mathbf{3}^+$ along the x- and y-axis and change in number of nodes for specific transitions.

		α			β	
MO	N	N_x	N_y	N	N_x	N_y
L+2	6	5	0	5	3	1
L+1	5	3	1	5	4	0
L	5	4	0	4	2	1
H	4	2	1	3	1	1
H-1	4	3	0	4	3	0
H-2	3	1	1	2	0	1
transition	ΔN	ΔN_x	ΔN_y	ΔN	ΔN_x	ΔN_y
H $\rightarrow$ L	1	2	-1	1	1	0
H$-1 \rightarrow$ L	1	1	0	0	-1	1
H $\rightarrow$ L+1	1	1	0	2	3	-1
H$-2 \rightarrow$ L	2	3	-1	2	2	0
H $\rightarrow$ L+2	2	3	-1	2	2	0
H$-1 \rightarrow$ L+1	1	0	1	1	1	0
H$-1 \rightarrow$ L+2	2	2	0	1	0	1
H$-2 \rightarrow$ L+1	2	2	0	3	4	-1
H$-2 \rightarrow$ L+2	3	4	-1	3	3	0

Within the unrestricted picture, now four transitions with the momentum transferΔN_x=1 and ΔN_y=0: αH$-1\rightarrow\alpha$L, αH $\rightarrow \alpha$L+1, βH $\rightarrow \beta$L and βH$-1 \rightarrow \beta$L+1. The defined criteria require the plasmonic excitation to be a linear combination of all m possible transitions of the same momentum transfer, which is fulfilled by ^{2}B$_\mathrm{b}$, as shown in **Table 3.15**. Furthermore, there are m-1 excited states described by the same transitions that are single-particle excitations, which, in this case, are ^{2}I$_\mathrm{b}$, ^{2}L$_\mathrm{b}$ and ^{2}L$_\mathrm{s}$. It should be noted that transitions with very small contributions have to be considered for this. Accordingly, the ^{2}B$_\mathrm{b}$ state of $\mathbf{3}^+$ fulfills the criteria for a molecular plasmon and the states ^{2}I$_\mathrm{b}$, ^{2}L$_\mathrm{b}$ and ^{2}L$_\mathrm{s}$ are in the same relation to ^{2}B$_\mathrm{b}$ as ^{1}L$_\mathrm{w}$ is to ^{1}B$_\mathrm{b}$ for the neutral acenes. The plasmonic character of ^{2}B$_\mathrm{b}$ of $\mathbf{3}^+$ is further supported by the transition density in **Figure 3.20**, which is very similar to that of ^{1}B$_\mathrm{b}$ of **3**. Again, the collective character of the excitation can be observed in the transition density, showing that molecular plasmons are also present in open-shell radical cations of acenes. Contrary to other studies, this shows that there are no other lower-lying plasmonic excitations in acene cations than in neutral acenes.[147,183,184]

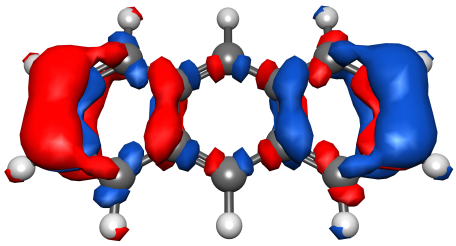

Figure 3.20: Transition densities of the ^2B_b state of $\mathbf{3}^+$. Obtained by averaging the α- and β-transition densities ($\frac{1}{2}(\rho_\alpha + \rho_\beta)$) obtained using TDA/CAM-B3LYP/6-311G* and visualized with an isovalue of 0.001 using IQmol.

3.4 Summary and Outlook

This chapter presents a thorough analysis of the low-energy excited states of acene radical cations and relates them to the characteristic excited states of neutral acenes ^1L_w, ^1L_s and ^1B_b. Furthermore, the behavior of the excitation energies and exciton properties, i.e. exciton size, hole and electron size and electron-hole correlation, with increasing acene length of the neutral and cationic acenes were investigated. Finally, the ^1B_b state of **3** and **5** and the ^2B_b state of $\mathbf{3}^+$ were investigated regarding their plasmonic character.

First, a benchmark of the excitation energies of **2**-**4** and $\mathbf{2}^+$-$\mathbf{4}^+$ obtained using ADC(2), ADC(2)-x, ADC(3) and IP-ADC(3) for the cations against experimental values was performed. The benchmark shows that for the neutral acenes, ADC(2)-x has the best agreement with experimental values for **2** and **3**, while ADC(3) shows the best performance for **4**. In the case of the cations, ADC(3) and IP-ADC(3) have the highest accuracy with respect to experimental absorption spectra.

Using ADC(2), the low-lying excited states of $\mathbf{2}^+$-$\mathbf{4}^+$ were analyzed regarding their prominent orbital transitions and, based on those, set into relation to their neutral counterparts. Several characteristic excited states were identified. The excited state ^2K, which is optically forbidden, belongs to the irreducible representation B_{1u}/B_{2g} for acene cations with an even/odd number of rings and is primarily described by the transition $\beta H-1 \rightarrow \beta L$. It is the lowest excited state for $\mathbf{2}^+$ and $\mathbf{3}^+$ and has no equivalent in the neutral acenes. The state ^2I_b is of B_{3g}/A_u symmetry (even/odd n) and mainly described by the transition $\beta H \rightarrow \beta L$. The corresponding absorption band was labeled cation q-band and is not present in the neutral acenes. For $\mathbf{4}^+$, this state is the first excited state. The cation counterpart to the excited state ^1L_w was identified based on the equivalent orbital transition. It was therefore labeled ^2L_w and belongs to the irreducible representation B_{2g}/B_{1u} (even/odd n). The corresponding absorption band was labeled cation p-band. Another bright state, which has no equivalent in the neutral acenes is ^1L_b, which is described by two transitions that correspond to the transition $H-1 \rightarrow L$ in the neutral acenes. This state is of B_{3g}/A_u symmetry (even/odd n) and the corresponding absorption band was labeled cation γ-band. The cation counterparts for the ^1L_s and ^1B_b excited states were identified, which belong to B_{3g}/A_u symmetry (even/odd n) as well. The excited states were labeled ^2L_s and ^2B_b and the corresponding absorption bands cation α- and cation β-band. The simulated absorption spectra of acene cations show an overall red-shift compared to those of their neutral counterparts, due to new excitations into the singly occupied molecular orbital (SOMO). The cation p-bands are also

red-shifted compared to the neutral p-bands. For the cation α- and β-bands, a smaller energetic gap is found compared to that between the neutral α- and β-bands, as well as an increased oscillator strength for the cation α-band. When comparing the excited states obtained at the ADC(2) and ADC(3) level of theory, it can be seen that the identification of characteristic excited states and their relation to their neutral counterparts is facilitated by choosing the ADC(2) method. The ADC(3) excited states show increasing participation of double-excitations going from $\mathbf{2}^+$-$\mathbf{4}^+$, which can not be related to any transitions relevant in the neutral excited states.
Subsequently, a benchmark of different DFT functionals against experimental values was performed for the excited states of **2**-**5** and $\mathbf{2}^+$-$\mathbf{5}^+$. The benchmark shows that for the neutral acenes, the best agreement with the experiment is achieved using the B3LYP functional. In the case of the cations, BLYP shows the best performance for the excited states of $\mathbf{2}^+$ and $\mathbf{3}^+$, while B3LYP has the highest accuracy for the excited states of $\mathbf{4}^+$ and $\mathbf{5}^+$. For both, neutrals and cations, it should be mentioned that the performance of both BHHLYP and CAM-B3LYP improved with growing acene length. Since for the correct description of excited states of extended π-systems a range-separated functional is necessary, the CAM-B3LYP functional was chosen for further investigations.
The excitation energies of ^1L_w, ^1L_s and ^1B_b and ^2I_b, ^2L_w, ^2L_b, ^2L_s and ^2B_b for the neutral and cationic acenes, respectively, were analyzed using the TDA/CAM-B3LYP level of theory. Overall, it was observed that the excitation energies of all investigated excited states decrease with increasing acene length and are converging towards a certain value. The excitation energies of ^1L_w, ^1L_s and ^1B_b show a drastic decrease as the acene length increases from **9** to **10**, while for ^2I_b, ^2L_w, ^2L_b only a slight discontinuity was observed. For both the neutrals and the cations, this can be explained by a decreasing excitation energy of the first excited state, which leads to an increased multi-reference character of the ground state. For the neutral acenes, this results in an increasing diradical character and means that not only the first excited singlet state mixes with the ground state, but also the triplet. The correct description of the ground state of longer acenes therefore requires a multi-configurational wavefunction and the description using (TD-)DFT deteriorates, until it reaches a "breaking point" at **10**. In the case of the cations, the effect of using a single-reference method on the energy of the ground state is smaller, as the state that mixes with the ground state is of the same multiplicity. However, convergence issues due to orbital degeneracies were observed for acene cations $\mathbf{10}^+$ and larger. In conclusion, the correct theoretical description for both neutral and cationic longer acenes requires a multi-configurational method such as CASSCF, CASPT2, MRCI, etc., which is presents a challenge due to the large size of the systems.
The investigation of the exciton properties of the excited states of both neutral and cationic acenes of increasing length at the TDA/CAM-B3LYP/6-311G* level of theory shows different trends in their development. For excited states with the same character, such as ^1L_w and ^2L_w, the exciton size of the neutral excited state is larger than of the respective cationic excited state, which can be explained by the larger electron-hole correlation in the cationic excited states. In the excited states of the cations, the hole size increases faster with growing acene length, while in the excited states of the neutrals, the hole and electron size increase equally, with the electron size being slightly larger. The reason for the stronger increase of the hole size in the cations could be the stronger delocalization of the already existing positive charge of the cation. It was further observed, that states described by mainly one transition show a similar development of the exciton size compared to hole and electron size, while those described by at least two transitions, show a stronger increase in hole and electron size than in exciton size with growing acene length. This is reflected in the

behavior of the correlation coefficient. Lastly, comparing the change in exciton size to the change in molecular size, illustrates the difference between the molecular orbitals, which are the uncorrelated probability of finding an electron at a certain location in the molecule and the exciton size, which is the expectation value of the spatial extent of the exciton.
In the final section, the ^1B_b excited state of **3** and **5** and the ^2B_b excited state of $\mathbf{3}^+$ were analyzed according to previously defined criteria for molecular plasmons. By relating the change in number of nodes in the molecular orbitals participating in a particle-hole transition to the momentum transfer of this transition, it was shown that these states fulfill these criteria. This is further supported by their transition densities, which reflect the collective character of the excitation. This procedure was applied to an open-shell system for the first time and it shows that the plasmonic state in both neutral and cationic acenes is essentially the same and that there are no other bright low-lying plasmonic excitations in the cation.
Future investigations could improve the understanding of the ground state of acene radical cations using multi-reference methods. It could also be investigated if the description of longer neutral acenes can be improved with a broken-symmetry ground state. Furthermore, the analysis could be extended to substituted acenes, such as *N*-heteroacenes.

Chapter 4

Diradical Organic Molecules

4.1 General Introduction

Diradicals present an extensively researched class of systems, due to their relevance as reaction intermediates, their potential applications and their difficult theoretical description.[43–45] Potential applications of diradicals include organic electronics, non-linear optics and spintronics, which are however complicated by the generally high reactivity of open-shell systems.[46–50] Research efforts have therefore been directed at developing stable diradical molecules, including bisphenylarenes, indenofluorenes, zenthrenes, longer acenes, extended quinodimethanes and diindenoacenes to name a few structural motifs.[51–63]

As discussed in **Section 2.4**, the correct description of the singlet ground state of diradicals requires the employment of a multireference methods. For most diradical organic materials of interest this is prohibitively expensive. Thus, other solutions for the computational investigation of organic molecules have to be considered. One approach is the broken-symmetry ansatz, which creates a wavefunction with $\langle \hat{S}^2 \rangle$=1 by breaking the symmetry between α- and β-orbitals in the initial guess of the SCF. The resulting wavefunction presents one part of the correct solution of the open-shell singlet (see **Section 2.4**) and is used as a single-reference substitute for the correct multi-reference wavefunction. Another possibility to describe a larger diradical molecule, is the spin-flip ansatz, which is able to describe multi-reference states as excited states created by spin-flip excitations from a single-reference triplet reference state. This approach is especially useful for the computation of singlet-triplet gaps. A frequently used measure for the extend of open-shell nature of a system is the diradical character y_0, which takes values between 0 for closed-shell and 1 for completely open-shell molecules.

In this chapter, three projects investigating larger organic diradicals are presented. In the first and second part properties of potential diradical organic materials are computed and in the third part two model systems are studied to explore and illustrate the connection between molecular geometry, open-shell nature and chosen theoretical description.

4.2 Regioisomeric Benzodithiophenazine Diradicals

The results presented in this chapter have already been published in:

- K. Fuchs, S. Medina Rivero, A. Weidlich, F. Rominger, N. Israel, A. A. Popov, A. Dreuw, J. Freudenberg, J. Casado and U. H. F. Bunz, "Dimerization of a Reactive Azaacene Diradical:

Synthesis of a Covalent Azaacene Cage", *Angew. Chem. Int. Ed.* **2023**, *62*, e202305712.

4.2.1 Introduction

As mentioned above, stable diradical(oid) molecules hold potential for various applications such as organic electronics, non-linear optics and spintronics.[46–50] A frequent approach to their synthesis is the employment of a formally quionoidal subsystem, which forms a diradical upon aromatization.[60,185–188] This concept has been applied to obtain isomeric azaacene-extended phenoxylbithiophenequionoidals/radicals, where the diradical character is strongly influenced by the position of the sulfur atoms.[188] It was observed that the molecule in which the *para*-quinoidal subsystem is conjugated with the azaacene has a lower diradical character of $y_0 = 0.26$, while the molecule, where the *ortho*-quinoid is conjugated has a much higher diradical character of $y_0 = 0.99$. In the project presented here, structurally related dicyanomethylene substituted benzodithionophenazines prepared by the Bunz group were investigated using quantum-chemical methods to support experimental studies.[24] Similar to the previously investigated systems, the *para*-isomer ***p*-1** exhibits a closed-shell ground state. The *ortho*-isomer ***o*-1** however has a higher diradical character and in the attempt to synthesize it, the dimer **(*o*-1)$_2$** was obtained instead. The formation of four long σ-bonds, which is not commonly observed in diradicals, results in the dimerization into a cage. The investigated molecules can be seen in **Figure 4.1** and the cage dimer is again depicted in **Figure 4.5**.

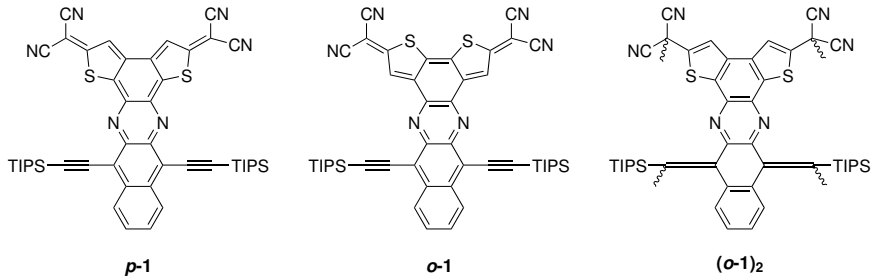

Figure 4.1: Chemical structures of the investigated compounds ***p*-1**, ***o*-1**, where the quinoidal structures are shown and one monomer subunit of the dimer **(*o*-1)$_2$**.

To gain further insight into the open-shell nature of the investigated monomers ***p*-1** and ***o*-1**, their respective diradical character y_0, singlet-triplet gap ΔE_{ST} as well as their spin-density and NICS-values are calculated. Furthermore, the formation of the dimer cage is investigated, by elongating one, two and four bonds at the same time to obtain information about possible intermediates and reaction barriers.

4.2.2 Methodology

All calculations were performed using Q-Chem 5.2 and the CAM-B3LYP(D3-BJ)/def2-svp level of theory, unless stated otherwise.[161–163,189] The geometries of the molecules ***p*-1** and ***o*-1** were optimized in the closed-shell singlet ground state and the stationary points were confirmed to be minima by harmonic frequency analysis. Spin-flip TD-DFT (SF-TD-DFT) calculations were performed to obtain the first five spin-flip excited states and excited state analyses as implemented in Q-Chem were performed.[65] The spin-density of the lowest spin-flip excited state with $\langle \hat{S}^2 \rangle \approx 2$ was computed and visualized with an isovalue of 0.001 using IQmol 2.8.0. Nucleus Independent Chemical shifts (NICS(1.7)$_{zz}$) were calculated for the singlet and triplet ground state at the B3LYP/def2-svp

level of theory using ORCA 5.0.1.[172,174,190–192] Natural orbital population analysis of a broken-symmetry singlet ground state was performed at the CAM-B3LYP/def-svp level of theory using Gaussian 16.[193] The diradical character y_0 was calculated according to Yamaguchi (see **Equation 4.3**) using the obtained natural orbital populations.[140] For the investigation of the mechanism of the dimer formation, geometry optimizations, frequency analysis and constraint optimizations were performed using GFN2-xTB.[194] Chemical structures were created using ChemDraw 21.0.0. All plots were created using Python 3 and the matplotlib library.[165]

4.2.3 Results and Discussion

In order to investigate the open-shell nature of the molecules ***p*-1** and ***o*-1**, the diradical character y_0 according to **Equation 4.3** was calculated at the CAM-B3LYP/def2-svp level of theory. For ***p*-1**, a diradical character of $y_0 = 0.01$ was obtained, showing the closed-shell character of the ground state. The equilibrium between the quinoidal closed-shell form and the aromatic open-shell form lies therefore on the quinoid side, which is shown in **Figure 4.2**. The intermediate ***o*-1** however shows a higher diradical character of $y_0 = 0.98$, which means that the molecule exists primarily in the aromatic diradical form also shown in **Figure 4.2**. These results are in agreement with those for the structurally related azaacene-extended phenoxylbithiophenequionoidals/radicals.[188]

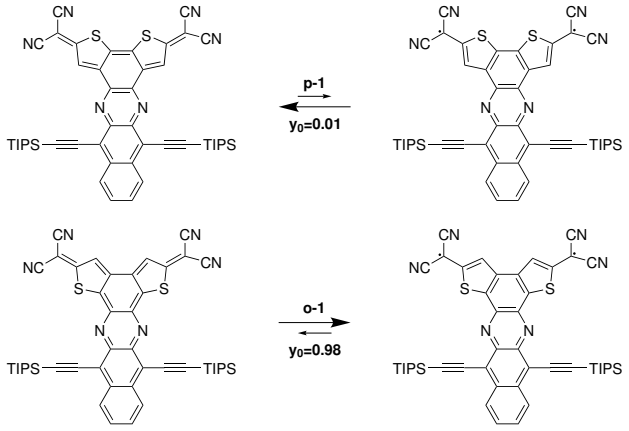

Figure 4.2: Quinoid closed-shell and aromatic open-shell resonance structures of ***p*-1** and ***o*-1** and their respective diradical character y_0.

To further explore the nature of their respective ground states, SF-TD-DFT calculations were performed using CAM-B3LYP/def2-svp to obtain the singlet-triplet gap ΔE_{ST}. This is calculated as the energy difference $\Delta E_{ST} = E_T - E_S$, where the E_S is the excitation energy of the first spin-flip excited singlet and E_T is the excitation energy of the first spin-flip excited triplet. The first singlet and triplet states were identified based on their respective $\langle \hat{S^2} \rangle$-values, which are 0 and 2 for spin-pure singlet and triplet states, respectively. It can be seen in **Figure 4.3** that the states, which were assigned to the lowest singlet and triplet show spin-contamination. The index $n_{u,nl}$ for the number of unpaired electrons was calculated for the spin-flip excited states (see **Equation 2.76**). The results are visualized in **Figure 4.3** and can also be found in **Table B.1** in **Appendix B**.

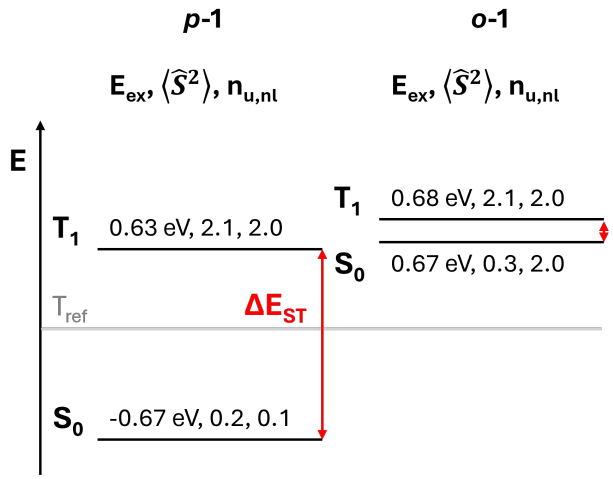

Figure 4.3: Schematic representation and summary of diradical character y_0, singlet-triplet gap ΔE_{ST} and number of unpaired electrons $n_{u,nl}$ for ***p*-1** and ***o*-1**.

It can be seen in **Figure 4.3** that in accordance with the computed diradical character of $y_0 = 0.01$, molecule ***p*-1** shows a large singlet-triplet gap of $\Delta E_{ST} = 1.3\,eV$. The number of unpaired electrons is $n_{u,nl}$=0.1 for the first spin-flip excited state, which is the closed-shell singlet ground state and $n_{u,nl}$=2.0 for the first spin-flip excited triplet state. The $\langle\hat{S}^2\rangle$-values of the first spin-flip excited singlet and triplet states show slight deviations from the spin-pure values with $\langle\hat{S}^2\rangle$=0.2 and $\langle\hat{S}^2\rangle$=2.1, respectively. In agreement with its higher diradical character of $y_0 = 0.98$, the molecule ***o*-1** shows a small singlet-triplet gap of $\Delta E_{ST} = 0.01\,eV$. The first two spin-flip excited states show $\langle\hat{S}^2\rangle$-values of $\langle\hat{S}^2\rangle$=0.3 and $\langle\hat{S}^2\rangle$=2.1, respectively, and can therefore be assigned as the singlet and triplet, even though they show spin-contamination. The number of unpaired electrons $n_{u,nl}$ is $n_{u,nl}$=2.0 in both cases. Since the spin-flip excited singlet is lower in energy than the triplet, this indicates that the ground state in this case is an open-shell singlet. To further characterize the conjugated π-systems of the quinoid/aromatic systems, spin-densities and NICS(1.7)$_{zz}$ values were computed for both molecules and can be seen in **Figure 4.4**.

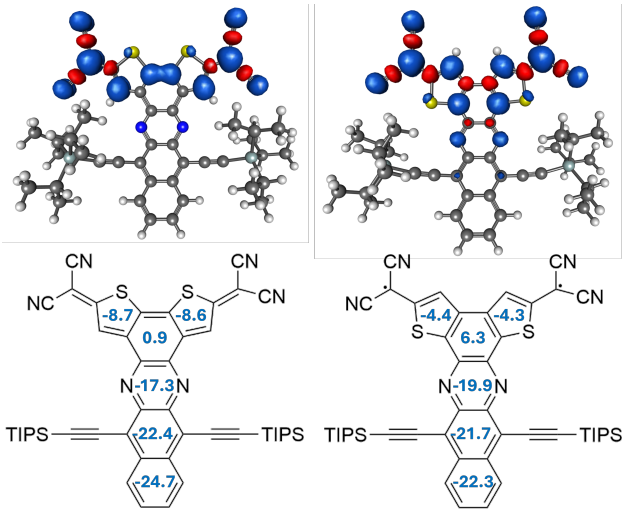

Figure 4.4: Spindensities (top) computed for the triplet state of ***p*-1** and ***o*-1** and NICS(1.7)$_{zz}$ values (bottom) computed for the singlet state of ***p*-1** and the triplet state of ***o*-1**. Spindensities were visualized with an isovalue of 0.001 using IQmol.

The spin densities of the triplet states of ***p*-1** and ***o*-1** are shown in **Figure 4.4**. For ***p*-1** the spin

density is confined to the quiniodal subsystem and shows the separation from the aromatic system of the azaacene. For ***o*-1** however, the spin-density is delocalized into the azaacene, reflecting the extension of the aromatic system over the whole molecule. Furthermore, $NICS(1.7)_{zz}$-values were computed for ***p*-1** and ***o*-1** in the singlet and triplet ground state respectively and are also shown in **Figure 4.4**. The closed-shell quionoid ground state of ***p*-1** results in lower aromatic NICS-values especially in the quinoid subsystem, but also in the azaacene. For ***o*-1**, higher aromatic NICS-values can be observed, due to the open-shell aromatic ground state.
Finally, the formation of the cage dimer $(\boldsymbol{o}\textbf{-1})_\mathbf{2}$ was investigated, by elongating one, two and four bonds at the same time, to obtain the energy profile along the bond breaking coordinate. The equilibrium bond length of the four σ-bonds is $\sim$1.55 Å, so that the scan was performed starting from 1.6 Å to 4.5 Å. The resulting scans along the respective bond breaking coordinates can be found in **Figure B.1-B.4** in **Appendix B**. The geometry with the lowest energy after the barrier of the bond breaking was chosen as a starting point for the subsequent optimization of the reaction intermediates. The optimization of transition states from the geometries with the highest energy in the scan were attempted as well but were not successful. Furthermore, the formation of the dimer $(\boldsymbol{o}\textbf{-1})^\mathbf{2}$ as opposed to the head-to-head-2σ-dimer is investigated. Frequency analyses were performed to obtain relative free energies. The results and proposed reaction mechanism are summarized in **Figure 4.5**.

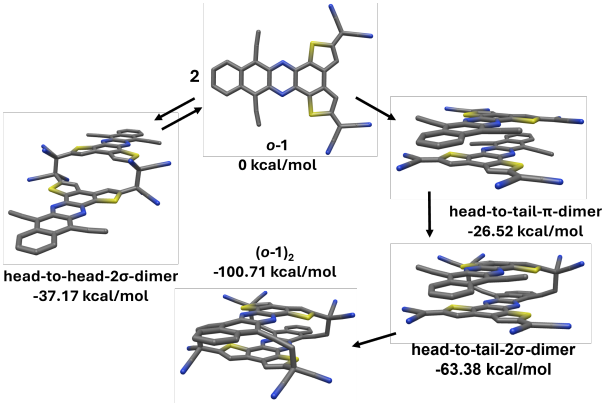

Figure 4.5: Possible reaction mechanism for the formation of $(\boldsymbol{o}\textbf{-1})_\mathbf{2}$, showing structures and relative free energies of ***o*-1**, $(\boldsymbol{o}\textbf{-1})_\mathbf{2}$ and possible intermediates calculated using GFN2-xTB. TIPS-groups and H-atoms are omitted for clarity.

From the energy profile obtained by elongating all four bonds simultaneously, the head-to-tail-π-dimer was obtained as a possible reaction intermediate. The distances between the carbon atoms that form the σ-bonds in $(\boldsymbol{o}\textbf{-1})_\mathbf{2}$ are between 3.1 Å and 3.2 Å. The respective energy profile can be found in **Figure B.4** in **Appendix B**. Another possible reaction intermediate was found by elongation two σ-bonds simultaneously as the head-to-tail-2σ-dimer, where the C-C distance is 3.2 Å and 3.3 Å for the elongated bonds and 1.6 Å for the remaining C-C bonds (see **Figure B.2**). Performing the same procedure for only one bond did not result in a minimum along the energy profile. By setting the number of unpaired electrons to two, an energy profile with a minimum was obtained, however the subsequent optimization was not successful in yielding a possible intermediate (see **Figure B.1**). Finally, one bond length was fixed at 3.3 Å, while a second bond was elongated, which resulted in a energy minimum at 3.2 Å of the second bond, therefore leading to the previously obtained intermediate head-to-tail-2σ-dimer (see **Figure B.3**). The maxima along the energy profile of elongating two bond simultaneously and consecutively were

taken as a measure for the respective reaction barrier and showed a lower barrier for the former by 3.9 kcal mol^{-1}. It has to be noted that the geometries at the maxima of the scan do not correspond to proper transition states and that the resulting reaction barriers should therefore be considered carefully. Based on these results, it is proposed that the first step of the reaction is the formation of the head-to-tail-π-dimer, which results in an energy gain of -26.52 kcal mol^{-1}. This could be followed by the consecutive formation of two C-C σ-bonds on one side of the molecule to give the head-to-tail-2σ-dimer (-63.38 kcal mol^{-1}). Finally the formation of two C-C σ-bonds on the other sides of the molecule results in the formation of the dimer **(*o*-1)$_2$** (-100.71 kcal mol^{-1}). Compared to the dimer **(*o*-1)$_2$**, the formation of the head-to-head-2σ-dimer is disfavored by 63.54 kcal mol^{-1}. Naturally, not all possible reaction pathways were explored, however the obtained results justify the consideration of the consecutive formation of two sets of two C-C σ-bonds as a possible reaction mechanism.

4.2.4 Summary

In this section, regioisomeric dicyanomethylene substituted benzodithiophenazines ***p*-1** and ***o*-1** were investigated with focus on the closed- or open-shell nature of their respective ground states using TD-DFT and SF-TD-DFT at the CAM-B3LYP/6-311G* level of theory. Furthermore, the dimerization reaction mechanism of ***o*-1** to the dimer cage **(*o*-1)$_2$** was studied using GFN2-xTB. The diradical character y_0 was calculated for both molecules as 0.01 and 0.98 for ***p*-1** and ***o*-1**, respectively. The equilibrium between their closen-shell quinoid and open-shell aromatic forms therefore lies on the side of the quinoid for ***o*-1** and on the side of the aromat for ***p*-1**. Accordingly, ***p*-1** has a large singlet-triplet gap of 1.3 eV, while ***o*-1** shows a very small singlet-triplet gap of 0.01 eV. It can concluded from the SF-TD-DFT results that the ground state of ***p*-1** is a closed-shell singlet, while that of ***o*-1** is a open-shell singlet. This further reflected in the calculated spin-densities of ***p*-1** and ***o*-1**, which show that in ***p*-1** the aromatic system of the acene is separated from the quinoid subsystem, while in ***o*-1** the aromatic system is delocalized over the whole molecule. The investigation of the dimer formation mechanism using GFN2-xTB resulted in a proposed reaction mechanism that proceeds via the consecutive formation of two sets of two C-C σ-bonds. Overall, the investigation was able to support experimental findings regarding the respective ground states of the monomers and give insight into a possible pathway for the dimer formation.

4.3 Indeno-Diazatetracene-σ-Dimer Diradical

4.3.1 Introduction

Another approach to the synthesis of a stable diradical(oid) was used by the Bunz group, resulting in the indeno-diazatetracene-σ-dimer **1-Tcp** shown in **Figure 4.6**, which is made up of two identical radical indenodiazatetracenes monomers bonded by a single carbon-carbon bond. In the hypothetical closed shell form shown on the left in **Figure 4.6**, a double bond is formed between the monomers, which requires them to adopt a parallel arrangement. In the open-shell form on the other hand, a single bond connects the two monomers. Due to the sterically demanding substituents, trichlorophenyl (Tcp) and triisopropylsilyl (TIPS), the molecule is forced to adopt a geometry, where the two monomer units stand orthogonally to each other, preventing the formation of a double bond between the subunits. The system is therefore forced into the open-shell

form by the sterically demanding substituents. These furthermore contribute to the stability of the diradical(oid) by shielding the radical centers.

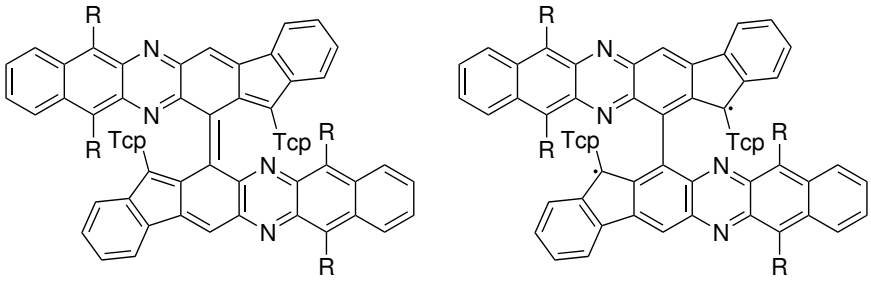

Figure 4.6: Chemical structure of the investigated compound **1-Tcp**, where the closed-shell (left) and open-shell form (right) are shown. The substituent R represents triisopropylsilyl groups (TIPS).

The open-shell nature of the system **1-Tcp** is investigated by calculating the diradical character y_0, the singlet-tripet gap ΔE_{ST}, as well as spin-densities and NICS(1.0)$_{zz}$-values.

4.3.2 Methodology

All calculations were performed using the Q-Chem 5.2 program package, unless stated otherwise.[161] The geometry of the investigated system **1-Tcp** was optimized using PBEh-3c/def2-msvp with a closed-shell singlet (cs), broken-symmetry (bs) and triplet (t) ground state.[195] The broken-symmetry ground state is obtained by mixing the highest molecular orbial (HOMO) with the lowest unoccupied molecular orbital (LUMO) in the initial guess of the SCF and has an $\langle \hat{S}^2 \rangle$-value of $\langle \hat{S}^2 \rangle = 1$. The finite difference Davidson method as implemented in Q-Chem was used to confirm the stationary points as local minima. The first five spin-flip excited states were obtained using SF-TD-DFT at the CAM-B3LYP/6-311G* level of theory.[65,162,164] Spin-densities of the first two spin-flip excited states at the triplet geometry were calculated and visualized with an isovalue of 0.001 using IQmol 2.8.0. The diradical character y_0 was computed according to Yamaguchi (see **Equation 4.3**) and the required Natural orbital populations were calculated at the CAM-B3LYP/6-311G* level of theory using Gaussian 16.[140,193] Nucleus Independent Chemical shifts (NICS(1.0)$_{zz}$) were calculated at the B3LYP/6-311G* level of theory for the singlet and triplet ground state at the triplet geometry.[172,174,190] Chemical structures were created using ChemDraw 21.0.0.

4.3.3 Results and Discussion

To gain initial insight into the open-shell nature of the ground state of **1-Tcp**, the geometry was optimized using a closed-shell singlet (cs), a broken-symmetry-singlet (bs) and a triplet (t) ground state. The broken-symmetry ground state is used as an approximation to the multi-reference open-shell singlet ground state. The obtained absolute and relative energies of the respective optimized geometries can be seen in **Table B.2** in **Appendix B**. The energy of the geometry obtained using the broken-symmetry optimization is lower than the closed-shell geometry by 0.672 eV, while the geometry using a triplet ground state is 0.692 eV lower than the closed-shell geometry. This indicates that the molecule shows a higher diradical character, since both open-shell optimizations lead to lower energies than the closed-shell optimization. Furthermore, the broken-symmetry and

triplet solutions show similar energies, which matches the expectation of nearly degenerate open-shell singlet and triplet states for diradicals.
Subsequently, the diradical character y_0 and the singlet-triplet gap ΔE_{ST} were computed. As mentioned above, the singlet-triplet gap ΔE_{ST} is computed as the energy difference $\Delta E_{ST} = E_T - E_S$, where E_T is the excitation energy of the first spin-flip excited triplet and E_S is the energy of the first spin-flip excited singlet. The results can be seen in **Table 4.1**.

Table 4.1: Excitation energies [eV], $\langle \hat{S^2} \rangle$-values and number of unpaired electrons $n_{u,nl}$ of the first singlet and triplet spin-flip excited states, singlet-triplet gap and diradical character of **1-Tcp** in its closed-shell (cs), broken-symmetry (bs) and triplet (t) geometry and ground state.

	E_S [eV] ($\langle \hat{S^2} \rangle$, $n_{u,nl}$)	E_T [eV] ($\langle \hat{S^2} \rangle$, $n_{u,nl}$)	ΔE_{ST} [eV]	y_0
cs	0.134 (0.5, 0.2)	0.837 (2.7, 2.1)	0.703	0.02
bs	0.86 (0.8, 1.7)	0.925 (2.7, 2.2)	0.065	0.75
t	0.896 (1.3, 2.1)	0.934 (2.2, 2.1)	0.038	0.86

It can be seen in **Table 4.1** that the geometry obtained using a closed-shell ground state resulted in the largest singlet-triplet gap of $\Delta E_{ST} = 0.703\,eV$, as well as the smallest diradical character of $y_0 = 0.02$, which is to be expected. The broken-symmetry geometry gave a smaller singlet-triplet gap of $\Delta E_{ST} = 0.065\,eV$ and accordingly a larger diradical character of $y_0 = 0.75$. Finally, the triplet geometry resulted in singlet-triplet gap of $\Delta E_{ST} = 0.038\,eV$ and a diradical character of $y_0 = 0.86$. It is important to note that the $\langle \hat{S^2} \rangle$-values of all calculated spin-flip excited states show spin-contamination, which can be seen in **Table 4.1**. The excitation energies of the singlet and triplet states and in turn the computed singlet-triplet gaps are affected by this, which has to be considered when comparing them to experimental values. For further calculations, the triplet geometry was chosen, based on comparison with the experimental crystal structure, as well as the measured singlet-triplet gap.
To investigate the aromaticity of the molecule, which is closely related to its open-shell character, spin-densities and NICS-values ($NICS(1.0)_{zz}$) were computed. The spin-densities of the first singlet and triplet spin-flip excited states at the triplet geometry are shown in **Figure 4.7**. The $NICS(1.0)_{zz}$-values are computed for both a closed-shell singlet and triplet ground state at the triplet geometry and also shown in **Figure 4.7**.

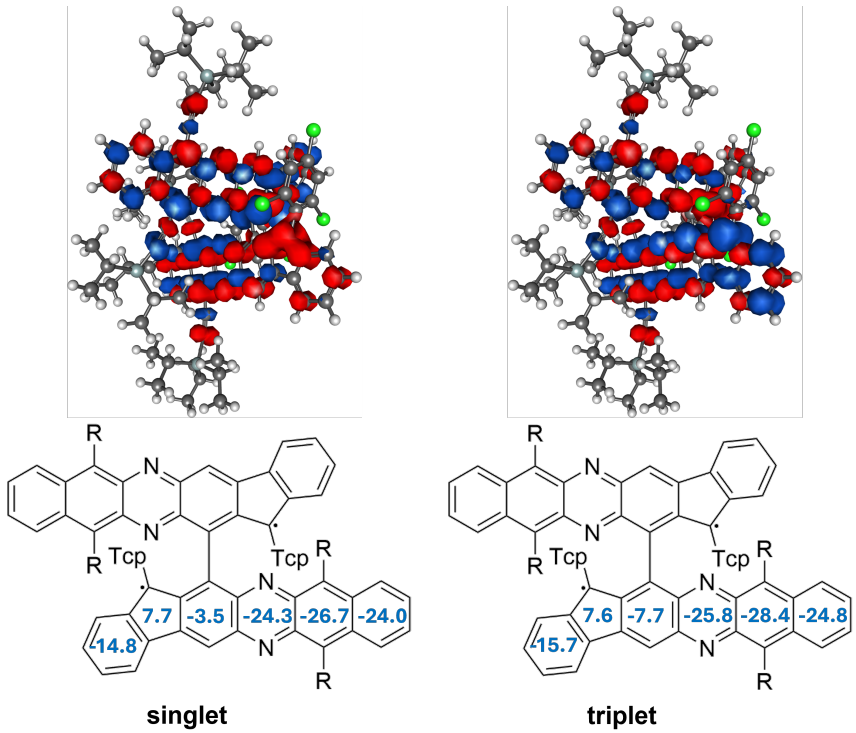

Figure 4.7: Spin-densities of the first singlet (left) and triplet (right) spin-flip excited states and NICS(1.0)$_{zz}$-values computed using a singlet (left) and triplet (right) ground state at the triplet geometry. The substituent R represents triisopropylsilyl groups (TIPS).

The spin-densities of the first singlet and triplet spin-flip excited states shown in **Figure 4.7**, are similar, where the spin-density extends over the entire π-systems of the two monomers for both. It can further be seen that there is an increased spin-density around the radical center on the five-membered ring. The completely delocalized spin-density is in agreement with the open-shell nature of **1**-Tcp, observed in the diradical character and energies of the different ground states. The NICS(1.0)$_{zz}$-values calculated for the singlet and triplet ground state both show negative and therefore aromatic values for all the rings, except the five-membered ring. The two adjacent six-membered rings show less aromatic values, than those on the opposite side of the monomer as well, which could be explained by the delocalization of the unpaired electron onto these rings. Another interpretation however could be the contribution of the closed-shell form depicted in **Figure 4.6**, which is plausible considering the values of the diradical character.

4.3.4 Summary

In this section, the open-shell character of the molecule **1-Tcp** was investigated using DFT and SF-TDDFT at the PBEh-3c/def2-svp and CAM-B3LYP/6-311G* level of theory, respectively. The geometry of **1-Tcp** was optimized using a closed-shell singlet, broken-symmetry singlet and triplet ground state. The results show that both the broken-symmetry and triplet geometry are lower in energy than the closed-shell singlet geometry and also energetically close together, which points towards an open-shell ground state. The diradical character y_0 was computed for each geometry and gave values of 0.02, 0.75 and 0.86 for the closed-shell, broken-symmetry and triplet geometry, respectively. Subsequently, the singlet-triplet gap ΔE_{ST} was calculated using the first singlet and triplet spin-flip excited states to give values of 0.703 eV, 0.065 eV and 0.038 eV for the closed-shell, broken-symmetry and triplet geometry, respectively. The computed spin-densities and NICS(1.0)$_{zz}$-

values indicate high aromaticity of the system, which is in agreement with the open-shell form of **1-Tcp**. Overall, all the obtained results show a diradical nature of the ground state of **1-Tcp**. Further investigations include the effect of the angle between the two monomer units on the open-shell character of the ground state, which is discussed in the next section.

4.4 Relation between Geometry, Methodology and Open-Shell Character in Diradical Model Dimers

4.4.1 Introduction

Based on the system investigated in the previous chapter, two model systems were created to investigate the influence of the angle between the two radical monomer units on the open-shell nature of the system, as well as the impact of the resulting diradical character on the theoretical description of the molecule. The first model dimer **MD-1** is a modified version of **1-Tcp**, where the azaacene is shortened and the large substituents TIPS and Tcp are replaced by methyl-groups. As the molecule investigated previously, **MD-1** is a Kekulé diradical, since it can exist in a closed-shell form for geometries, where the two momoners are (nearly) parallel. As for **1-Tcp**, it is expected that the diradical character increases as the angle between the two momoners approaches 90°, since the formation of the double bond in the closed-shell form becomes unfeasible and the electronic separation of the two aromatic system is increased. In the second model dimer **MD-2** on the other hand, the monomer units are arranged in a way that places the radical centers to face away from each other. This results in a system, where the unpaired electrons can not recombine within the molecule, making this a non-Kekulé diradical. The angle between the monomer units therefore only influences the distance between the radical centers, however it does not affect the ability of the system to exist in a closed-shell form. The model systems **MD-1** and **MD-2** are shown in **Figure 4.8**.

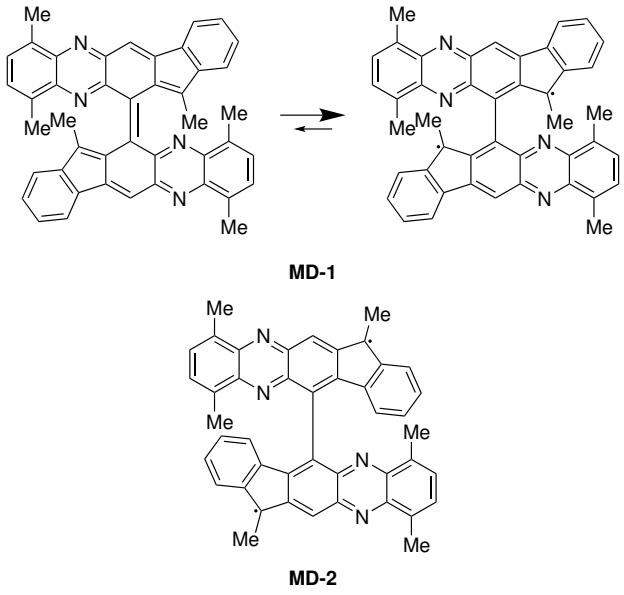

Figure 4.8: Model dimers investigated in this section: **MD-1** and **MD-2**, where for **MD-1** both the closed-shell and open-shell form are shown.

Using these model systems, the dependence of the diradical nature of the system on the angle

between the monomer units is investigated. Since the angle is expected to strongly influence the diradical character, different descriptions of the ground state might be suitable at different angles. The geometry optimizations are therefore performed using a closed-shell, broken-symmetry and triplet ground state. Naturally, the chosen ground state also influences the diradical character. The model systems are expected to display a wide range of values for the diradical character with varying angle, which furthermore enables the investigation of the suitability of different ground state descriptions and illustration of the dependence of the singlet-triplet gap on the diradical character. Finally, the different behaviour of Kekulé or non-Kekulé for the investigated properties can be observed.

4.4.2 Methodology

The calculations were performed using Q-Chem 6.0, unless stated otherwise.[161] The geometry optimizations were performed at the PBEh-3c/def2-msvp level of theory using a closed-shell, broken-symmetry and triplet ground state.[195] The broken-symmetry ground state is obtained by mixing the highest molecular orbial (HOMO) with the lowest unoccupied molecular orbital (LUMO) in the initial guess of the SCF and has an $\langle \hat{S}^2 \rangle$-value of $\langle \hat{S}^2 \rangle = 1$. The minimum nature of the stationary points was verified based on the final Hessian obtained during optimization. Constraint optimizations were performed, where the angle between the two monomer units was constraint to values from 40° to 140° in steps of 10° using a closed-shell, broken-symmetry and triplet ground state. The diradical character was computed using **Equation 4.3**, based on natural orbital population analyis performed at the CAM-B3LYP/6-311G* level of theory using Gaussian 16.[140,162,164,193] Spin-flip TD-DFT calculations were performed at the same level of theory to obtain the first five spin-flip excited states.[65] Chemical structures were created using ChemDraw 21.0.0. All plots were created using Python 3 and the matplotlib library.[165]

4.4.3 Results and Discussion

Initially, the geometries of both dimers were optimized without constraints using a closed-shell, broken-symmetry and triplet ground state at the PBEh-3c/def2-msvp level of theory, to investigate the effect on the angle α (see **Figure 4.9**) between the monomers and the diradical character y_0. The results are shown in **Table 4.2**.

Table 4.2: Energies [eV] of the broken-symmetry (bs) and triplet (t) geometry and ground state relative to the closed-shell (cs) geometry and ground state obtained using PBEh-3c/def2-msvp, angle α between the monomers and diradical character.

	ΔE(cs − x) [eV]	Angle α [°]	y_0
MD-1			
cs	-	53.0	0.11
bs	0.29	66.5	0.44
t	0.22	77.2	0.67
MD-2			
cs	-	82.1	0.97
bs	1.28	76.1	0.98
t	1.28	76.1	0.98

In case of **MD-1**, the closed-shell optimization gives an angle between the monomers of 53.0° and a low diradical character of 0.11. Using a broken-symmetry ground state, the equilibrium geometry has a higher angle of 66.5° and a diradical character of 0.44. An even larger angle of 77.2° is observed for the triplet geometry, with a diradical character of 0.67. This shows that the ground state chosen for optimization can have a large influence on the geometry and diradical character. For the optimization of new compounds, a comparison with experimental values can therefore deliver valuable insights into which geometry should be chosen for the computational investigation. The results obtained here are in line with the expectation that an angle closer to 90° goes along with a higher diradical character. Considering the relative energies obtained for the respective geometries and ground states, the broken-symmetry solution leads to the lowest energy, which is 0.294 eV below the closed-shell singlet, while the triplet solution leads to an energy gain of 0.218 eV with respect to the closed-shell ground state. This suggests an open-shell nature of the ground state of **MD-1**. It can be noted at this point that a broken-symmetry solution might be lower in energy than the closed-shell solution due to a higher degree of freedom of the unrestricted wavefunction.

For **MD-2**, the closed-shell optimization gives a geometry with an angle of 82.1° between the monomers units and a diradical character of 0.97. The broken-symmetry optimization, as well as the triplet optimization, both lead to an angle of 76.1° and a diradical character of 0.98. Here, the closed-shell optimization shows an angle closer to 90° than the unrestricted solutions though this is of limited relevance, since the angle has no influence on the interaction of the unpaired electrons via the connecting bond between the monomer units. The broken-symmetry and triplet geometries are both lower in energy than the closed-shell geometry by 1.28 eV. All computed values point at a ground state with a high open-shell character, where the lowest singlet and triplet states are close in energy.

Subsequently, the effect of the angle on both the relative energies obtained for the closed-shell, broken-symmetry and triplet geometries, as well as on the diradical character is investigated. The angle between the monomer units of both model dimers, as shown in **Figure 4.9**, was constraint to values between 40° and above 140°. Even though sterically less demanding methyl-groups were chosen in the model dimers, they still affect the geometry. Angles below 40° and 140° gave distorted

geometries, where the planarity of the monomers was lost, therefore the scan was restricted to the chosen range. The relative orientation of the dimers is depicted in **Figure 4.9**.

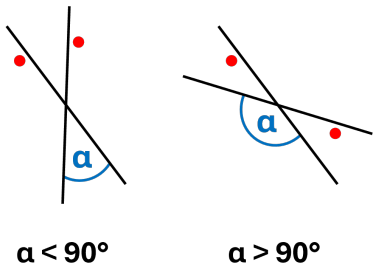

Figure 4.9: Schematic representation of the arrangement of the two monomer units in the model dimers, with the angle between the monomers α.

The scan of the angle between the monomer units of **MD-1** using a closed-shell, broken-symmetry and triplet ground state at the PBEh-3c/def2-msvp level of theory as well as the respective diradical character is shown in **Figure 4.10**.

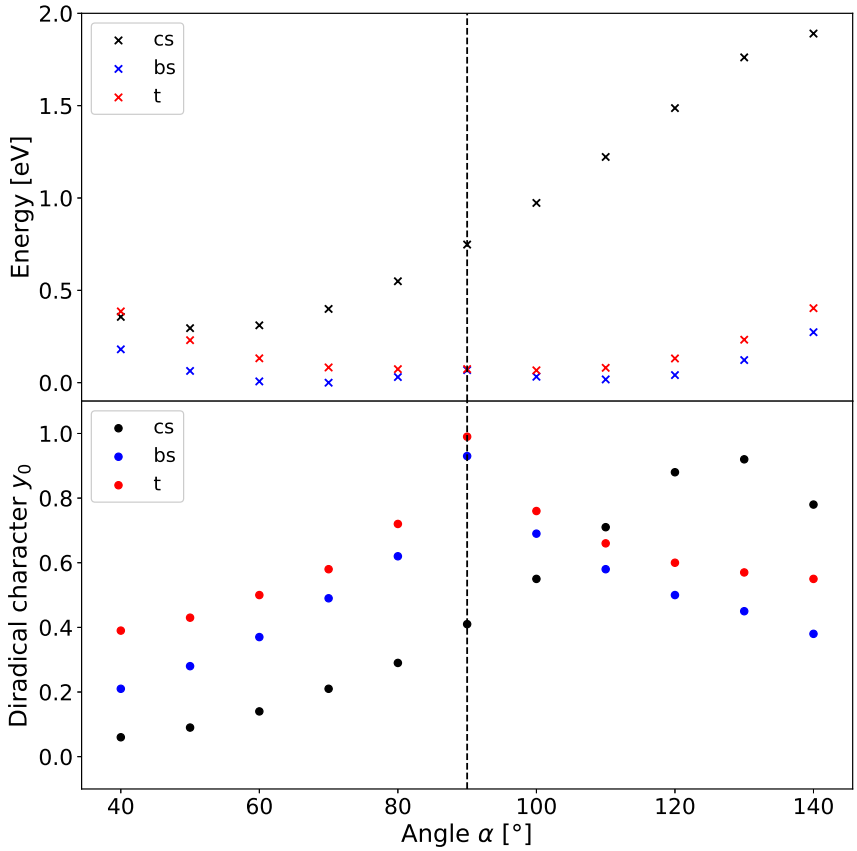

Figure 4.10: Development of the total energies [eV] obtained by optimizing **MD-1** at angles α from 40° to 140° using PBEh-3c/def2-msvp. The scale was set to zero for the lowest obtained value. (top) Development of the diradical character y_0 for the different obtained geometries with the angle α. (bottom)

In **Figure 4.10**, the energy of the geometries obtained using a closed-shell ground state for an angle α of 40°-140° can be seen. Interestingly, the energy shows an increase with increasing angle. The broken-symmetry and triplet geometries show a decrease in energy as the angle approaches 90°, where the broken-symmetry geometries are lower in energy for all angles. The diradical char-

acter of the closed-shell geometries increases as well with increasing angle, except for the final value at 140°. For the broken-symmetry and triplet geometries, the diradical character increases and comes close to 1.0 as α approaches 90°, where the diradical character of the triplet is always higher. The diradical character decreases going to both angles below and above 90°, where the decrease is smaller for angles above 90°.

The trend of both the energies and diradical character of the broken-symmetry and triplet calculations are in line with the expected trend, since the two aromatic systems are maximally separated at 90°. A different trend is however observed for the closed-shell geometries, as the energy increases with the angle. To explain this, it is important to consider that for small angles, the two diradical centers are brought closer to each other, while for larger angles the distance increases (see **Figure 4.9**). A possible reason for this behavior could therefore be that the two unpaired electrons interact increasingly through space as the radical centers are brought closer together. This effect can also be observed in the weaker decrease of the diradical character for the broken-symmetry and triplet geometries, when going from 90° to higher angles. The interaction between the unpaired electron is however not the only reason for the increase in energy with smaller or larger angles, as the increased spatial proximity of the methyl-groups contributes to the increase in energy. It is worth noting that the relative energy development of the closed shell geometry with increasing diradical character aligns with the expectation that the closed shell ground state rises in energy as the diradical character of the system increases.

The same analysis was performed for **MD-2** and the results can be seen in **Figure 4.11**.

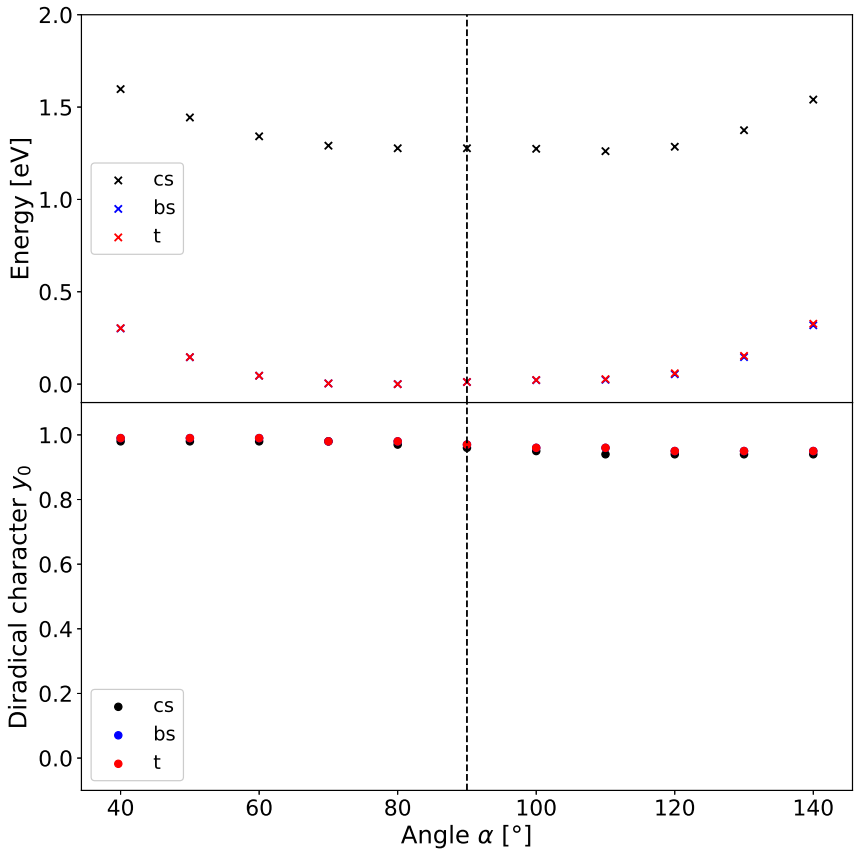

Figure 4.11: Development of the total energies [eV] obtained by optimizing **MD-2** at angles α from 40° to 140° using PBEh-3c/def2-msvp. The scale was set to zero for the lowest obtained value. (top) Development of the diradical character for the different obtained geometries with the angle α. (bottom)

The development of the energy of the closed-shell geometries with angles α of 40°-140° for **MD-2** shows a slight decrease as the angle approaches 90°. The same is the case for the broken-symmetry and triplet geometries, which are however much lower in energy than the closed-shell singlet. The diradical character y_0 lies between 0.94 and 0.98 for all geometries and ground states investigated. Since it is not possible for the unpaired electrons to recombine at any molecular geometry, this is the expected result. The large diradical character is further reflected in the relatively high energy of the closed-shell geometries and ground states, as well as in the similar energies for the broken-symmetry and triplet geometries and ground states. Interestingly, interaction between the unpaired electrons through space seems to have no effect on the energy of the closed-shell ground state in this case. The increase in energy towards smaller and larger angles than 90° can again be explained by the interaction between the methyl-groups, which are being forced closer to each other.
It is furthermore investigated, how the diradical character, which comes with the different angles, affects the excitation energies of lowest spin-flip excited singlet and triplet state and the energy gap between them calcultated using SF-TD-DFT at the CAM-B3LYP/6-311G* level of theory. The spin-flip excited singlet and triplet states show spin-contamination with values around 0.2 for the singlet and 2.3 for the triplet in all cases. The trend of the singlet and triplet states as well as the gap between them and the diradical character for the closed-shell geometries and ground state are shown in **Figure 4.12**.

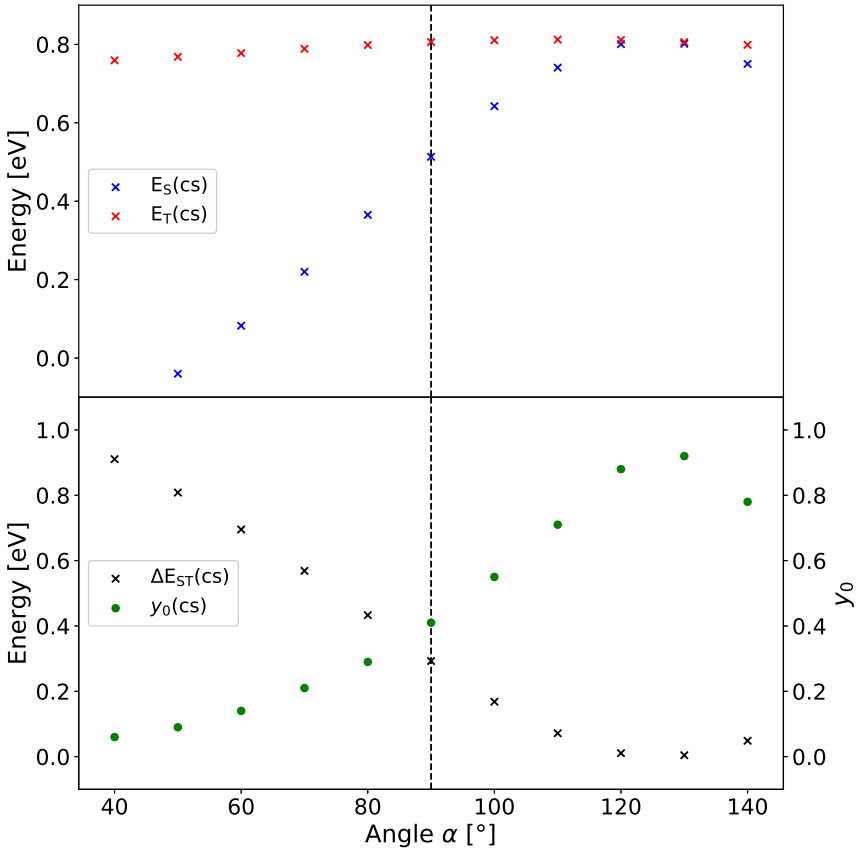

Figure 4.12: Excitation energies [eV] of the first singlet and triplet spin-flip excited states (top) and the energy gap between them ΔE_{ST} [eV] obtained using CAM-B3LYP/6-311G* and the diradical character y_0 (bottom) at closed-shell geometries of **MD-1** with angles α between 40°-140°.

The geometries obtained using a closed-shell ground state show an increase in energy and diradical character with increasing angle. This is reflected in the increase in energy of the first spin-flip

excited singlet state. The excitation energy of the first spin-flip excited triplet state is however barely affected by the angle, which results in the decreasing singlet-triplet gap, shown in **Figure 4.12**. The diradical character was plotted as well to illustrate the expected mirrored behavior of the singlet-triplet gap and diradical character. It is worth mentioning that the number of unpaired electrons $n_{u,nl}$ for the singlet state increases with increasing diradical character, while it remains around 2.0 for the triplet in all cases.
The trend of the excitation energies of the first singlet and triplet spin-flip excited states as well as the gap between them and the diradical character for the broken-symmetry geometries and ground state are shown in **Figure 4.13**.

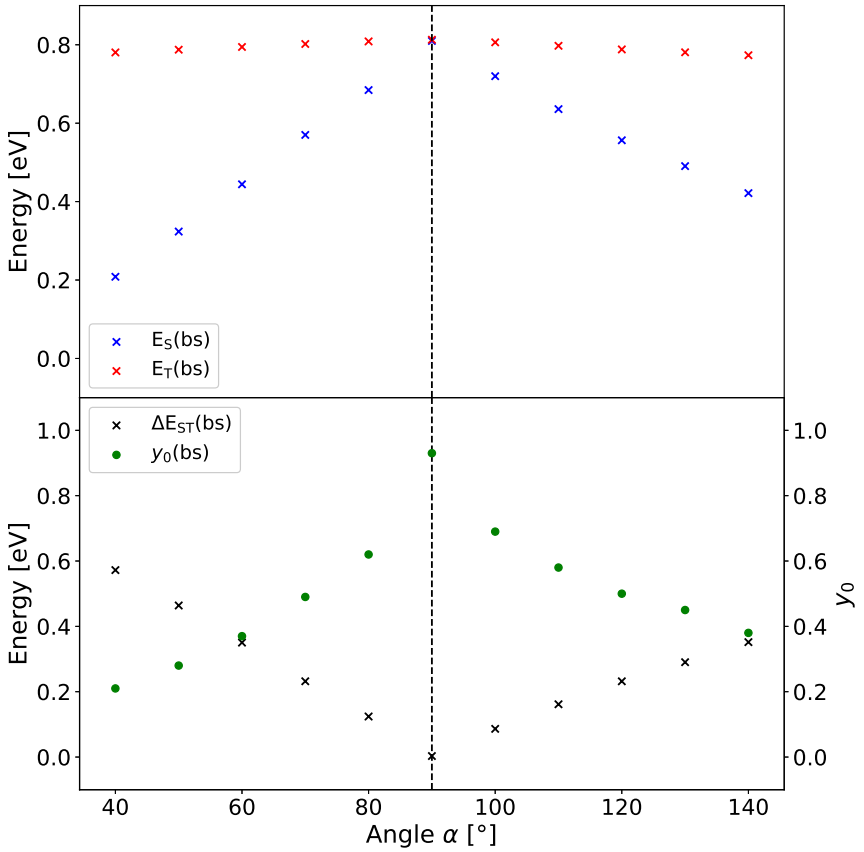

Figure 4.13: Excitation energies [eV] of the first singlet and triplet spin-flip excited states (top) and the energy gap between them ΔE_{ST} [eV] obtained using CAM-B3LYP/6-311G* and the diradical character y_0 (bottom) at broken-symmetry geometries of **MD-1** with angles α between 40°-140°.

In case of the broken-symmetry geometries, the excitation energy of the first spin-flip excited singlet state increases up to 90° and then decreases after that, while the excitation energy of the triplet only shows small changes. The singlet-triplet gap therefore decreases with increasing angle up to 90° and then increases again for higher angles, which again mirrors the trend of the diradical character. The observed trends are in line with expectation based on the results presented above. The trend of the excitation energies of the first spin-flip excited singlet and triplet states as well as the energy gap between them and the diradical character for the triplet geometries are shown in **Figure 4.14** and show the same trends as the broken-symmetry results, while the decrease of the excitation energy of the spin-flip excited singlet towards smaller and larger angles than 90° is smaller.

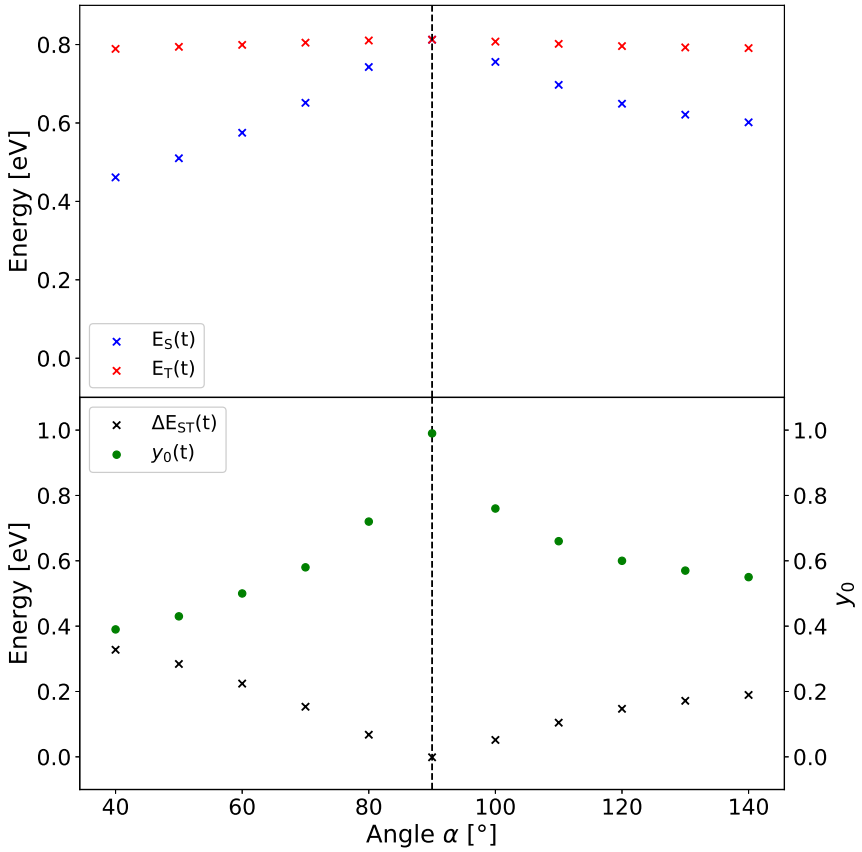

Figure 4.14: Excitation energies [eV] of the first singlet and triplet spin-flip excited states (top) and the energy gap between them ΔE_{ST} [eV] obtained using CAM-B3LYP/6-311G* and the diradical character y_0 (bottom) at triplet geometries of **MD-1** with angles α between 40°-140°.

The same analysis was performed for the closed-shell, broken-symmetry and triplet geometries of **MD-2** and the results are shown in **Figure 4.15** for the closed-shell case.

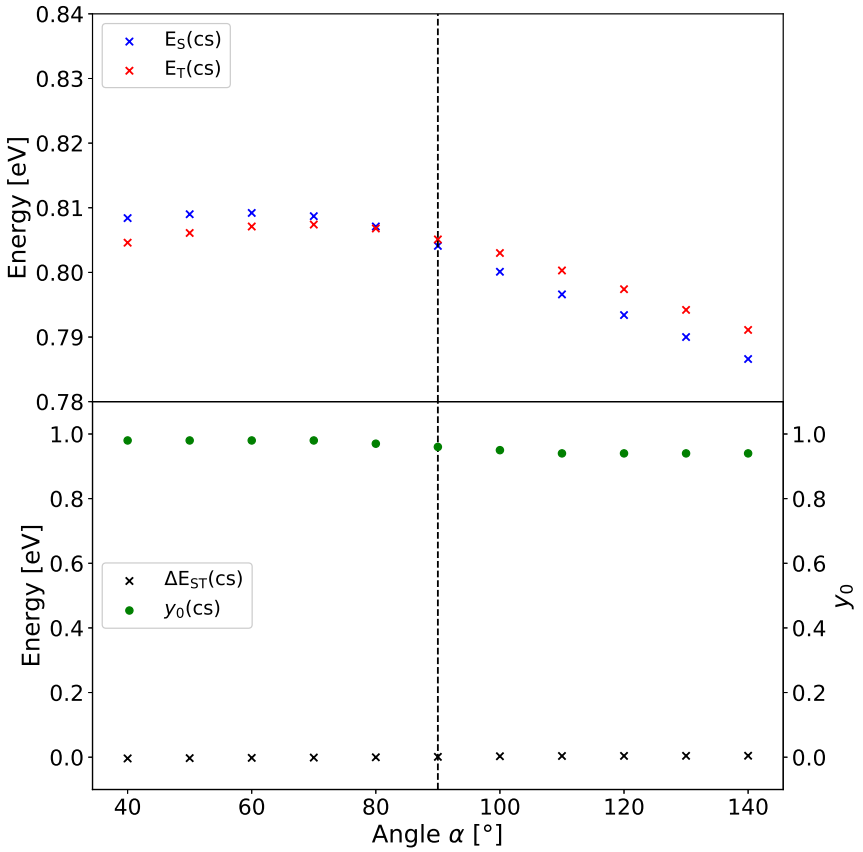

Figure 4.15: Excitation energies [eV] of the first singlet and triplet spin-flip excited states (top) and the energy gap between them ΔE_{ST} [eV] obtained using CAM-B3LYP/6-311G* and the diradical character y_0 (bottom) at closed-shell geometries of **MD-2** with angles α between 40°-140°.

Figure 4.15 shows the development of the excitation energies of the first singlet and triplet spin-flip excited states and the singlet-triplet gap between them, as well as the diradical character. The variation of the respective excitation energy is smaller than for **MD-1**, however the lowest excited states is the singlet for angles smaller than 90° and the triplet is the lowest for angles larger than 90° degrees. The singlet-triplet gap therefore only shows small changes and is negative for angles below 90°. The diradical character lies between 0.94 and 0.98 for all angles. As discussed above, in the case of **MD-2**, the diradical character is not strongly influenced by the relative orientation of the monomer subunits, since the unpaired electrons can not be paired at any geometry. The through-space interaction between the electrons seems to have only a small effect on the singlet triplet gap and diradical character, which is in contrast to the effect observed for **MD-1**. The corresponding results using the broken-symmetry and triplet geometries and ground states are shown in **Figure B.5** and **B.6** in **Appendix B** and show similar results as those for the closed-shell singlet case. Interestingly, this means that for the non-Kekulé diradical **MD-2**, the choice of ground state in the optimization does not have a large influence on diradical character and singlet-triplet gap.
Overall, the two systems nicely display the expected behavior of the open-shell nature with the angle between the monomer units, as well as the influence of the diradical character on the energies of different ground states and singlet-triplet gaps.

4.4.4 Summary

In this section, two diradical model dimer systems were investigated regarding the connection between geometry, chosen ground state and open-shell character using DFT and SF-TD-DFT at the PBEh-3c/def2-msvp and CAM-B3LYP/6-311G* level of theory, respectively. The influence of the angle between the monomer units on the diradical character was studied, where for the first dimer **MD-1**, a high diradical character was expected for angles of 90° between the monomer units, while no dependency on the angle was expected for the second dimer **MD-2**. Furthermore, the influence of the diradical character on the energies obtained using different ground states for optimization and the singlet-triplet gaps was studied. The two systems were constructed to obtain a Kekulé and a non-Kekulé diradical, to observe differences in their behavior.

First, both model dimers **MD-1** and **MD-2** were optimized using a closed-shell, broken-symmetry and triplet ground state and for each obtained geometry, the angle α between the monomer units and the diradical character y_0 was determined. For **MD-1**, the different ground states yielded geometries with angles α of 53.0°, 66.5° and 77.2°, respectively and diradical characters of 0.11, 0.44 and 0.67, respectively, which reflects the expected correlation between angle and diradical character. In the case of **MD-2**, the optimization using a closed-shell, broken-symmetry and triplet ground state resulted in values for the angle α of 82.1°, 76.1° and 76.1°, respectively and diradical character y_0 of 0.97, 0.98 and 0.98., respectively, which is also in line with expectation.

Subsequently, the influence of the angle on the diradical character and the energies of the geometries obtained at different ground states was investigated by constraining the angle α to values between 40° and 140° in steps of 10°. For the first model dimer **MD-1**, an unexpected behavior was observed for the closed-shell geometries, as the energy and diradical character increases with increasing angle α. A possible explanation for this is the interaction of the unpaired electrons though space as the radical centers are brought closer together at low angles. However, the trend for broken-symmetry and triplet geometries is in line with expectation as it shows an increase in the diradical character as the angle approaches 90°, while the energies decreases. The same analysis was performed for **MD-2**, which shows high values for the diradical character at all angles and for all ground states used for optimization, again displaying the independence of the open-shell character of the angle. The open-shell nature is reflected in the relatively high energy of the closed-shell geometry and the similar energies for the broken-symmetry and triplet geometries.

Finally, the influence of the diradical character on the excitation energies of the first singlet and triplet spin-flip excited states and the singlet-triplet gap between them, was observed for the geometries obtained at different ground states. Overall, the results for **MD-1** show an increase of the excitation energy of the first spin-flip excited singlet state with the diradical character, while that of the spin-flip excited triplet state is not influenced. Naturally, this results in lower singlet-triplet gaps for higher values of the diradical character. In the case of **MD-2**, the excitation energies are not strongly influenced by the diradical character, however for angles below 90°, the singlet-triplet gaps is negative, and then becomes positive for values above 90°. In the results for both model systems, the mirrored behavior of the singlet-triplet gap and the diradical character can be observed. By using different ground states for the optimization of the model dimers, the strong influence on the geometry and corresponding diradical character was observed for the Kekulé diradical, but not for the non-Kekulé diradical.

Future studies could include the investigation of absorption spectra of the model dimers dependent on the angle and diradical character also in respect of excitonic coupling between the radical

monomers. Naturally, the dimer systems could be employed to study the influence of the diradical character on other properties, however, due to their relatively large size, the investigation would still be limited to low-cost single-reference methods. The development of smaller model systems on the other hand would enable the employment of multi-reference methods and allow for more reliable insight into the influence of the diradical character on molecular properties, as well as on the quality of these properties obtained using single-reference methods.

Chapter 5

Inverted Singlet-Triplet Gaps in Small Organic Molecules

5.1 Introduction

The energy gap between the first excited singlet (S_1) and triplet (T_1) states presents an important measure for applications of molecules as organic light emitting diode (OLED) materials, as well as in photovoltaics and photocatalysis.[67–71] As a result of Hund's rule, which states that in open-shell systems the configuration with the higher multiplicity is energetically favored, the energy gap between the first excited singlet (S_1) and triplet (T_1) states $\Delta E_{S_1T_1} = E_{T_1} - E_{S_1}$ is positive for most systems.[72–74] At this point it is important to note that this singlet-triplet gap is not identical to the singlet-triplet gap between the singlet ground state and triplet state ΔE_{ST} discussed in the previous chapter. The efficiency of fluorescence OLEDs is fundamentally limited by the population of the fluorescent singlet state from recombination of electron-hole pairs of 25 %, due to spin-statistics.[196,197] The generally positive singlet-triplet gap presents an additional problem, since it favors inter-system crossing (ISC) from the singlet to the triplet state, leading to fluorescence quenching. A popular approach to improve both these issues, are thermally-activated delayed fluorescence (TADF) emitters, which have a small energy gap between the S_1 and T_1.[198,199] This enables reverse ISC (rISC) from the triplet state to the singlet state at room-temperature, thereby increasing the population of the emitting state.[200,201]

Violations of Hund's rule are rare for organic molecules and while they have been discussed in theoretical studies, the first experimental evidence of an inverted singlet-triplet gap between S_1 and T_1 was presented recently for a heptazine derivative.[202–206] In the development of OLED materials, such systems present an apparent opportunity to avoid quenching of fluorescence by ISC to the triplet altogether and even enhance the population of the singlet, since it is now energetically favorable.[75,76]

The energy difference between S_1 and T_1, which are described by the same spatial wavefunction, is determined mainly by the exchange interaction.[207] Electrons of the same spin avoid each other due to Pauli exclusion, which results in smaller coulomb repulsion in the triplet and therefore an energetic stabilization over the singlet.[208] This exchange interaction is minimized for systems with a small overlap of highest occupied molecular orbital (HOMO) and lowest unpccupied molecular orbital (LUMO), which can be observed for molecules with inverted singlet-triplet gap such as heptazine.[206] When this condition is fulfilled, small correlation effects, termed dynamic spin

polarization, can stabilize the singlet over the triplet state and lead to inverted singlet triplet gaps.[202,203,205] This can be further illustrated by considering the contributions to the diagonal elements to the ADC intermediate basis states discussed in **Section 2.3**. At the ADC(0) level, the energy of the intermediate basis states describing the first excited singlet and triplet states is the orbital energy difference between the participating orbitals (see **Equation 2.50**). The excitation energies of both S_1 and T_1 are therefore identical. Going to the ADC(1) level, the Coulomb and exchange interaction between electron and hole is included, where the exchange interaction lowers the energy of the triplet excited states below the singlet excited state (see **Equation 2.51**). At the ADC(2) level, correlation effect are included which can stabilize the excited singlet state to be lower in energy than the excited triplet state (see **Equation 2.52**).
In a previous study, the behavior of the singlet-triplet gaps $\Delta E_{S_1T_1}$ of heptazine, cycl[3.3.3]azine and cycl[3.3.3]borane was investigated, where it was observed that the negative singlet-triplet gaps become positive with increasing quality of the theoretical description.[77] In this project, small molecules, which have shown inverted singlet-triplet gaps in other studies, were chosen in order to enable an investigation at higher levels of theory.[205,209] The excitation energies for the first excited singlet and triplet state and the energy difference between them $\Delta E_{S_1T_1}$ of the molecules **1-6** shown in **Figure 5.1** are computed at various levels of theory with the goal of observing the influence on the singlet-triplet gap.

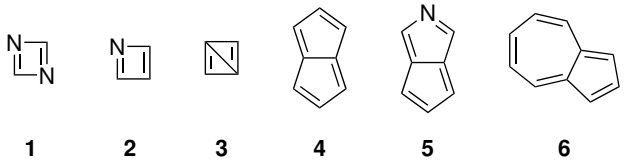

Figure 5.1: Investigated systems: 1,3-diazacyclobutadiene (**1**), 1-azacyclobutadiene (**2**), propalene (**3**), pentalene (**4**), 3-azapentalene (**5**), azulene (**6**).

5.2 Methodology

All calculations were performed using Q-Chem 6.0, unless stated otherwise.[161] The geometry optimizations were performed at the RI-MP2/def2-tzvp level of theory.[189,210,211] A verification of the minimum nature of the stationary point was performed based on the final Hessian obtained during optimization. The geometries were optimized both without employing symmetry constraints as well as constraint to assume the highest possible symmetry for the respective molecule. The excitation energies of the lowest singlet S_1 and triplet T_1 states were calculated for **1-6** using TD-DFT with and without employing the TDA and SF-TD-DFT at the CAM-B3LYP/cc-pVTZ level of theory and ADC(2)/cc-pVTZ.[127,162,169,212,213] The excitation energies of the lowest singlet and triplet excited states of **1**, **3**, **4** and **6** were also calculated using all computationally feasible combinations of the methods ADC(0)-ADC(4), EOM-CCSD and EOM-CCSDT with the basis sets cc-pVDZ, cc-pVTZ and cc-pVQZ, as well as additionally those of **1**, **3** and **4** using ADC(2) with aug-cc-pVTZ and aug-cc-pVQZ.[127,169,170,212–216] The ADC(4) calculations were performed using a development version of Q-Chem, where a more efficient ADC(4) method is implemented.[217] Chemical structures were created using ChemDraw 21.0.0. All plots were created using Python 3 and the matplotlib library.[165]

5.3 Results and Discussion

5.3.1 Assessment of Inverted Singlet-triplet Gaps

First, it was ensured that the molecules chosen based on literature research show negative singlet-triplet gaps using lower-level methods. The excitation energies of the first excited singlet S_1 and triplet T_1 state of all investigated molecules **1-6** were calculated using TD-DFT both with and without employing the TDA, SD-TD-DFT and ADC(2), with the basis set cc-pVTZ. The results can be seen in **Table 5.1**.

Table 5.1: Excitation energies [eV] for the first excited singlet S_1 and triplet T_1 states and the energy gap between them ΔE for **1-6** using TD-DFT, SF-TD-DFT and ADC(2) wit the basis set cc-pvtz at unsymmetric geometries.

	1	**2**	**3**	**4**	**5**	**6**
TDA						
S_1	3.021	3.321	3.039	1.776	1.952	2.552
T_1	2.070	1.471	2.195	0.845	1.115	2.045
ΔE	0.951	1.850	0.844	0.931	0.837	0.506
TD-DFT						
S_1	2.995	3.017	3.014	-[b]	1.813	2.413
T_1	1.577	0.669	1.891	-	0.7323	1.690
ΔE	1.418	2.348	1.123	-	1.080	0.723
SF-TD-DFT						
S_1	-[a]	1.600	-[a]	0.706	0.716	0.825
T_1	-	1.009	-	0.536	0.575	0.535
ΔE	-	0.591	-	0.170	0.141	0.290
ADC(2)						
S_1	2.788	3.339	3.381	1.915	1.940	2.251
T_1	2.369	1.783	2.490	1.150	1.410	2.253
ΔE	0.419	1.555	0.893	0.766	0.531	-0.002

[a] Spin-flip excited states show large spin-contamination.

[b] Imaginary root encountered.

Using TD-DFT at the CAM-B3LYP/cc-pVTZ level of theory with the TDA as well as full TD-DFT, only positive singlet-triplet gaps were obtained for all investigated molecules. This is in line with expectation, since it has been observed in other studies that TD-DFT does not reproduce negative singlet-triplet gaps, due to missing correlation effects from double excitations.[75,218,219] Applying the spin-flip variant of TD-DFT, positive singlet-triplet gaps were obtained for the molecules **2**, **4**, **5** and **6**, while for **1** and **3** strongly spin-contaminated excited states were obtained with $\langle \hat{S}^2 \rangle \approx 1$. It was therefore not possible to identify the singlet and triplet state based on the $\langle \hat{S}^2 \rangle$-value. Moreover, employing the ADC(2) method, all obtained singlet-triplet gaps were positive, with the exception of

that for molecule **6**. Since it was observed in other studies that highly symmetric geometries can be necessary to obtain inverted singlet-triplet gaps, all molecules were again optimized in their highest possible symmetry group.[205] Subsequently, the same analysis was performed for the symmetric geometries and the results are shown in **Table 5.2**.

Table 5.2: Excitation energies [eV] for the first excited singlet S_1 and triplet T_1 states and the energy gap between them ΔE for **1**-**6** using TD-DFT, SF-TD-DFT and ADC(2) with the basis set cc-pvtz at geometries with highest possible symmetry.

	1	**2**	**3**	**4**	**5**	**6**
symmetry	D_{2h}	C_{2v}	D_{2h}	D_{2h}	C_{2v}	C_{2v}
TDA						
S_1	0.739	-[c]	1.801	0.411	0.836	2.551
T_1	0.511	-	1.541	0.158	0.591	2.045
ΔE	0.228	-	0.260	0.253	0.245	0.506
TD-DFT						
S_1	0.710	-[b]	1.774	-[b]	-[b]	2.413
T_1	0.480	-	1.517	-	-	1.690
ΔE	0.230	-	0.257	-	-	0.723
SF-TD-DFT						
S_1	-[a]	-[a]	-[a]	-[a]	-[a]	0.825
T_1	-	-	-	-	-	0.535
ΔE	-	-	-	-	-	0.290
ADC(2)						
S_1	0.247	-[c]	1.555	0.145	0.530	2.251
T_1	0.612	-	1.763	0.378	0.796	2.253
ΔE	-0.365	-	-0.208	-0.234	-0.266	-0.002

[a] Spin-flip excited states show large spin-contamination.

[b] Imaginary root encountered.

[c] Negative excitation energy for S_1 and T_1.

As observed for the unsymmetric geometries, TD-DFT(TDA) and full TD-DFT do not show negative singlet-triplet gaps for any of the investigated molecules. The low-lying spin-flip excited states for all molecules except **6**, with $\langle \hat{S}^2 \rangle \approx 1$ show strong spin-contamination so that the singlet and triplet states could not be identified. For molecule **6**, a positive singlet triplet gap was obtained. Finally, employing ADC(2) for the symmetric geometries, inverted singlet-triplet gaps were computed for all investigated compounds except **2**, where negative excitation energies are encountered for S_1 and T_1. This system seems to show near degeneracies with the ground state for the symmetric geometry and is therefore not suitable for this investigation, since only single-reference methods are employed. Based on the obtained results and the respective system sizes, molecules **1**, **3**, **4** and **5** were chosen for further analysis of the dependence of the singlet-triplet gaps on the level of theory.

It is important to note that the unsymmetric geometries are lower in total energy than the symmetric geometries by 0.784 eV, 1.243 eV, 0.379 eV, 0.368 eV, 0.221 eV for **1**-**5**, respectively. In the case of molecule **6**, both geometries have a similar energy. The total and relative energies of the symmetric and unsymmetric geometries of all investigated molecules can be seen in **Table C.1** in **Appendix C**. The symmetric geometries investigated in the following might therefore not be the correct equilibrium geometries of the investigated systems.

5.3.2 Behavior of Inverted Singlet-triplet Gaps with Level of Theory

For this purpose, the excitation energies of the first excited singlet and triplet states and the singlet-triplet gap between them were calculated with all computationally feasible combinations of ADC(0)-ADC(4), EOM-CCSD and EOM-CCSDT with the basis sets cc-pVDZ, cc-pVTZ and cc-pVQZ. The results for all employed methods with the basis set cc-pVDZ can be seen in **Table 5.3** and those obtained using ADC(1)-ADC(4) are shown in **Figure 5.2**. The results for the basis sets cc-pVTZ and cc-pVQZ can be found in **Figure C.1** and **C.2** and **Table C.2** and **C.3** in **Appendix C**.

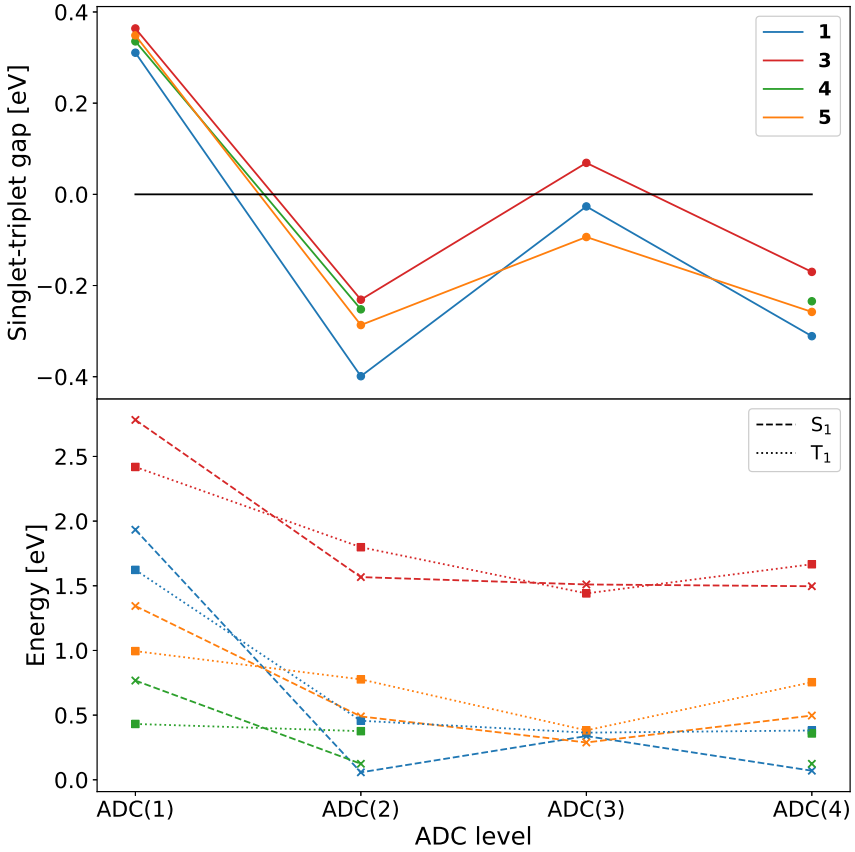

Figure 5.2: Singlet-triplet gaps [eV] of molecules **1**, **3**, **4** and **5** computed using ADC(1)-ADC(4)/cc-pvdz (top) and excitation energies [eV] of the corresponding singlet and triplet excited states. (bottom)

It can be seen in **Figure 5.2** that the values for singlet-triplet gaps of molecules **1**, **3**, **4** and **5** with increasing ADC level follow the same trend for each system. The results for ADC(0) are not shown, but can be seen in **Table 5.3**. At the level of ADC(1), only positive singlet-triplet gaps of 0.311 eV, 0.364 eV, 0.336 eV and 0.349 eV for **1**, **3**, **4** and **5**, respectively were observed. In the case

of ADC(2), the values for the singlet-triplet gaps are negative for all investigated molecules with values of −0.399 eV, −0.231 eV, −0.252 eV and −0.287 eV for **1**, **3**, **4** and **5**, respectively. Going to ADC(3), the singlet-triplet gaps increase for all systems, which however only results in a positive singlet-triplet gap for **3** of 0.069 eV and negative singlet-triplet gap of −0.027 eV and −0.094 eV for **1** and **5**, respectively. It was not possible to calculate the singlet-triplet gap using ADC(3) for **4**, since negative excitation energies were obtained for S_1 and T_1. Finally, the values for the singlet-triplet gap obtained using ADC(4) are smaller than those using ADC(3) in all cases with singlet triplet gaps of −0.311 eV, −0.170 eV, −0.235 eV and −0.258 eV for **1**, **3**, **4** and **5**, respectively. While large differences can be observed between ADC(1) to ADC(4), the overall trend seems to show convergence to negative values for the singlet-triplet gaps of the investigated molecules with increasing ADC level.

Figure 5.2 also shows the corresponding excitation energies for S_1 and T_1, which show different trends for the different investigated systems. For ADC(1) however, the singlet-triplet gap is positive in all cases, since here the only difference in the excitation energies of the singlet and triplet is the exchange interaction, which favors the triplet energetically, as discussed above. Going from ADC(1) to ADC(2), the excitation energies of the S_1 decreases more than that of the T_1 leading to negative singlet-triplet gaps. Since at the ADC(2) level, correlation effects are included, this could be interpreted as the inclusion of dynamic spin polarization, mentioned above. The development of the excitation energies going to ADC(3) shows a stronger decrease for the T_1 than for S_1 for **3** and **5**, while it is only small for **1**. The excitation energy of the S_1 however, does not show a strong decrease for **3** and **5** and even an increase for **1**. At this level, no new excitation classes are included, however the description of the double excitations is improved compared to ADC(2). Moving to ADC(4), the excitation energy of the S_1 decreases in case of **1** and **3** and increases for **5**, while the excitation energy of the T_1 increases for **1**, **3** and **5**. In the case of **4**, the singlet-triplet gap could not be obtained using ADC(3), however ADC(4) shows similar excitation energies as ADC(2). The trend observed for the results obtained using cc-pVTZ and cc-pVQZ is similar, however it was not possible to perform all the calculations due to computational cost (see **Figure C.1** and **C.2** and **Table C.2** and **C.3** in **Appendix C**).

Furthermore, the excitation energies of S_1 and T_1 and the singlet-triplet gap were computed using ADC(0), EOM-CCSD and EOM-CCSDT only for **1**, which are shown in **Table 5.3** together with the results already discussed.

Table 5.3: Excitation energies [eV] for the first excited singlet S_1 and triplet T_1 states and the singlet-triplet gap [eV] between them ΔE for **1-6** using ADC(0)-ADC(4) and EOM-CCSD with the basis set cc-pvdz at geometries with highest possible geometry.

	1	**3**	**4**	**5**
Symmetry	D_{2h}	D_{2h}	D_{2h}	C_{2v}
ADC(0)				
S_1	10.206	10.680	7.059	7.743
T_1	10.206	10.680	7.059	7.743
ΔE	0	0	0	0

ADC(1)				
S_1	1.933	2.782	0.767	1.344
T_1	1.623	2.419	0.432	0.995
ΔE	0.311	0.364	0.336	0.349
ADC(2)				
S_1	0.058	1.567	0.124	0.490
T_1	0.457	1.798	0.376	0.776
ΔE	-0.399	-0.231	-0.252	-0.287
ADC(3)				
S_1	0.338	1.510	-[c]	0.289
T_1	0.364	1.441	-	0.382
ΔE	-0.027	0.069	-	-0.094
ADC(4)				
S_1	0.070	1.497	0.124	0.497
T_1	0.381	1.667	0.358	0.755
ΔE	-0.311	-0.170	-0.235	-0.258
EOM-CCSD				
S_1	0.302	1.667	0.146	0.550
T_1	0.459	1.715	0.295	0.714
ΔE	-0.157	-0.048	-0.150	-0.165
EOM-CCSDT				
S_1	0.240	-[d]	-[d]	-[d]
T_1	0.474	-	-	-
ΔE	-0.234	-	-	-

[c] Negative excitation energy for S_1 and T_1.

[d] Not feasible due to computational cost.

Since excitation energies in ADC(0) are orbital energy differences, those of S_1 and T_1 are identical and the singlet-triplet gap is therefore zero in all cases. Furthermore, EOM-CCSD shows negative singlet-triplet gaps of $-0.157\,\text{eV}$, $-0.048\,\text{eV}$, $-0.150\,\text{eV}$ and $-0.165\,\text{eV}$ for **1**, **3**, **4** and **5**, respectively, while EOM-CCSDT gave an inverted singlet-triplet gap of $-0.234\,\text{eV}$ for **1**.

5.3.3 Behavior of Inverted Singlet-triplet Gaps with Basis Set Size

Subsequently, the influence of the basis set size was analyzed, by comparing the singlet-triplet gaps of **1**, **3**, **4** and **5** calculated using ADC(2) with the basis sets cc-pVDZ, cc-pVTZ and cc-pVQZ, shown in **Figure 5.3**. The results obtained at the ADC(3) level can be seen in **Figure C.3** in **Appendix C**.

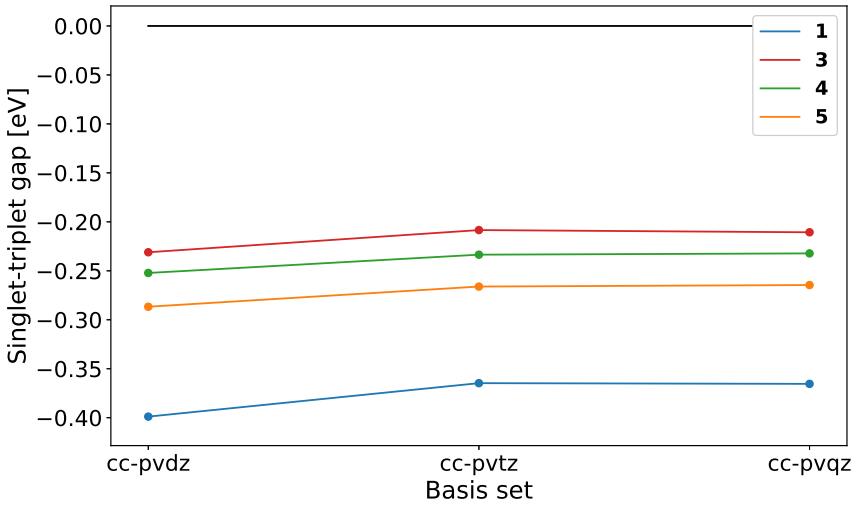

Figure 5.3: Singlet-triplet gaps [eV] of molecules **1**, **3**, **4** and **5** computed at the ADC(2) level of theory with the basis sets cc-pVDZ, cc-pVTZ and cc-pVQZ.

It can be seen in **Figure 5.3** that with increasing basis set size, the values of the singlet-triplet gap increases slightly for all investigated molecules. Increasing the basis set size going from cc-pVDZ to cc-pVTZ the value of the singlet-triplet gap increase by 0.034 eV, 0.023 eV, 0.019 eV and 0.021 eV for **1**, **3**, **4** and **5**, respectively. Increasing it further to cc-pVQZ, the gap increases by 0.0007 eV, 0.0023 eV, 0.0013 eV and 0.0016 eV, respectively. While a consistent increase in the singlet-triplet gap was observed for all the molecules, the change is small in comparison to that achieved using different levels of ADC. The same trend could be observed in the results for ADC(3) in **Figure C.3** in **Appendix C**, where it is worth mentioning that the singlet-triplet gap of **1** becomes positive for cc-pVTZ and cc-pVQZ.
To investigate the influence of using an augmented basis set, the singlet-triplet gaps of **1**, **3** and **4** were further calculated using ADC(2) with the basis sets aug-cc-pVTZ and aug-cc-pVQZ. The results can be seen in **Table 5.4**.

Table 5.4: Singlet-triplet gaps [eV] of molecules **1**, **3** and **4** computed using ADC(2) and the basis sets cc-pVTZ, aug-cc-pVTZ, cc-pVQZ and aug-cc-pVQZ.

	1	**3**	**4**
	D_{2h}	D_{2h}	D_{2h}
cc-pvtz			
S_1	0.2469	1.5550	0.1448
T_1	0.6116	1.7634	0.3783
ΔE	-0.3647	-0.2084	-0.2335
aug-cc-pvtz			
S_1	0.3142	1.5454	0.1619
T_1	0.6730	1.7490	0.3879
ΔE	-0.3589	-0.2035	-0.2261
cc-pvqz			
S_1	0.3032	1.5353	-[d]
T_1	0.6686	1.7559	-
ΔE	-0.3654	-0.2107	-
aug-cc-pvqz			
S_1	0.3295	1.5412	-[d]
T_1	0.6943	1.7512	-
ΔE	-0.3648	-0.2104	-

[d] Not feasible due to computational cost.

Compared to the singlet-triplet gaps obtained using cc-pVTZ, the basis set aug-cc-pVTZ gives singlet-triplet gaps, which are increased by 0.006 eV, 0.005 eV and 0.007 eV for **1**, **3** and **4**, respectively. In the case of the quadruple-zeta basis sets, the singlet-triplet gap increases by 0.0006 eV and 0.0003 eV going from cc-pVQZ to aug-cc-pVQZ for **1** and **3**, respectively. The influence of including diffuse basis functions therefore seems to be small.

5.4 Summary and Outlook

Molecules that exhibit an inverted singlet-triplet gap present potential for the application in fluorescence OLED materials, since the population of the emitting singlet state is energetically favored. It was observed in a previous study that inverted singlet-triplet gaps of heptazine derivatives seem to turn positive as the level of theory applied is increased.[77] This effect was further investigated in this chapter for small molecules **1**-**6**, which allowed for the application of high-level methods. The influence of the level of theory on the singlet-triplet gap of several small molecules was investigated, employing TD-DFT, SF-TDDFT, ADC(0)-ADC(4), EOM-CCSD and EOM-CCSDT. Furthermore, the dependency on the basis set size was observed by using different basis sets cc-pVDZ, cc-pVTZ, cc-pVQZ and the augmented basis sets aug-cc-pVTZ and aug-cc-pVQZ.

Initially, the singlet-triplet gaps of all investigated molecules were computed using TD-DFT(TDA), full TD-DFT, SF-TD-DFT and ADC(2) with the cc-pVTZ basis set. For unsymmetric geometries, no inverted singlet-triplet gaps were observed, expect for **6** using ADC(2). Performing the same analysis for molecular geometries in the highest possible symmetry, negative singlet-triplet gaps were observed for ADC(2). TD-DFT(TDA) and full TD-DFT do not show inverted singlet-triplet gaps, while SF-TD-DFT gives spin-contaminated excited states that could not be assigned as singlet and triplet states.
Based on these results, the singlet-triplet gaps of the smallest systems **1**, **3**, **4** and **5** were computed using all feasible combinations of ADC(0)-ADC(4), EOM-CCSD and EOM-CCSDT with the basis sets cc-pVDZ, cc-pVTZ and cc-pVQZ. It was observed that for one basis set, increasing the level of ADC method from zero to four, gave the same trend for all investigated molecules. For ADC(1), a positive singlet-triplet gap was observed, since the exchange interaction is the only difference between the singlet and triplet state. The obtained values for the singlet-triplet gap using the cc-pVDZ basis set are 0.311 eV, 0.364 eV, 0.336 eV and 0.349 eV for **1**, **3**, **4** and **5**, respectively. Going to ADC(2), negative singlet-triplet gaps were observed for all molecules with values of −0.399 eV, −0.231 eV, −0.252 eV and −0.287 eV for **1**, **3**, **4** and **5**, respectively, which can be explained by the effect of dynamic spin polarization. For ADC(3), the singlet-triplet gaps increase again, to give a positive value for **3**, but still negative values for **1** and **5** with −0.027 eV, 0.069 eV and −0.094 eV for **1**, **3** and **5**, respectively. Another decrease was observed going to ADC(4), where the calculated singlet-triplet gaps are −0.311 eV, −0.170 eV, −0.235 eV and −0.258 eV for **1**, **3**, **4** and **5**, respectively. Furthermore, EOM-CCSD and EOM-CCSDT show negative singlet-triplet gaps in all cases. Using the ADC(2) method and increasing the size of the basis set, an increase in the singlet-triplet gap was observed going from cc-pVDZ to cc-pVTZ between 0.019 eV and 0.035 eV. Increasing the basis set size to cc-pVQZ increases the singlet-triplet gap again between 0.0007 eV and 0.0023 eV, while the gaps remain negative in all cases. The application of augmented basis set shows a slight decrease in the singlet-triplet gap.
Overall, with increasing level of theoretical description using ADC, the value of the singlet-triplet gap seems to be slowly converging towards a certain value, which seems to be negative. This stands in contrast to previous findings, is however in line with other studies employing high-level theories that point towards negative singlet-triplet gaps for heptazine, cyclazine and derivatives at the CC3/aug-cc-pVDZ level of theory.[77,220] It was furthermore observed that the influence of the basis set size on the singlet-triplet gap is small compared to that of the level of theory. Unfortunately, even for the small systems investigated, computations combining highly-accurate level of description with a large basis set were not feasible, which could be improved upon in future investigations. It is worth mentioning that all computations yielding inverted singlet-triplet gaps are performed on highly symmetric geometries, which raises the question, if this would be the geometry actually assumed by a molecule. Finally, the ADC methods might serve as a convenient framework to analyze which effects lead to the increase or decrease of the excitation energies of the S_1 and T_1 at different levels in future studies.

Chapter 6

Exploration of the Deexcitation Pathway and Design of an RNA Label

This project presents a cooperation with the Wachtveitl group of Goethe University Frankfurt.

6.1 Introduction

Spectroscopic experiments can deliver valuable insight into the structure of biomolecules, such as deoxyribonucleic acid (DNA) and ribonucleic acid (RNA), which is central to the understanding of their operating mechanism and function. The introduction of label molecules allows for the application of fluorescence and EPR-spectroscopy to DNA and RNA, which are otherwise not responsive to the respective measuring techniques.[78–89] The label molecule **Ç** is a spin label that belongs to the group of fluorophore-nitroxides (FNRO·).[90,91] It can be built into DNA, since it forms a stable base pair with guanine and has been employed to measure distances within DNA strands using EPR spectroscopy.[92] The reduced form of **Ç**, **Ç$^{\mathbf{f}}$**, can be used as a fluorescence label and has been employed to identify mismatches within DNA-strings.[93]
By substituting the 2'-position of the ribose group of **Ç** and **Ç$^{\mathbf{f}}$** with a methoxy group, one obtains the label molecules **Ç$_{\mathbf{m}}$** and **Ç$_{\mathbf{m}}{}^{\mathbf{f}}$**, which can be incorporated into RNA and are shown in **Figure 6.1**.[94,95] The photophysics of both systems has been studied in detail using both experimental and computational methods in preceding work.[15]

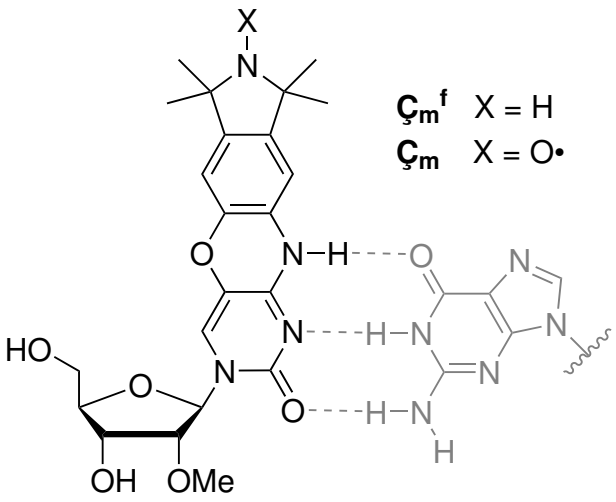

Figure 6.1: Structure of the spin label $\mathbf{Ç_m}$ and fluorescence label $\mathbf{Ç_m^f}$ and base pairing with guanine.

Using steady-state and time-resolved spectroscopy it was observed that, as for the related compounds **Ç** and $\mathbf{Ç^f}$, the molecule $\mathbf{Ç_m^f}$ shows fluorescence, which is quenched in $\mathbf{Ç_m}$. Quantum chemical calculations revealed that the first excited singlet state (S_1) in $\mathbf{Ç_m^f}$ is a bright $\pi\pi^*$-state, which corresponds to the second excited doublet state (D_2) in $\mathbf{Ç_m}$ based on excitation energies and transition densities. The first excited doublet state in $\mathbf{Ç_m}$, however, is a dark $n\pi^*$-state, which is located on the nitroxide group and has no equivalent in $\mathbf{Ç_m^f}$. The proposed excited state pathway for $\mathbf{Ç_m^f}$ is that after excitation to the S_1, the system relaxes into the lowest vibrational state of S_1 and subsequently interacts with the solvent to form its solvated geometry. From here, deexcitation to the S_0 occurs both radiatively, resulting in fluorescence, and non-radiatively. In $\mathbf{Ç_m^f}$, a different pathway is suggested. The system is primarily excited into the D_2, which has the same character as the S_1 in $\mathbf{Ç_m}$, and also undergoes vibrational relaxation to the lowest vibrational level of D_2. However, the system is proposed to subsequently undergo fast internal conversion (IC) to the dark D_1 state, which is not present in $\mathbf{Ç_m^f}$, from where non-radiative decay occurs to the ground state. The conversion to the solvated geometry of D_2 and subsequent fluorescence are thus efficiently quenched, due to the fast IC to D_1.[15]
As $\mathbf{Ç_m}$ is only a spin label and $\mathbf{Ç_m^f}$ only a fluorescence label, separate samples have to be prepared to conduct a fluorescence or EPR experiment on a certain RNA molecule. The aim of the present work is to explore the possibility of designing a related molecule that can function as both spin and fluorescence label, which would enable EPR and fluorescence spectroscopy on the same RNA sample. The excited state landscape of the original spin label $\mathbf{Ç_m}$, as well as three derived structures will be further investigated with respect to the proposed deexcitation pathway and the goal to gain first insights into the design of a combined spin and fluorescence label.

6.2 Methodology

All calculations were performed using the ORCA 5.0.1 or 6.0.1 program package, unless stated otherwise.[191,192,221] The investigated systems are the spin label $\mathbf{Ç_m}$ and derivatives of $\mathbf{Ç_m}$, $\mathbf{Ç_m1}$, $\mathbf{Ç_m2}$ and $\mathbf{Ç_m3}$ depicted in **Figure 6.2**, where the ribose ring shown in **Figure 6.1** is replaced by a methyl group for simplicity. The equilibrium geometries were obtained by geometry optimization at the CAM-B3LYP(D3-BJ)/6-311G* level of theory.[162–164] Harmonic frequency analyses were

performed to confirm that all stationary points are local minima. The $\langle \hat{S}^2 \rangle$-values of the doublet ground states are 0.75 for all investigated molecules. All excited state calculations were done using TD-DFT at the TDA/CAM-B3LYP(D3-BJ)/6-311G* level of theory. The excitation energies, oscillator strengths and $\langle \hat{S}^2 \rangle$-values of the first ten excited states were calculated. Doublet states are denoted as D_x and quartet states are denoted as Q_x. For spin-pure doublet and quartet states, the value of $\langle \hat{S}^2 \rangle$ is 0.75 and 2.75, respectively. The α- and β-transition densities (ρ_α and ρ_β) of the first and second excited doublet state (D_1 and D_2) at different geometries were calculated using Q-Chem 6.0 and averaged to give the total transition density according to $\frac{1}{2}(\rho_\alpha + \rho_\beta)$.[161] Geometry optimizations of the excited states D_1 and D_2 were performed, using the root following scheme implemented in ORCA 5.0.1, and harmonic frequency analyses confirmed the stationary points to be local minima. A conical-intersection (CI) optimization, as implemented in ORCA 5.0.1, was performed to find the minimum energy crossing point (MECP) of the CI seam space between D_1 and D_2, which will be called $MECI_{D_1,D_2}$ in the following. The molecules and transition densities (isovalue = 0.001) were visualized using IQmol 2.8.0. Chemical structures were created using ChemDraw 21.0.0.

6.3 Results and Discussion

6.3.1 Excited States of Ç$_m$ and Derivatives

As described above, the pathway suggested in preceding work for the depopulation from D_2 to D_1 in **Ç$_m$** is internal conversion. Based on this possible deexcitation pathway, several modified molecules were designed, shown in **Figure 6.2**, with the goal to spatially and electronically separate the transition densities of D_1 and D_2 and thereby decrease the rate of conversion from the bright D_2 to the dark D_1 excited state. It was then investigated, how the chemical modification influences the properties of the excited states of interest compared to **Ç$_m$** as the reference system.

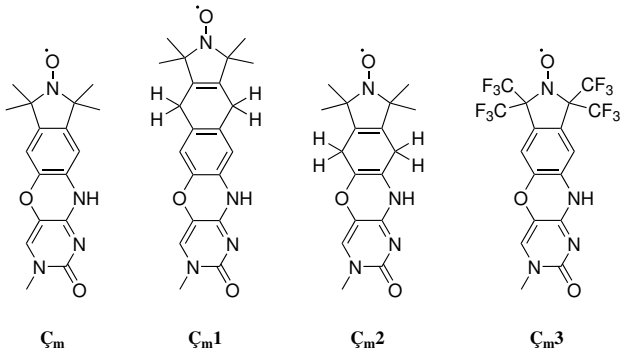

Figure 6.2: Systems investigated in this chapter: original spin label **Ç$_m$** and modified molecules **Ç$_m$1**, **Ç$_m$2** and **Ç$_m$3**.

First, the excitation energies, oscillator strengths and $\langle \hat{S}^2 \rangle$-values of the low-energy excited states of the derivatives **Ç$_m$1**, **Ç$_m$2** and **Ç$_m$3** were compared to those of the reference system **Ç$_m$**, in order to ensure that the modification does not greatly alter the character or order of the excited states. The first ten excited states of **Ç$_m$**, **Ç$_m$1**, **Ç$_m$2** and **Ç$_m$3** were obtained using TDA/CAM-B3LYP(D3-BJ)/6-311G* and the results for the first five excited states can be seen in **Table 6.1**. The results for the first ten excited states can be found in **Table D.1** in **Appendix D**.

Table 6.1: Excitation energies [eV], oscillator strengths [10^2] and $\langle\hat{S}^2\rangle$-values of the first five excited states of **Çm**, **Çm1**, **Çm2** and **Çm3** calculated using TDA/CAM-B3LYP(D3-BJ)/6-311G*.

state	E [eV]	f [10^2]	$\langle\hat{S}^2\rangle$
Çm			
Q_1	3.00	∼0.0	2.75
D_1	3.05	∼0.0	0.75
Q_2	3.62	∼0.0	2.75
Q_3	3.80	0.01	2.68
D_2	4.21	2.80	0.75
Çm1			
Q_1	2.88	∼0.0	2.75
D_1	3.06	∼0.0	0.75
Q_2	3.57	∼0.0	2.75
D_2	4.13	1.75	0.75
Q_3	4.26	∼0.0	2.75
Çm2			
Q_1	3.01	∼0.0	2.75
D_1	3.06	∼0.0	0.75
Q_2	3.63	∼0.0	2.75
Q_3	3.86	∼0.0	2.75
D_2	4.23	2.95	0.75
Çm3			
D1	2.68	∼0.0	0.76
Q_1	3.04	∼0.0	2.75
Q_2	3.49	∼0.0	2.74
Q_3	3.67	0.09	2.46
D_2	4.12	1.84	0.79

It can be seen that the modified molecules **Çm1**, **Çm2** and **Çm3** show similar excitation energies and oscillator strengths of the first two excited doublet states D_1 and D_2 to those of **Çm**. The first excited doublet state D_1 has excitation energies of 3.05 eV, 3.06 eV, 3.06 eV and 2.68 eV for **Çm**, **Çm1**, **Çm2** and **Çm3**, respectively, and is nearly dark in all cases. The second excited doublet state D_2 shows excitation energies of 4.21 eV, 4.13 eV, 4.23 eV and 4.12 eV for **Çm**, **Çm1**, **Çm2** and **Çm3**, respectively, and is the first bright excited state for all investigated systems. The $\langle\hat{S}^2\rangle$-values of all calculated excited states show either no or only small deviation from the values of spin-pure doublet and quartet states, 0.75 and 2.75, respectively.

6.3.2 Transition Densities and Equilibrium Geometries of D_1 and D_2

In order to investigate whether the excited states D_1 and D_2 also retain their character in the modified molecules, their respective transition densities were calculated. The total transition densities, obtained by averaging the α- and β-transition densities, can be seen for the excited states D_1 and D_2 of all investigated molecules in **Figure 6.3**.

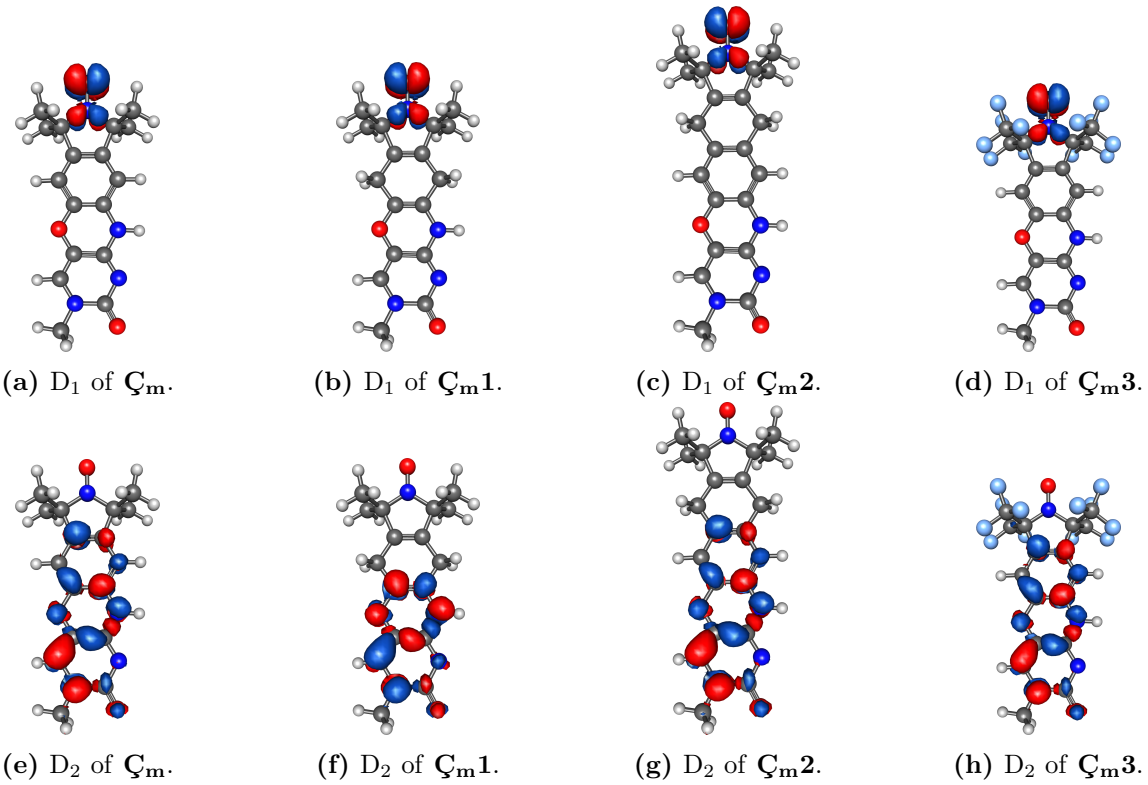

(a) D_1 of **Çm**. **(b)** D_1 of **Çm1**. **(c)** D_1 of **Çm2**. **(d)** D_1 of **Çm3**.

(e) D_2 of **Çm**. **(f)** D_2 of **Çm1**. **(g)** D_2 of **Çm2**. **(h)** D_2 of **Çm3**.

Figure 6.3: Transition densities of the excited states D_1 and D_2 of **Çm**, **Çm1**, **Çm2** and **Çm3** calculated using TDA/CAM-B3LYP(D3-BJ)/6-311G* obtained from averaging the α- and β-transition densities ($\frac{1}{2}(\rho_\alpha + \rho_\beta)$). The transition densities were visualized with an isovalue of 0.001 using IQmol.

The transition densities of the excited states D_1 and D_2 of the modified systems show a similar character to those of the reference system **Çm**. The first excited doublet state D_1 is entirely located on the nitroxide group, while the second excited doublet state D_2 is delocalized over the π-system of the molecules, opposite of the nitroxide group. Subsequently, optimized geometries of both excited states D_1 and D_2 were obtained and are shown in **Figure 6.4**.

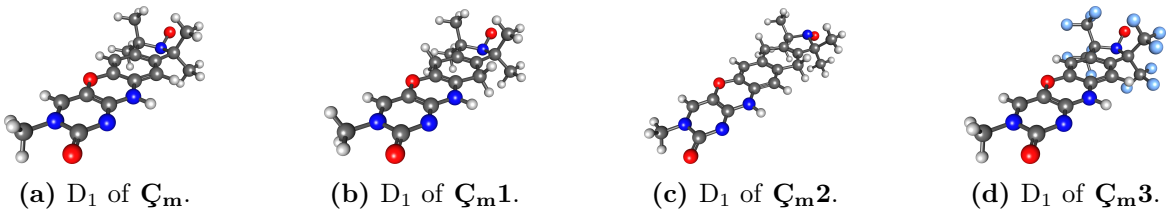

(a) D_1 of **Çm**. (b) D_1 of **Çm1**. (c) D_1 of **Çm2**. (d) D_1 of **Çm3**.

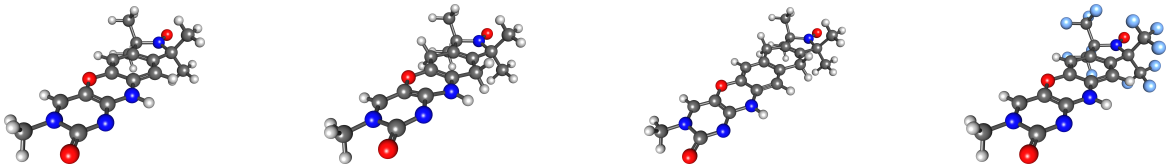

(e) D_2 of **Çm**. (f) D_2 of **Çm1**. (g) D_2 of **Çm2**. (h) D_2 of **Çm3**.

Figure 6.4: Geometries at the obtained minima of the excited states D_1 and D_2 of **Çm**, **Çm1**, **Çm2** and **Çm3** calculated using TDA/CAM-B3LYP(D3-BJ)/6-311G*. The geometries were visualized using IQmol.

In the optimized geometry of the first excited doublet state D_1, the nitroxide group is bent out of the molecular plane for all investigated systems. The optimized geometry of the second excited doublet state D_2 is planar and similar to the ground state geometry for **Çm** and **Çm3**. In the case of **Çm2**, the whole five-membered ring containing the nitroxide group is bent slightly below the molecular plane, while the geometry of **Çm1** shows bending in the two six-membered rings opposite the nitroxide-group. This is in accordance with the location of the transition densities of the respective excited states in the molecules. The transition densities of D_1 and D_2 at the optimized geometries were again visualized to ensure that the correct excited states were optimized and can be seen in **Figure D.1** in **Appendix D**. It should be noted that at the minimum geometry of the excited state which is initially D_2 of **Çm1** this state becomes the first excited state and should therefore be labeled D_1 at this point. For clarity the name of this state is kept as D_2 and it can be confirmed by the transition density in **Figure D.1** that this is the state of interest. For the other systems, the ordering of the two excited states D_1 and D_2 does not change at the optimized geometries.

6.3.3 Minimum Energy Conical Intersection between D_1 and D_2

In order to gain more insight into the excited state landscape, the location of the minimum energy crossing point (MECP) of the conical-intersection (CI) seam space (MECI) between the D_1 and D_2 of **Çm** ($MECI_{D_1,D_2}$) was explored. It is worth mentioning that opposed to the performance concerning CIs between the ground and first excited state, TD-DFT can provide accurate CI topologies between two excited states.[222] The respective obtained geometries can be seen in **Figure 6.5**.

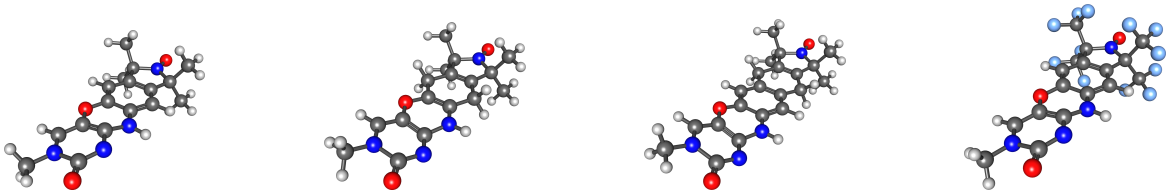

(a) CI of **Çm**. (b) CI of **Çm1**. (c) CI of **Çm2**. (d) CI of **Çm3**.

Figure 6.5: Geometry at the MECP of the CI seam space between the excited states D_1 and D_2 ($MECI_{D_1,D_2}$) of **Çm**, **Çm1**, **Çm2** and **Çm3** calculated using TDA/CAM-B3LYP(D3-BJ)/6-311G*. The geometries were visualized using IQmol.

Figure 6.5 shows that the geometry at the $MECI_{D_1,D_2}$ of all investigated compounds shows bending in the aromatic rings opposite to the nitroxide group. Especially in the case of **Çm1**, but also for the other compounds, the CI geometry shows similarity to the equilibrium geometry of the excited state D_2. It is therefore possible that the fast deexcitation of **Çm** proceeds through the CI which is located close to the equilibrium geometry of the D_2 excited state. The energies at the obtained geometries of the exited states D_1 and D_2 and the differences between them can now be used to obtain an outline of the excited state landscape. Since all investigated molecules show an overall similar picture in the excitation energies, oscillator strengths, transition densities and geometries of D_1, D_2 and MECI, it is reasonable to assume they will have similar deexcitation pathways.

6.3.4 Excited State Landscapes of Çm and Derivatives

The minima of the excited state PES of D_1 and D_2 were labeled M_{D_1} and M_{D_2}, respectively. The point on the PES of D_2 at the equilibrium geometry of the ground state was labeled FC_{D_2} (Frank-Condon point). The excitation energy from the ground state D_0 to D_2 is denoted as $E_{exc}(D_2)$ and was added to the total energy of the ground state at its equilibrium geometry to give the energy at FC_{D_2}. The following energy differences were calculated according to $\Delta E(1,2) = E(1) - E(2)$. The difference in energy between FC_{D_2} and the equilibrium geometry of D_2 was therefore labeled $\Delta E(FC_{D_2}, M_{D_2})$ and gives information about the excess energy available to the system after excitation with respect to the D_2 minimum. Furthermore, the difference between the energy at the equilibrium geometry of D_2 and the energy at the $MECI_{D_1,D_2}$ ($\Delta E(M_{D_2}, MECI_{D_1,D_2})$) as well as the energy difference between the equilibrium geometries of D_2 and D_1 ($\Delta E(M_{D_2}, M_{D_1})$) were calculated. The former holds information about the amount of energy the system needs to reach the CI geometry from the D_2 minimum geometry, while the latter is a measure for the overall thermodynamic driving force of the transition from D_1 to D_2. The obtained energy differences can be seen in **Table 6.2** and are visualized schematically in **Figure 6.6**.

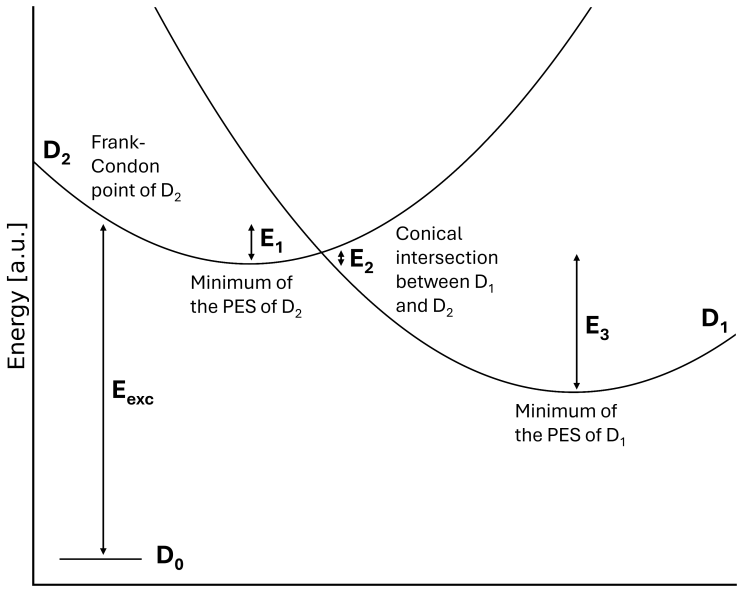

Figure 6.6: Schematic representation of the excited state landscape of the investigated molecules including the ground state D_0, the excited states D_1 and D_2 and showing the points on the PES FC_{D_2}, M_{D_1}, M_{D_2} and $MECI_{D_1,D_2}$ and the energy differences, where $E_{exc} = E_{exc}(D_2)$, $E_1 = \Delta E(FC_{D_2}, M_{D_2})$, $E_2 = \Delta E(M_{D_2}, MECI_{D_1,D_2})$ and $E_3 = \Delta E(M_{D_2}, M_{D_1})$.

As observed before, the investigated compounds show similar excitation energies for the second excited doublet state D_2, which are 4.21 eV, 4.13 eV, 4.23 eV and 4.12 eV for **Çm**, **Çm1**, **Çm2** and **Çm3**, respectively. Also the energy difference $\Delta E(FC_{D_2}, Min_{D_2})$ shows only slight variations for **Çm** **Çm2** and **Çm3**, with values of 0.32 eV, 0.33 eV and 0.31 eV. The value for **Çm1** however is larger with 0.46 eV. In regard to the proposed depopulation mechanism, this can be considered counterproductive, since **Çm1** has more excess energy after excitation to reach the CI geometry than **Çm**. The next energy difference of interest, $\Delta E(Min_{D_2}, MECI_{D_1,D_2})$, shows values that are similar between **Çm** and **Çm2**, with 0.017 eV and 0.024 eV, respectively. The system **Çm1** shows an even smaller energetic difference with 0.005 eV, which can be interpreted as the CI geometry being easier to reach than in **Çm**. For **Çm3**, however, $\Delta E(Min_{D_2}, MECI_{D_1,D_2})$ is larger than for **Çm** by almost an order of magnitude, meaning that the CI geometry should be more difficult to reach in this system. It can be noted that since $\Delta E(Min_{D_2}, MECI_{D_1,D_2})$ is very small in all cases, the first energy difference $\Delta E(FC_{D_2}, Min_{D_2})$ is of limited relevance. Finally, the difference in energy $\Delta E(Min_{D_2}, Min_{D_1})$ is 1.68 eV, 1.47 eV, 1.70 eV and 1.72 eV for **Çm**, **Çm1**, **Çm2** and **Çm3**, respectively. It shows similar values for **Çm**, **Çm2** and **Çm3** and a decreased value for **Çm1**, which means that there is a decreased thermodynamic driving force behind the IC in this case.

Table 6.2: Differences in energy [eV] between relevant points on the PESs: $E_{exc}(D_2)$, $\Delta E(FC_{D_2}, Min_{D_2})$, $\Delta E(Min_{D_2}, MECI_{D_1,D_2})$ and $\Delta E(Min_{D_2}, Min_{D_1})$ of **Çm**, **Çm1**, **Çm2** and **Çm3** obtained at the TDA/CAM-B3LYP(D3-BJ)/6-311G* level of theory.

molecule	$E_{exc}(D_2)$	$\Delta E(FC_{D_2}, Min_{D_2})$	$\Delta E(Min_{D_2}, MECI_{D_1,D_2})$	$\Delta E(Min_{D_2}, Min_{D_1})$
Çm	4.21	0.32	0.017	1.68
Çm1	4.13	0.46	0.005	1.47
Çm2	4.23	0.33	0.024	1.70
Çm3	4.12	0.31	0.145	1.72

Considering the aspects observed in this chapter, the modified molecule **Çm1** could show an even faster IC rate than **Çm**, based on $\Delta E(FC_{D_2}, Min_{D_2})$ and $\Delta E(Min_{D_2}, MECI_{D_1,D_2})$. However, the overall thermodynamic driving force behind the transition is smaller. The system **Çm2** shows little difference to the reference system **Çm** in all the investigated aspects and is therefore not likely to show improvement in the IC rate. Finally, the modified structure **Çm3** shows favorable difference from **Çm** in $\Delta E(FC_{D_2}, Min_{D_2})$ and $\Delta E(Min_{D_2}, MECI_{D_1,D_2})$, which could mean that the IC rate would be slower for this molecule. It is important to note that the pathway of depopulation of the D_2 via CI to the D_1 is only one possibility and that further studies have to be conducted to support it.

6.4 Summary and Outlook

In this chapter, the excited state landscapes of the spin label **Çm** and modified derivatives **Çm1**, **Çm2** and **Çm3** were investigated, using DFT and TD-DFT at the TDA/CAM-B3LYP(D3-BJ)/6-311G* level of theory, with the goal of exploring the design of a combined spin and fluorescence label. It has been suggested in preceding work that in the original molecule **Çm**, fluorescence from the bright D_2 state is quenched by fast internal conversion to the dark D_1 state. The modified structures were therefore designed to separate the two excited state both spatially and energetically

to decrease the rate of internal conversion from D_2 to D_1. The excitation energies, oscillator strengths and transition densities of D_1 and D_2 of the modified molecules were compared to those of **Çm**. It was found that the excited states retain their character and relative order in all cases, where the first excited doublet state is nearly dark and located on the nitroxide group and the second exited doublet state is the first bright excited state and delocalized over the π-system of the molecule. The geometries of both excited states were optimized. The minimum geometry of D_1 shows bending of the nitroxide group out of the molecular plane for all investigated molecules, while in the case of D_2 the geometry is planar for **Çm** and **Çm3** and shows bending in the aromatic rings for **Çm1** and of the five-membered ring in **Çm2**. Subsequently, a CI optimization was performed to find the MECI between the D_1 and D_2 excited states, $MECI_{D_1,D_2}$, which was found to be located energetically and geometrically close to the D_2 minimum geometry. The obtained geometries show bending in the aromatic rings for all investigated molecules. To create an illustrative outline of the excited state landscape, the energy differences between the Frank-Condon point of D_2 and the minimum of D_2, $\Delta E(FC_{D_2}, Min_{D_2})$, the difference between the D_2 minimum and $MECI_{D_1,D_2}$, $\Delta E(Min_{D_2}, MECI_{D_1,D_2})$, and the difference between the minima of D_1 and D_2, $\Delta E(Min_{D_2}, Min_{D_1})$, were calculated. Based on these, the modified molecule **Çm1** should show an even faster internal conversion from D_2 to D_1, while **Çm2** should exhibit a behavior similar to the original spin label **Çm**. The modified system **Çm3** however might show a decreased rate of internal conversion. It is important to note that the suggested depopulation pathway is only one possibility and that further studies have to be performed to support or correct it. The results therefore have to be considered carefully.

As part of future investigations, it should be verified that the geometries of the global minima of the excited state D_1 and D_2 were obtained, since they are central to the depopulation mechanism. All performed excited state calculations could be repeated using SF-TD-DFT, which might be especially interesting to confirm the geometry at the CI. However, problems might be encountered due to spin contamination, which will make the identification of the excited states D_1 and D_2 more difficult. Furthermore, it is possible to compute the rate for internal conversion based on Fermis Golden Rule for the radiationless transition between two states, which has been done in other studies.[223–230] Preliminary attempts to employ the rate equation using semiclassical Marcus' theory however produced unreasonable results. One option for the following steps in this project would be to re-examine this approach and to test other IC rate equations. Finally, also the design of the modified molecules might have to be revised, taking into account that the molecules still need to be able to form a base pair with guanine. Overall, the validation of the obtained results on the excited state pathway and the effect of chemical modification by experimental data is absolutely essential.

Chapter 7

Summary

In this thesis, molecular properties of different functional organic molecules were investigated. In **Chapter 3**, the low-lying excited states of acene radical cations were analyzed and set into relation to the excited states of their neutral counterparts, the ^1L_w, ^1L_s and ^1B_b states. A benchmark study against experimental absorption spectra of naphthalene, anthracene and tetracene and their respective cations was performed for ADC(2), ADC(2)-x, ADC(3) and, only for the cations, IP-ADC(3). The results showed that the highest accuracy was achieved employing ADC(2)-x and ADC(3) for the neutral acenes and with ADC(3) and IP-ADC(3) for the cationic acenes. By assigning the molecular orbitals of the acene cations to those of the corresponding neutral acenes, several characteristic low-energy excited states of acene radical cations were identified and characterized. These are the excited states ^2K, ^2I_b, ^2L_w, ^2L_b, ^2L_s and ^2B_b, where the ^2L_w, ^2L_s and ^2B_b states are of the same character as the neutral excited states ^1L_w, ^1L_s and ^1B_b, respectively, and are therefore retained when going from neutral to cationic acenes. The absorption bands were labeled cation q-band (^2I_b), cation p-band (^2L_w), cation γ-band (^2L_b), cation α-band (^2L_s) and cation β-band (^2B_b). Additionally, a benchmark against experimental absorption spectra of cationic and neutral naphthalene, anthracene, tetracene and pentacene was performed for TD-DFT with the functionals BLYP, B3LYP, BHLYP and CAM-B3LYP. The functional CAM-B3LYP was chosen and employed to analyze the development of the excitation energies of all investigated excited states with increasing acene length. All excitation energies showed a decrease with growing length of the acene and seemed to slowly converge. Especially in the excitation energies of the neutral acenes, a discontinuity was observed going from nonacene to dodecacene, which was present to a smaller degree for the acene cations as well. This can be explained by the increasing degeneracy of the ground and first excited states in both cases, which leads to an incorrect description of the ground state using (TD-)DFT.

Furthermore, the exciton properties, i.e. exciton size, hole and electron size and correlation coefficient, of the excited states of neutral and cationic acenes were investigated with increasing acene length at the same level of theory. It was observed that for excited states of the same character in neutral and cationic acenes, for example ^1L_w and ^2L_w, the exciton size of the cation excited state is smaller than that of the neutral excited state. This can be explained by the larger correlation coefficient of the excited states of the cations. Also both hole and electron size increase equally fast for the neutral excited states, while the hole size grows faster than the electron size for the cation excited states, which could be explained by the increasing delocalization of the positive charge of the cation with acene length. For excited states mainly described by a single orbital transition,

the exciton size showed a similar increase as the hole and electron size, while for excited states described by at least two orbital transitions, the hole and electron size increased faster than the exciton size. This behavior is related to the correlation coefficient, which is larger and increases faster in the former case and is smaller and increases slower in the latter case. It was furthermore observed that the exciton size grows slower than the size of the acenes, which reflects that the exciton size is a measure for the actual spatial extend of the exciton. Finally, the plasmonic character of the excited states ^1B_b and ^2B_b of anthracene and its cation was demonstrated by analyzing them with regard to previously established plasmon characteristics, which were thereby applied to an open-shell system for the first time.

In the subsequent **Chapter 4**, several diradical systems were investigated with respect to the multiplicity of their ground state, diradical character and singlet-triplet gap using DFT, TD-DFT and SF-TD-DFT. In the first project, the open-shell nature of regioisomeric dicyanomethylene substituted benzodithiophenazines was examined, as well as the dimerization reaction of the *ortho*-derivative to form a dimer cage. It was observed that the *para*-derivative has a closed-shell singlet ground state, while the *ortho*-derivative has an open-shell singlet ground state with a high diradical character, which could be the reason for its instability towards dimerization. For the formation of the cage, the consecutive formation of two sets of two carbon-carbon σ-bonds was proposed as a possible reaction mechanism. The second project analyzes the open-shell nature of an indeno-diazatetracene-σ-dimer, built from two radical monomer units. For this, the geometry was optimized using a closed-shell singlet, broken-symmetry singlet and triplet ground state, where the broken-symmetry singlet and the triplet gave lower total energies than the closed-shell singlet. The diradical character, the singlet-triplet gap, spin densities and NICS values were computed for the triplet geometry, which all point toward a high diradical character of the ground state. Based on this system, two model dimers were designed and examined in the third project, in order to gain insight into the relationship between molecular geometry, chosen ground state and diradical nature. The first model dimer was designed as a Kekulé diradical and the second model dimer as a non-Kekulé diradical. For the first model dimer, the diradical character was expected to increase as the angle between the monomers approaches 90°. For the second model dimer, no dependence of the diradical character on the angle was expected. Both dimers were optimized using a closed-shell singlet, broken-symmetry singlet and triplet ground state and the diradical character was calculated for all geometries, where the expected relations between the angle, the ground state and the diradical character were observed. Subsequently, constraint geometry optimizations were performed with closed-shell singlet, broken-symmetry singlet and triplet ground states, to obtain geometries with different angles between the monomers. The connection between the angle, the total energies obtained using different ground states for optimization and the diradical character was examined. The results for the first dimer mostly showed the expected behavior of an increased diradical character as the angle approaches 90°, as well as the expected relative energies obtained with different ground states. For angles which lead to a higher diradical character, the triplet and broken-symmetry optimizations gave lower energies than the closed-shell singlet optimizations and vice versa. The second dimer showed a high diradical character for all angles, which is in line with expectation. Finally, the excitation energies of the first spin-flip excited singlet and triplet states and the energy gap between them were calculated for different angles and therefore different diradical character. For the first model dimer, the excitation energy of the singlet state increases with growing diradical character, while that of the triplet state remains almost constant. In the case of

the second model dimer, the diradical character is high in all cases and the excitation energies of the singlet and triplet remain similar. The results showed the expected mirrored behavior of the singlet-triplet gap and the diradical character.

The energy gap between the first excited singlet and triplet states of small organic molecules expected to show inverted singlet-triplet gaps were investigated in **Chapter 5**. In a previous publication, it was observed that negative singlet-triplet gaps seemed to become smaller and eventually vanish, when the level of theory at which the excitation energies were obtained was increased. This observation was further examined by computing the singlet-triplet gaps of the investigated molecules using increasing levels of ADC from ADC(0) to ADC(4) and increasing basis set sizes with the basis sets cc-pVDZ, cc-pVTZ and cc-pVQZ. First, it was observed that inverted singlet-triplet gaps were only obtained for these molecules, if their geometry was optimized to have the highest possible molecular symmetry. For increasing levels of ADC, a trend of the singlet-triplet gap was observed where the gap is positive for ADC(1) and negative for ADC(2). Going to ADC(3), the gap increases again, however gave only a positive value for one of the molecules and negative values for the others. The values decrease again for ADC(4), to give negative values for the singlet-triplet gap for all investigated molecules. With increasing basis set size, the singlet-triplet gap increased, however only to a small extent compared to the influence of the level of ADC employed. The results therefore point toward a negative singlet-triplet gap for the investigated molecules, although only at geometries of the highest possible symmetry.

The computational design of a label molecule, which can be employed for both fluorescence and EPR spectroscopy was explored in **Chapter 6** using DFT and TD-DFT. In an existing fluorophore-nitroxide spin label, fluorescence is quenched, which was proposed to proceed via fast internal conversion to the dark first excited doublet state in previous work. Its molecular structure was modified to give three derivatives with the goal of decreasing the IC rate. Their excited states were analyzed with regard to excitation energies, oscillator strengths and transitions densities to ensure that the excited-state landscapes are comparable to that of the original spin label. All of the investigated molecules showed a nearly dark first excited doublet state followed by a bright second excited doublet state. To further explore the excited state landscape, the equilibrium geometry of both excited states and the minimum energy crossing point of the CI seam space between them were optimized. From the obtained points on the potential energy surfaces of the excited states of interest, it was concluded that a decrease in the IC rate is expected for one of the proposed derivatives.

Appendix A

Excited States of Acenes and their Radical Cations

Table A.1: Assignment of the orbitals obtained at HF/6-311G* of $\mathbf{2}^+$ to those of **2** according to their shape and irreducible representation.

orbital no.	α-orbital	assignment neutral	β-orbital	assignment neutral
38	L+3	L+5	L+4	L+5
37	L+2	L+3	L+3	L+2
36	L+1	L+1	L+2	L+1
35	L	L	L+1	L
34	H	H-1	L	H
33	H-1	H	H	H-2
32	H-2	H-2	H-1	H-1
31	H-3	H-3	H-2	H-3

Table A.2: Assignment of the orbitals obtained at HF/6-311G* of $\mathbf{3}^+$ to those of **3** according to their shape and irreducible representation.

orbital no.	α-orbital	assignment neutral	β-orbital	assignment neutral
51	L+3	L+3	L+4	L+3
50	L+2	L+2	L+3	L+2
49	L+1	L+1	L+2	L+1
48	L	L	L+1	L
47	H	H	L	H
46	H-1	H-1	H	H-2
45	H-2	H-2	H-1	H-1
44	H-3	H-3	H-2	H-3

Table A.3: Assignment of the orbitals obtained at HF/6-311G* of $\mathbf{4}^+$ to those of **4** according to their shape and irreducible representation.

orbital no.	α-orbital	assignment neutral	β-orbital	assignment neutral
64	L+3	L+6	L+4	L+3
63	L+2	L+1	L+3	L+2
62	L+1	L+2	L+2	L+1
61	L	L	L+1	L
60	H	H	L	H
59	H-1	H-1	H	H-2
58	H-2	H-2	H-1	H-1
57	H-3	H-3	H-2	H-3

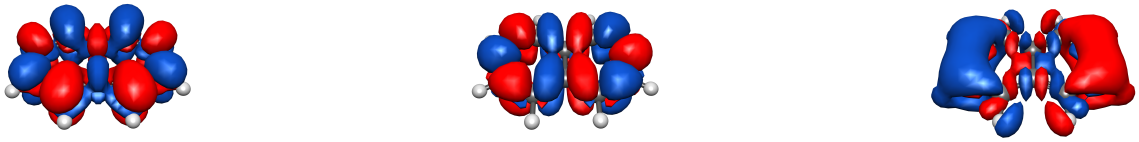

(a) ^1L_w **(b)** ^1L_s **(c)** ^1B_b

Figure A.1: Transition densities excited states of **2** obtained using ADC(2)/6-311G* and visualized with an isovalue of 0.001 using IQmol.

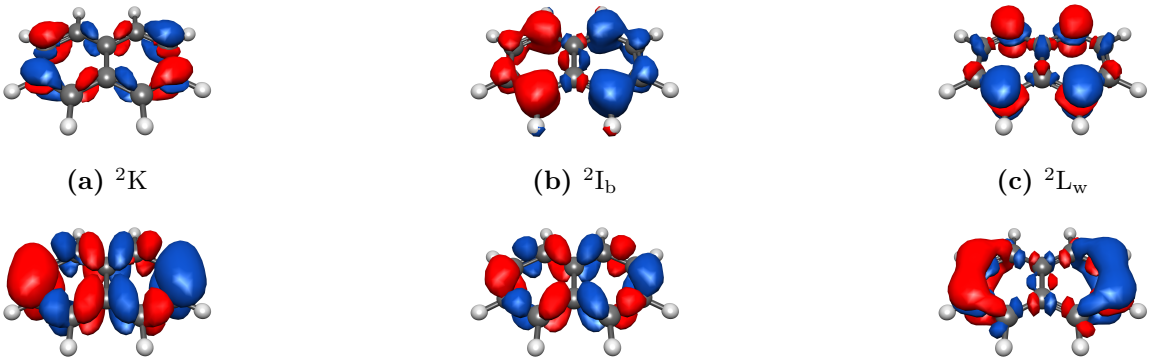

(a) ^2K **(b)** ^2I_b **(c)** ^2L_w

(d) ^2L_b **(e)** ^2L_s **(f)** ^2B_b

Figure A.2: Transition densities of excited states of $\mathbf{2}^+$ obtained using ADC(2)/6-311G* and visualized with an isovalue of 0.001 using IQmol.

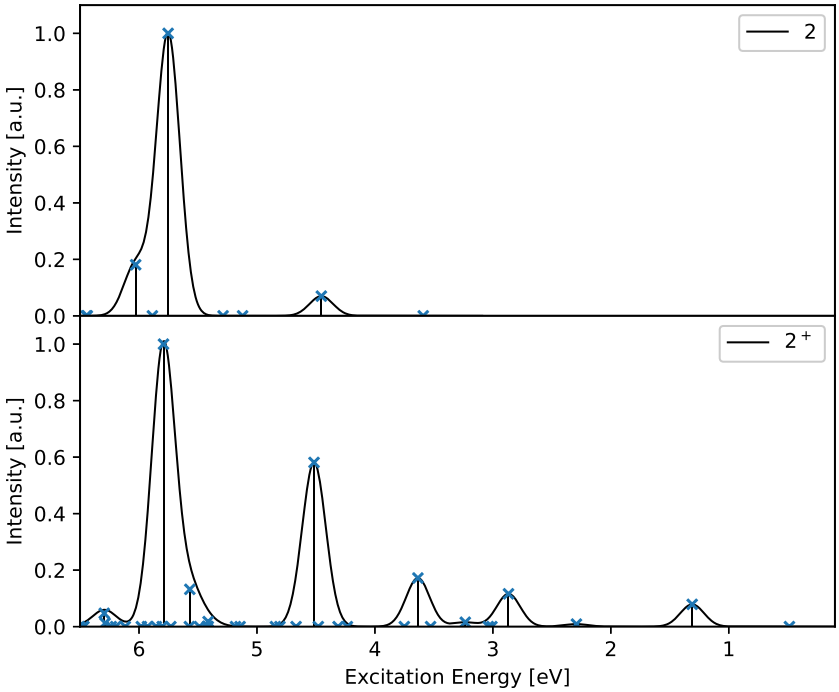

Figure A.3: Simulated absorption spectra of **2** (top) and $\mathbf{2}^+$ (bottom) obtained by convolution of excitation energies (ADC(2)-x/6-311G*) using a Gaussian broadening function with a standard deviation of 0.1 eV.

Table A.4: Excitation energies [eV], oscillator strengths, orbital contributions and assignment of ADC(2)-x states of $\mathbf{2}^+$.

ADC(2)-x	f_{osc} [10^{-2}]	main contrib.	assignment neutral	state (name)
0.49	0.00	βH−1→βL	-	1^2B_{1u} (^{2}K)
1.31	0.45	βH→βL	-	2^2B_{3g} (^2I_b, cation q-band)
2.29	0.05	βH−2→βL	-	1^2B_{2g}
		αH−1→αL	H→L	
2.87	0.66	αH−1→αL	H→L	2^2B_{2g} (^2L_w, cation p-band)
		βH−2→βL	-	
3.23	0.09	βH−1→βL+1	H−1→L	2^2B_{3g} (^2L_b, cation γ-band)
		αH→αL	H-1→L	
3.64	0.98	αH−1→αL+1	H→L+1	3^2B_{3g}
		βH→βL	H−1→L	
4.52	3.32	βH→βL	H→L+1	4^2B_{3g}
		αH−1→αL+1	H−1→L	
5.79	5.72	βH−1→βL+1	H−1→L	5^2B_{3g} (^2B_b, cation β-band)
		αH−1→αL+1	H→L+1	

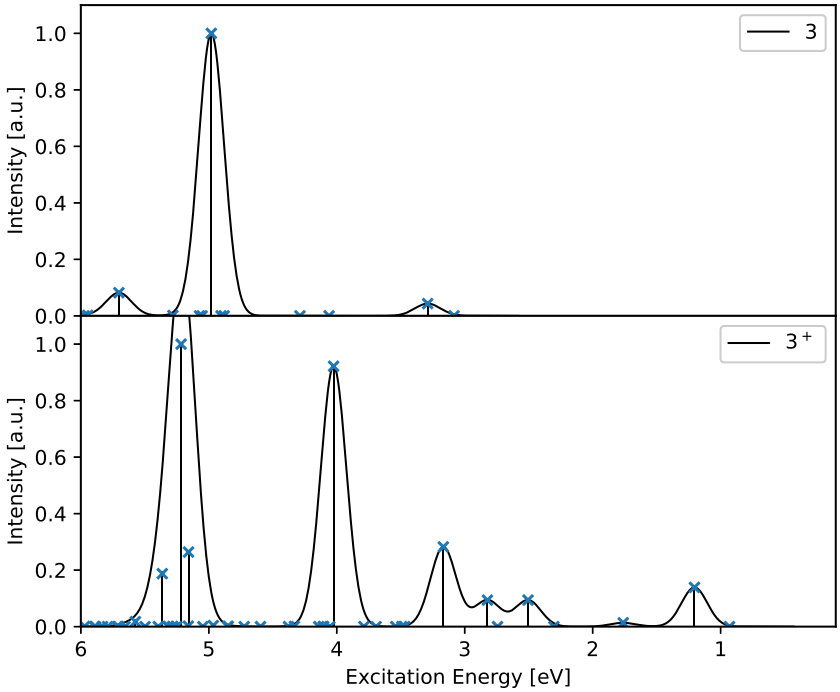

Figure A.4: Simulated absorption spectra of **3** (top) and $\mathbf{3}^+$ (bottom) obtained by convolution of excitation energies (ADC(2)-x/6-311G*) using a Gaussian broadening function with a standard deviation of 0.1 eV.

Table A.5: Excitation energies [eV], oscillator strengths, orbital contributions and assignment of ADC(2)-x states of $\mathbf{3}^+$.

ADC(2)-x	f_{osc} [10^{-2}]	main contrib.	assignment neutral	state (name)
0.93	0.00	βH$-1\rightarrow\beta$L	-	1^2B_{2g} (^{2}K)
1.20	0.84	βH$\rightarrow\beta$L	-	1^2A_u (^2I_b, cation q-band)
1.76	0.08	βH$-3\rightarrow\beta$L	-	1^2B_{1u}
		αH$\rightarrow\alpha$L	H$\rightarrow$L	
2.51	0.57	αH$\rightarrow\alpha$L	H$\rightarrow$L	2^2B_{1u} (^2L_w, cation p-band)
		βH$-3\rightarrow\beta$L	-	
2.82	0.57	αH$-1\rightarrow\alpha$L	H$-1\rightarrow$L	2^2A_u (^2L_b, cation γ-band)
		βH$-1\rightarrow\beta$L$+1$	H$-1\rightarrow$L	
3.17	1.71	βH$-1\rightarrow\beta$L$+1$	H$-1\rightarrow$L	3^2A_u
		αH$\rightarrow\alpha$L$+1$	H$\rightarrow$L$+1$	
4.02	5.58	αH$\rightarrow\alpha$L$+1$	H$\rightarrow$L$+1$	4^2A_u
		αH$-1\rightarrow\alpha$L	H$-1\rightarrow$L	
5.22	6.05	αH$\rightarrow\alpha$L$+1$	H$\rightarrow$L$+1$	6^2A_u (^2B_b, cation β-band)
		βH$-1\rightarrow\beta$L$+1$	H$-1\rightarrow$L	

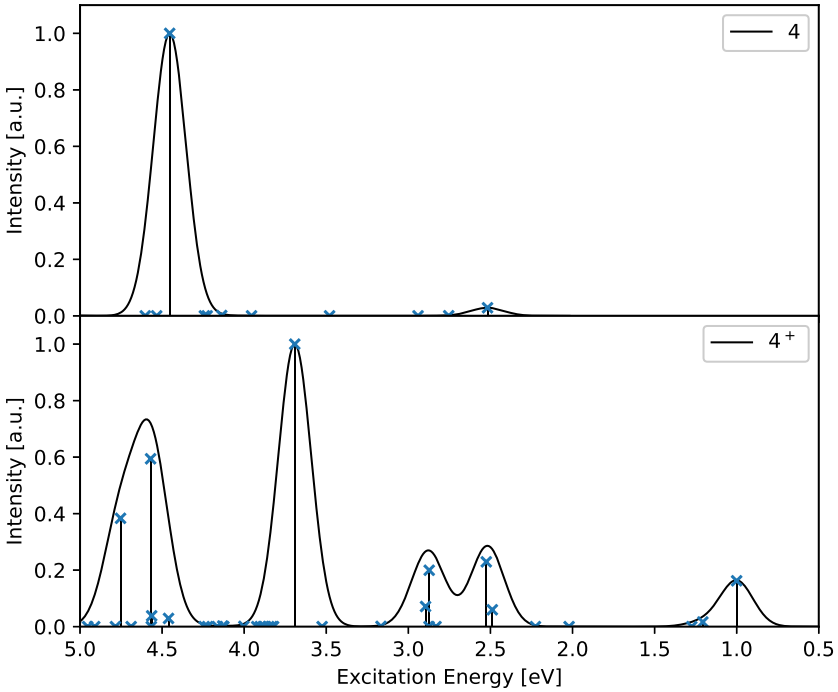

Figure A.5: Simulated absorption spectra of **4** (top) and $\mathbf{4}^+$ (bottom) obtained by convolution of excitation energies (ADC(2)-x/6-311G*) using a Gaussian broadening function with a standard deviation of 0.1 eV.

Table A.6: Excitation energies [eV], oscillator strengths, orbital contributions and assignment of ADC(2)-x states of $\mathbf{4}^+$.

ADC(2)-x	f_{osc} [10^{-2}]	main contrib.	assignment neutral	state (name)
1.00	1.20	βH→βL	-	1^2B_{3g} (^2I_b, cation q-band)
1.21	0.12	αH→αL	H→L	1^2B_{2g} (^2L_w, cation p-band)
1.27	0.00	βH−1→βL	-	1^2B_{1u} (^2K)
2.53	1.69	αH−1→αL	H−1→L	2^2B_{3g} (^2L_b, cation γ-band)
		βH−1→βL+1	H−1→L	
2.87	1.47	βH−1→βL+1	H−1→L	3^2B_{3g}
		βH−4→βL	-	
2.90	0.53	βH−4→βL	-	4^2B_{3g}
		βH−1→βL+1	H−1→L	
3.69	7.38	αH→αL+2	H→L	5^2B_{3g}
		αH,βH−1→αL,βL	-	
4.57	4.38	αH−6→αL	-	6^2B_{3g}
		βH→βL+11	-	
4.75	2.83	βH−5→βL+1	-	7^2B_{3g}
		αH−6→αL	-	

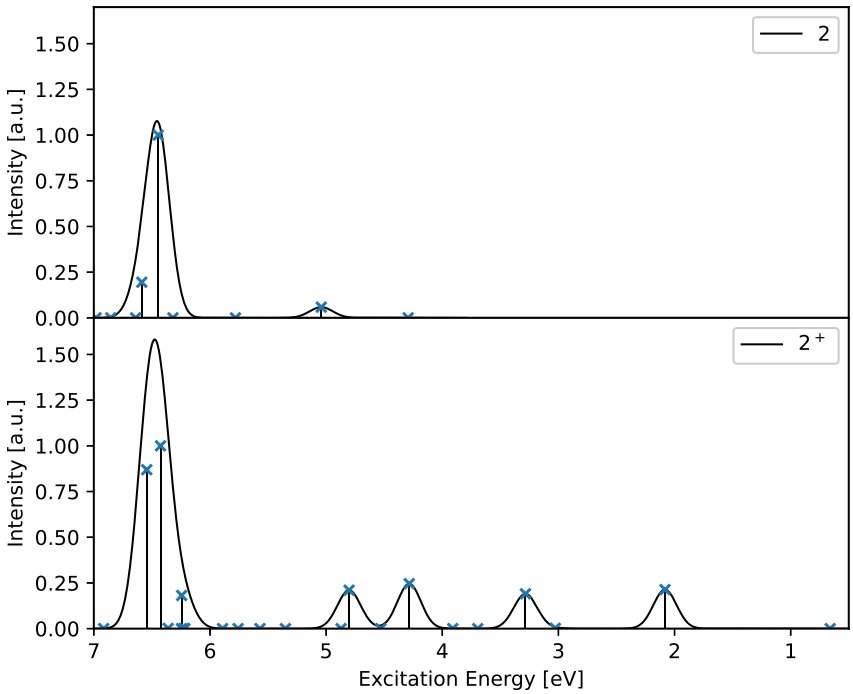

Figure A.6: Simulated absorption spectra of **2** (top) and $\mathbf{2}^+$ (bottom) obtained by convolution of excitation energies (ADC(3)/6-311G* (top) and IP-ADC(3)/6-311G* (bottom)) using a Gaussian broadening function with a standard deviation of 0.1 eV.

Table A.7: Excitation energies [eV], oscillator strengths and assignment of IP-ADC(3) states of $\mathbf{2}^+$.

IP-ADC(3)	f_{osc} [10^{-2}]	state (name)
0.66	0.00	1^2B_{1u} (^2K)
2.08	0.91	1^2B_{3g} (^2I_b, cation q-band)
3.03	0.01	1^2B_{2g}
3.28	0.82	1^2B_{2g} (^2L_w, cation p-band)
4.28	1.05	2^2B_{3g} (^2L_b, cation γ-band)
4.80	0.90	3^2B_{3g} (^2L_s, cation α-band)
6.42	4.28	4^2B_{3g}
6.54	3.72	5^2B_{3g}

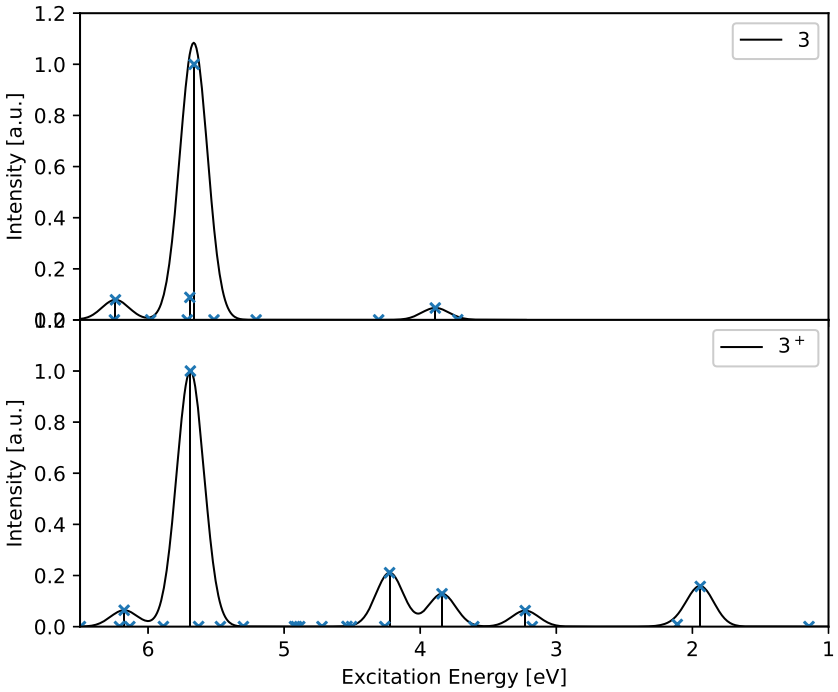

Figure A.7: Simulated absorption spectra of **3** (top) and $\mathbf{3}^+$ (bottom) obtained by convolution of excitation energies (ADC(3)/6-311G* (top) and IP-ADC(3)/6-311G* (bottom)) using a Gaussian broadening function with a standard deviation of 0.1 eV.

Table A.8: Excitation energies [eV], oscillator strengths and assignment of IP-ADC(3) states of $\mathbf{3}^+$.

IP-ADC(3)	f_{osc} [10^{-2}]	state (name)
1.14	0.00	1^2B_{2g} (^2K)
1.94	1.77	1^2A_u (^2I_b, cation q-band)
2.11	0.09	1^2B_{1u}
3.23	0.71	1^2B_{1u} (^2L_w, cation p-band)
3.84	1.45	2^2A_u (^2L_b, cation γ-band)
4.23	2.38	3^2A_u (^2L_s, cation α-band)
5.69	11.29	4^2A_u (^2B_b, cation β-band)

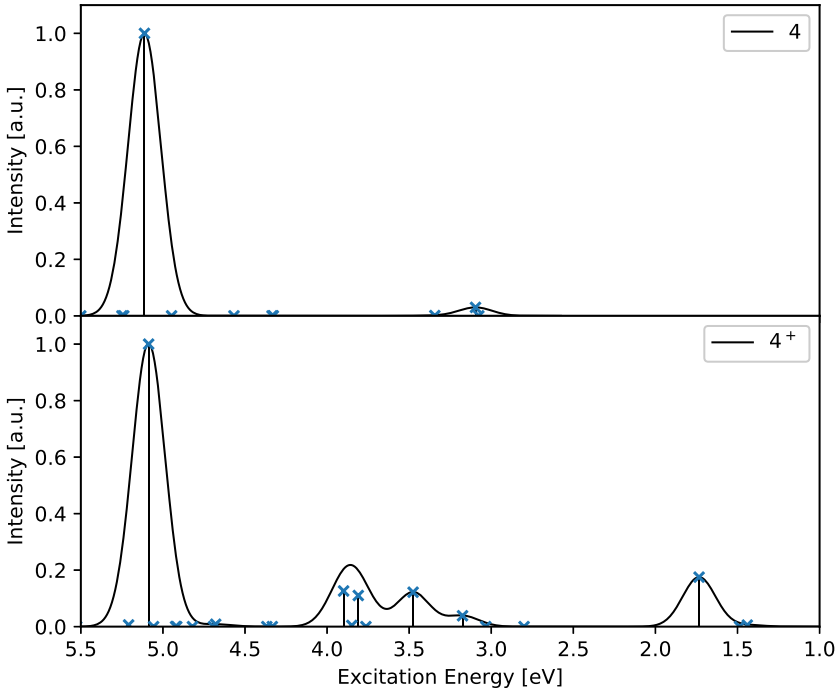

Figure A.8: Simulated absorption spectra of **4** (top) and $\mathbf{4}^+$ (bottom) obtained by convolution of excitation energies (ADC(3)/6-311G* (top) and IP-ADC(3)/6-311G* (bottom)) using a Gaussian broadening function with a standard deviation of 0.1 eV.

Table A.9: Excitation energies [eV], oscillator strengths and assignment of IP-ADC(3) states of $\mathbf{4}^+$.

IP-ADC(3)	f_{osc} [10^{-2}]	state (name)
1.44	0.09	1^2B_{2g}
1.49	0.00	1^2B_{1u} (^{2}K)
1.73	2.72	1^2B_{3g} (^2I_b, cation q-band)
3.18	0.60	1^2B_{2g} (^2L_w, cation p-band)
3.48	1.89	2^2B_{3g} (^2L_b, cation γ-band)
3.81	1.71	3^2B_{3g}
3.90	1.96	4^2B_{3g}
5.09	15.53	5^2B_{3g} (^2B_b, cation β-band)

Table A.10: Excitation energies [eV] of low-lying excited states of **2**-**12** and $\mathbf{2}^{+}$-$\mathbf{12}^{+}$ calculated at the TDA/CAM-B3LYP/6-311G* level of theory.

	2	3	4	5	6	7	8	9	10	11	12
^1L_w	5.02	3.92	3.17	2.41	2.25	1.96	1.74	1.57	0.48	0.53	0.56
^1L_s	4.77	4.19	3.82	3.47	3.38	3.24	3.14	3.06	1.10	1.04	0.98
^1B_b	6.78	5.97	5.39	4.89	4.62	4.35	4.14	3.96	2.72	2.58	2.45
	2+	3+	4+	5+	6+	7+	8+	9+	10+	11+	12+
^2I_b	2.36	2.19	1.96	1.76	1.60	1.46	1.34	1.24	1.29	1.21	1.13
^2L_w	4.00	2.71	2.11	1.65	1.31	1.04	0.84	0.67	0.32	0.23	0.15
^2L_b	4.18	3.67	3.32	3.08	2.90	2.77	2.66	2.58	2.43	2.39	2.36
^2L_s	4.99	4.44	4.12	3.86	3.67	3.58	3.47	3.39	3.31	3.25	3.19
^2B_b	6.58	5.80	5.25	4.83	4.51	4.25	4.05	3.87	3.74	3.62	3.52

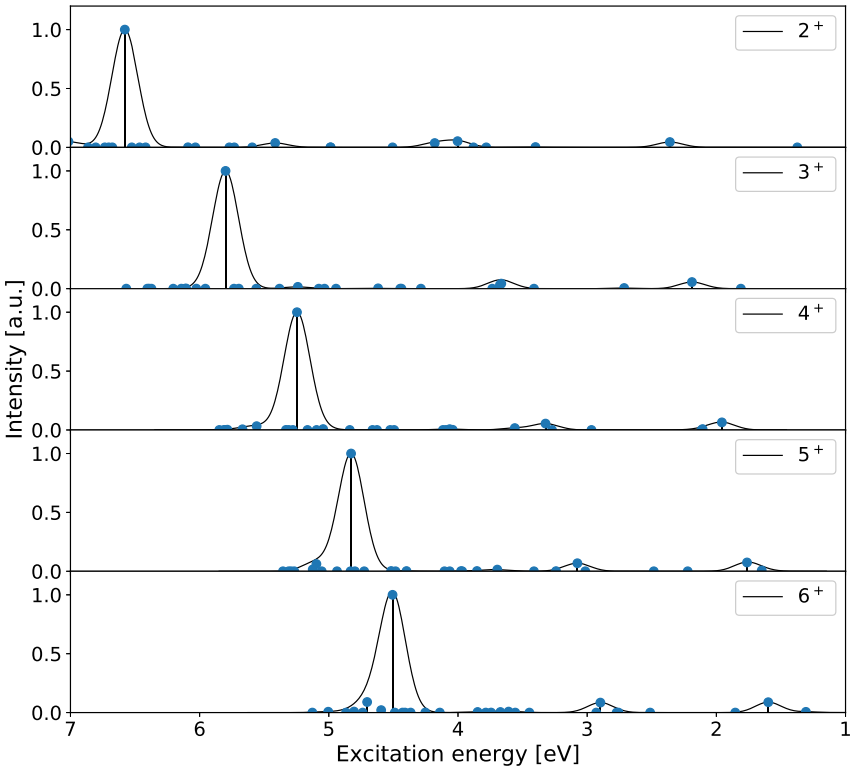

Figure A.9: Simulated absorption spectra of $\mathbf{2}^{+}$-$\mathbf{6}^{+}$ obtained by convolution of excitation energies (TDA/CAM-B3LYP/6-311G*) using a Gaussian broadening function with a standard deviation of 0.1 eV.

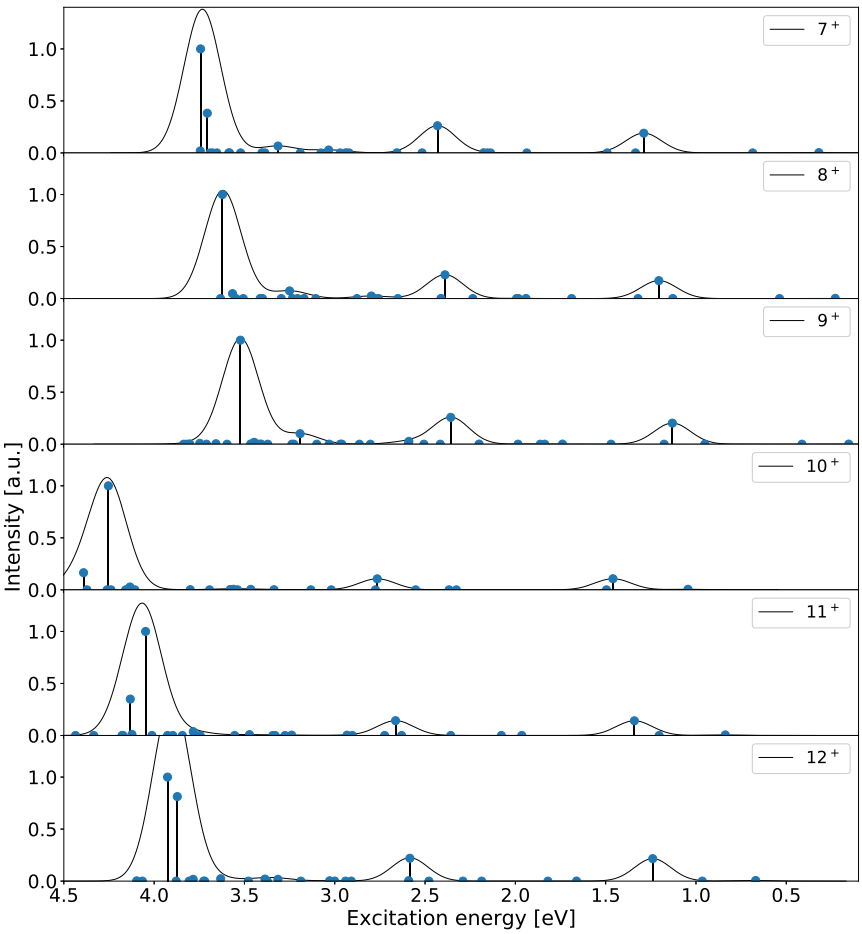

Figure A.10: Simulated absorption spectra of $\mathbf{7}^{+}$-$\mathbf{12}^{+}$ obtained by convolution of excitation energies (TDA/CAM-B3LYP/6-311G*) using a Gaussian broadening function with a standard deviation of 0.1 eV.

Table A.11: Main orbital contributions of ^1L_s, ^1B_b, ^2L_s and ^2B_b of **2-12** calculated at the TDA/CAM-B3LYP/6-311G* level of theory.

molecule	^1L_s and ^1B_b	^2L_s	^2B_b
2	H−1→L	αH→αL+1	αH→αL+1
	H→L+1	βH→βL+1	βH→βL+1
3	H−1→L	αH−1→αL	αH→αL+1
	H→L+1	βH−1→βL+1	βH−1→βL+1
4	H−1→L	αH−1→αL	αH→αL+2
	H→L+1	βH−1→βL+1	βH−1→βL
5	H−2→L	αH−2→αL	αH→αL+2
	H→L+2	βH−1→βL+1	βH−1→βL+1
6	H−2→L	αH−2→αL	αH→αL+2
	H→L+2	βH−2→βL+1	βH−2→βL+1
7	H−2→L	αH−2→αL	αH→αL+2
	H→L+2	-	βH−2→βL+1
8	H−3→L	αH−3→αL	αH→αL+3
	H→L+3	-	βH−2→βL+1
9	H−3→L	αH−3→αL	αH→αL+3
	H→L+3	-	βH−3→βL+1
10	H−1→L	αH→αL+3	αH→αL+3
	H→L+1	βH−3→βL+1	-
11	H−1→L	αH→αL+4	αH→αL+4
	H→L+1	βH−3→βL+1	-
12	H−1→L	αH→αL+4	αH→αL+4
	H→L+1	βH−4→βL+1	-

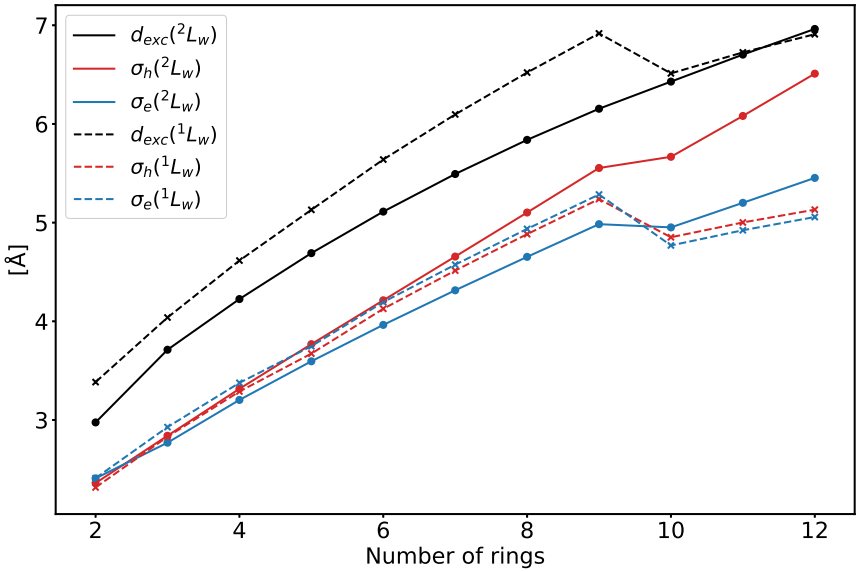

Figure A.11: Exciton (d_{exc}), hole (σ_h) and electron size (σ_e) of the excited states ^2L_w and ^1L_w of **2**$^+$-**12**$^+$ and **2-12** calculated using TDA/CAM-B3LYP/6-311G*.

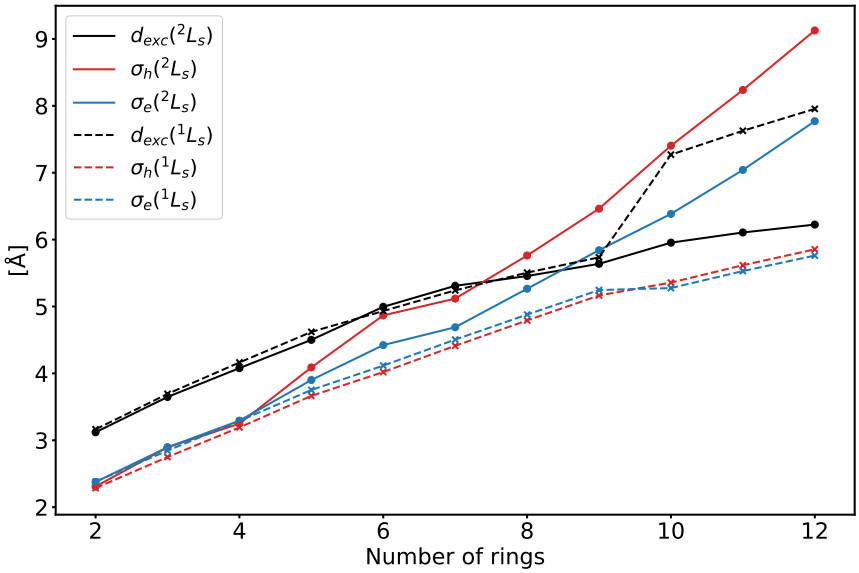

Figure A.12: Exciton (d_{exc}), hole (σ_h) and electron size (σ_e) of the excited states ^2L_s and ^1L_s of **2**$^+$-**12**$^+$ and **2-12** calculated using TDA/CAM-B3LYP/6-311G*.

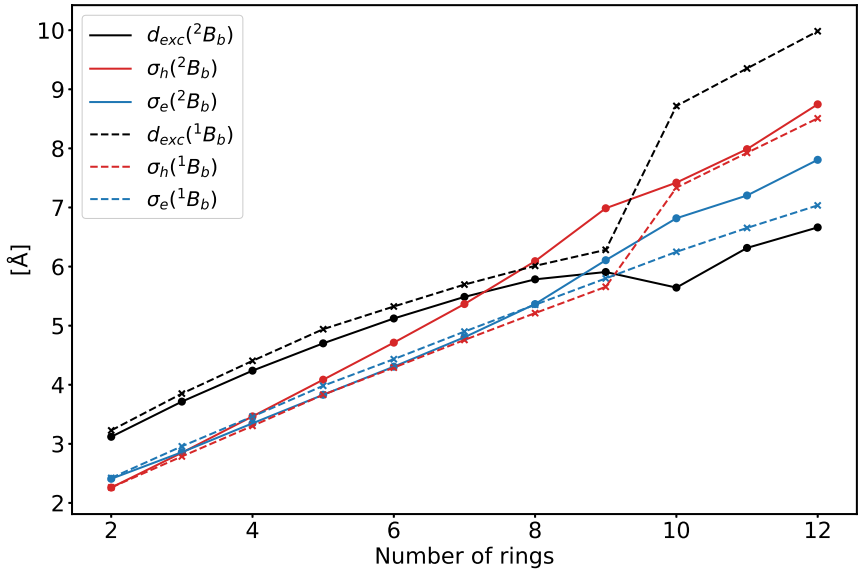

Figure A.13: Exciton (d_{exc}), hole (σ_h) and electron size (σ_e) of the excited states ^{2}B$_b$ and ^{1}B$_b$ of $\mathbf{2}^+$-$\mathbf{12}^+$ and **2**-**12** calculated using TDA/CAM-B3LYP/6-311G*.

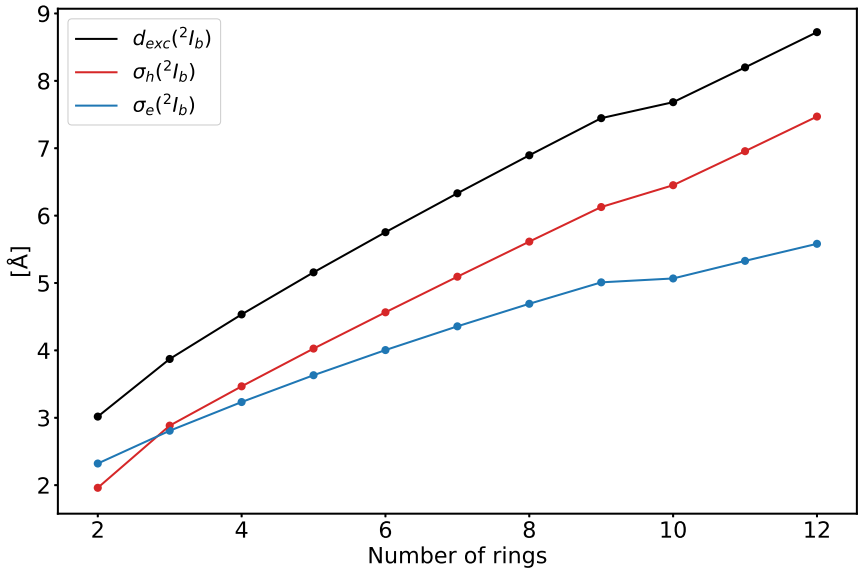

Figure A.14: Exciton (d_{exc}), hole (σ_h) and electron size (σ_e) of the excited states ^{2}I$_b$ $\mathbf{2}^+$-$\mathbf{12}^+$ calculated using TDA/CAM-B3LYP/6-311G*.

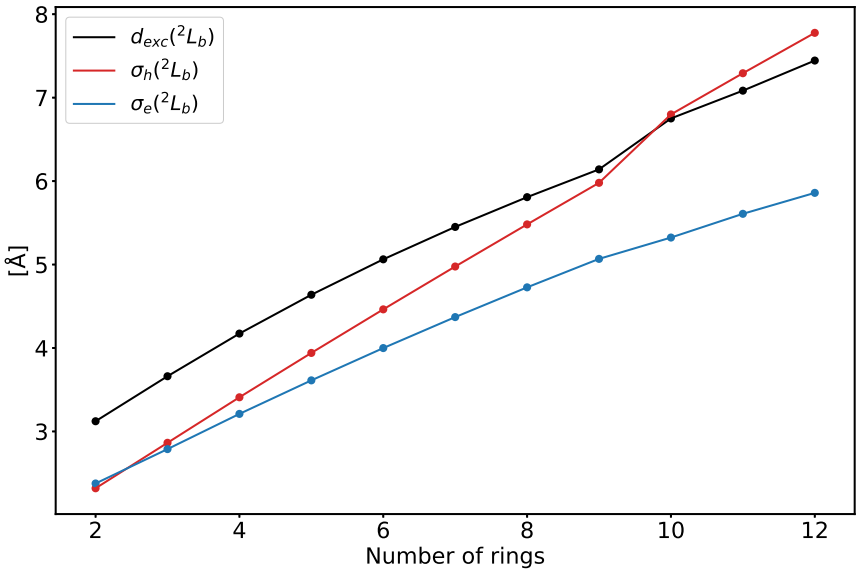

Figure A.15: Exciton (d_{exc}), hole (σ_h) and electron size (σ_e) of the excited states ^2L_b **2**$^+$-**12**$^+$ calculated using TDA/CAM-B3LYP/6-311G*.

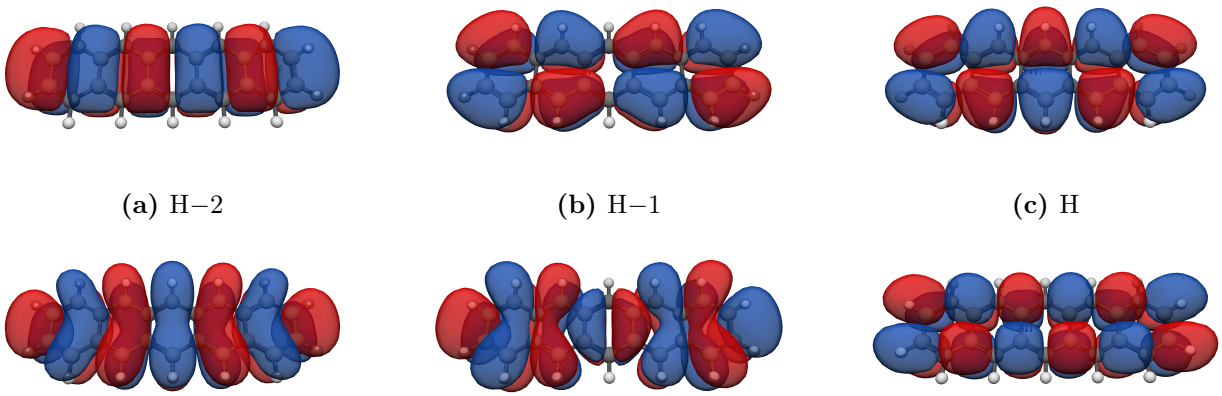

(a) H−2 **(b)** H−1 **(c)** H

(d) L **(e)** L+1 **(f)** L+2

Figure A.16: Frontier molecular orbitals H−2, H−1, H, L, L+1 and L+2 of **5** obtained at TDA/CAM-B3LYP/6-311G* and visualized with an isovalue of 0.02 using IQmol.

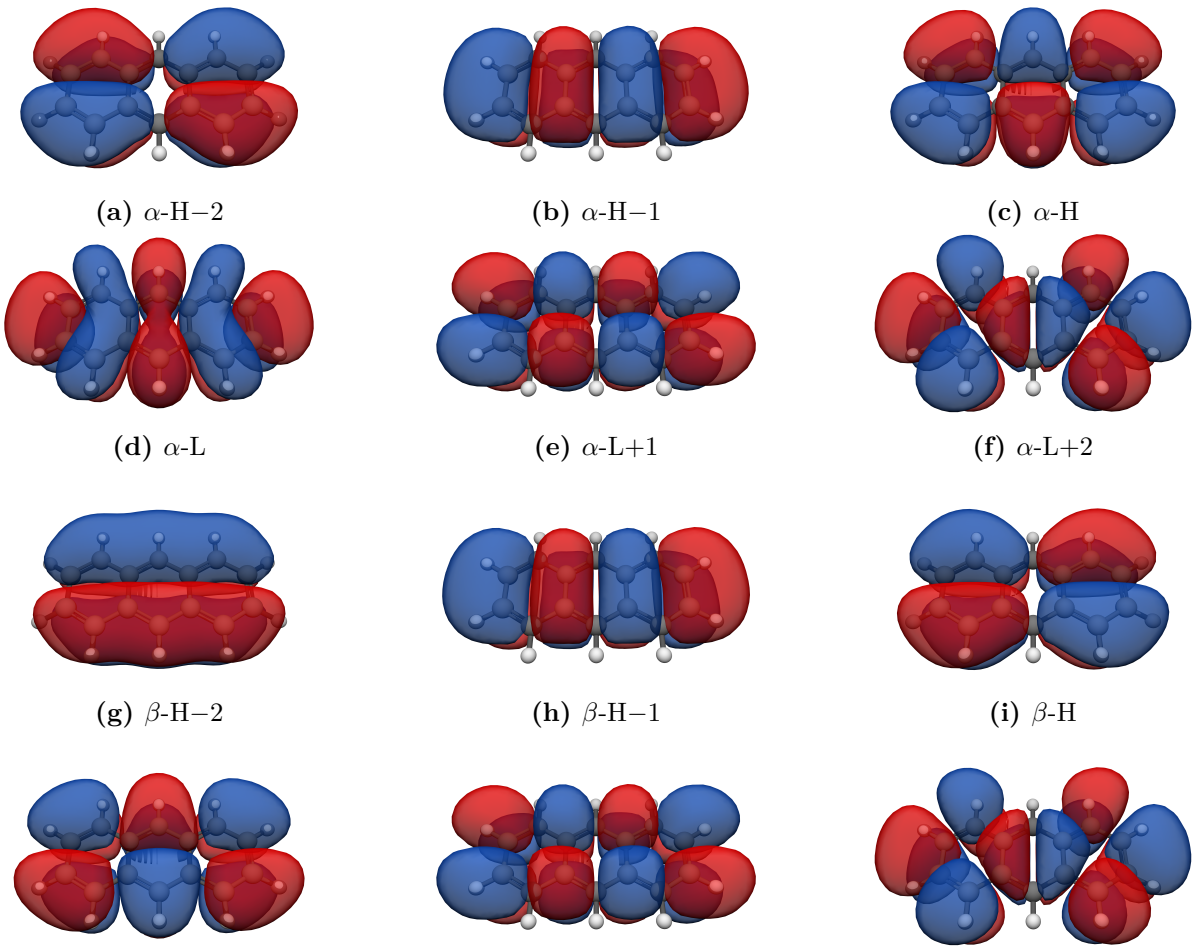

(a) α-H$-$2 **(b)** α-H$-$1 **(c)** α-H

(d) α-L **(e)** α-L+1 **(f)** α-L+2

(g) β-H$-$2 **(h)** β-H$-$1 **(i)** β-H

(j) β-L **(k)** β-L+1 **(l)** β-L+2

Figure A.17: Frontier molecular orbitals α- and β-H$-$2, H$-$1, H, L, L+1 and L+2 of $\mathbf{3}^+$ obtained at TDA/CAM-B3LYP/6-311G* and visualized with an isovalue of 0.02 using IQmol.

Appendix B

Diradical Organic Molecules

Table B.1: Excitation energies [eV], $\langle \hat{S}^2 \rangle$-values and number of unpaired electron $n_{u,nl}$ of the first spin-flip excited singlet and triplet states of ***p*-1** and ***o*-1**.

state	E [eV]	$\langle \hat{S}^2 \rangle$	$n_{u,nl}$
		***p*-1**	
S_1	-0.67	0.2	0.1
T_1	0.63	2.1	2.0
		***o*-1**	
S_1	0.67	0.3	2.0
T_1	0.68	2.1	2.0

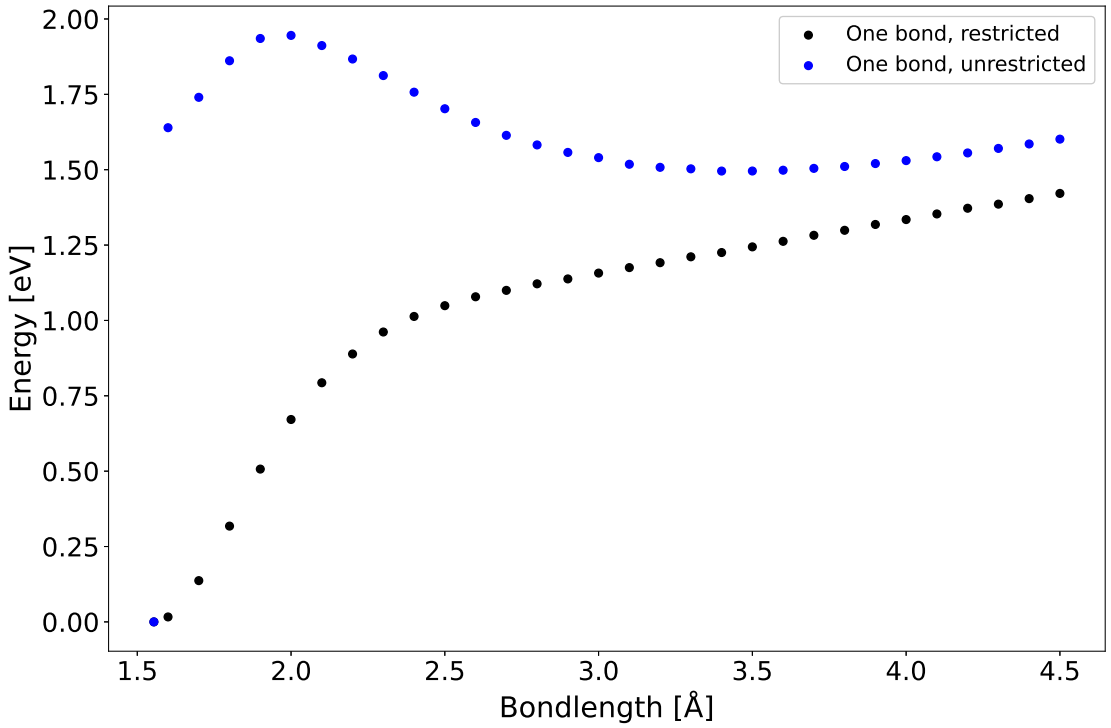

Figure B.1: Energies of constraint geometries of $(\boldsymbol{o}\text{-}\mathbf{1})_\mathbf{2}$ at bondlengths from 1.5 Å-4.5 Å of one C-C σ-bond between the monomer units obtained using GFN2-xTB.

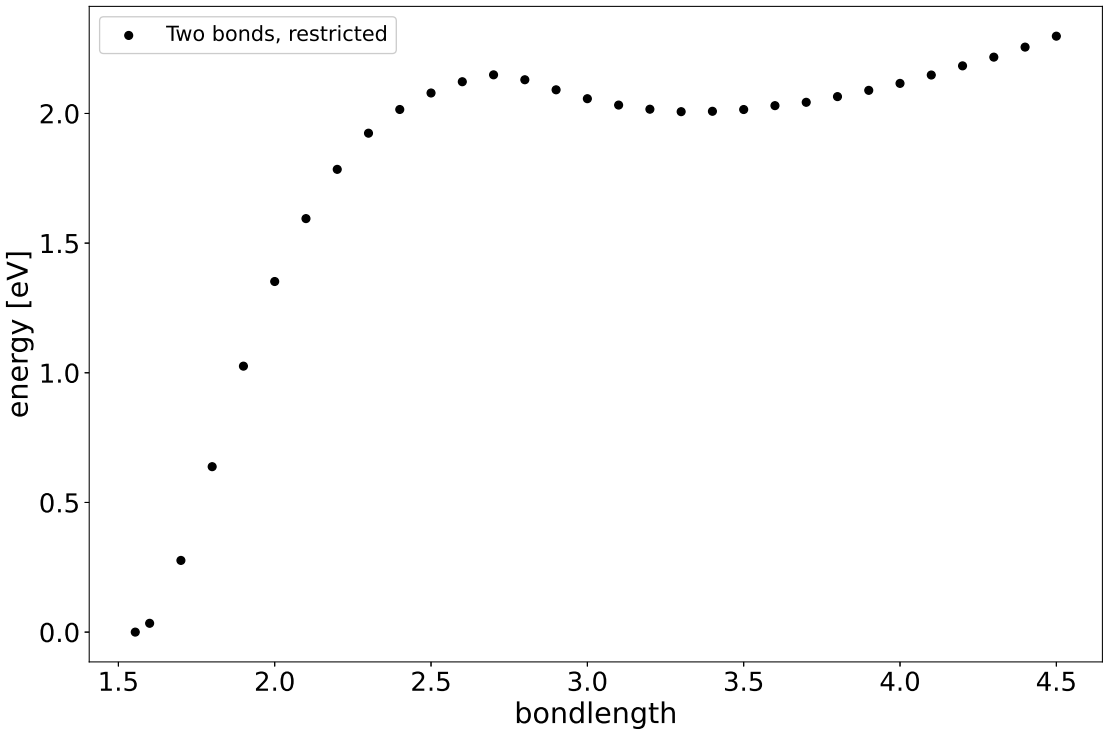

Figure B.2: Energies of constraint geometries of $(o\text{-}\mathbf{1})_2$ at bondlengths from 1.5 Å-4.5 Å of two C-C σ-bond between the monomer units obtained using GFN2-xTB.

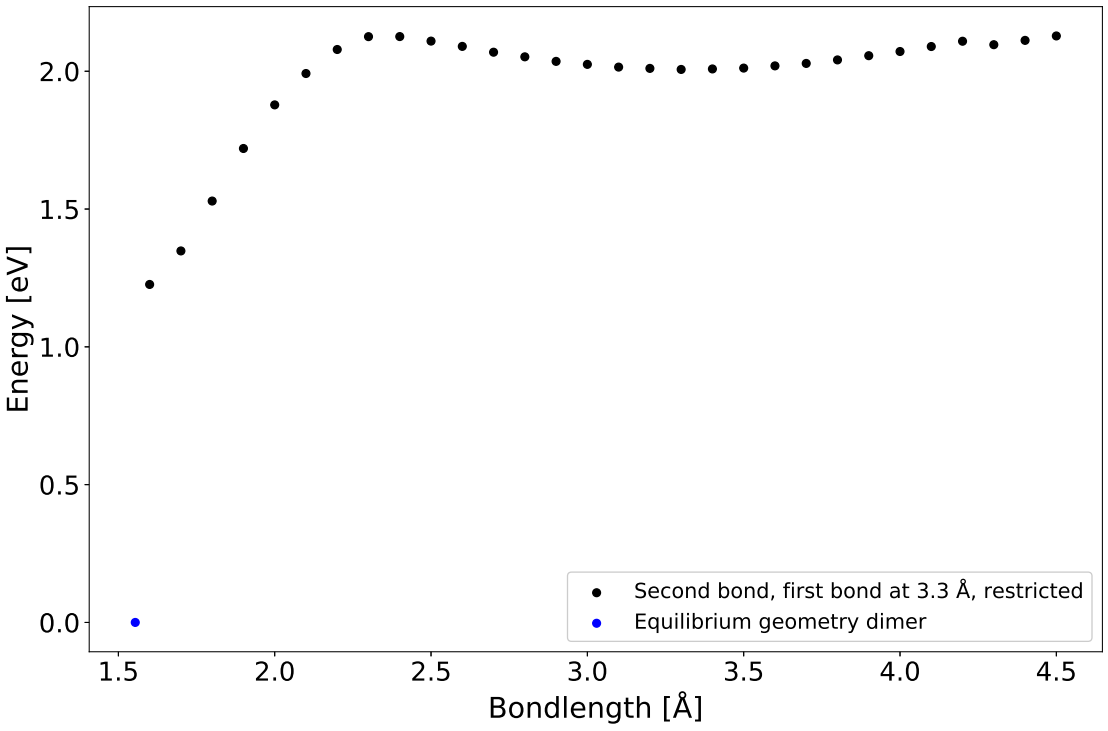

Figure B.3: Energies of constraint geometries of $(o\text{-}\mathbf{1})_2$ at bondlength from 1.5 Å-4.5 Å of one C-C σ-bond between the monomer units, while a second C-C distance was kept at 3.3 Å obtained using GFN2-xTB.

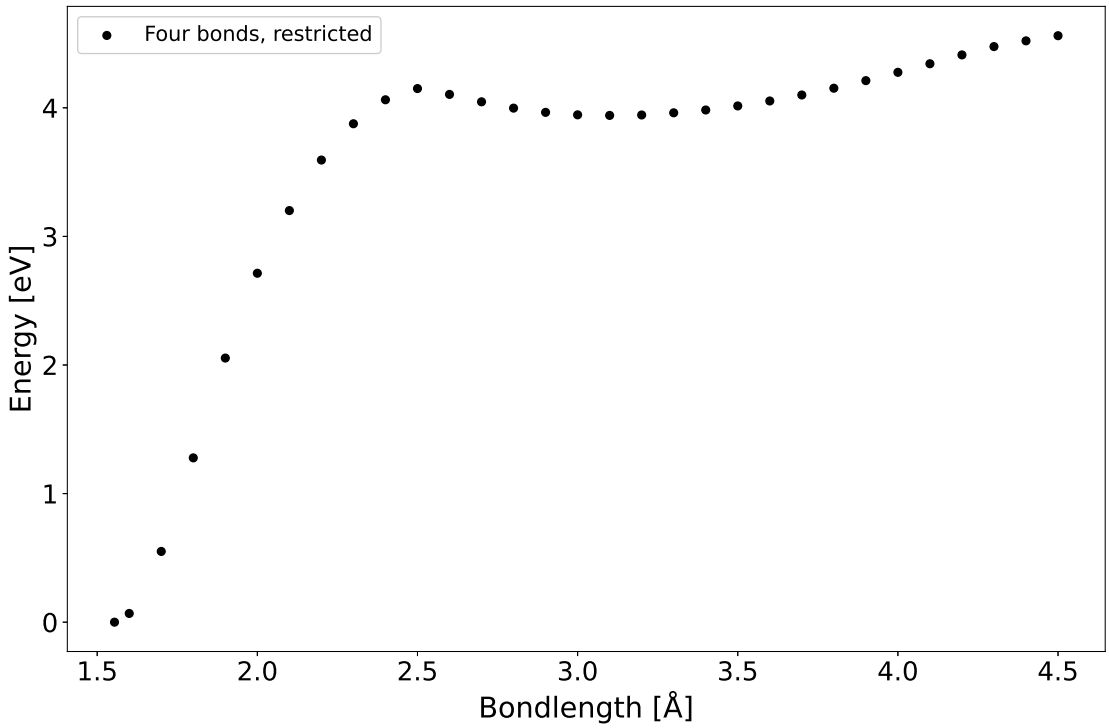

Figure B.4: Energies of constraint geometries of **(*o*-1)$_2$** at bondlengths from 1.5 Å-4.5 Å of four C-C σ-bond between the monomer units obtained using GFN2-xTB.

Table B.2: Total energies E_{total} of the optimized geometries using a closed-shell (cs), broken-symmetry (bs) and triplet (t) ground state and relative energies to the closed-shell geometry ($\Delta E(cs-x)$) of the broken-symmetry and triplet geometry.

	E_{total} [E_h]	$\Delta E(cs-x)$ [E_h]	$\Delta E(cs-x)$ [eV]
cs	-8075.355308	-	-
bs	-8075.380002	0.024694	0.672
t	-8075.38074	0.254321	0.692

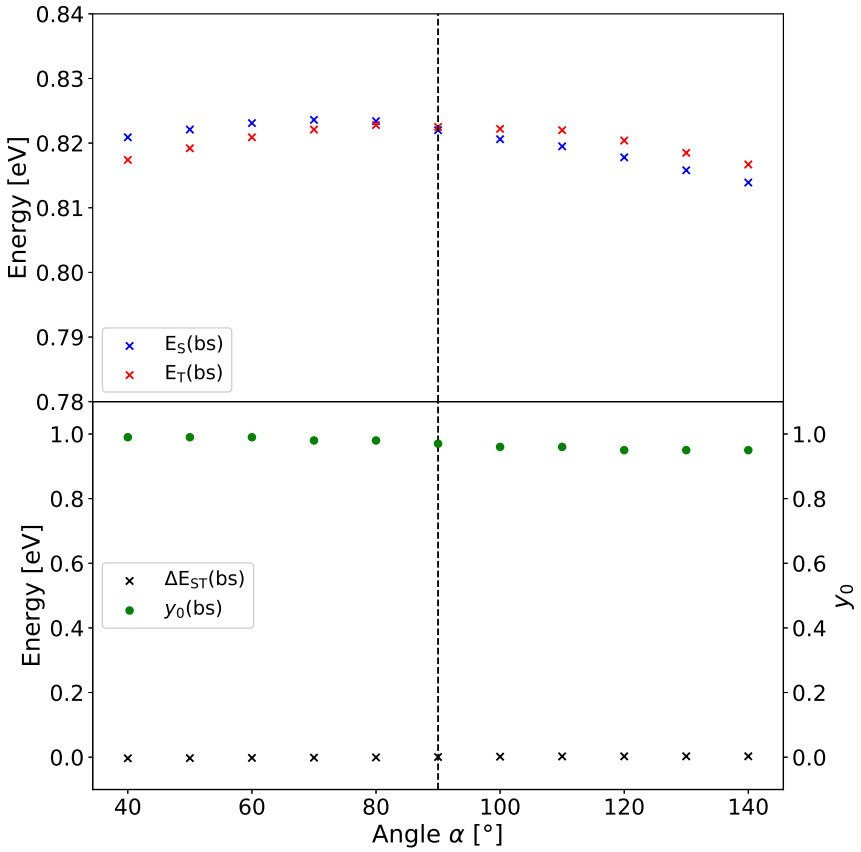

Figure B.5: Excitation energies [eV] of the first singlet and triplet spin-flip excited states (top) and the energy gap between them ΔE_{ST} [eV] obtained using CAM-B3LYP/6-311G* and the diradical character y_0 (bottom) at broken-symmetry geometries of **MD-2** with angles α between 40°-140°.

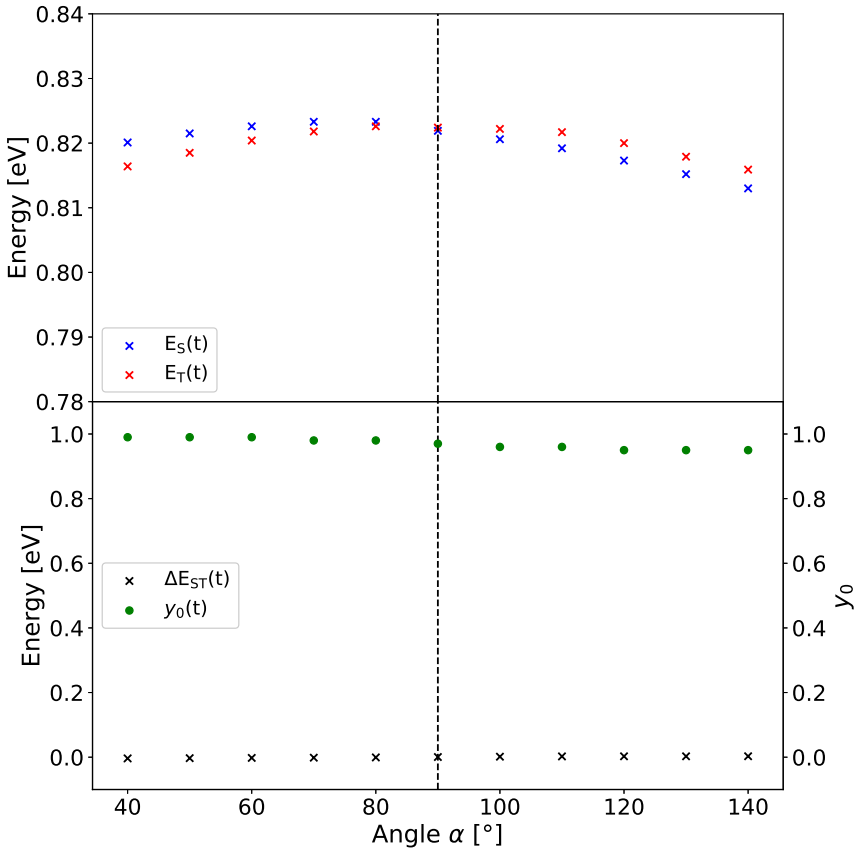

Figure B.6: Excitation energies [eV] of the first singlet and triplet spin-flip excited states (top) and the energy gap between them ΔE_{ST} [eV] obtained using CAM-B3LYP/6-311G* and the diradical character y_0 (bottom) at triplet geometries of **MD-2** with angles α between 40°-140°.

Appendix C

Inverted Singlet-Triplet Gaps in Small Organic Molecules

Table C.1: Total and relative energies of symmetric and unsymmetric geometries of the molecules **1**-**6**.

	E_{total}(sym)	E_{total}(unsym)	ΔE(unsym − sym) [E_h]	ΔE(unsym − sym) [eV]
1	-186.386382	-186.415202	-0.028820	-0.784
2	-170.319363	-170.365033	-0.045671	-1.243
3	-153.037471	-153.051382	-0.013912	-0.379
4	-307.666686	-307.680192	-0.013506	-0.368
5	-323.711169	-323.719281	-0.008111	-0.221
6	-384.971564	-384.971564	-0.00000006	-0.000002

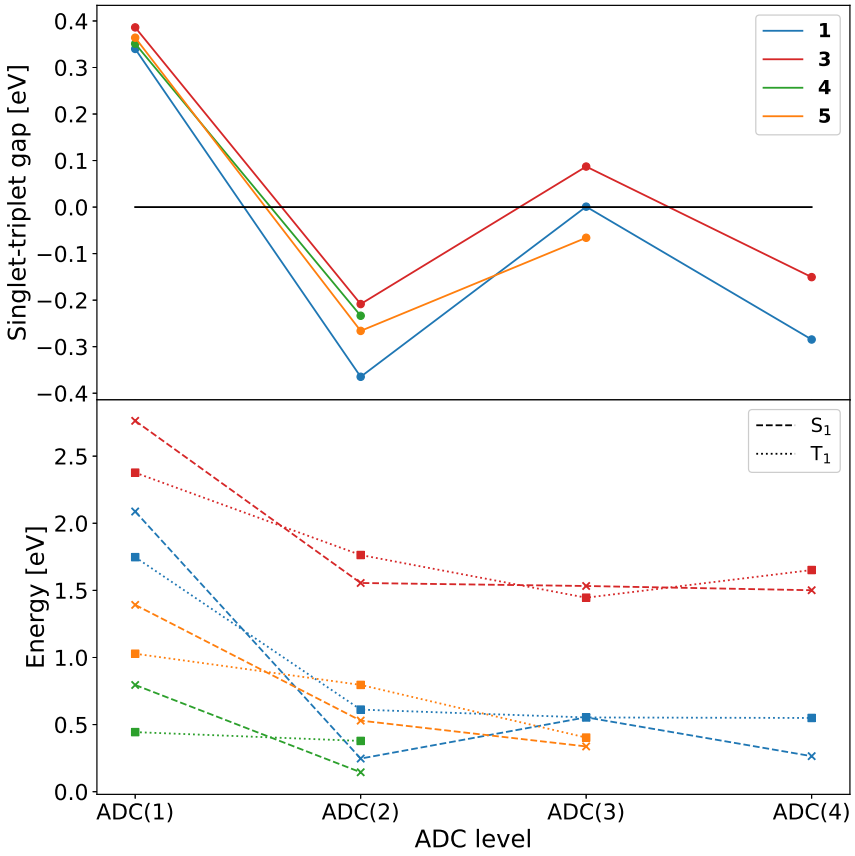

Figure C.1: Singlet-triplet gaps of molecules **1**, **3**, **4** and **5** computed using ADC(1)-ADC(4)/cc-pVTZ (top) and excitation energies of the corresponding singlet and triplet excited states. (bottom)

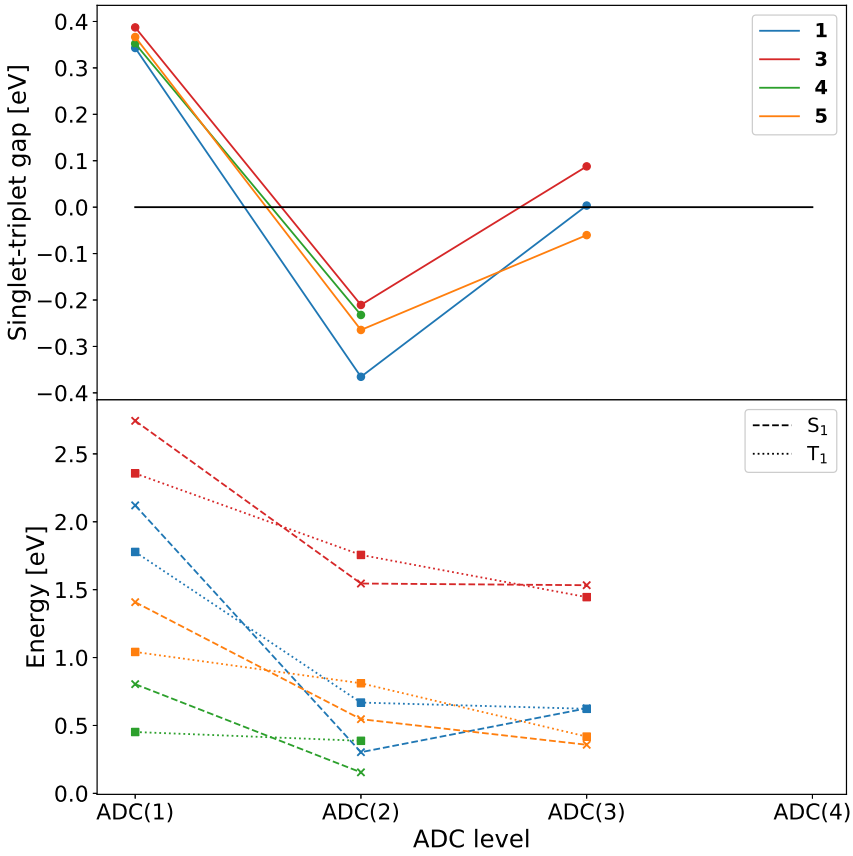

Figure C.2: Singlet-triplet gaps of molecules **1**, **3**, **4** and **5** computed using ADC(1)-ADC(4)/cc-pVQZ (top) and excitation energies of the corresponding singlet and triplet excited states. (bottom)

Table C.2: Excitation energies [eV] for the first excited singlet S_1 and triplet T_1 states and the energy gap between them ΔE for **1-6** using ADC(0)-ADC(4) and EOM-CCSD with the basis set cc-pVTZ at geometries with highest possible geometry.

	1	**3**	**4**	**5**
	D_{2h}	D_{2h}	D_{2h}	C_{2v}
ADC(0)				
S_1	10.271	10.542	7.022	7.742
T_1	10.271	10.542	7.022	7.742
ΔE	0	0	0	0
ADC(1)				
S_1	2.088	2.763	0.795	1.392
T_1	1.748	2.377	0.444	1.028
ΔE	0.340	0.386	0.351	0.364
ADC(2)				
S_1	0.247	1.555	0.145	0.530
T_1	0.612	1.763	0.378	0.796
ΔE	-0.364	-0.208	-0.234	-0.266
ADC(3)				
S_1	0.554	1.533	-[c]	0.337
T_1	0.553	1.446	-	0.403
ΔE	0.001	0.087	-	-0.066
ADC(4)				
S_1	0.265	1.501	-[d]	-[d]
T_1	0.549	1.652	-	-
ΔE	-0.285	-0.151	-	-
EOM-CCSD				
S_1	0.535	1.695	0.189	0.617
T_1	0.657	1.716	0.306	0.749
ΔE	-0.122	-0.022	-0.118	-0.132

[c] Negative excitation energy for S_1 and T_1.

[d] Not feasible due to computational cost.

Table C.3: Excitation energies [eV] for the first excited singlet S_1 and triplet T_1 states and the energy gap between them ΔE for **1**-**6** using ADC(0)-ADC(4) and EOM-CCSD with the basis set cc-pVQZ at geometries with highest possible geometry.

	1	**3**	**4**	**5**
Symmetry	D_{2h}	D_{2h}	D_{2h}	C_{2v}
ADC(0)				
S_1	10.238	10.428	6.995	7.728
T_1	10.238	10.428	6.995	7.728
ΔE	0	0	0	0
ADC(1)				
S_1	2.121	2.744	0.804	1.408
T_1	1.778	2.356	0.452	1.041
ΔE	0.343	0.387	0.3523	0.367
ADC(2)				
S_1	0.303	1.545	0.155	0.546
T_1	0.669	1.756	0.387	0.811
ΔE	-0.365	-0.211	-0.232	-0.265
ADC(3)				
S_1	0.626	1.533	-[c]	0.358
T_1	0.623	1.445	-	0.418
ΔE	0.003	0.088	-	-0.060
ADC(4)				
S_1	-[d]	-[d]	-[d]	[d]
T_1	-	-	-	-
ΔE	-	-	-	-
EOM-CCSD				
S_1	0.609	1.697	-[d]	-[d]
T_1	0.727	1.716	-	-
ΔE	-0.118	-0.019	-	-

[c] Negative excitation energy for S_1 and T_1.

[d] Not feasible due to computational cost.

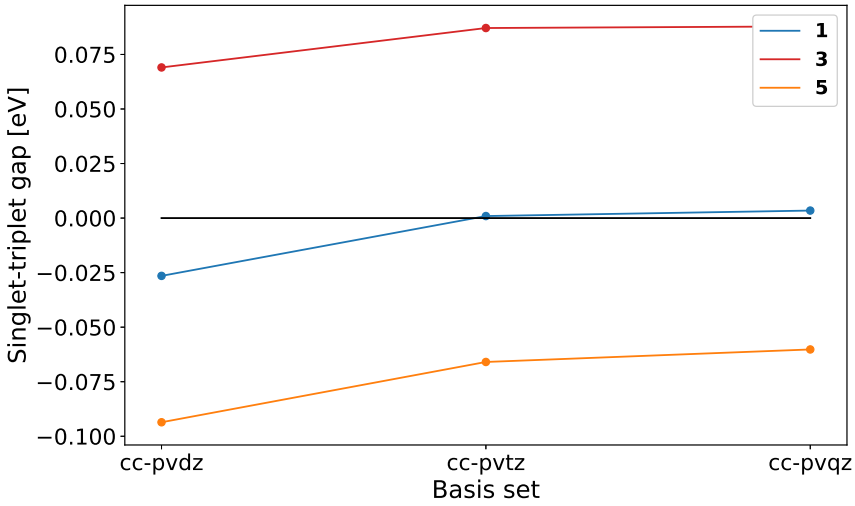

Figure C.3: Singlet-triplet gaps [eV] of molecules **1**, **3**, **4** and **5** computed at the ADC(3) level of theory with the basis sets cc-pVDZ, cc-pVTZ and cc-pVQZ.

Appendix D

Exploration of the Deexcitation Pathway and Design of an RNA Label

Table D.1: Excitation energies [eV], oscillator strengths [10^2] and $\langle\hat{S}^2\rangle$-value of the first ten excited states of **Çm**, **Çm1**, **Çm2** and **Çm3** calculated using TDA/CAM-B3LYP(D3-BJ)/6-311G*.

state	E [eV]	f [10^2]	$\langle\hat{S}^2\rangle$
Çm			
Q_1	3.00	∼0.0	2.75
D_1	3.05	∼0.0	0.75
Q_2	3.62	∼0.0	2.75
Q_3	3.80	0.01	2.68
D_2	4.21	2.80	0.75
Q_4	4.26	∼0.0	2.75
Q_5	4.42	∼0.0	2.73
D_3	4.72	0.71	0.79
Q_6	4.75	∼0.0	2.73
D_4	4.92	∼0.0	0.80
Çm1			
Q_1	2.88	∼0.0	2.75
D_1	3.06	∼0.0	0.75
Q_2	3.57	∼0.0	2.75
D_2	4.13	1.75	0.75
Q_3	4.26	∼0.0	2.75

Q_4	4.45	∼0.0	2.75
Q_5	4.74	∼0.0	2.75
Q_6	4.93	∼0.0	2.75
D_3	5.02	0.93	0.75
D_4	5.20	0.03	0.81
Çm2			
Q_1	3.01	∼0.0	2.75
D_1	3.06	∼0.0	0.75
Q_2	3.63	∼0.0	2.75
Q_3	3.86	∼0.0	2.75
D_2	4.23	2.95	0.75
Q_4	4.25	∼0.0	2.75
Q_5	4.39	∼0.0	2.75
Q_6	4.47	∼0.0	2.75
Q_7	4.74	∼0.0	2.75
D_3	4.79	0.56	0.75
Çm3			
D1	2.68	∼0.0	0.76
Q_1	3.04	∼0.0	2.75
Q_2	3.49	∼0.0	2.74
Q_3	3.67	0.09	2.46
D_2	4.12	1.84	0.79
Q_4	4.25	∼0.0	2.71
Q_5	4.41	0.07	2.51
D_3	4.41	0.54	1.14
Q_6	4.68	∼0.0	2.73
D_4	4.81	0.71	0.83

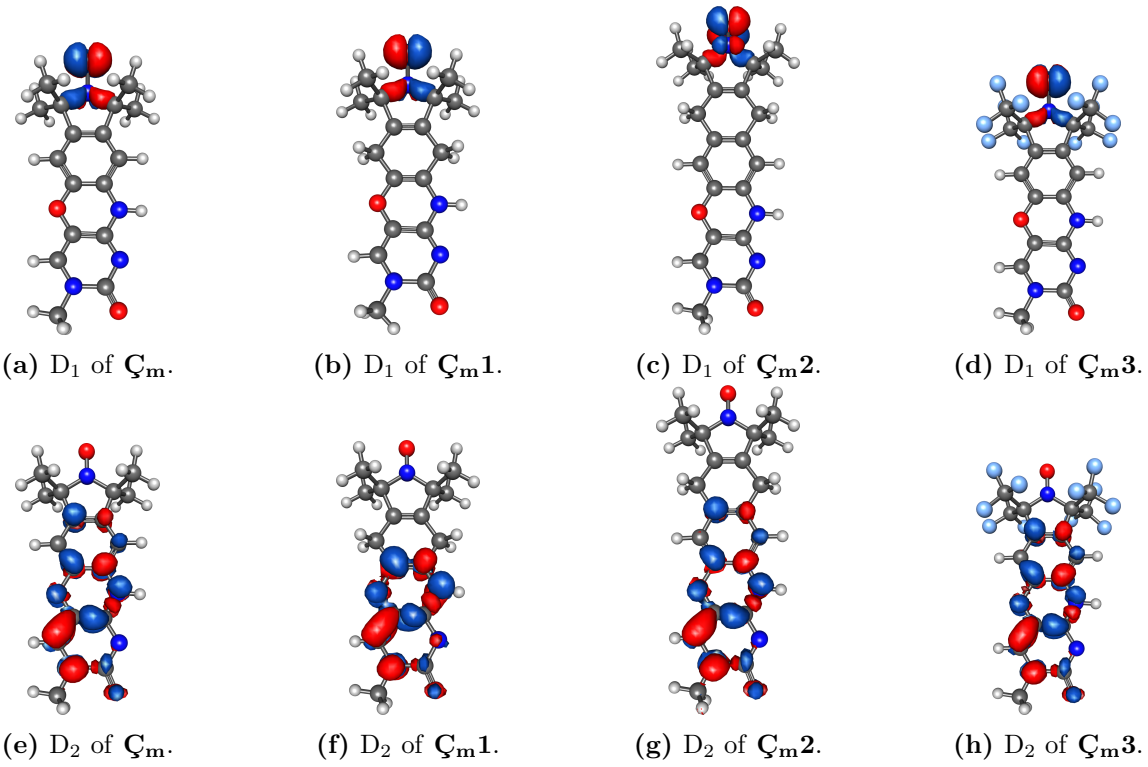

(a) D_1 of **Çm**. **(b)** D_1 of **Çm1**. **(c)** D_1 of **Çm2**. **(d)** D_1 of **Çm3**.

(e) D_2 of **Çm**. **(f)** D_2 of **Çm1**. **(g)** D_2 of **Çm2**. **(h)** D_2 of **Çm3**.

Figure D.1: Transition densities of the excited states D_1 and D_2 of **Çm**, **Çm1**, **Çm2** and **Çm3** at their respective minimum geometries calculated using TDA/CAM-B3LYP(D3-BJ)/6-311G* obtained from averaging the α- and β-transition densities ($\frac{1}{2}(\rho_\alpha + \rho_\beta)$) and visualized using IQmol.

Bibliography

[1] J. E. Anthony, *Chem. Rev.* **2006**, *106*, 5028–5048.

[2] S. Allard, M. Forster, B. Souharce, H. Thiem, U. Scherf, *Angew. Chem. Int. Ed.* **2008**, *47*, 4070–4098.

[3] R. K. Gupta, R. N. Arunagirinathan, M. A. Afroz, R. Garai, A. Choudhury, M. Hossain, R. B. Yathirajula, P. K. Iyer in *Chemical Solution Synthesis for Materials Design and Thin Film Device Applications*, (Eds.: S. Das, S. Dhara), Elsevier, **2021**, pp. 119–165.

[4] S. S. Zade, M. Bendikov, *Angew. Chem. Int. Ed.* **2010**, *49*, 4012–4015.

[5] A. Naibi Lakshminarayana, A. Ong, C. Chi, *J. Mater. Chem. C* **2018**, *6*, 3551–3563.

[6] N. Oberhof, A. E. Hillers-Bendtsen, O. B. Obel, K. Schjelde, K. V. Mikkelsen, A. Dreuw, *Phys. Chem. Chem. Phys.* **2025**, *27*, 96–102.

[7] E. Franz, N. Oberhof, D. Krappmann, N. Baggi, Z. Hussain, K. Moth-Poulsen, H. Hölzel, A. Hirsch, A. Dreuw, O. Brummel, J. Libuda, *Chem. Eur. J.* **2025**, *31*, e02294.

[8] D. Wu, A. C. Sedgwick, T. Gunnlaugsson, E. U. Akkaya, J. Yoon, T. D. James, *Chem. Soc. Rev.* **2017**, *46*, 7105–7123.

[9] J. F. Callan, A. P. de Silva, D. C. Magri, *Tetrahedron* **2005**, *61*, 8551–8588.

[10] K. I. Zamaraev, *Top. Catal.* **1996**, *3*, 1–76.

[11] C. Wan, X. Duan, Y. Huang, *Adv. Energy Mater.* **2020**, *10*, 1903815.

[12] A. M. Diez-Pascual, A. Rahdar, *ChemMedChem* **2022**, *17*, e202200142.

[13] J. Zheng, R. Yang, M. Shi, C. Wu, X. Fang, Y. Li, J. Li, W. Tan, *Chem. Soc. Rev.* **2015**, *44*, 3036–3055.

[14] A. Tunuhe, Z. Zheng, X. Rao, H. Yu, F. Ma, Y. Zhou, S. Xie, *BioDesign Res.* **2025**, *7*, 100004.

[15] H. Gustmann, D. Lefrancois, A. J. Reuss, D. B. Gophane, M. Braun, A. Dreuw, S. T. Sigurdsson, J. Wachtveitl, *Phys. Chem. Chem. Phys.* **2017**, *19*, 26255–26264.

[16] L. Wang, G. Nan, X. Yang, Q. Peng, Q. Li, Z. Shuai, *Chem. Soc. Rev.* **2010**, *39*, 423–434.

[17] A. Pulido, L. Chen, T. Kaczorowski, D. Holden, M. A. Little, S. Y. Chong, B. J. Slater, D. P. McMahon, B. Bonillo, C. J. Stackhouse, et al., *Nature* **2017**, *543*, 657–664.

[18] N. M. OBoyle, C. M. Campbell, G. R. Hutchison, *J. Phys. Chem. C* **2011**, *115*, 16200–16210.

[19] A. B. Zakharov, M. Kyrpa, A. V. Kyrychenko, S. M. Kovalenko, O. N. Kalugin, V. V. Ivanov, L. Adamowicz, *Struct. Chem.* **2025**, *36*, 723–738.

[20] J. Westermayr, J. Gilkes, R. Barrett, R. J. Maurer, *Nat. Comput. Sci.* **2023**, *3*, 139–148.

[21] B. Sanchez-Lengeling, A. Aspuru-Guzik, *Science* **2018**, *361*, 360–365.

[22] Y. Du, A. R. Jamasb, J. Guo, T. Fu, C. Harris, Y. Wang, C. Duan, P. Liò, P. Schwaller, T. L. Blundell, *Nat. Mach. Intell.* **2024**, *6*, 589–604.

[23] W. Sun, Y. Zheng, K. Yang, Q. Zhang, A. A. Shah, Z. Wu, Y. Sun, L. Feng, D. Chen, Z. Xiao, et al., *Sci. Adv.* **2019**, *5*, eaay4275.

[24] K. Fuchs, S. Medina Rivero, A. Weidlich, F. Rominger, N. Israel, A. A. Popov, A. Dreuw, J. Freudenberg, J. Casado, U. H. F. Bunz, *Angew. Chem. Int. Ed.* **2023**, *62*, e202305712.

[25] N. Zeitter, N. Hippchen, A. Weidlich, P. Jäger, P. Ludwig, F. Rominger, A. Dreuw, J. Freudenberg, U. H. F. Bunz, *Chem. Eur. J.* **2023**, *29*, e202302323.

[26] A. Jocic, D. Galindo, A. Weidlich, J. Zerhoch, F. Rominger, T. Buckup, F. Deschler, A. Dreuw, M. Kivala, *Adv. Opt. Mater.* **2024**, *12*, 2401656.

[27] E. Franz, G. Fickenscher, E. J. Schulze, D. Krappmann, A. Weidlich, T. Luchs, A. Dreuw, A. Hirsch, O. Brummel, J. Libuda, *ACS Energy Lett.* **2025**, *10*, 3196–3202.

[28] F. Jensen, *Introduction to computational chemistry*, John wiley & sons, **2017**.

[29] J. R. Platt, *J. Chem. Phys.* **1949**, *17*, 484–495.

[30] E. Clar, R. Schoental, *Polycylic Hydrocarbons*, Acad. Press, London, **1964**.

[31] D. Biermann, W. Schmidt, *J. Am. Chem. Soc.* **1980**, *102*, 3163–3173.

[32] S. S. Zade, M. Bendikov, *J. Phys. Org. Chem.* **2012**, *25*, 452–461.

[33] J. E. Anthony, *Angew. Chem. Int. Ed.* **2008**, *47*, 452–483.

[34] M. Bendikov, H. M. Duong, K. Starkey, K. N. Houk, E. A. Carter, F. Wudl, *J. Am. Chem. Soc.* **2004**, *126*, 7416–7417.

[35] J. Hachmann, J. J. Dorando, M. Avilés, G. K.-L. Chan, *J. Chem. Phys.* **2007**, *127*, 134309.

[36] D. Pines, D. Bohm, *Phys. Rev.* **1952**, *85*, 338–353.

[37] S. A. Bäppler, F. Plasser, M. Wormit, A. Dreuw, *Phys. Rev. A* **2014**, *90*, 052521.

[38] F. Plasser, B. Thomitzni, S. A. Bäppler, J. Wenzel, D. R. Rehn, M. Wormit, A. Dreuw, *J. Comput. Chem.* **2015**, *36*, 1609–1620.

[39] S. A. Mewes, A. Dreuw, *Phys. Chem. Chem. Phys.* **2019**, *21*, 2843–2856.

[40] C. M. Krauter, J. Schirmer, C. R. Jacob, M. Pernpointner, A. Dreuw, *J. Chem. Phys.* **2014**, *141*, 104101.

[41] C. M. Krauter, S. Bernadotte, C. R. Jacob, M. Pernpointner, A. Dreuw, *J. Phys. Chem. C* **2015**, *119*, 24564–24573.

[42] M. Hoffmann, S. A. Mewes, S. Wieland, C. Popp, A. Dreuw, *J. Phys. Chem. Lett.* **2019**, *10*, 6112–6117.

[43] L. Salem, C. Rowland, *Angew. Chem. Int. Ed.* **1972**, *11*, 92–111.

[44] F. Breher, *Coord. Chem. Rev.* **2007**, *251*, 19th Main Group Chemistry, 1007–1043.

[45] M. Abe, *Chem. Rev.* **2013**, *113*, 7011–7088.

[46] H. Koike, M. Chikamatsu, R. Azumi, J. Tsutsumi, K. Ogawa, W. Yamane, T. Nishiuchi, T. Kubo, T. Hasegawa, K. Kanai, *Adv. Funct. Mater.* **2016**, *26*, 277–283.

[47] Y. Zhang, Y. Zheng, H. Zhou, M.-S. Miao, F. Wudl, T.-Q. Nguyen, *Adv. Mater.* **2015**, *27*, 7412–7419.

[48] X. Hu, W. Wang, D. Wang, Y. Zheng, *J. Mater. Chem. C* **2018**, *6*, 11232–11242.

[49] M. Nakano, B. Champagne, *J. Phys. Chem. Lett.* **2015**, *6*, 3236–3256.

[50] Y. Morita, S. Suzuki, K. Sato, T. Takui, *Nat. Chem.* **2011**, *3*, 197–204.

[51] Z. Zeng, X. Shi, C. Chi, J. T. López Navarrete, J. Casado, J. Wu, *Chem. Soc. Rev.* **2015**, *44*, 6578–6596.

[52] G. Tan, X. Wang, *Acc. Chem. Res.* **2017**, *50*, 1997–2006.

[53] C. K. Frederickson, B. D. Rose, M. M. Haley, *Acc. Chem. Res.* **2017**, *50*, 977–987.

[54] P. Hu, J. Wu, *Can. J. Chem.* **2017**, *95*, 223–233.

[55] Y. Li, W.-K. Heng, B. S. Lee, N. Aratani, J. L. Zafra, N. Bao, R. Lee, Y. M. Sung, Z. Sun, K.-W. Huang, R. D. Webster, J. T. López Navarrete, D. Kim, A. Osuka, J. Casado, J. Ding, J. Wu, *J. Am. Chem. Soc.* **2012**, *134*, 14913–14922.

[56] A. Konishi, Y. Hirao, K. Matsumoto, H. Kurata, R. Kishi, Y. Shigeta, M. Nakano, K. Tokunaga, K. Kamada, T. Kubo, *J. Am. Chem. Soc.* **2013**, *135*, 1430–1437.

[57] Z. Zeng, M. Ishida, J. L. Zafra, X. Zhu, Y. M. Sung, N. Bao, R. D. Webster, B. S. Lee, R.-W. Li, W. Zeng, Y. Li, C. Chi, J. T. L. Navarrete, J. Ding, J. Casado, D. Kim, J. Wu, *J. Am. Chem. Soc.* **2013**, *135*, 6363–6371.

[58] A. Shimizu, Y. Hirao, K. Matsumoto, H. Kurata, T. Kubo, M. Uruichi, K. Yakushi, *Chem. Commun.* **2012**, *48*, 5629–5631.

[59] B. Purushothaman, M. Bruzek, S. R. Parkin, A.-F. Miller, J. E. Anthony, *Angew. Chem. Int. Ed.* **2011**, *50*, 7013–7017.

[60] A. Shimizu, R. Kishi, M. Nakano, D. Shiomi, K. Sato, T. Takui, I. Hisaki, M. Miyata, Y. Tobe, *Angew. Chem. Int. Ed.* **2013**, *52*, 6076–6079.

[61] J. J. Dressler, A. Cárdenas Valdivia, R. Kishi, G. E. Rudebusch, A. M. Ventura, B. E. Chastain, C. J. Gómez-García, L. N. Zakharov, M. Nakano, J. Casado, M. M. Haley, *Chem* **2020**, *6*, 1353–1368.

[62] G. E. Rudebusch, J. L. Zafra, K. Jorner, K. Fukuda, J. L. Marshall, I. Arrechea-Marcos, G. L. Espejo, R. Ponce Ortiz, C. J. Gómez-García, L. N. Zakharov, M. Nakano, H. Ottosson, J. Casado, M. M. Haley, *Nat. Chem.* **2016**, *8*, 735–759.

[63] X. Xu, S. Takebayashi, H. Hanayama, S. Vasylevskyi, T. Onishi, T. Ohto, H. Tada, A. Narita, *J. Am. Chem. Soc.* **2023**, *145*, 3891–3896.

[64] D. Casanova, A. I. Krylov, *Phys. Chem. Chem. Phys.* **2020**, *22*, 4326–4342.

[65] Y. Shao, M. Head-Gordon, A. I. Krylov, *J. Chem. Phys.* **2003**, *118*, 4807–4818.

[66] L. V. Slipchenko, A. I. Krylov, *J. Chem. Phys.* **2002**, *117*, 4694–4708.

[67] N. Aizawa, Y.-J. Pu, Y. Harabuchi, A. Nihonyanagi, R. Ibuka, H. Inuzuka, B. Dhara, Y. Koyama, K.-i. Nakayama, S. Maeda, et al., *Nature* **2022**, *609*, 502–506.

[68] Y.-Z. Shi, H. Wu, K. Wang, J. Yu, X.-M. Ou, X.-H. Zhang, *Chem. Sci.* **2022**, *13*, 3625–3651.

[69] H. Nakanotani, Y. Tsuchiya, C. Adachi, *Chem. Lett.* **2021**, *50*, 938–948.

[70] G. Han, Y. Yi, *Angew. Chem.* **2022**, *134*, e202213953.

[71] F. Strieth-Kalthoff, F. Glorius, *Chem* **2020**, *6*, 1888–1903.

[72] F. Hund, *Z. Phys.* **1925**, *33*, 345–371.

[73] J. D. Morgan III, W. Kutzelnigg, *J. Phys. Chem.* **1993**, *97*, 2425–2434.

[74] W. Kutzelnigg, J. Morgan III, *Z. Phys. D* **1996**, *36*, 197–214.

[75] P. de Silva, *J. Phys. Chem. Lett.* **2019**, *10*, 5674–5679.

[76] L. Wrigley, C. W. Schlenker, *Annu. Rev. Phys. Chem.* **2025**, *76*, 329–355.

[77] A. Dreuw, M. Hoffmann, *Front. Chem.* **2023**, *Volume 11 - 2023*.

[78] G. Jeschke, Y. Polyhach, *Phys. Chem. Chem. Phys.* **2007**, *9*, 1895–1910.

[79] G. Z. Sowa, P. Z. Qin in (Ed.: P. M. Conn), Progress in Nucleic Acid Research and Molecular Biology, Acad. Press, **2008**, pp. 147–197.

[80] S. A. Shelke, G. B. Sandholt, S. T. Sigurdsson, *Org. Biomol. Chem.* **2014**, *12*, 7366–7374.

[81] P. Nguyen, P. Z. Qin, *Wiley Interdiscip. Rev. Comput. Mol. Sci. RNA* **2012**, *3*, 62–72.

[82] N. Piton, Y. Mu, G. Stock, T. F. Prisner, O. Schiemann, J. W. Engels, *Nucleic Acids Res.* **2007**, *35*, 3128–3143.

[83] P. Z. Qin, K. Hideg, J. Feigon, W. L. Hubbell, *Biochem.* **2003**, *42*, 6772–6783.

[84] S. Preus, K. Kilså, L. M. Wilhelmsson, B. Albinsson, *Phys. Chem. Chem. Phys.* **2010**, *12*, 8881–8892.

[85] S. Preus, K. Börjesson, K. Kilså, B. Albinsson, L. M. Wilhelmsson, *J. Phys. Chem. B* **2010**, *114*, 1050–1056.

[86] L. M. Wilhelmsson, *Quarterly Reviews of Biophysics* **2010**, *43*, 159–183.

[87] R. Kawai, M. Kimoto, S. Ikeda, T. Mitsui, M. Endo, S. Yokoyama, I. Hirao, *J. Am. Chem. Soc.* **2005**, *127*, 17286–17295.

[88] K. Rombouts, K. Braeckmans, K. Remaut, *Bioconjugate Chem.* **2016**, *27*, 280–297.

[89] M. S. T. Gonçalves, *Chem. Rev.* **2009**, *109*, 190–212.

[90] N. Barhate, P. Cekan, A. P. Massey, S. T. Sigurdsson, *Angew. Chem. Int. Ed.* **2007**, *46*, 2655–2658.

[91] P. Cekan, A. L. Smith, N. Barhate, B. H. Robinson, S. T. Sigurdsson, *Nucleic Acids Res.* **2008**, *36*, 5946–5954.

[92] O. Schiemann, P. Cekan, D. Margraf, T. F. Prisner, S. T. Sigurdsson, *Angew. Chem. Int. Ed.* **2009**, *48*, 3292–3295.

[93] C. M. Grytz, A. Marko, P. Cekan, S. T. Sigurdsson, T. F. Prisner, *Phys. Chem. Chem. Phys.* **2016**, *18*, 2993–3002.

[94] C. Höbartner, G. Sicoli, F. Wachowius, D. B. Gophane, S. T. Sigurdsson, *J. Org. Chem.* **2012**, *77*, 7749–7754.

[95] I. Tkach, S. Pornsuwan, C. Höbartner, F. Wachowius, S. T. Sigurdsson, T. Y. Baranova, U. Diederichsen, G. Sicoli, M. Bennati, *Phys. Chem. Chem. Phys.* **2013**, *15*, 3433–3437.

[96] R. Parr, Y. Weitao, *Density-Functional Theory of Atoms and Molecules*, Oxford University Press, **1994**.

[97] L. H. Thomas in Math. Proc. Camb. Phil. Soc. *Vol. 23*, Cambridge University Press, **1927**, pp. 542–548.

[98] F. Enrico, *Rend. Accad. Naz. Lincei* **1927**, *6*, 602–607.

[99] P. Hohenberg, W. Kohn, *Phys. Rev.* **1964**, *136*, B864.

[100] W. Kohn, L. J. Sham, *Phys. Rev.* **1965**, *140*, A1133.

[101] C. R. Jacob, M. Reiher, *Int. J. Quantum Chem.* **2012**, *112*, 3661–3684.

[102] J. P. Perdew, K. Schmidt in AIP conference proceedings, *Vol. 577*, American Institute of Physics, **2001**, pp. 1–20.

[103] P. A. Dirac in Mathematical proceedings of the Cambridge philosophical society, *Vol. 26*, Cambridge University Press, **1930**, pp. 376–385.

[104] D. M. Ceperley, B. J. Alder, *Phys. Rev. Lett.* **1980**, *45*, 566.

[105] E. Gross, R. Dreizler, *Z. Phys. A* **1981**, *302*, 103–106.

[106] A. D. Becke, *J. Chem. Phys.* **1993**, *98*, 1372–1377.

[107] C. Møller, M. S. Plesset, *Phys. Rev.* **1934**, *46*, 618–622.

[108] S. Grimme, *J. Chem. Phys.* **2006**, *124*.

[109] A. Savin, H.-J. Flad, *Int. J. Quantum Chem.* **1995**, *56*, 327–332.

[110] P. M. Gill, R. D. Adamson, *Chem. Phys. Lett.* **1996**, *261*, 105–110.

[111] P. Hobza, J. poner, T. Reschel, *J. Comput. Chem.* **1995**, *16*, 1315–1325.

[112] S. Kristyán, P. Pulay, *Chem. Phys. Lett.* **1994**, *229*, 175–180.

[113] M. Elstner, P. Hobza, T. Frauenheim, S. Suhai, E. Kaxiras, *J. Chem. Phys.* **2001**, *114*, 5149–5155.

[114] Q. Wu, W. Yang, *J. Chem. Phys.* **2002**, *116*, 515–524.

[115] U. Zimmerli, M. Parrinello, P. Koumoutsakos, *J. Chem. Phys.* **2004**, *120*, 2693–2699.

[116] A. J. Cohen, P. Mori-Sánchez, W. Yang, *Chem. Rev.* **2012**, *112*, 289–320.

[117] E. Runge, E. K. Gross, *Phys. Rev. Lett.* **1984**, *52*, 997.

[118] E. Gross, W. Kohn, *Phys. Rev. Lett.* **1985**, *55*, 2850.

[119] E. Gross, W. Kohn in *Adv. Quantum Chem. Vol. 21*, Elsevier, **1990**, pp. 255–291.

[120] M. E. Casida in *Recent Advances In Density Functional Methods: (Part I)*, World Scientific, **1995**, pp. 155–192.

[121] J. Schirmer, *Phys. Chem. Chem. Phys.* **2025**, *27*, 4992–5005.

[122] R. Bauernschmitt, R. Ahlrichs, *Chem. Phys. Lett.* **1996**, *256*, 454–464.

[123] A. Dreuw, M. Head-Gordon, *Chem. Rev.* **2005**, *105*, 4009–4037.

[124] R. Bauernschmitt, M. Häser, O. Treutler, R. Ahlrichs, *Chem. Phys. Lett.* **1997**, *264*, 573–578.

[125] S. Hirata, M. Head-Gordon, *Chem. Phys. Lett.* **1999**, *302*, 375–382.

[126] S. Hirata, T. J. Lee, M. Head-Gordon, *J. Chem. Phys.* **1999**, *111*, 8904–8912.

[127] J. Schirmer, *Phys. Rev. A* **1982**, *26*, 2395–2416.

[128] W. von Niessen, J. Schirmer, L. S. Cederbaum, *Comput. Phys. Rep.* **1984**, *1*, 57–125.

[129] L. Cederbaum, *Int. J. Quantum Chem.* **1990**, *38*, 393–404.

[130] J. Schirmer, *Phys. Rev. A* **1991**, *43*, 4647.

[131] F. Mertins, J. Schirmer, *Phys. Rev. A* **1996**, *53*, 2140.

[132] F. Mertins, J. Schirmer, A. Tarantelli, *Phys. Rev. A* **1996**, *53*, 2153.

[133] A. Dreuw, A. Papapostolou, A. L. Dempwolff, *J. Phys. Chem. A* **2023**, *127*, 6635–6646.

[134] J. H. Starcke, M. Wormit, A. Dreuw, *J. Chem. Phys.* **2009**, *130*, 024104.

[135] J. Schirmer, A. Trofimov, G. Stelter, *J. Chem. Phys.* **1998**, *109*, 4734–4744.

[136] A. B. Trofimov, J. Schirmer, *J. Chem. Phys.* **2005**, *123*, 144115.

[137] A. Dreuw, M. Wormit, *Wiley Interdiscip. Rev. Comput. Mol. Sci.* **2015**, *5*, 82–95.

[138] **2025**, DOI `doi:10.1351/goldbook.B00671`.

[139] **2025**, DOI `doi:10.1351/goldbook.D01765`.

[140] K. Yamaguchi, *Chem. Phys. Lett.* **1975**, *33*, 330–335.

[141] M. Head-Gordon, *Chem. Phys. Lett.* **2003**, *372*, 508–511.

[142] G. F. Bertsch, A. Bulgac, D. Tománek, Y. Wang, *Phys. Rev. Lett.* **1991**, *67*, 2690–2693.

[143] I. V. Hertel, H. Steger, J. de Vries, B. Weisser, C. Menzel, B. Kamke, W. Kamke, *Phys. Rev. Lett.* **1992**, *68*, 784–787.

[144] C. M. Aikens, S. Li, G. C. Schatz, *J. Phys. Chem. C* **2008**, *112*, 11272–11279.

[145] S. M. Morton, D. W. Silverstein, L. Jensen, *Chem. Rev.* **2011**, *111*, 3962–3994.

[146] S. Bernadotte, F. Evers, C. R. Jacob, *J. Phys. Chem. C* **2013**, *117*, 1863–1878.

[147] A. Manjavacas, F. Marchesin, S. Thongrattanasiri, P. Koval, P. Nordlander, D. Sánchez-Portal, F. J. García de Abajo, *ACS Nano* **2013**, *7*, 3635–3643.

[148] E. B. Guidez, C. M. Aikens, *J. Phys. Chem. C* **2013**, *117*, 21466–21475.

[149] E. B. Guidez, C. M. Aikens, *Nanoscale* **2014**, *6*, 11512–11527.

[150] L. Bursi, A. Calzolari, S. Corni, E. Molinari, *ACS Photonics* **2016**, *3*, 520–525.

[151] R. L. M. Gieseking, A. P. Ashwell, M. A. Ratner, G. C. Schatz, *J. Phys. Chem. C* **2020**, *124*, 3260–3269.

[152] J. Langford, X. Xu, Y. Yang, *J. Phys. Chem. Lett.* **2021**, *12*, 9391–9397.

[153] K. N. Houk, P. S. Lee, M. Nendel, *J. Org. Chem.* **2001**, *66*, 5517–5521.

[154] G. Trinquier, G. David, J.-P. Malrieu, *J. Phys. Chem. A* **2018**, *122*, 6926–6933.

[155] G. Gidofalvi, D. A. Mazziotti, *J. Chem. Phys.* **2008**, *129*, 134108.

[156] B. Hajgató, D. Szieberth, P. Geerlings, F. De Proft, M. S. Deleuze, *J. Chem. Phys.* **2009**, *131*, 224321.

[157] F. Plasser, H. Paali, M. H. Gerzabek, F. Libisch, R. Reiter, J. Burgdörfer, T. Müller, R. Shepard, H. Lischka, *Angew. Chem. Int. Ed.* **2013**, *52*, 2581–2584.

[158] M. Hoffmann, A. Dreuw, *J. Comput. Chem.* **2021**, *42*, 793–800.

[159] M. T. Hoffmann, Ph.D. thesis, Ruprecht Karl University of Heidelberg, **2021**.

[160] V. Ratheesh, M. Sc. thesis, Ruprecht Karl University of Heidelberg, **2025**.

[161] A. I. Krylov, *J. Chem. Phys.* **2021**, *155*, 084801.

[162] T. Yanai, D. P. Tew, N. C. Handy, *Chem. Phys. Lett.* **2004**, *393*, 51–57.

[163] S. Grimme, S. Ehrlich, L. Goerigk, *J. Comput. Chem.* **2011**, *32*, 1456–1465.

[164] R. Krishnan, J. S. Binkley, R. Seeger, J. A. Pople, *J. Chem. Phys.* **1980**, *72*, 650–654.

[165] J. D. Hunter, *Comput. Sci. Eng.* **2007**, *9*, 90–95.

[166] F. Salama, L. J. Allamandola, *J. Chem. Phys.* **1991**, *94*, 6964–6977.

[167] J. Szczepanski, M. Vala, D. Talbi, O. Parisel, Y. Ellinger, *J. Chem. Phys.* **1993**, *98*, 4494–4511.

[168] J. Szczepanski, J. Drawdy, C. Wehlburg, M. Vala, *Chem. Phys. Lett.* **1995**, *245*, 539–548.

[169] A. B. Trofimov, J. Schirmer, *J. Phys. B: At. Mol. Opt. Phys.* **1995**, *28*, 2299.

[170] A. B. Trofimov, G. Stelter, J. Schirmer, *J. Chem. Phys.* **1999**, *111*, 9982–9999.

[171] A. D. Becke, *Phys. Rev. A* **1988**, *38*, 3098–3100.

[172] C. Lee, W. Yang, R. G. Parr, *Phys. Rev. B* **1988**, *37*, 785–789.

[173] A. D. Becke, *J. Chem. Phys.* **1993**, *98*, 1372–1377.

[174] A. D. Becke, *J. Chem. Phys.* **1993**, *98*, 5648–5652.

[175] P. H. P. Harbach, M. Wormit, A. Dreuw, *J. Chem. Phys.* **2014**, *141*, 064113.

[176] C. Niederalt, S. Grimme, S. Peyerimhoff, *Chem. Phys. Lett.* **1995**, *245*, 455–462.

[177] T. M. Halasinski, D. M. Hudgins, F. Salama, L. J. Allamandola, T. Bally, *J. Phys. Chem. A* **2000**, *104*, 7484–7491.

[178] Z.-L. Cai, K. Sendt, J. R. Reimers, *J. Chem. Phys.* **2002**, *117*, 5543–5549.

[179] S. Grimme, M. Parac, *ChemPhysChem* **2003**, *4*, 292–295.

[180] R. M. Richard, J. M. Herbert, *J. Chem. Theory Comput.* **2011**, *7*, 1296–1306.

[181] S. Tretiak, K. Igumenshchev, V. Chernyak, *Phys. Rev. B* **2005**, *71*, 033201.

[182] S. A. Mewes, F. Plasser, A. Dreuw, *J. Chem. Phys.* **2015**, *143*, 171101.

[183] A. Lauchner, A. E. Schlather, A. Manjavacas, Y. Cui, M. J. McClain, G. J. Stec, F. J. García de Abajo, P. Nordlander, N. J. Halas, *Nano Lett.* **2015**, *15*, 6208–6214.

[184] G. J. Stec, A. Lauchner, Y. Cui, P. Nordlander, N. J. Halas, *ACS Nano* **2017**, *11*, 3254–3261.

[185] Z. Sun, S. Lee, K. H. Park, X. Zhu, W. Zhang, B. Zheng, P. Hu, Z. Zeng, S. Das, Y. Li, C. Chi, R.-W. Li, K.-W. Huang, J. Ding, D. Kim, J. Wu, *J. Am. Chem. Soc.* **2013**, *135*, 18229–18236.

[186] M. M. Hansmann, M. Melaimi, D. Munz, G. Bertrand, *J. Am. Chem. Soc.* **2018**, *140*, 2546–2554.

[187] R.-Q. Lu, S. Wu, L.-L. Yang, W.-B. Gao, H. Qu, X.-Y. Wang, J.-B. Chen, C. Tang, H.-Y. Shi, X.-Y. Cao, *Angew. Chem. Int. Ed.* **2019**, *58*, 7600–7605.

[188] S. N. Intorp, M. Hodecker, M. Müller, O. Tverskoy, M. Rosenkranz, E. Dmitrieva, A. A. Popov, F. Rominger, J. Freudenberg, A. Dreuw, U. H. F. Bunz, *Angew. Chem. Int. Ed.* **2020**, *59*, 12396–12401.

[189] F. Weigend, R. Ahlrichs, *Phys. Chem. Chem. Phys.* **2005**, *7*, 3297–3305.

[190] P. v. R. Schleyer, C. Maerker, A. Dransfeld, H. Jiao, N. J. R. van Eikema Hommes, *J. Am. Chem. Soc.* **1996**, *118*, 6317–6318.

[191] F. Neese, *Wiley Interdiscip. Rev. Comput. Mol. Sci. Comput. Molec. Sci.* **2012**, *2*, 73–78.

[192] F. Neese, *Wiley Interdiscip. Rev. Comput. Mol. Sci. Comput. Molec. Sci.* **2022**, *12*, e1606.

[193] M. J. Frisch, G. W. Trucks, H. B. Schlegel, G. E. Scuseria, M. A. Robb, J. R. Cheeseman, G. Scalmani, V. Barone, G. A. Petersson, H. Nakatsuji, X. Li, M. Caricato, A. V. Marenich, J. Bloino, B. G. Janesko, R. Gomperts, B. Mennucci, H. P. Hratchian, J. V. Ortiz, A. F. Izmaylov, J. L. Sonnenberg, D. Williams-Young, F. Ding, F. Lipparini, F. Egidi, J. Goings, B. Peng, A. Petrone, T. Henderson, D. Ranasinghe, V. G. Zakrzewski, J. Gao, N. Rega, G. Zheng, W. Liang, M. Hada, M. Ehara, K. Toyota, R. Fukuda, J. Hasegawa, M. Ishida, T. Nakajima, Y. Honda, O. Kitao, H. Nakai, T. Vreven, K. Throssell, J. A. Montgomery, Jr., J. E. Peralta, F. Ogliaro, M. J. Bearpark, J. J. Heyd, E. N. Brothers, K. N. Kudin, V. N. Staroverov, T. A. Keith, R. Kobayashi, J. Normand, K. Raghavachari, A. P. Rendell, J. C. Burant, S. S. Iyengar, J. Tomasi, M. Cossi, J. M. Millam, M. Klene, C. Adamo, R. Cammi, J. W. Ochterski, R. L. Martin, K. Morokuma, O. Farkas, J. B. Foresman, D. J. Fox, Gaussian16 Revision B.01, Gaussian Inc. Wallingford CT, **2016**.

[194] C. Bannwarth, S. Ehlert, S. Grimme, *J. Chem. Theory Comput.* **2019**, *15*, 1652–1671.

[195] S. Grimme, J. G. Brandenburg, C. Bannwarth, A. Hansen, *J. Chem. Phys.* **2015**, *143*, 054107.

[196] M. Segal, M. Baldo, R. Holmes, S. Forrest, Z. Soos, *Phys. Rev. B* **2003**, *68*, 075211.

[197] M. A. Baldo, D. Obrien, M. Thompson, S. Forrest, *Phys. Rev. B* **1999**, *60*, 14422.

[198] H. Uoyama, K. Goushi, K. Shizu, H. Nomura, C. Adachi, *Nature* **2012**, *492*, 234–238.

[199] X.-K. Chen, D. Kim, J.-L. Brédas, *Acc. Chem. Res.* **2018**, *51*, 2215–2224.

[200] J. Eng, T. J. Penfold, *Commun. Chem.* **2021**, *4*, 91.

[201] T.-A. Lin, T. Chatterjee, W.-L. Tsai, W.-K. Lee, M.-J. Wu, M. Jiao, K.-C. Pan, C.-L. Yi, C.-L. Chung, K.-T. Wong, et al., *Adv. Mater.* **2016**, *28*, 6976–6983.

[202] W. T. Borden, *J. Am. Chem. Soc.* **1975**, *97*, 5968–5970.

[203] H. Kollmar, V. Staemmler, *J. Am. Chem. Soc.* **1977**, *99*, 3583–3587.

[204] H. Kollmar, V. Staemmler, *Theor. Chim. Acta* **1978**, *48*, 223–239.

[205] S. Koseki, T. Nakajima, A. Toyota, *Can. J. Chem.* **1985**, *63*, 1572–1579.

[206] J. Ehrmaier, E. J. Rabe, S. R. Pristash, K. L. Corp, C. W. Schlenker, A. L. Sobolewski, W. Domcke, *J. Phys. Chem. A* **2019**, *123*, 8099–8108.

[207] J. C. Slater, *Phys. Rev.* **1929**, *34*, 1293.

[208] R. F. Bader, A. Streitwieser, A. Neuhaus, K. E. Laidig, P. Speers, *J. Am. Chem. Soc.* **1996**, *118*, 4959–4965.

[209] R. Pollice, B. Ding, A. Aspuru-Guzik, *Matter* **2024**, *7*, 1161–1186.

[210] F. Weigend, M. Häser, H. Patzelt, R. Ahlrichs, *Chem. Phys. Lett.* **1998**, *294*, 143–152.

[211] F. Weigend, A. Köhn, C. Hättig, *J. Chem. Phys.* **2002**, *116*, 3175–3183.

[212] J. Dunning, Thom H., *J. Chem. Phys.* **1989**, *90*, 1007–1023.

[213] D. E. Woon, J. Dunning, Thom H., *J. Chem. Phys.* **1993**, *98*, 1358–1371.

[214] J. Leitner, A. L. Dempwolff, A. Dreuw, *J. Chem. Phys.* **2022**, *157*, 184101.

[215] H. Koch, P. Jo/rgensen, *J. Chem. Phys.* **1990**, *93*, 3333–3344.

[216] J. F. Stanton, R. J. Bartlett, *J. Chem. Phys.* **1993**, *98*, 7029–7039.

[217] A. J. Müller, D. R. Rehn, A. Dreuw, *in preparation*.

[218] G. Ricci, E. San-Fabián, Y. Olivier, J.-C. Sancho-García, *ChemPhysChem* **2021**, *22*, 553–560.

[219] S. Ghosh, K. Bhattacharyya, *J. Phys. Chem. A* **2022**, *126*, 1378–1385.

[220] P.-F. Loos, F. Lipparini, D. Jacquemin, *J. Phys. Chem. Lett.* **2023**, *14*, 11069–11075.

[221] F. Neese, *Wiley Interdiscip. Rev. Comput. Mol. Sci.* **2025**, *15*, e70019.

[222] J. T. Taylor, D. J. Tozer, B. F. E. Curchod, *J. Chem. Phys.* **2023**, *159*, 214115.

[223] K. Shizu, H. Kaji, *J. Phys. Chem. A* **2021**, *125*, 9000–9010.

[224] T. Nakajima, S. Kato, *J. Chem. Phys.* **1996**, *105*, 5927–5938.

[225] K. Miyazaki, N. Ananth, *J. Chem. Phys.* **2022**, *156*, 044111.

[226] R. A. Marcus, *J. Chem. Phys.* **1956**, *24*, 966–978.

[227] R. A. Marcus, *J. Chem. Phys.* **1984**, *81*, 4494–4500.

[228] R. A. Marcus, *Rev. Mod. Phys.* **1993**, *65*, 599–610.

[229] R. A. Marcus, *J. Chem. Phys.* **1956**, *24*, 979–989.

[230] A. S. Bozzi, W. R. Rocha, *J. Chem. Theory Comput.* **2023**, *19*, 2316–2326.

List of Publications

- K. Fuchs, S. Medina Rivero, A. Weidlich, F. Rominger, N. Israel, A. A. Popov, A. Dreuw, J. Freudenberg, J. Casado and U. H. F. Bunz, "Dimerization of a Reactive Azaacene Diradical: Synthesis of a Covalent Azaacene Cage", *Angew. Chem. Int. Ed.* **2023**, *62*, e202305712.
- N. Zeitter, N. Hippchen, A. Weidlich, P. Jäger, P. Ludwig, F. Rominger, A. Dreuw, J. Freudenberg and U. H. F., "Hexakis-TIPS-Alkynylated Nonacenes: Persistent and Processible", *Chem. Eur. J.*, **2023**, *29*, e202302323.
- A. Jocic, D. Galindo, A. Weidlich, J. Zerhoch, F. Rominger, T. Buckup, F. Deschler, A. Dreuw and M. Kivala, "Control of Photoinduced Charge Transfer Through Selective Cyanation of Spirofluorene-Bridged N-Heterotriangulenes", *Adv. Opt. Mater.*, **2024**, *12*, 2401656.
- A. M. Weidlich and A. Dreuw, "The Relation Between the Excited Electronic States of Acene Radical Cations and Neutrals - A Computational Analysis", *J. Comput. Chem.*, **2025**, *46*, e70095.
- E. Franz, G. Fickenscher, E. J. Schulze, D. Krappmann, A. Weidlich, T. Luchs, A. Dreuw, A. Hirsch, O. Brummel and J. Libuda, "Electroswitchable Noble-Metal-Free Catalysis for Molecular Solar Thermal Systems", *ACS Energy Lett.*, **2025**, *10*, 3196-3202.
- A. M. Weidlich and A. Dreuw, "Molecular Excitons and Plasmons in Acenes and Their Radical Cations", *J. Comput. Chem.*, **2025**, *46*,e70211.

Manuscripts in Preparation

- P. Merten, S. Maier, F. Jester, F. Rominger, G. Sauter, A. Pollien, B. Beier, A. Weidlich, J. Freudenberg, A. Dreuw, R. Klingeler, P. Tegeder, U. H. F. Bunz, "Indeno-Diazatetracene-σ-Dimer: A Diradical with High Two-Photon Absorption Cross Sections", manuscript in preparation.
- A. Jocic, A. Weidlich, J. Dannenberger, F. Rominger, A. Dreuw, E. Zysman-Colman, M. Kivala, "Modulating the Photoluminescence Properties of Cyano-Functionalized Spiro-Bridged N-heterotriangulenes Between Pronounced Thermally Activated Delayed Fluorescence and Fast Room Temperature Phosphorescence", manuscript in preparation.
- L. Martins, A. Weidlich, P. de Bary, F. Rominger, A. Dreuw, M. Kivala, "Tuning the Diradical Character of p-Expanded Cyclopenta-Bridged Tetraphenylene: From Closed-shell to Open-shell Singlet Groud States", manuscript in preparation.
- V. Ratheesh, A. Weidlich, A. Dreuw, "Tuning Excited-State Properties of Anthracenes through Heteroatom Substitution", manuscript in preparation.

Danksagung

Zunächst möchte ich mich bedanken bei Prof. Dr. Andreas Dreuw dafür, dass ich meine Promotion in seiner Arbeitsgruppe absolvieren durfte. Außerdem danke ich ihm für die offene Atmosphäre in der Arbeitsgruppe und dafür, dass ich meine Projekte selbstständig bearbeiten und auch Interessen über das Promotionsthema hinaus verfolgen durfte.
Meinen Dank möchte ich auch aussprechen gegenüber Felicitas und Manfred, dafür, dass sie mir bei (verwaltungs)technischen Fragen und Problemen geholfen haben und immer eine Lösung parat hatten.
Bei den ehemaligen Mitgliedern der Arbeitsgruppe Dr. Nils Oberhof, Dr. Marco Bauer, Dr. Sebastian Thielen und Dr. Benjamin Thomitzni und allen weiteren aktuellen Mitgliedern der DAP Gruppe Antonia Papapostolou, Anna Ulrich, Friederike Schneider, Moritz Huber, Adrian Müller, Oscar Obel, Dr. Dirk Rehn, Lin Tian, Vyshna Ratheesh, Lukas Rindt, Jonas Leitner, Tobias Kaczun, Dr. Adrian Dempwolff, Dr. Philipp Pracht, Dr. Adem Kulahlioglu, Dr. Giovanni Parolin, Prof. Dr. Saeed Amirjalayer, Linus Dittmer, Sebastian Pauly, Letao Huang, Linghua Zhang, Dr. Golokesh Santra, Melih Ceylan und Christoph Popko möchte ich mich bedanken für das schöne Gruppenleben. Insbesondere danke ich Antonia, Freddy, Nils, Lin, Vyshna, Tobi, Jonas, Adrian II, Adrian III, Linus, Sebastian, Letao, Sebi, Ben, Dirk und Marco, die meine Zeit im Arbeitskreis besonders geprägt haben, für die schöne Zeit, die Unterstützung in allen Fragen und dafür, dass irgendjemand immer irgendwelchen Unsinn im Schilde führt. Euretwegen hat zur Arbeit gehen und meine Freunde sehen die letzten Jahre das Selbe bedeutet. Ich möchte mich bei Freddy bedanken für die schöne Atmosphäre in unserem Büro, für die Hilfe bei verschiedensten Fragen und für alle spontanen kleinen Pausen bei der Arbeit. Außerdem möchte ich mich besonders bedanken bei Antonia, für ihre Unterstützung in vielerlei Hinsicht und für die gemeinsamen Erlebnisse von Bartouren bis zum Kraftraum. Ich bin sehr glücklich darüber, dass wir seit der Bachelorarbeit unseren Weg gewissermaßen ein Stück weit zusammen gegangen sind.
Für das Korrekturlesen meiner Dissertation bedanke ich mich bei Antonia, Freddy, Adrian II, Adrian III, Tobi und Marco. Vielen Dank für eure Hilfe!
Des Weiteren bedanke ich mich bei meinen Kollaborationspartnern Dr. Kathleen Fuchs, Dr. Nico Zeitter, Angelina Jocic, Dr. Evanie Franz, Dr. Philipp Ludwig, Pascal Merten, Leon Martins, Sven Mühl, PD Dr. Markus Braun, Prof. Dr. Uwe Bunz und Prof. Dr. Milan Kivala, sowie bei den Studierenden, die ich betreuen durfte Sonya Höhne, Lukas Becker, Luca Mailänder, Sara Murray, Owen Paine, Patrick Mayerhofer, Julian Oczlon, Lilliana Florido Martins, Eva Roeski, Abdinasir Adow, Simon Weipert, Jakob Alberts, Pascal Bootz, Vyshna Ratheesh und Jose Morales für die Zusammenarbeit.
Auch möchte ich meinen Dank aussprechen gegenüber der Heidelberg Graduate School of Mathematical and Computational Methods for the Sciences für die finanzielle Unterstütung von Dien-

streisen und Kursen während meiner Promotion.
Ganz besonders möchte ich mich auch bedanken, im Namen von Marco und mir, bei Prof. Dr. Andreas Dreuw und Prof. Dr. Patrick Norman, dafür, dass wir beide Arbeitsplätze in Heidelberg und Stockholm haben durften, was uns unser Leben sehr erleichtert hat.
Ich bedanke mich herzlich bei meinen Freunden und bei meiner Familie, dafür, dass sie mich unterstützen und für mich da sind. Vielen Dank an meine PubQuiz-Gruppe für die schönen Quiz-Abende, die immer ein guter Start in die Woche waren. Insbesondere danke ich meinen Eltern ohne deren Unterstützung ich mein Studium und meine Promotion nicht hätte absolvieren können.
Abschließend gilt mein besonderer Dank Marco, dafür, dass er mich in allen meinen Ideen und Zielen unterstützt, mir zur Seite steht und immer für mich da ist. Danke für alles!

Eidesstattliche Versicherung gemäß §8 der Promotionsordnung für die Gesamtfakultät für Mathematik, Ingenieur- und Naturwissenschaften der Universität Heidelberg

1. Bei der eingereichten Dissertation zu dem Thema **"Quantum Chemical Investigation of Open-Shell Functional Organic Molecules"** handelt es sich um meine eigenständig erbrachte Leistung.

2. Ich habe nur die angegebenen Quellen und Hilfsmittel (inkl. KI-basierter Hilfsmittel) benutzt und mich keiner unzulässigen Hilfe Dritter bedient. Insbesondere habe ich wörtlich oder sinngemäß aus anderen Werken übernommene Inhalte als solche kenntlich gemacht.

3. Die Arbeit oder Teile davon habe ich bislang nicht an einer anderen Hochschule des In- oder Auslands als Bestandteil einer Prüfungs- oder Qualifikationsleistung vorgelegt.

4. Die Richtigkeit der vorstehenden Erklärungen bestätige ich.

5. Die Bedeutung der eidesstattlichen Versicherung und die strafrechtlichen Folgen einer unrichtigen oder unvollständigen eidesstattlichen Versicherung sind mir bekannt.

Ich versichere an Eides statt, dass ich nach bestem Wissen die reine Wahrheit erklärt und nichts verschwiegen habe.

Ort, Datum: _____ Unterschrift: _____